Solution of Linear Elastostatic and Elastodynamic Plane Problems by the Meshless Local Petrov-Galerkin Method

Hsu-Kuang Ching

Dissertation submitted to the Faculty of the
Virginia Polytechnic Institute and State University
in partial fulfillment of the requirements for the degree of

Doctor of Philosophy
in
Engineering Mechanics

Prof. Romesh C. Batra, Chair
Prof. Scott L. Hendricks
Prof. Rakesh K. Kapania
Prof. Liviu Librescu
Prof. Surot Thangjitham

July 11, 2002
Blacksburg, Virginia

Keywords: MLPG method, *J*-integral, Stress intensity factors, Coulomb friction, The Newmark family of methods

Solution of Linear Elastostatic and Elastodynamic Plane Prolems by the Meshless Local Petrov-Galerkin Method

Hsu-Kuang Ching

(Abstract)

The meshless local Petrov-Galerkin (MLPG) method is used to numerically find an approximate solution of plane strain/stress linear elastostatic and elastodynamic problems. The MLPG method requires only a set of nodes both for the interpolation of the solution variables and the evaluation of various integrals appearing in the problem formulation. The monomial basis functions in the MLPG formulation have been enriched with those for the linear elastic fracture mechanics solutions near a crack tip. Also, the diffraction and the visibility criteria have been added to make the displacement field discontinuous across a crack. A computer code has been developed in Fortran and validated by comparing computed solutions of three static and one dynamic problem with their analytical solutions. The capabilities of the code have been extended to analyze contact problems in which a displacement component and the complementary traction component are prescribed at the same point of the boundary.

The code has been used to analyze stress and deformation fields near a crack tip and to find the stress intensity factors by using contour integrals, the equivalent domain integrals and the *J*-integral and from the intercepts with the ordinate of the plots, on a logarithmic scale, of the stress components versus the distance ahead of the crack tip. We have also computed time histories of the stress intensity factors at the tips of a central crack in a rectangular plate with plate edges parallel to the crack loaded in tension. These are found to compare favorably with those available in the literature. The code has been used to compute time histories of the stress intensity factors in a double edge-notched plate with the smooth edge between the notches loaded in compression. It is found that the deformation fields near the notch tip are mode-II dominant. The mode mixity parameter can be changed in an orthotropic plate by adjusting the ratio of the Young's moduli in the axial and the transverse direction.

The plane strain problem of compressing a linear elastic material confined in a rectangular cavity with rough horizontal walls and a smooth vertical wall has been studied with the developed code. Computed displacements and stresses are found to agree well with the analytical solution of the problem obtained by the Laplace transform technique.

The Appendix describes the analysis with the finite element code ABAQUS of the dependence of the energy release rate upon the crack length in a polymeric disk enclosed in a steel ring and having a star shaped hole at its center. A starter crack is assumed to exist in one of the leaflets of the hole. The disk is loaded either by a pressure acting on the surfaces of the hole and the crack or by a temperature rise. Computed values of the energy release rate obtained by modeling the disk material as Hookean are found to be about 30% higher than those obtained when the disk material is modeled as Mooney-Rivlin. The latter set of results accounts for both material and geometric nonlinearities.

Acknowledgments

First and foremost, I would like to express my gratitude and appreciation to my advisor, Professor Romesh C. Batra for his invaluable guidance, continuous support and great patience during the course of this study. I would also like to thank Professors Scott L. Hendricks, Rakesh K. Kapania, Liviu Librescu and Surot Thangjitham for their helpful suggestions and for making time in their busy schedules to serve on my committee. Special thanks are due to Professor David Y. Gao for his encouragement.

I would like to thank all the friends I have met in Balcksburg. In particular, I would like to thank Professor Senthil S. Vel and Dr. Naim Jaber for the constructive discussions about my research work. In addition, thanks to Dr. Twzen-Shang Geng, Mr. Ravisankar Mattipalli, Mr. Matthew Lear, Mr. Zhongfu Ge and Mr. Xiaopeng Zhao for their friendship.

I would like to thank Professors Edmund G. Henneke and Don H. Morris for the financial support I had during my studies as a teaching assistant in the Department of Engineering Science and Mechanics. I am also grateful to Ms. Loretta Tickle for taking care of my student records, Ms. Norma Guynn for typing my papers for publications and Mr. Tim Tomlin for solving technical problems whenever I have difficulties using computers in the ESM Computer Lab.

Furthermore, I would like to acknowledge the support of the Office of Naval Research (ONR) under grant N00014-98-1-0300 to Virginia Polytechnics Institute and State University with Dr. Y. D. S. Rajapakse as the program manager and Prof. Batra as the principal investigator.

I would like to thank my girlfriend, Miss Xiaolan Song, for her love and care. Her presence in my life enriched my mind and made me happier.

I am greatly indebted to my brothers and sisters, and especially, my sister, Mei-Kuang Cheng and brother-in-law, John Cheng for their support over the past years.

Most importantly, my deepest thanks go to my parents Jui-Hsien Ching and Tong-Sung Kwan Ching for their dedication and inspiration that enabled me to reach this milestone in my life.

Contents

List of Figures

List of Tables

Chapter 1

Introduction

Abstract

This chapter very briefly reviews the literature on meshless methods. The Meshless Local Petrov-Galerkin (MLPG) method is adopted to solve plane strain/stress solid mechanics problems. The MLPG formulation including the moving least squares method, the choice of the weight function, the local symmetric weak form (LSWF), and the discretization of the weak form are presented. A code based on the MLPG method is developed, and three numerical examples, namely, a cantilever beam loaded by tangential tractions at the unclamped edge, an infinite plate with a circular hole subjected to a uniform tensile force at infinity, and a hollow circular cylinder subjected to a pressure on the inner surface are demonstrated to validate the developed code.

Key Words: MLPG; Moving least squares (MLS) approximation; Weight function; Local symmetric weak form.

1.1 Literature Review

Over the past 50 years, the finite element method (FEM) has been a popular method for solving problems in solid mechanics. However, there are certain classes of problems for which the finite element method is not very suitable. For example, in the simulation of problems with moving discontinuities such as crack growth, the finite element method may require frequent remeshing of the domain ahead of the crack. Such remeshings can lead to the degradation of the solution.

In the last two decades, a newly developed numerical approach using the particle-based discretization has gradually emerged as an effective tool to solve boundary value problems. The essential feature of this approach is that it only requires a set of node points to construct the approximate solution and does not require any connectivity among nodes. In contrast to the conventional finite element method, this numerical approach saves the work of mesh generation as no element is required in the entire model. Furthermore, remeshing appears easier because nodes can be easily added or removed in the analysis domain. In view of its convenience and flexibility in use, this particle-based method has gained considerable attention in the computational mechanics community.

This method is often called meshless, meshfree, gridless, or particle methods. Due to the lack of a unified name, this numerical approach will be termed as “meshless method” in this dissertation.

A large variety of different meshless methods have been developed in the last few years such as the Smooth Particle Hydrodynamics (SPH), the Diffuse Element Method (DEM), the Element-Free Galerkin (EFG) method, the Hp-Clouds, the Reproducing Kernel Particle Method (RKPM), the Partition of Unity Finite Element Method (PUFEM), and the Meshless Local Petrov-Galerkin method (MLPG). All meshless methods share a common feature: only nodes are required to describe the interpolation of field variables. The major difference among these methods lies in the interpolation techniques. Generally, three different

interpolation techniques used in meshless methods are the kernel method, the moving least squares approximation and the partition of unity.

Although the meshless method is just becoming popular in recent years, the initial use of this method dates back to the late 1970's. Lucy (1977) introduced the Smooth Particle Hydrodynamics (SPH) for simulating astrophysical phenomena. Monaghan (1982) provided a theoretical aspect for the interpolation scheme of the SPH by adopting the notion of a kernel function. This kernel function allows a local representation for the trial function. Libersky and Petchek (1991) applied this method to solve solid mechanics problems.

Nayroles et al. (1992) proposed another branch of the meshless method under the name of the Diffuse Element Method (DEM). This method is based on the moving least squares (MLS) approximation which had been developed by Lancaster and Salkauskas (1981) for curve and surface fitting of random data. Belytschko et al. (1994) made improvements to the DEM and developed the Element Free Galerkin (EFG) method. For example, a high-order quadrature rule based on a background mesh of cells was used and certain terms in the derivatives of the interpolants, which were omitted in the DEM, were included in the EFG method. These improvements were found to be necessary for achieving good accuracy and convergence.

Liu et al. (1995) introduced a correction function in the kernel of the integral transformation in the SPH to impose reproducing conditions (i.e., consistency requirements). Adding this correction function in the kernel enhances the accuracy of the solution when compared with the SPH. This method using integral transformation with a corrected kernel function is called the Reproducing Kernel Particle Method (RKPM). Belytschko et al. (1996) have shown that the discrete form of the convolution integral yields approximants which are identical to those in the MLS approximation.

Duarte and Oden (1996), and Melenk and Babuska (1996) proposed the Hp-Clouds method and the Partition of Unity Finite Element Method (PUFEM), respectively. Both methods employ a partition of unity to construct the meshless approximation. They

recognized that the method based on the moving least squares is a specific case of the partition of unity. The Hp-Clouds and the PUFEM allow for an extrinsic basis to enhance the solution.

Similarities in some of the above meshless methods have been summarized by Belytschko et al. (1996), and Duarte (1995). However, the above-mentioned meshless methods use background cells or shadow elements to integrate a global Galerkin weak formulation. The requirement of background cells for integration implies that the method is not "truly meshless".

Atluri and Zhu (1998) presented a "true meshless" method that does not require an explicit mesh either for the interpolation of solution variables or for the integration of the weak formulation. This method is based on a local symmetric weak form (LSWF) in conjunction with the moving least squares approximation and thus is known as the Meshless Local Petrov-Galerkin (MLPG) method. In the MLPG method, the weak formulation is constructed over a sub-domain (usually taken as a circle in 2 dimensional problems and a sphere in 3 dimensional problems). All integrals in this formulation are carried out over a regularly shaped domain using Gauss quadrature, thereby eliminating the need for a background mesh.

Atluri et al. (1999a) have pointed out that, by taking test functions the same as the basis functions for the trial solution, this MLPG method reduces to the Galerkin method and leads to a symmetric stiffness matrix. Atluri et al. (1999b) have extended the moving least squares approximation by incorporating the derivative of the field variables into this interpolation scheme so that an approximate solution of fourth-order differential equations can be obtained.

Elasto-statics problems by using the MLPG method have been studied by Atluri and Zhu (2000); they examined its accuracy and convergence by numerical experiments. In the MLPG method the computed stresses and strains vary smoothly in the domain. Numerical results show that this method gives good results for nearly incompressible materials. Kim and

Atluri (2000) demonstrated the use of the secondary nodes in conjunction with the MLPG method. The secondary nodes allow for the adaptive computation by adding nodes at any location and achieve a priori prescribed accuracy.

Lin and Atluri (2000a) introduced the upwinding scheme in the MLPG method to analyze steady convection-diffusion problems. Good results are obtained even for flows with very high Peclet numbers. Lin and Atluri (2000b) also solved the incompressible Navier-Stokes equations by adding the "perturbation" terms into the mixed weak form to overcome the Babuska-Brezzi stability condition. Thus, the spurious pressure and velocity fields were eliminated.

The meshless methods are not computationally as efficient as finite element methods. It is desirable to use the meshless model only in those domains where their greater versatility is needed and the finite element model for the rest of the domain and on the boundary where the essential boundary conditions can be exactly satisfied. Liu and Gu (2000) coupled the MLPG method with either the finite element or the boundary element method to enhance the efficiency of the MLPG method.

Ching and Batra (2001) augmented the polynomial basis functions in the MLPG method with the enriched basis functions. They used either the visibility or the diffraction criterion to account for discontinuous displacement fields across a crack and analyzed 2D mixed-mode problems. Numerical results are presented for several examples, and the singular stress fields near a crack tip were well predicted. The computed stress intensity factors agreed well with the available reference values. Gu and Liu (2001a,b) applied the MLPG method to free and forced vibrations of a beam and a thin plate. Due to the ill-conditioning of the stiffness matrix caused by the penalty method used to satisfy the essential boundary conditions, an orthogonal transformation technique was utilized to implement the essential boundary conditions so that frequecies and eigenmodes can be accurately obtained. In the forced vibration analysis, both the Newmark method and the central difference method were used for the time integration schemes.

Warlock et al. (2002) analyzed analytically by the Laplace transformation technique and numerically by the MLPG method, the plane-strain deformations of an elastic material compressed in a rough rectangular cavity. Constraints imposed by the contact conditions were satisfied by using the penalty method.

Long and Atluri (2002) have presented a MLPG solution for the bending of a thin plate. The numerical examples showed that highly accurate solutions can be obtained for the clamped and simply-supported plates. Atluri and Shen (2002) have summarized the current development of the MLPG method, and have compared the efficiency and accuracy of a variety of trial and test functions. Numerical examples reveal that some of these MLPG methods posses better convergence rate and incur less computational cost than the FEM or the BEM.

The author believes that the MLPG method will have the same importance as the well-known Galerkin finite element method in future.

1.2 Meshless Local Petrov-Galerkin Method

In this section, the moving least squares approximation and the weak formulation on which the MLPG method is based are introduced. We use the MLPG method as a numerical tool to solve solid mechanics problems. The following derivation of the MLPG formulation is borrowed from Atluri and Zhu (2000a).

1.2.1 Moving least squares approximation

In the MLPG method, the field variable $u(\mathbf{x})$ is approximated by the moving least squares (MLS) technique. This approximation is based on three components: a weight function of compact support associated with each node, polynomial basis functions, and a set of coefficients that depend on the position $\mathbf{x}$ of the point.

First, we consider a sub-domain $\Omega_{\mathbf{x}}$, called the domain of definition of the MLS approximation for the trial function at the point $\mathbf{x}$, which is located in the problem domain Ω. The unknown trial approximant $u^h(\mathbf{x})$ of the function $u(\mathbf{x})$ is defined by

$$u^h(\mathbf{x}) = \mathbf{p}^T(\mathbf{x})\mathbf{a}(\mathbf{x}), \quad \forall \mathbf{x} \in \Omega_{\mathbf{x}}, \tag{1.1}$$

where $\mathbf{p}^T(\mathbf{x}) = [p_1(\mathbf{x}), p_2(\mathbf{x}), ..., p_m(\mathbf{x})]$ is a vector of the complete monomial basis of order m, and $\mathbf{a}(\mathbf{x})$ is a vector containing unknown coefficients $a_j(\mathbf{x})$, j = 1,2,…,m. Examples of $\mathbf{p}^T(\mathbf{x})$ in a 2-D problem are:

$$\mathbf{p}^T(\mathbf{x}) = [1, x^1, x^2] \quad \text{for linear basis, } m = 3; \tag{1.2a}$$

$$\mathbf{p}^T(\mathbf{x}) = [1, x^1, x^2, (x^1)^2, x^1x^2, (x^2)^2] \quad \text{for quadratic basis, } m = 6. \tag{1.2b}$$

The coefficient vector $\mathbf{a}(\mathbf{x})$ is determined by minimizing a weighted discrete L_2 norm defined as:

$$J(\mathbf{x}) = \sum_{i=1}^{n} w_i(\mathbf{x})[\mathbf{p}^T(\mathbf{x}_i)\mathbf{a}(\mathbf{x}) - \hat{u}_i]^2, \tag{1.3}$$

where $w_i(\mathbf{x})$ is the weight function associated with the node *i* with $w_i(\mathbf{x}) > 0$ for all $\mathbf{x}$ in the support of $w_i(\mathbf{x})$, $\mathbf{x}_i$ denotes the value of $\mathbf{x}$ at node *i*, *n* is the number of nodes in $\Omega_{\mathbf{x}}$ for which the weight functions $w_i(\mathbf{x}) > 0$ (see Fig. 1.1), and $\hat{u}_i$ is the fictitious nodal value and need not equal $u^h(\mathbf{x}_i)$.

Finding the extremum of $J(\mathbf{x})$ in Eq.(1.3) with respect to $\mathbf{a}(\mathbf{x})$ leads to the following linear relation:

$$\mathbf{A}(\mathbf{x})\mathbf{a}(\mathbf{x}) = \mathbf{B}(\mathbf{x})\hat{\mathbf{u}}, \tag{1.4}$$

where

$$\mathbf{A}(\mathbf{x}) = \sum_{i=1}^{n} w_i(\mathbf{x})\mathbf{p}(\mathbf{x}_i)\mathbf{p}^T(\mathbf{x}_i), \tag{1.5}$$

$$\mathbf{B}(\mathbf{x}) = [w_1(\mathbf{x})\mathbf{p}(\mathbf{x}_1), w_2(\mathbf{x})\mathbf{p}(\mathbf{x}_2), ..., w_n(\mathbf{x})\mathbf{p}(\mathbf{x}_n)], \tag{1.6}$$

$$\hat{\mathbf{u}}^T = [\hat{u}_1, \hat{u}_2, ..., \hat{u}_n]. \tag{1.7}$$

Eq. (1.4) can be solved for $\mathbf{a}(\mathbf{x})$ and yields

$$\mathbf{a}(\mathbf{x}) = \mathbf{A}^{-1}(\mathbf{x})\mathbf{B}(\mathbf{x})\hat{\mathbf{u}}. \tag{1.8}$$

As can be seen from Eq. (1.8), the unknown coefficients $\mathbf{a}(\mathbf{x})$ can be obtained only if $\mathbf{A}(\mathbf{x})$ defined by Eq. (1.5) is non-singular. So, a necessary condition for a well-defined MLS approximation is that at least *m* weight functions are non-zero (i.e. $n \geq m$) for each sample point $\mathbf{x} \in \Omega$.

Substituting for $\mathbf{a}(\mathbf{x})$ into Eq. (1.1) gives the following relation for nodal interpolation

$$u^h(\mathbf{x}) = \sum_{i=1}^{n} \phi_i(\mathrm{x})\, \hat{u}_i, \qquad u^h(\mathbf{x}_i) \equiv u_i \neq \hat{u}_i, \quad \mathbf{x} \in \Omega_{\mathbf{x}}, \tag{1.9}$$

where

$$\phi_i(\mathbf{x}) = \sum_{j=1}^{m} p_j(\mathbf{x})[\mathbf{A}^{-1}(\mathbf{x})\mathbf{B}(\mathbf{x})]_{ji}. \tag{1.10}$$

$\phi_i(\mathbf{x})$ is usually called the shape function of the MLS approximation corresponding to node *i.* The spatial derivatives of the shape function $\phi_i(\mathbf{x})$ are

$$\phi_{i,k} = \sum_{j=1}^{m} [p_{j,k}(\mathbf{A}^{-1}\mathbf{B})_{ji} + p_j(\mathbf{A}^{-1}\mathbf{B}_{,k} + \mathbf{A}^{-1}_{,k}\mathbf{B})_{ji}], \tag{1.11}$$

where $(\ )_{,i} \equiv \partial(\ )/\partial x^i$. The derivative of $\mathbf{A}^{-1}$ in Eq. (1.11) can be computed by taking the derivative of $\mathbf{A}^{-1}\mathbf{A} = \mathbf{I}$. Thus

$$\mathbf{A}^{-1}_{,k} = -\mathbf{A}^{-1}\mathbf{A}_{,k}\mathbf{A}^{-1}. \tag{1.12}$$

It should be noted that shape functions derived from the MLS approximation do not satisfy the criterion, $\phi_i(\mathbf{x}_j) \neq \delta_{ij}$, i.e., they are not nodal interpolants. (see Fig. 1.2 for the distinction between u_i and $\hat{u}_i$ in a one dimensional case). This property makes the satisfaction of essential boundary conditions more difficult than that in the finite element method. Several techniques have been developed to enforce essential boundary conditions, including the method of Lagrange multipliers (Belytschko et al. 1994), modified variational principles (Lu et al. 1994), and the penalty method (Atluri and Zhu, 1998).

1.2.2 Weight function

The weight function is an important ingredient in the meshless method. To illustrate how weight functions affect the trial function $u^h(\mathbf{x})$ in the MLS approximation, three different

weight functions are chosen to approximate the function $u(\mathbf{x})$ in one dimension by $u^h(\mathbf{x})$ with five nodes shown in Fig. 1.3. In each case, a weight function corresponding to node 3 (x=2) and the resulting MLS approximation using linear basis are plotted.

In the first example, Fig. 1.3a, the weight function associated with each node is a constant over the entire domain. The minimization process at each point $\mathbf{x}$ involves all nodes in the domain (n=5) and $J(\mathbf{x})$ in Eq. (1.3) reverts to the standard least squares norm ($w_i(\mathbf{x})=1$) resulting in a linear polynomial fit through the data.

In the second example, Fig. 1.3b, the weights are still constants but each weight function has compact support since w_i is nonzero only over a sub-domain centered at the node; the size of the sub-domain is chosen such that for any point, $w_i(\mathbf{x})>0$ only for two nodes. That is, n=m=2. These weight functions generate a piecewise linear interpolation of data, which is equivalent to a linear finite element approximation. Because of the compact support for a weight function, this minimization process becomes local and includes only neighboring nodes; the resulting approximation reflects this local character.

In the third example, Fig. 1.3c, the weight functions are still with compact support, but now they are continuously differentiable functions that cover larger sub-domains such that n>m=2. The minimization of $J(\mathbf{x})$ in Eq. (1.3) is just the type of MLS approximation which has been used in the EFG method and is now used in the MLPG method. This approximation is continuous and smooth even though the polynomial basis is linear since the approximation inherits the continuity of the weight function. This approximation also possesses local character due to the finite support of the weight function.

The above three examples illustrate that a smooth and continuously differentiable weight function with a compact support should be defined at each node in the MLS approximation. Two weight functions are commonly used in meshless methods; one is the Gaussian weight function and the other is the quartic spline weight function. The Gaussian and the spline weight functions are given, respectively, in Eqs. (1.13) and (1.14).

$$w_i(\mathbf{x}) = \begin{cases} \dfrac{\exp[-(d_i/c_i)^{2k}] - \exp[-(r_i/c_i)^{2k}]}{1-\exp[-(r_i/c_i)^{2k}]} \\ \\ 0 \end{cases}, \quad \begin{array}{l} 0 \le d_i \le r_i, \\ \\ d_i \ge r_i. \end{array} \tag{1.13}$$

$$w_i(\mathbf{x}) = \begin{cases} 1-6(\dfrac{d_i}{r_i})^2 + 8(\dfrac{d_i}{r_i})^3 - 3(\dfrac{d_i}{r_i})^4 \\ \\ 0 \end{cases}, \quad \begin{array}{l} 0 \le d_i \le r_i, \\ \\ d_i \ge r_i. \end{array} \tag{1.14}$$

Here $d_i = |\mathbf{x} - \mathbf{x}_i|$ is the distance from the sampling point $\mathbf{x}$ to the node $\mathbf{x}_i$, and r_i is the radius of the domain of influence for the weight function w_i. The parameters c_i and k in Eq. (1.13) control the shape of the Gaussian weight function w_i. The parameter k can be taken as 1 in Eq. (1.13). So far, there is no theory to determine an optimal value of the parameter c_i and is chosen empirically. Lu et al. (1994) recommended a method to choose the constant c_i. We follow their suggestion and define c_i as the distance from node $\mathbf{x}_i$ to the third nearest neighboring node. The domain of influence r_i can be chosen as $\frac{r_i}{c_i} \ge 3.5$ so that the weight function w_i covers sufficient number of nodes to ensure the non-singularity of $\mathbf{A}$ in Eq. (1.10).

It has been reported in the literature that the Gaussian weight function usually performs better than the spline weight function. Therefore, unless otherwise stated, the Gaussian weight function is used in this work.

1.2.3 The MLPG weak formulation

Consider the following two-dimensional elasto-statics problem on the domain Ω bounded by the boundary Γ.

$$\sigma_{ij,j} + b_i = 0, \qquad \text{in } \Omega, \tag{1.15}$$

where σ_{ij} is the stress tensor, b_i is the body force, a repeated index implies summation over the range of the index, and we have used rectangular Cartesian coordinates. The boundary conditions are given as follows:

$$u_i = \bar{u}_i, \qquad \text{on } \Gamma_u, \tag{1.16a}$$

$$t_i \equiv \sigma_{ij} n_j = \bar{t}_i, \qquad \text{on } \Gamma_t, \tag{1.16b}$$

where $\bar{u}_i$ and $\bar{t}_i$ are the prescribed displacements and tractions, respectively, on the boundary Γ_u and the boundary Γ_t, and n_i is the unit outward normal to the boundary Γ. Γ_u and Γ_t are complementary subsets of Γ.

Unlike the Element Free Galerkin (EFG) method which is based on the global Galerkin formulation, the present local Petrov-Galerkin formulation is constructed over a local sub-domain Ω_s which is located inside the global domain Ω. This local sub-domain Ω_s is taken to be either a circle or a part of a circle in a 2-D problem.

A generalized local weak form of Eq. (1.15) and Eq. (1.16) over a local sub-domain Ω_s can be written as follows:

$$\int_{\Omega_s} (\sigma_{ij,j} + b_i) v_i \, d\Omega - \int_{\Gamma_{su}} \alpha (u_i - \bar{u}_i) v_i \, d\Gamma = 0, \tag{1.17}$$

where u_i and v_i are the trial and the test functions, respectively, and Γ_{su} is the part of the boundary $\partial\Omega_s$ over which essential boundary conditions are specified. In general, $\partial\Omega_s = \Gamma_s \cup L_s$ with Γ_s being the part of the local boundary located on the global boundary and L_s being the other part of the local boundary over which no boundary condition is specified, i.e., $\Gamma_s = \partial\Omega_s \cap \Gamma$ and $\Gamma_s = \partial\Omega_s - L_s$ (see Fig. 1.4). In Eq. (1.17), α is a penalty parameter ($\alpha >>$ Young's modulus/Length) which is used to impose the essential boundary conditions. Also,

the dimensions of α are such that the two terms in Eq. (1.17) have the same units. α could be a function of **x** but is usually taken to be a constant. Henceforth, we also take α to be a constant.

Using $\sigma_{ij,j}v_i = (\sigma_{ij}v_i)_{,j} - \sigma_{ij}v_{i,j}$ and the divergence theorem in Eq. (1.17) leads to

$$\int_{\partial\Omega_s} \sigma_{ij} n_j v_i d\Gamma - \int_{\Omega_s} (\sigma_{ij} v_{i,j} - b_i v_i) d\Omega - \alpha \int_{\Gamma_{su}} (u - \bar{u}_i) v_i d\Gamma = 0, \tag{1.18}$$

where n_i is a unit outward normal to the boundary $\partial\Omega_s$.

It should be mentioned that Eq. (1.18) holds regardless of the size and the shape of Ω_s provided that Ω_s is smooth enough for the divergence theorem to apply. So, the shape of a sub-domain Ω_s can be taken to be a circle in 2-D problems without loosing generality (see Fig. 1.4).

Applying the natural boundary condition, $t_i \equiv \sigma_{ij} n_j = \bar{t}_i$ on Γ_{st} where $\Gamma_{st} = \partial\Omega_s \cap \Gamma_t$, we get

$$\begin{aligned} \int_{L_s} t_i v_i d\Gamma + \int_{\Gamma_{su}} t_i v_i d\Gamma + \int_{\Gamma_{st}} \bar{t}_i v_i d\Gamma - \int_{\Omega_s} (\sigma_{ij} v_{i,j} - b_i v_i) \mathrm{d}\Omega \\ - \alpha \int_{\Gamma_{su}} (u_i - \bar{u}_i) v_i d\Gamma = 0. \end{aligned} \tag{1.19}$$

In order to simplify equation (1.19), the test functions v_i are chosen such that they vanish on L_s. This can be accomplished by using the weight function w_i in the MLS approximation as also the test function v_i, but the radius r_i of the support of the weight function is replaced by the radius r_o of the local domain Ω_s.

Using these test functions and rearranging Eq. (1.19), we obtain the following local symmetric weak form (LSWF):

$$\begin{aligned}\int_{\Omega_s} \sigma_{ij} v_{i,j} d\Omega + \alpha \int_{\Gamma_{su}} u_i v_i d\Gamma - \int_{\Gamma_{su}} t_i v_i d\Gamma \\ = \int_{\Gamma_{st}} \bar{t}_i v_i d\Gamma + \alpha \int_{\Gamma_{su}} \bar{u}_i v_i d\Gamma + \int_{\Omega_s} b_i v_i d\Omega.\end{aligned} \tag{1.20}$$

For 2-D problems, two independent sets of test functions should be applied in Eq. (1.20), which gives

$$\begin{aligned}\int_{\Omega_s} \sigma_{ij} v_{ki,j} d\Omega + \alpha \int_{\Gamma_{su}} u_i v_{ki} d\Gamma - \int_{\Gamma_{su}} t_i v_{ki} d\Gamma \\ = \int_{\Gamma_{st}} \bar{t}_i v_{ki} d\Gamma + \alpha \int_{\Gamma_{su}} \bar{u}_i v_{ki} d\Gamma + \int_{\Omega_s} b_i v_{ki} d\Omega,\end{aligned} \tag{1.21}$$

where v_{ki} is the ith component of the kth test function. For simplicity, Eq. (1.21) can be written in matrix form as:

$$\begin{aligned}\int_{\Omega_s} \varepsilon_v \sigma d\Omega + \alpha \int_{\Gamma_{su}} \mathbf{v}\mathbf{u} d\Gamma - \int_{\Gamma_{su}} \mathbf{v}\mathbf{t} d\Gamma \\ = \int_{\Gamma_{st}} \mathbf{v}\bar{\mathbf{t}} d\Gamma + \alpha \int_{\Gamma_{su}} \mathbf{v}\bar{\mathbf{u}} d\Gamma + \int_{\Omega_s} \mathbf{v}\mathbf{b} d\Omega,\end{aligned} \tag{1.22}$$

where ε_v denotes the strain matrix derived from the test functions, and σ is the stress vector derived from the trial functions. That is,

$$\sigma = \begin{Bmatrix} \sigma_{11} \\ \sigma_{22} \\ \sigma_{12} \end{Bmatrix}, \qquad \varepsilon_v = \begin{bmatrix} \varepsilon_{11}^{(1)} & \varepsilon_{22}^{(1)} & \gamma_{12}^{(1)} \\ \varepsilon_{11}^{(2)} & \varepsilon_{22}^{(2)} & \gamma_{12}^{(2)} \end{bmatrix}, \tag{1.23}$$

where the superscript i denotes the ith test function. Functions **v**, **u**, **t**, and **b** are defined as follows:

$$\mathrm{v} = \begin{bmatrix} v_{11} & v_{12} \\ v_{21} & v_{22} \end{bmatrix}, \qquad \mathrm{u} = \begin{Bmatrix} u_1 \\ u_2 \end{Bmatrix}, \qquad \mathrm{t} = \begin{Bmatrix} t_1 \\ t_2 \end{Bmatrix}, \qquad \mathrm{b} = \begin{Bmatrix} b_1 \\ b_2 \end{Bmatrix}. \tag{1.24}$$

The two sets of test functions **v** in Eq. (1.24) should be linearly independent. The simplest choice for **v** is

$$v_{ij} = v\delta_{ij} \qquad \text{or} \quad \mathbf{v} = v\mathbf{I},$$

where δ_{ij} is the Kronecker delta and $\mathbf{I}$ is the identity matrix.

As long as the union of all local sub-domains covers the global domain, the equilibrium equations (1.15) and the boundary conditions (1.16) will be satisfied in the global domain Ω and on its boundary Γ respectively.

1.2.4 Discretization of the weak form

Substituting the MLS approximation (1.9) into Eq. (1.22) and summing over all nodes leads to the following discretized system of linear equations:

$$\begin{aligned}
&\sum_{j=1}^{n}\int_{\Omega_s}\varepsilon_v(\mathbf{x},\mathbf{x}_i)\mathbf{D}\mathbf{B}_j\hat{\mathbf{u}}_j d\Omega + \alpha\sum_{j=1}^{n}\int_{\Gamma_{su}}\mathbf{v}(\mathbf{x},\mathbf{x}_i)\mathbf{S}\phi_j\hat{\mathbf{u}}_j d\Gamma \\
&-\sum_{j=1}^{n}\int_{\Gamma_{su}}\mathbf{v}(\mathbf{x},\mathbf{x}_i)\mathbf{N}\mathbf{D}\mathbf{S}\mathbf{B}_j\hat{\mathbf{u}}_j d\Gamma \\
&=\int_{\Gamma_{st}}\mathbf{v}(\mathbf{x},\mathbf{x}_i)\bar{\mathbf{t}}d\Gamma + \alpha\int_{\Gamma_{su}}\mathbf{v}(\mathbf{x},\mathbf{x}_i)\mathbf{S}\bar{\mathbf{u}}d\Gamma + \int_{\Omega_s}\mathbf{v}(\mathbf{x},\mathbf{x}_i)\mathbf{b}d\Omega,
\end{aligned} \tag{1.25}$$

where $\mathbf{v}(\mathbf{x}, \mathbf{x}_i)$ is the value at $\mathbf{x}$ of the test function, corresponding to node *i,* and

$$\mathbf{N} = \begin{bmatrix} n_1 & 0 & n_2 \\ 0 & n_2 & n_1 \end{bmatrix}, \tag{1.26}$$

$$\mathbf{B}_j = \begin{bmatrix} \phi_{j,1} & 0 \\ 0 & \phi_{j,2} \\ \phi_{j,2} & \phi_{j,1} \end{bmatrix}, \tag{1.27}$$

$$\mathbf{D} = \frac{\bar{E}}{1-\bar{v}^2}\begin{bmatrix} 1 & \bar{v} & 0 \\ \bar{v} & 1 & 0 \\ 0 & 0 & (1-\bar{v})/2 \end{bmatrix}. \tag{1.28}$$

We note that

$$\overline{E} = \begin{cases} E \\ E/(1-\nu^2), \end{cases} \qquad \overline{\nu} = \begin{cases} \nu \\ \nu/(1-\nu), \end{cases} \qquad \begin{matrix} \text{for plane stress,} \\ \text{for plane strain,} \end{matrix} \tag{1.29}$$

and

$$\mathbf{S} = \begin{bmatrix} S_1 & 0 \\ 0 & S_2 \end{bmatrix}, \qquad S_i = \begin{cases} 1 & \text{if } u_i \text{ is prescribed on } \Gamma_u, \\ 0, & \text{if } u_i \text{ is not prescribed on } \Gamma_u. \end{cases} \tag{1.30}$$

Eq. (1.25) can be simplified into the following system of linear algebraic equations in $\hat{\mathbf{u}}_j$.

$$\sum_{j=1}^{N} \mathbf{K}_{ij} \hat{\mathbf{u}}_j = \mathbf{f}_i, \qquad i = 1,2,...,N, \tag{1.31}$$

where N is the total number of nodes. The so-called "stiffness" matrix $\mathbf{K}$ and the "load" vector $\mathbf{f}$ are defined by

$$\begin{aligned} \mathbf{K}_{ij} = & \int_{\Omega_s} \varepsilon_v(\mathbf{x}, \mathbf{x}_i) \mathbf{D}\mathbf{B}_j d\Omega + \alpha \int_{\Gamma_{su}} \mathbf{v}(\mathbf{x}, \mathbf{x}_i) \mathbf{S} \phi_j d\Gamma \\ & - \int_{\Gamma_{su}} \mathbf{v}(\mathbf{x}, \mathbf{x}_i) \mathbf{N}\mathbf{D}\mathbf{B}_j \mathbf{S} d\Gamma, \end{aligned} \tag{1.32}$$

and

$$\mathbf{f}_i = \int_{\Gamma_{st}} \mathbf{v}(\mathbf{x}, \mathbf{x}_i) \bar{\mathbf{t}} d\Gamma + \alpha \int_{\Gamma_{su}} \mathbf{v}(\mathbf{x}, \mathbf{x}_i) \mathbf{S} \bar{\mathbf{u}} d\Gamma + \int_{\Omega_s} \mathbf{v}(\mathbf{x}, \mathbf{x}_i) \mathbf{b} d\Omega. \tag{1.33}$$

As can be seen from Eq. (1.32), the system "stiffness matrix" is banded but unsymmetric.

1.3 Validation of the Code

Based on the MLPG method described above, we have developed a computer code to solve plane stress/strain elastostatics problems. This code is validated by solving the following three elasticity problems each of which has an analytical solution.

1.3.1 A ″cantilever″ beam loaded by a tangential traction on the unclamped end

The first problem studied is a ″cantilever″ beam (Fig. 1.5) deformed by applying a tangential traction on the unclamped end. The exact solution taken from Timoshenko and Goodier (1970) is

$$u_1 = -\frac{P}{6\bar{E}I}(x^2 - \frac{D}{2})[3x^1(2L - x^1) + (2 + \bar{\nu})x^2(x^2 - D)], \tag{1.34a}$$

$$u_2 = \frac{P}{6\bar{E}I}[(x^1)^2(3L - x^1) + 3\bar{\nu}(L - x^1)(x^2 - \frac{D}{2})^2 + \frac{4 + 5\bar{\nu}}{4}D^2x^1], \tag{1.34b}$$

where I is the moment of inertia, and P is the resultant of the tangential tractions applied at the unclamped edge. For a beam with rectangular cross-section and unit thickness,

$$I = \frac{D^3}{12}, \tag{1.35}$$

and D is the height of the beam.

The stresses are given by

$$\sigma_{11} = -\frac{P}{I}(L - x^1)(x^2 - \frac{D}{2}), \tag{1.36a}$$

$$\sigma_{22} = 0, \tag{1.36b}$$

$$\sigma_{12} = -\frac{Px^2}{2I}(x^2 - D). \tag{1.36c}$$

We impose the following boundary conditions at the bounding surfaces of the beam. Displacements given by Eqs (1.34a) and (1.34b) are specified at nodes on the left edge, and tractions computed from Eqs. (1.36a)-(1.36c) are prescribed at the remaining three surfaces of the beam. This is solved as a plane stress problem ($\text{i.e.}, \sigma_{13} = \sigma_{23} = \sigma_{33} = 0$). In a

consistent set of units, we take P=1, E=1000, D=1, L=8, ν=0.25 and the penalty parameter $\alpha = 10^8$. A regular nodal mesh (shown in Fig. 1.6) of 72 nodes with 18 nodes along the x^1 direction and 4 nodes along the x^2 direction is used. The radius r_o of the local sub-domain is taken to be the distance between two neighboring nodes in x^2 direction, and the Gaussian weight function is adopted with $r_i = 4c_i, k = 1$; the parameter c_i in the Gaussian weight function is chosen as the distance to the third nearest neighboring node in the x^2 direction. In the computation, 8×8 Gauss points are used in each local sub-domain Ω_s and 8 Gauss points are used along each section of Γ_s.

Figures 1.7, 1.8 and 1.9 show, respectively, the variations of the horizontal displacement u_1, the vertical displacement u_2, and the longitudinal stress σ_{11} vs. x^1 on the top face. It is clear that these agree very well with the analytical solution. Figures 1.10 and 1.11 illustrate the through-the-thickness variation of the normal stress σ_{11} and the shear stress σ_{12} at $x^1 = L/2 = 4$. Both stress components are almost the same as those in the exact solution.

We now examine if the MLPG method gives good results for nearly incompressible materials by taking ν=0.4999. As can be seen in Figs. 1.12a-1.12d, the numerical solution matches well with the analytical solution. Figures 1.12c and 1.12d show respectively the normal stress σ_{11} and the shear stress σ_{12} at $x^1 = L/2 = 4$ along the thickness direction. It is found that the MLPG method does not exhibit the locking phenomenon seen in the Finite Element Method.

The deflection at point A (shown in Fig. 1.5) computed by the FE and the MLPG methods are compared in the following table; the FE solution is taken from Belytschko (1994). A plane strain state rather than a plane stress state of deformation is assumed to prevail in the beam.

$u_2^{num}/\ u_2^{exact}$ at point A (Plane Strain Case)		
Method	ν=0.25	ν=0.4999
FEM : Q4	0.824	0.027
MLPG : Linear	1.000	1.007
MLPG : Quadratic	1.000	1.000

Table 1.1

It is obvious that the FEM using the 4-node quadrilateral element (Q4) performs poorly especially when ν=0.4999 while the MLPG method works well. A similar trend was observed by Atluri and Zhu (2000) in their analysis of the problem.

1.3.2 An infinite plate with a circular hole subjected to a uniform tensile traction at infinity

Consider an infinite plate with a circular hole and subjected to a unit normal traction at infinity in the x^1 direction. The exact solution for stresses [Timoshenko and Goodier, 1970] is

$$\sigma_{11} = 1 - \frac{a^2}{r^2}\left(\frac{3}{2}\cos(2\theta) + \cos(4\theta)\right) + \frac{3a^4}{2r^4}\cos(4\theta), \tag{1.37a}$$

$$\sigma_{22} = -\frac{a^2}{r^2}\left(\frac{1}{2}\cos(2\theta) - \cos(4\theta)\right) - \frac{3a^4}{2r^4}\cos(4\theta), \tag{1.37b}$$

$$\sigma_{12} = -\frac{a^2}{r^2}\left(\frac{1}{2}\sin(2\theta) + \sin(4\theta)\right) + \frac{3a^4}{2r^4}\sin(4\theta), \tag{1.37c}$$

where (r,θ) are the polar coordinates of a point, θ is measured counterclockwise from the positive x^1 axis, and a is the radius of the circular hole. Due to the symmetry of the problem about the horizontal and the vertical centroidal axes, only the upper right quadrant of the plate, shown in Fig. 1.13, is considered. This quadrant is modeled as a square plate with the length of a side equal to 4a. Boundary conditions resulting from the symmetry of the problem are imposed on the left and the bottom edges, and the boundary of the hole is traction free.

Traction boundary conditions given by the exact solution (Eq. 1.37) are imposed on the right (x^1=4a) and the top (x^2=4a) edges. A plane stress state of deformation is assumed to prevail in the plate. In a consistent set of units, we take E=1000, ν=0.25, and a=1 in this computation.

Two different nodal meshes with 49 (7×7 : 7 nodes in the r direction, 7 nodes in the θ direction) and 81 (9×9) nodes (see Fig. 1.14) are considered. The Gaussian weight function is adopted with c_i and r_i taken according to the criteria in section 1.2.2. 9×9 Gauss points are used in each local sub-domain Ω_s and 9 Gauss points are used on each section of Γ_s for numerical integration.

The stress σ_{11} at x^1=0 using a linear basis is compared with the analytical solution in Fig. 1.15. It can be seen that the stress σ_{11} is very well approximated when the number of nodes is increased to 81. Fig. 1.16 displays the stress field σ_{11} over the entire domain, and it shows that the stress concentration around the hole can be captured.

1.3.3 A hollow cylinder loaded by pressure on the inner and outer surfaces

We consider a hollow cylinder subjected to tractions shown in Fig. 1.17. The exact solution [Timoshenko and Goodier, 1970] is

$$u_\theta = 0, \tag{1.38}$$

$$u_r = \frac{(p_b b^2 - p_a a^2)r}{2(b^2-a^2)(\lambda+G)} - \frac{a^2b^2(p_b-p_a)}{2(b^2-a^2)G}\frac{1}{r}, \tag{1.39a}$$

$$\sigma_{rr} = \frac{p_b b^2 - p_a a^2}{b^2-a^2} - \frac{a^2b^2(p_b-p_a)}{(b^2-a^2)r^2}, \tag{1.39b}$$

$$\sigma_{\theta\theta} = \frac{p_b b^2 - p_a a^2}{b^2-a^2} + \frac{a^2b^2(p_b-p_a)}{(b^2-a^2)r^2}, \tag{1.39c}$$

where p_a and p_b denote pressures on the inner and outer surfaces, respectively, *a* and *b* are the inner and the outer radii of the cylinder, and λ and G are Lame′ constants. The problem is axisymmetric, so the deformations and the stresses are functions of the radial coordinate *r* only. Note that the sum $\sigma_{rr} + \sigma_{\theta\theta}$ is constant throughout the wall of the cylinder.

Due to the symmetries about the horizontal and the vertical centroidal axes, only a quarter of the cylinder is modeled with 840 nodes (see Fig. 1.18, $21 \times 40 : 21$ nodes in the r direction, 40 nodes in the θ direction). A plane strain state of deformation is assumed to prevail in the plate. In a consistent set of units, we take *E*=1000, *v* = 0.25, a = 5, *b* = 10, $p_b = 0$, $p_a = -1$. Symmetry boundary conditions are applied on the left and the bottom edges.

Weight function and the number of quadrature points used are the same as in the previous problem of an infinite plate with a circular hole.

Figures 1.19a-c show that the deformation and the stress fields obtained by the MLPG method match well with the analytical solution. It is noted that the MLPG method satisfies the traction boundary conditions ($p_a = -1$ at r = 5 and $p_b = 0$ at r = 10) almost exactly. Fig. 1.19d verifies that $\sigma_{rr} + \sigma_{\theta\theta}$ is constant throughout the wall of the cylinder.

1.4 References

Atluri S. N. and Zhu T. (1998): A new Meshless Local Petrov-Galerkin (MLPG) approach in computational mechanics. *Computational Mechanics*, 22(2), 117-127.

Atluri S. N., Kim H. G. and Cho J. Y. (1999a): A critical assessment of the truly meshless local Petrov-Galerkin (MLPG) and local boundary integral equation (LBIE) methods. *Computational Mechanics*, 24(5), 348-372.

Atluri S. N., Cho J. Y. and Kim H. G. (1999b): Analysis of thin beam, using the meshless local Petrov-Galerkin method, with generalized moving least squares interpolants. *Computational Mechanics*, 24(5), 334-347.

Atluri S. N. and Zhu T. (2000): The Meshless Local Petrov-Galerkin (MLPG) approach for solving problems in Elasto-Statics. *Computational Mechanics*, 25(2-3), 169-179.

Atluri S. N. and Shen S. P. (2002): The Meshless Local Petrov-Galerkin (MLPG) method : A simple & less-costly alternative to the finite element methods. *Computer Modeling in Engineering & Sciences*, 3(1), 11-51.

Belytschko T., Lu Y. Y. and Gu L. (1994): Element-free Galerkin methods. *International Journal for Numerical Methods in Engineering*, 37, 229-256.

Belytschko T., Krongauz Y, Organ D. J., Fleming M. and Krysl P. (1996): Meshless methods: An overview and recent developments. *Computer Methods in Applied Mechanics and Engineering*, 139, 3-47.

Ching H. K. and Batra R. C. (2001): Determination of crack tip fields in linear elastostatics by the Meshless Local Petrov-Galerkin (MLPG) method. *Computer Modeling in Engineering & Sciences*, 2(2), 273-289.

Duarte C. A. (1995): A review of some meshless methods to solve partial differential equations. TICAM Report.

Duarte C. A. and Oden J. T. (1996): H-*p* clouds — an *hp* meshless method. *Numerical Methods for Partial Differential Equations*, 1-34.

Gu Y. T. and Liu G. R. (2001a): A Meshless Local Petrov-Galerkin (MLPG) Method for free and forced vibration analyses for solids. *Computational Mechanics*, 27(3), 188-198.

Gu Y. T. and Liu G. R. (2001b): A Meshless Local Petrov-Galerkin (MLPG) formulation for static and free vibration analyses of thins plates. *Computer Modeling in Engineering & Sciences,* 2(4), 463-476.

Kim H. G. and Atluri S. N. (2000): Arbitrary placement of secondary nodes, and error control, in the meshless local Petrov-Galerkin (MLPG) method. *Computer Modeling in Engineering & Sciences*, 1(3), 11-32

Lancaster P. and Salkauskas K. (1981): Surfaces generated by moving least squares methods. *Mathematics of Computation 37*, 141-158.

Libersky L. D. and Petschek A. G. (1991): Smoothed particle hydrodynamics with strength of materials. In H. Trease, J. Fritts, and W. Crowley (Eds.), *The Next Free Lagrange Conference*, 248-257.

Lin H. and Atluri S. N. (2000a): Meshless Local Petrov-Galerkin (MLPG) Method for Convection-diffusion Problems. *Computer Modeling in Engineering & Sciences*, 1(2), 45-60.

Lin H. and Atluri S. N. (2000b): The Meshless Local Petrov-Galerkin (MLPG) Method for solving incompressible Navier-Stokes equations. *Computer Modeling in Engineering & Sciences*, 2(2), 117-142.

Liu G. R. and Gu Y. T. (2000): Meshless Local Petrov-Galerkin (MLPG) method in combination with finite element and boundary element approaches. *Computational Mechanics*, 26(6), 536-546.

Liu W. K., Jun S. and Zhang Y. F. (1995): Reproducing kernel particle methods. *International Journal for Numerical Methods in Engineering* 20, 1081-1106.

Long S. and Atluri S. N. (2002): A Meshless Local Petrov-Galerkin method for solving the bending problem of a thin plate, *Computer Modeling in Engineering & Sciences* 3(1), 53-63.

Lu Y. Y., Belytschko T. and Gu L. (1994): A new implementation of the element free Galerkin method. *Computer Methods in Applied Mechanics and Engineering* 113, 397-414.

Lucy L. B. (1977): A numerical approach to the testing of the fission hypothesis. *The Astronomical Journal* 82(12), 1013-1024.

Melenk J. M. and Babuska I. (1996): The partition of unity finite element method: Basic theory and applications. *Computer Methods in Applied Mechanics and Engineering.*

Monaghan J. J. (1982): Why particle methods work. *SIAM Journal of Scientific and Statistical Computing* 3(4), 422-.

Nayroles B., Touzot G. and Villon P. (1992): Generalizing the finite element method: diffuse approximation and diffuse elements. *Computational Mechanics* 10, 307-318.

Timoshenko S. P. and Goodier J. N. (1970): *Theory of Elasticity* (Third Ed.). New York: McGraw Hill.

Warlock A., Ching H. K., Kapila A. K. and Batra R. C. (2002): Plane Strain Deformations of an Elastic Material Compressed in a Rough Rectangular Cavity. *International Journal of Engineering Science*, Vol. 40, pp. 991-1010.

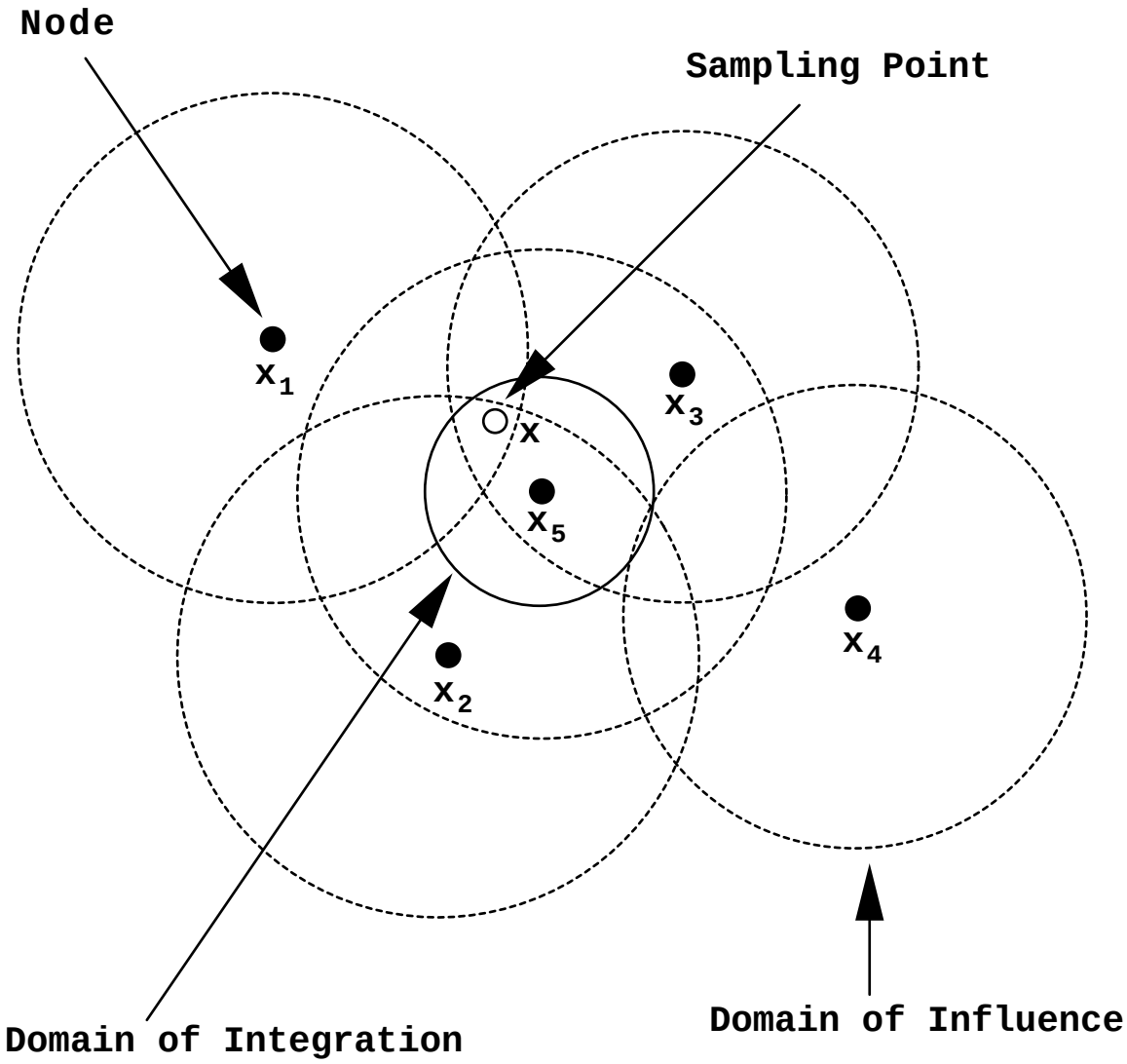

Fig. 1.1 Illustration of the domain of influence in two dimensions.
The neighbor list for point **x** includes 1,2,3, and 5
since their domains of influence contain **x**;
node 4 is excluded from the neighbor list for point **x**.

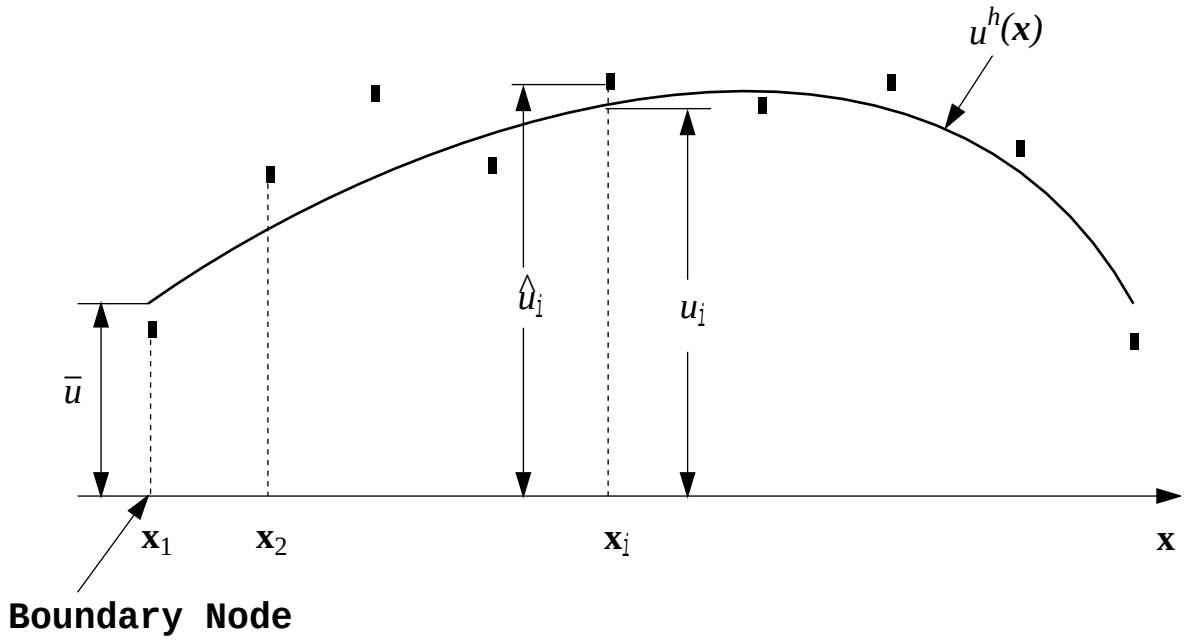

Fig. 1.2 The distinction between u_i and $\hat{u}_i$

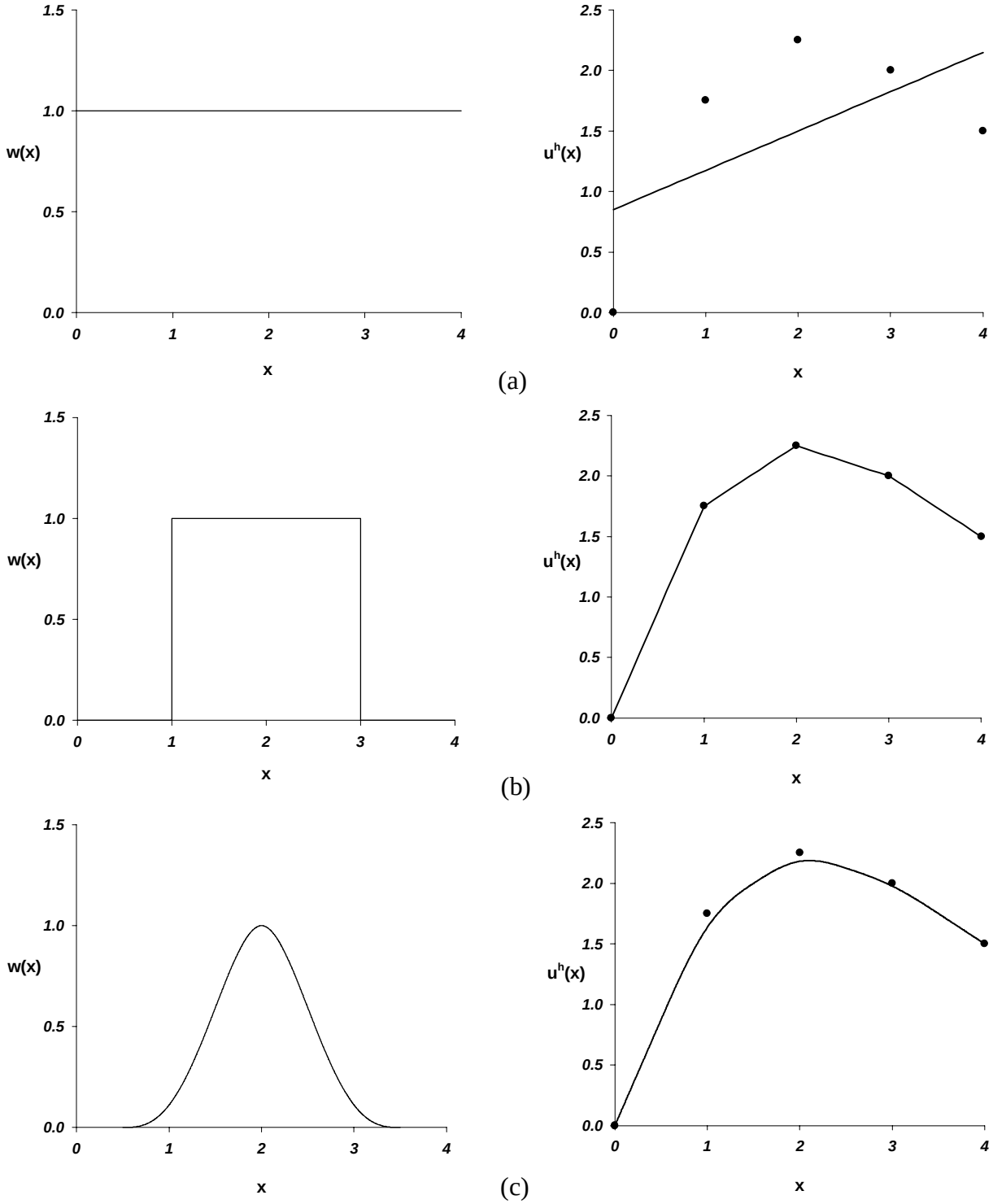

Fig. 1.3a-c : (a) Constant weight function and the correpsonding approximant $u^h(x)$
(b) Constant weight function with the compact support and the corresponding approximant $u^h(x)$
(c) Continuous weight function and the corresponding approximant $u^h(x)$

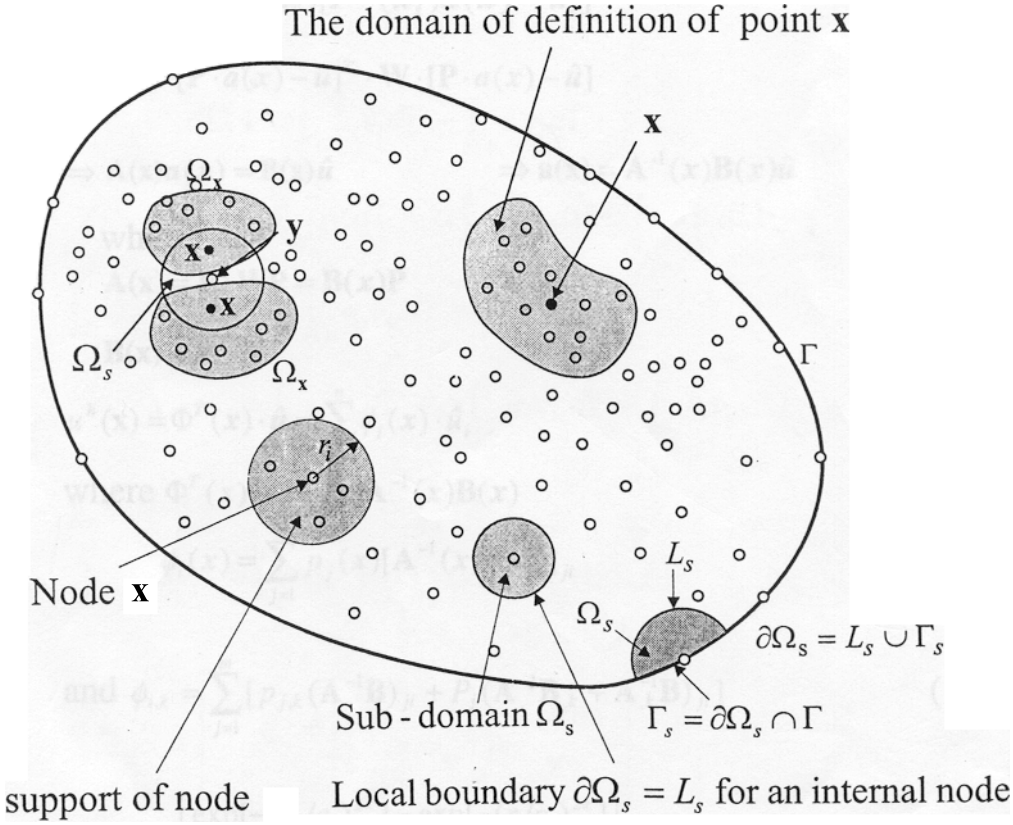

Fig. 1.4 The local domains, the supports of nodes, the domain of definition of a point, and the domain of influence of a node

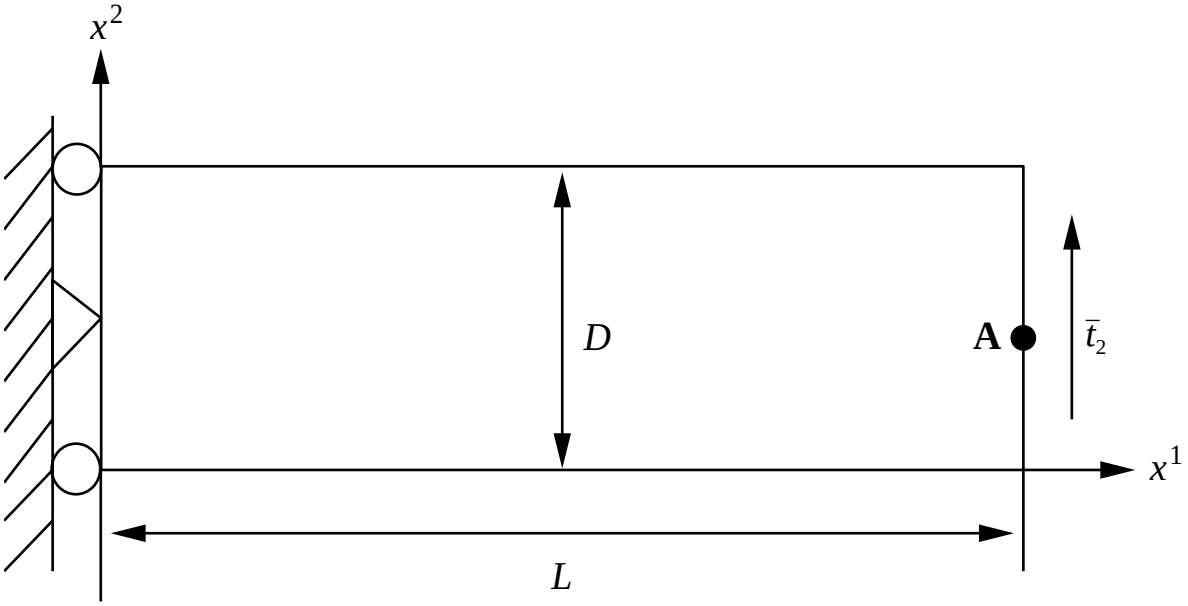

Fig. 1.5 The cantilever beam

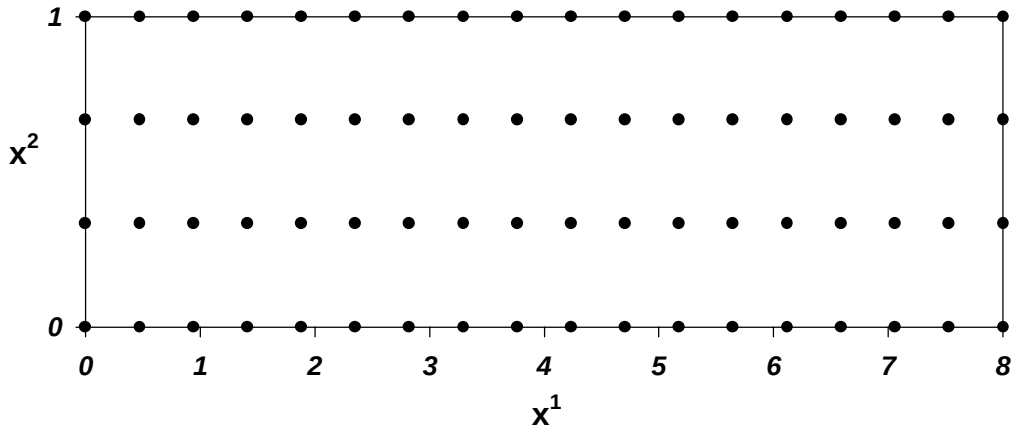

Fig. 1.6 The nodal mesh with 72 nodes

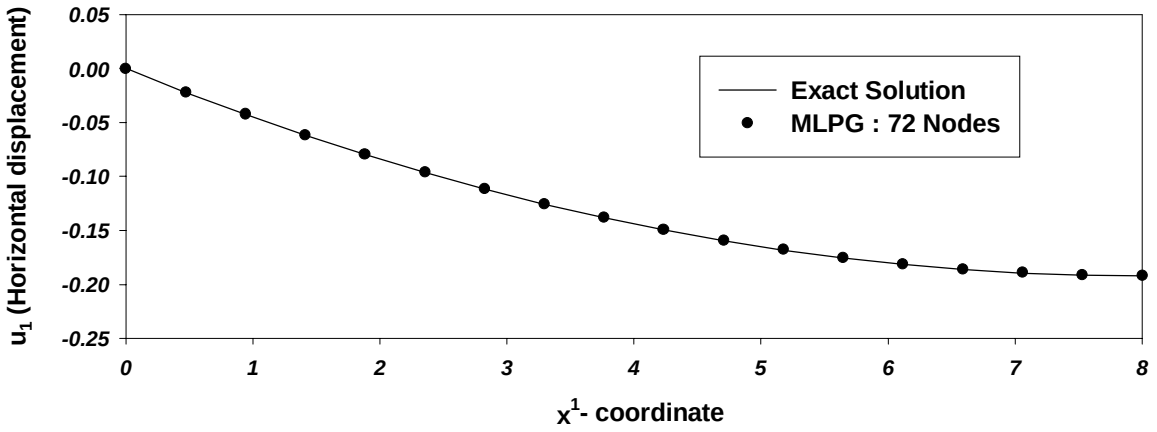

Fig. 1.7 Horizontal displacement u_1 vs. x^1 on the top face

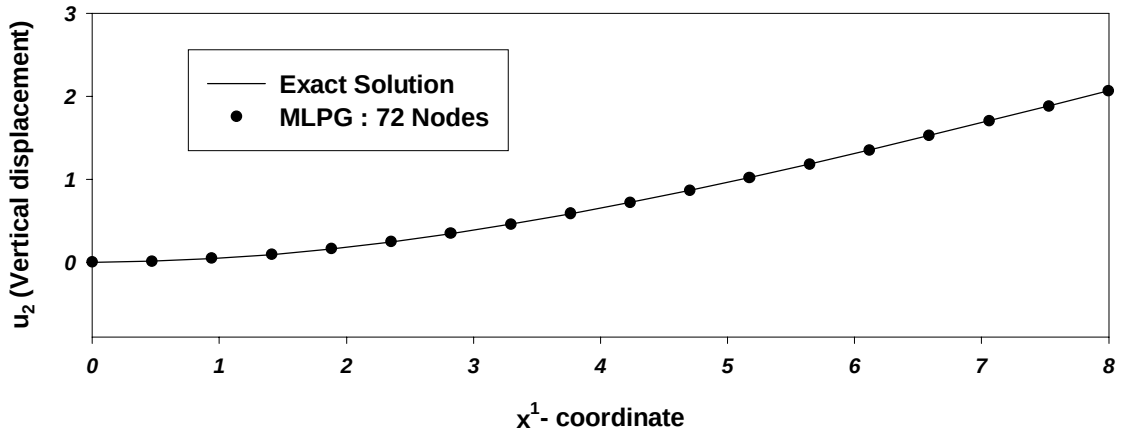

Fig. 1.8 Vertical displacement u_2 vs. x^1 on the top face

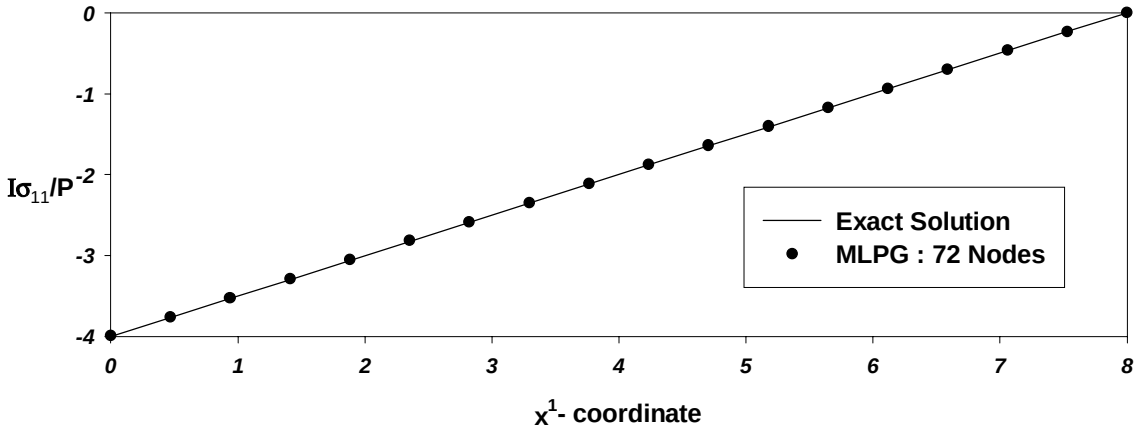

Fig. 1.9 σ_{11} vs. x^1 on the top face

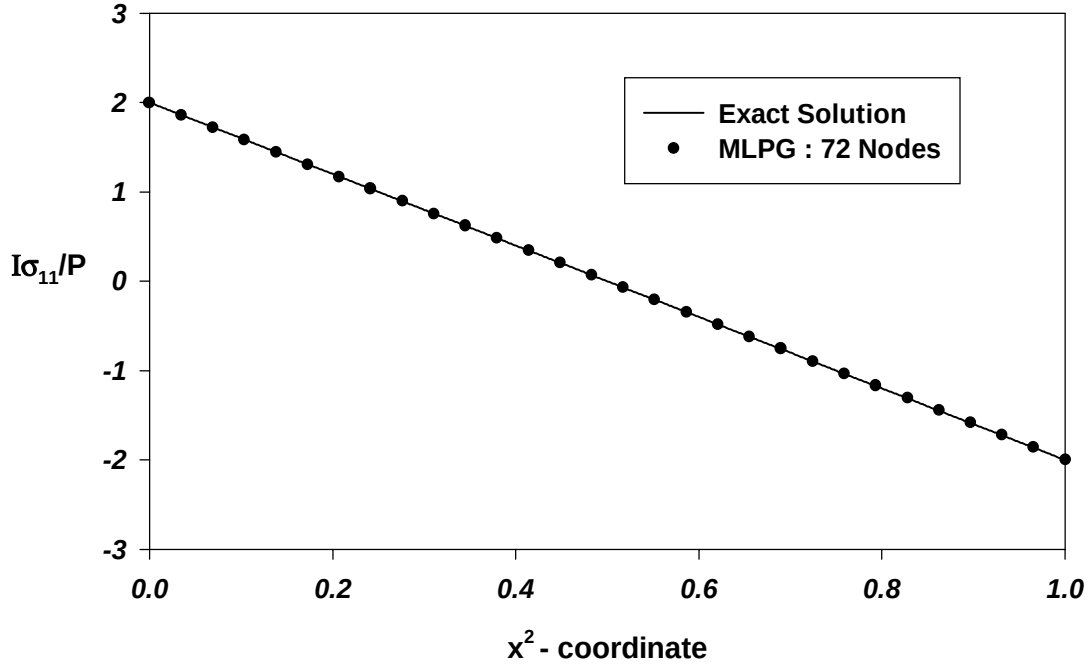

Fig. 1.10 Through-the-thickness distribution of σ_{11} on the plane $x^1 = 4$

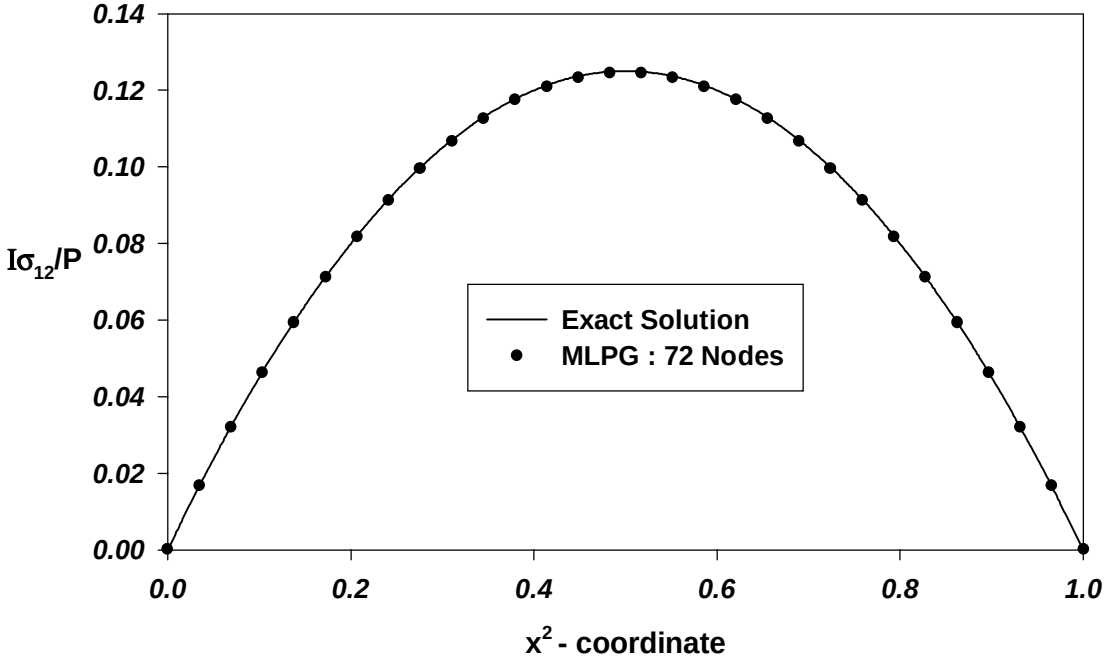

Fig. 1.11 Through-the-thickness distribution of σ_{12} on the plane $x^1 = 4$

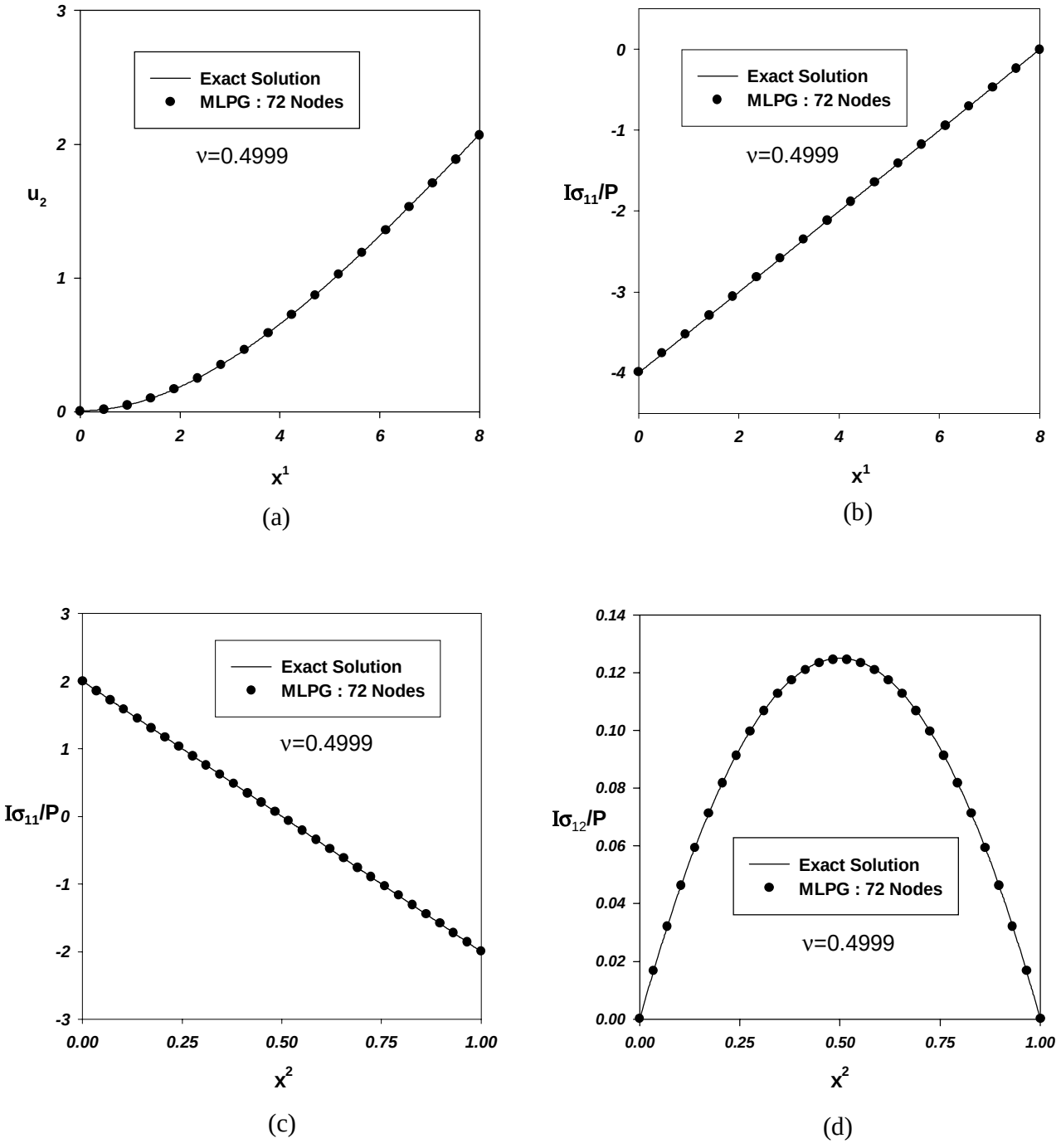

Fig. 1.12a-d : (a) Vertical displacement u_2 vs. x^1 on the top surface
(b) σ_{11} vs. x^1 on the top surface
(c) σ_{11} vs. x^2 at $x^1 = 4$
(d) σ_{12} vs. x^2 at $x^1 = 4$

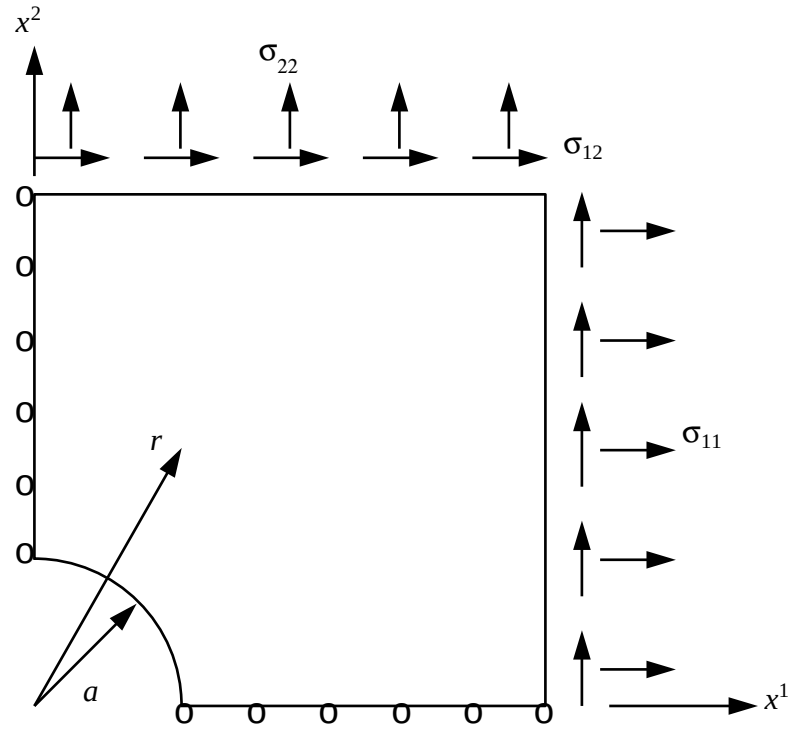

Fig. 1.13 The analysis domain for a plate with a circular hole

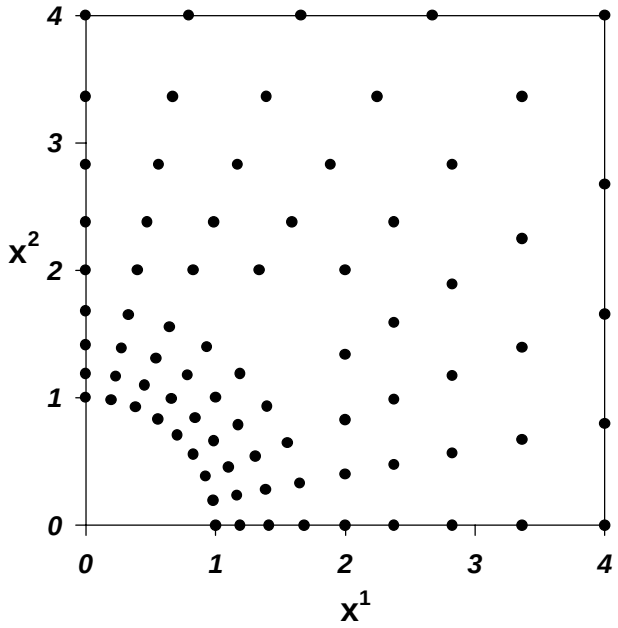

Fig. 1.14 The nodal mesh with 81 nodes

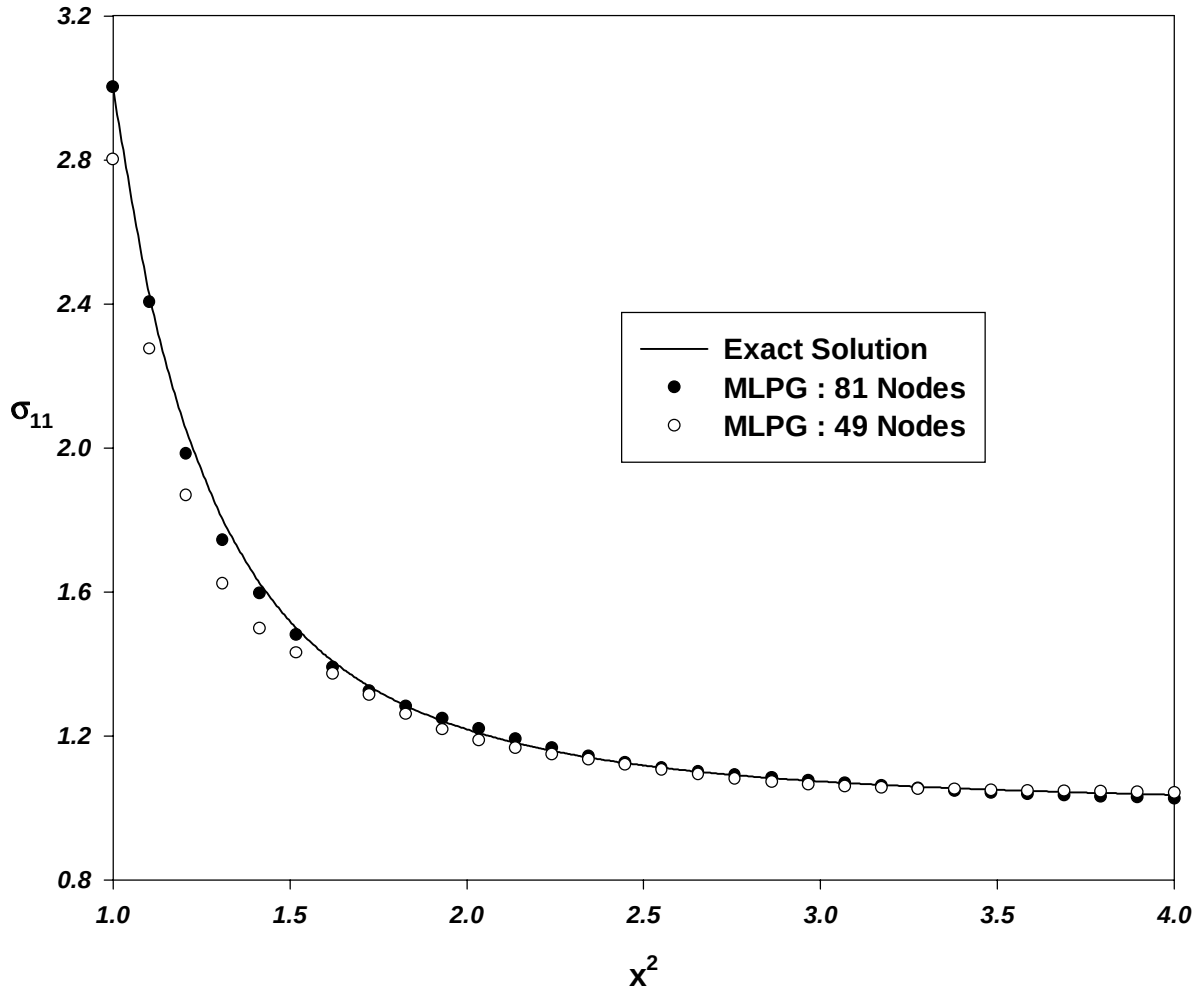

Fig. 1.15 σ_{11} vs. x^2 at $x^1 = 0$

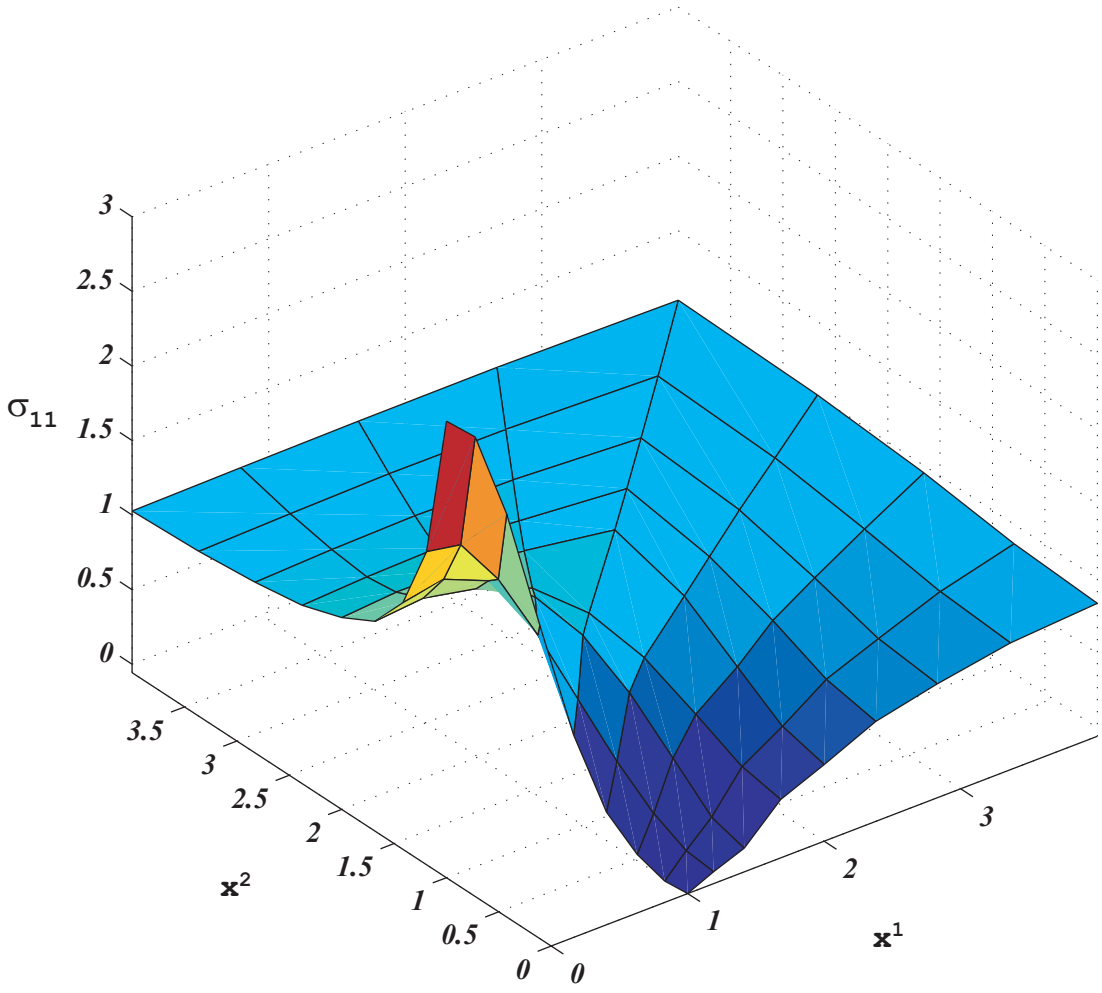

Fig. 1.16 The distribution of σ_{11} over the domain

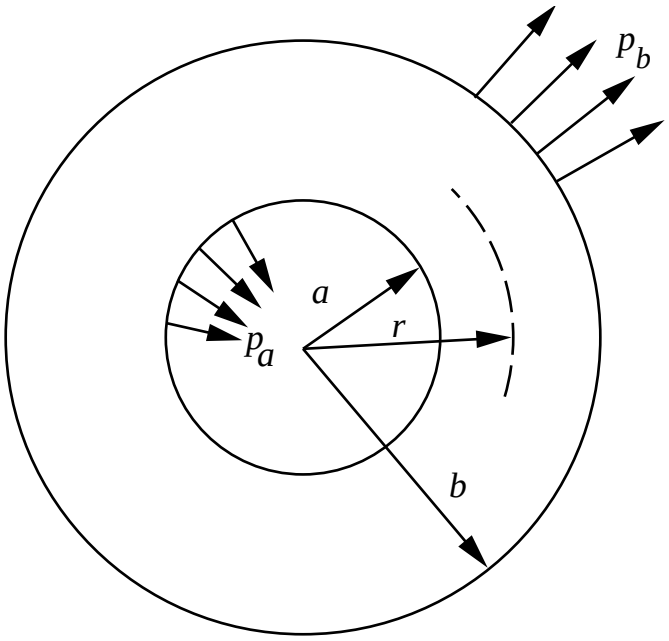

Fig. 1.17 A hollow circular cylinder with pressure applied on the inner and outer surfaces

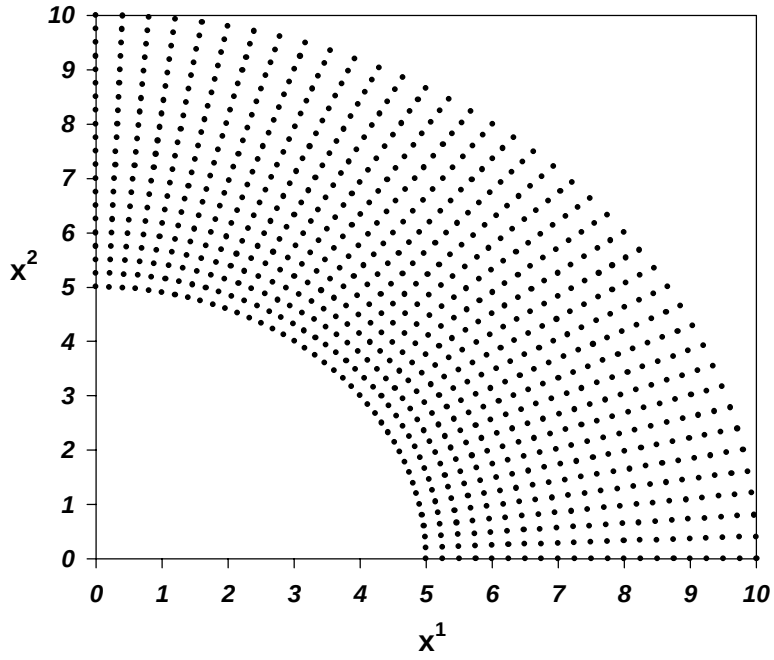

Fig. 1.18 The nodal mesh with 840 nodes

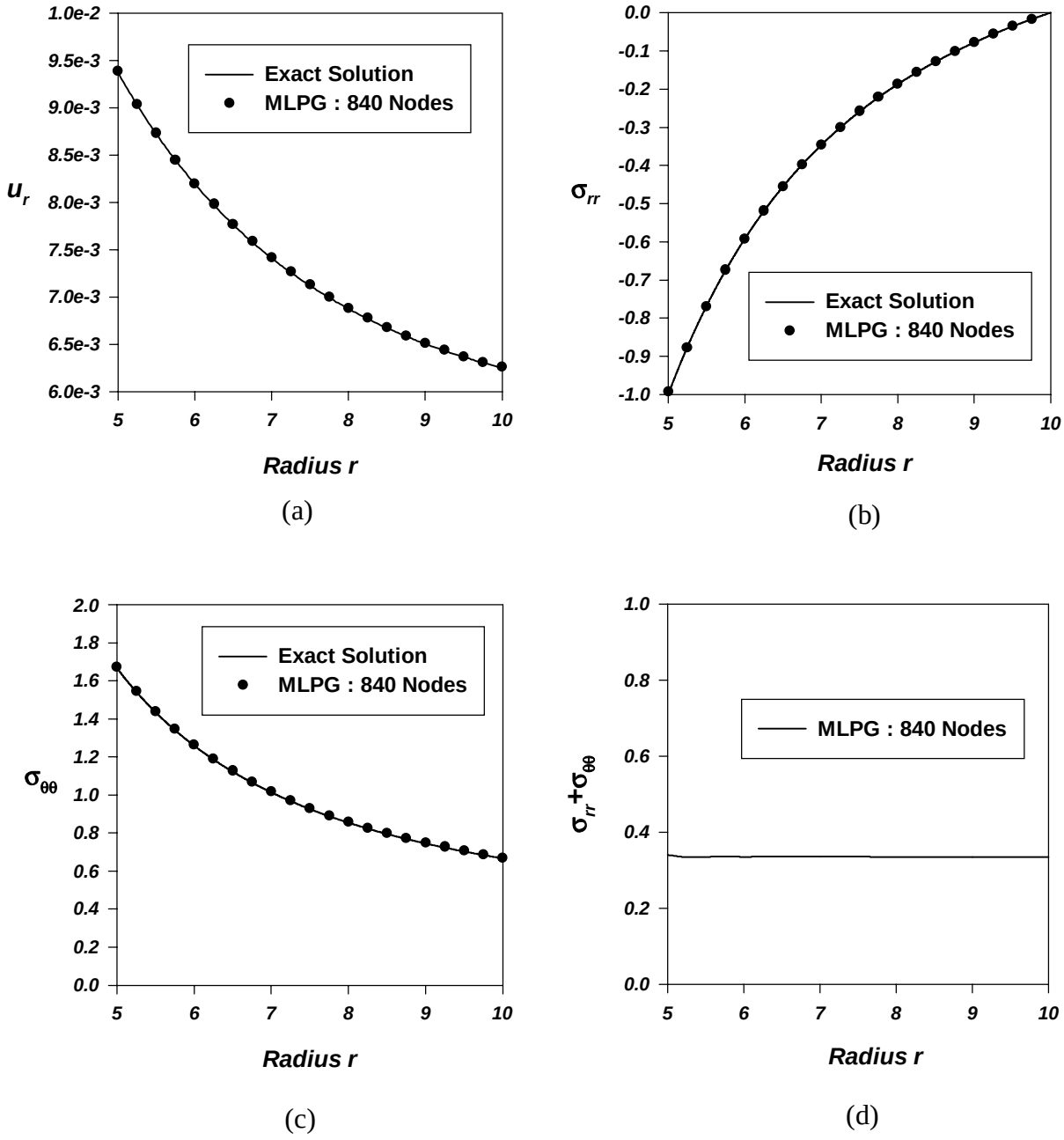

Fig. 1.19 (a) u_r vs. r
(b) σ_{rr} vs. r
(c) $\sigma_{\theta\theta}$ vs. r
(d) $\sigma_{rr}+\sigma_{\theta\theta}$ vs. r

Chapter 2

Determination of Crack Tip Fields in Linear Elastostatics by the Meshless Local Petrov-Galerkin (MLPG) Method

Abstract

It is shown that the MLPG method augmented with the enriched basis functions and either the visibility criterion or the diffraction criterion successfully predicts the singular stress fields near a crack tip. Results are presented for a single edge-cracked plate and a double edge-cracked plate with plate edges parallel to the crack axis loaded in tension, the single edge-cracked plate with one plate edge parallel to the crack axis clamped and the other loaded by tangential tractions, and for a double edge-notched plate with the side between the notches loaded in compression. For the first three problems, the stress intensity factors computed with the equivalent domain and the contour integrals are found to agree well with those available in the literature. For the edge-notched plate, results computed with the MLPG method agree well with those obtained from the finite element method; the effect of the shape of the notch tip is also delineated by varying the ratio, a/b, of the principal axes of an elliptic notch.

Key Words: Singular fields; Stress intensity factors; Mixed-mode deformations; Edge-cracked plates; Edge-notched plates.

A slightly modified version of this chapter has appeared in the C*omputer Modeling in Engineering & Sciences*, Vol. 2, pp. 273-289, 2001.

2.1 Introduction

Atluri and Zhu (1998, 2000), Kim and Atluri (2000), Atluri et al. (1999a,b) and Lin and Atluri (2000) have recently developed the meshless local Petrov-Galerkin (MLPG) approach and have applied it to analyze several linear elastostatics and convection-diffusion problems. We refer the reader to their papers for a review of the developments in meshless methods and how the MLPG technique differs from the other so-called meshless methods. More specifically, Atluri et al. (1999a) discuss the generality of the MLPG method in choosing the local basis for the trial and the test functions of a wide variety, leading to either symmetric or asymmetric system of equations.

Recently, Kim and Atluri (2000) demonstrated the use of the MLPG formulation, in conjunction with the use of secondary nodes and no special crack tip modeling, for finding elastostatic deformation fields near the crack tip. Here, on the other hand, we use the MLPG method in conjunction with either the visibility criterion of Belytschko et al. (1994) or the diffraction criterion of Organ et al. (1996) to analyze deformation fields near a crack tip. It is found that singular fields near a crack tip in a single edge-cracked plate and a double edge-cracked plate with the sides parallel to the crack subjected to uniformly distributed tensile surface tractions, in a single edge-cracked plate with one side parallel to the crack clamped and the other loaded by tangential surface tractions, and a double edge-prenotched plate with the edge between the two notches loaded in compression can be successfully computed with the present MLPG method which is augmented with the known crack-tip singular fields.

2.2 Formulation of the Problem

2.2.1 Governing equations

In rectangular Cartesian coordinates, the static deformations of an isotropic homogeneous linear elastic body are governed by the following equations:

$$\sigma_{ij,j} + b_i = 0, \text{ in } \Omega, \ (i, j = 1,2,3), \tag{2.1}$$

$$\sigma_{ij} = \lambda \varepsilon_{kk} \delta_{ij} + 2\mu \varepsilon_{ij}, \text{ in } \Omega, \tag{2.2}$$

$$\varepsilon_{ij} = (u_{i,j} + u_{j,i})/2, \text{ in } \Omega, \tag{2.3}$$

$$u_i = \bar{u}_i, \text{ on } \Gamma_u, \tag{2.4a}$$

$$t_i \equiv \sigma_{ij} n_j = \bar{t}_i, \text{ on } \Gamma_t. \tag{2.4b}$$

Here σ is the stress tensor, ε the infinitesimal strain tensor, **u** the displacement, **b** the density of body forces, a comma followed by the index *i* denotes partial differentiation with respect to x_i, a repeated index implies summation over the range of the index, **x** is the present position of a material point, Ω the region of space occupied by the body, Γ_u and Γ_t are disjoint parts of the boundary $\partial\Omega$ of Ω, i.e., $\Gamma_u \bigcap \Gamma_t = \phi$, $\Gamma_u \bigcup \Gamma_t = \partial\Omega$, $\bar{\mathbf{u}}$ the prescribed displacements on Γ_u, $\bar{\mathbf{t}}$ the prescribed surface tractions on Γ_t, **n** an outward unit normal to Γ, and λ and μ are Lame′ constants for the material of the body. Substitution from (2.2) and (2.3) into (2.1) yields second order partial differential equations for **u** which are to be solved under the boundary conditions (2.4).

2.2.2 Weak formulation

The following brief derivation of the local symmetric weak form (LSWF) follows that given by Atluri and Zhu (1998, 2000) and Lin and Atluri (2000) and is included for the sake of completeness. Even though the derivation is valid for a three-dimensional problem, we restrict ourselves to two-dimensional problems. Thus, the range of indices is 1,2.

Let $\Omega_s \subset \Omega$ be a subdomain of Ω, $\Gamma_s = \partial\Omega_s \bigcap \partial\Omega$, $L_s = \partial\Omega_s - \Gamma_s$ and **v** be a smooth function defined on Ω_s that vanishes on L_s. Let $\Gamma_{su} = \Gamma_s \bigcap \Gamma_u = \partial\Omega_s \bigcap \Gamma_u$, and $\Gamma_{st} = \Gamma_s \bigcap \Gamma_t = \partial\Omega_s \bigcap \Gamma_t$. That is, Γ_{su} and Γ_{st} are the parts of the boundary Γ_s where the essential and the natural boundary conditions are prescribed respectively. Taking the inner

product of Eq. (2.1) with **v** and of Eq. (2.4a) with $\alpha\mathbf{v}$, integrating the resulting equations over Ω_s and Γ_{su} respectively, adding them, using the divergence theorem and the natural boundary condition (2.4b) on Γ_{st}, we obtain

$$\int_{\Omega_s}(\sigma_{ij}v_{i,j}-b_iv_i)d\Omega+\int_{\Gamma_{su}}\alpha(u_i-\bar{u}_i)v_i d\Gamma-\int_{\Gamma_{st}}\bar{t}_iv_i d\Gamma-\int_{\Gamma_{su}}t_iv_i d\Gamma=0. \tag{2.5}$$

Here α is a scalar function of **x** which is defined on Γ_{su} and can be regarded either as a Lagrange multiplier in which case it is to be determined as a part of the solution of the problem or a preassigned penalty parameter necessary to satisfy the essential boundary conditions on Γ_{su}. In either case, its units are force/(length)^3 so that Eq. (2.5) is dimensionally correct. Atluri et al. (1999a) have demonstrated that by using a simple nodal degree of freedom transformation on Γ_{su}, the essential boundary conditions can be exactly satisfied without using either Lagrange multipliers or a penalty approach.

In the Galerkin formulation, $\Omega_s=\Omega$ and the test function **v** is taken as one of the basis functions defined on Ω which are used to approximate the trial solution **u** on Ω. Here the test function **v** and the trial solution **u** are from different spaces of functions, and hence the formulation is the Petrov-Galerkin. Atluri et al. (1999a) show how, within the context of the MLPG formulation, the subdomains for the trial and the test functions can be of different sizes and shapes; and how the trial and the test functions can be from different or the same spaces, leading to either symmetric or unsymmetric system of equations. In order to obtain two sets of equations for the two components of **u**, we select two linearly independent functions $\mathbf{v}^{(1)}$ and $\mathbf{v}^{(2)}$ for **v** in Eq. (2.5), and write it in the matrix form as

$$\begin{aligned}&\int_{\Omega_s}\varepsilon_v\sigma d\Omega+\int_{\Gamma_{su}}\alpha\mathbf{v}\mathbf{u}d\Gamma-\int_{\Gamma_{su}}\mathbf{v}\mathbf{t}d\Gamma\\&=\int_{\Gamma_{st}}\mathbf{v}\bar{\mathbf{t}}d\Gamma+\int_{\Gamma_{su}}\alpha\mathbf{v}\bar{\mathbf{u}}d\Gamma+\int_{\Omega_s}\mathbf{v}\mathbf{b}d\Omega.\end{aligned} \tag{2.6}$$

Here ε_v is the matrix of strain components derived from **v**, and σ is the matrix of stress components derived from the trial solution **u**. For 2-dimensional problems,

$$\sigma = \begin{Bmatrix} \sigma_{11} \\ \sigma_{22} \\ \sigma_{12} \end{Bmatrix}, \qquad \varepsilon_v = \begin{bmatrix} \varepsilon_{11}^{(1)} & \varepsilon_{22}^{(1)} & 2\varepsilon_{12}^{(1)} \\ \varepsilon_{11}^{(2)} & \varepsilon_{22}^{(2)} & 2\varepsilon_{12}^{(2)} \end{bmatrix},$$

$$\mathbf{u} = \begin{Bmatrix} u_1 \\ u_2 \end{Bmatrix}, \qquad \mathbf{v} = \begin{bmatrix} v_1^{(1)} & v_2^{(1)} \\ v_1^{(2)} & v_2^{(2)} \end{bmatrix},$$

$$\mathbf{t} = \begin{Bmatrix} t_1 \\ t_2 \end{Bmatrix}, \qquad \mathbf{b} = \begin{Bmatrix} b_1 \\ b_2 \end{Bmatrix}. \tag{2.7}$$

Here superscripts (1) and (2) signify, respectively, the quantity derived from test functions $\mathbf{v}^{(1)}$ and $\mathbf{v}^{(2)}$. A simple choice for two linearly independent test functions $\mathbf{v}^{(1)}$ and $\mathbf{v}^{(2)}$ is

$$\mathbf{v} = \begin{bmatrix} v & 0 \\ 0 & v \end{bmatrix}. \tag{2.8}$$

2.2.3 Trial solutions

Let $\Omega_{\mathbf{x}} \subset \Omega$ be the neighborhood of a point $\mathbf{x} \in \Omega$. We approximate the trial solution $\mathbf{u}^h(\mathbf{x})$ on $\Omega_{\mathbf{x}}$ by

$$u_i^h(\mathbf{x}) = \phi_\alpha(\mathbf{x})\hat{u}_{\alpha i}, \qquad (\alpha = 1, 2, ..., n;\ i = 1, 2), \tag{2.9}$$

where $\phi_1(\mathbf{x}), \phi_2(\mathbf{x}), ... \phi_n(\mathbf{x})$ are linearly independent functions defined on $\Omega_{\mathbf{x}}$ and $\hat{u}_{\alpha i}$ are $2n$ scalar quantities which are not necessarily associated with the values of $\mathbf{u}^h(\mathbf{x})$ at any point in $\Omega_{\mathbf{x}}$. We use the Moving Least Squares (MLS) approach to ascertain $\phi_1(\mathbf{x}), \phi_2(\mathbf{x}), ..., \phi_n(\mathbf{x})$.

Let at every point $\mathbf{x} \in \Omega_{\mathbf{x}}$,

$$u_1^h(\mathbf{x}) = p_\Lambda(\mathbf{x})a_\Lambda(\mathbf{x}), \qquad (\Lambda = 1,2,...,m), \tag{2.10}$$

and a similar relation hold for $u_2^h(\mathbf{x})$. Here $\mathbf{p}(\mathbf{x}) = [p_1(\mathbf{x}), p_2(\mathbf{x}),..., p_m(\mathbf{x})]$ is a complete monomial basis of order *m*, $\mathbf{a}(\mathbf{x})$ is an *m*-dimensional vector valued function of $\mathbf{x}$ whose components are determined by finding an extremal of the following weighted discrete L_2 norm:

$$J(\mathbf{x}) = \sum_{\alpha=1}^{n} w_\alpha(\mathbf{x})\left[p_\Lambda(\mathbf{x}_\alpha)a_\Lambda(\mathbf{x}) - \hat{u}_{\alpha 1}\right]^2. \tag{2.11}$$

Here $w_\alpha(\mathbf{x})$ is the weight function associated with the spatial point $\mathbf{x}_\alpha$, $w_\alpha(\mathbf{x}) > 0$ in its compact support, and $\mathbf{x}_1, \mathbf{x}_2, ..., \mathbf{x}_n$ are the points in $\Omega_\mathbf{x}$ for which $w_\alpha(\mathbf{x}) > 0$. Points $\mathbf{x}_1, \mathbf{x}_2, ..., \mathbf{x}_n$ are called nodes.

Solving the set of *m* linear simultaneous equations $\partial J / \partial a_\Lambda(\mathbf{x}) = 0$ for $a_\Lambda(\mathbf{x})$, substituting the solution in Eq. (2.10) and comparing the result with Eq. (2.9) we obtain

$$\phi_\alpha(\mathbf{x}) = p_\Gamma(\mathbf{x})[\mathbf{A}^{-1}(\mathbf{x})\mathbf{B}(\mathbf{x})]_{\Gamma\alpha}, \tag{2.12}$$

$$A_{\Lambda\Gamma}(\mathbf{x}) = \sum_{\alpha=1}^{n} w_\alpha(\mathbf{x}) p_\Lambda(x_\alpha) p_\Gamma(x_\alpha), \tag{2.13}$$

$$B_{\Gamma\alpha}(\mathbf{x}) = p_\Gamma(x_\alpha) w(x_\alpha), \text{ no sum on } \alpha. \tag{2.14}$$

Necessary conditions for the matrix $\mathbf{A}$ to be invertible are that for $\alpha = 1,2,...,m \le n, w_\alpha(\mathbf{x}) \ne 0$ for every $\mathbf{x} \in \Omega_\mathbf{x}$, and that the *n* nodal points $\mathbf{x}_\alpha \in \Omega_\mathbf{x}$ used to evaluate $J(\mathbf{x})$ in Eq. (2.11) are not arranged in a special pattern such as a straight line.

The function $\phi_\alpha(\mathbf{x})$ is called the shape function of the MLS approximation corresponding to the node point $\mathbf{x}_\alpha$. Note that $\phi_\alpha(\mathbf{x}_\beta)$ need not equal $\delta_{\alpha\beta}$ where $\delta_{\alpha\beta}$ is the

Kronecker delta. We have assumed the weight function $w_\alpha(\mathbf{x})$ to have the Gaussian distribution, viz.,

$$w_\alpha(\mathbf{x}) = \begin{cases} \dfrac{\exp(-d_\alpha / c_\alpha)^{2k} - \exp(-r_\alpha / c_\alpha)^{2k}}{1 - \exp(-r_\alpha / c_\alpha)^{2k}}, & 0 \le d_\alpha \le r_\alpha, \\ 0, & d_\alpha \ge r_\alpha, \end{cases} \tag{2.15}$$

there is no sum on the index α, $d_\alpha = |\mathbf{x} - \mathbf{x}_\alpha|$ is the distance from node $\mathbf{x}_\alpha$, to point $\mathbf{x}$, k and c_α are constants, and r_α is the radius of the support of $w_\alpha(\mathbf{x})$. The values of the constants $c_\alpha, r_\alpha,$ and k may affect the accuracy of computed results and should be chosen carefully. Following Lu et al.'s (1994) recommendation we have taken $k = 1$, c_α equal to the distance to the third nearest neighboring node from the node $\mathbf{x}_\alpha$, and $r_\alpha = 4c_\alpha$; when finding the third nearest neighboring node from $\mathbf{x}_\alpha$, nodes equidistant from $\mathbf{x}_\alpha$ are counted once. The support of the weight function, w_α, includes at least m nodes to ensure the invertibility of the matrix $\mathbf{A}$ defined by Eq. (2.13).

We note that the domain of definition of an MLS approximation for the trial function at a point $\mathbf{x}$, hereafter termed the domain of definition of a point $\mathbf{x}$, is a subdomain which covers all nodes whose weight functions do not vanish at $\mathbf{x}$. The support of node $\mathbf{x}_\alpha$ is a subdomain, usually taken as a circle of radius r_α, in which the weight function w_α in the MLS approximation, associated with node $\mathbf{x}_\alpha$, is nonzero.

2.2.4 Enriched basis functions

In the application of the meshless method to linear elastic fracture mechanics (LEFM) problems, it is advantageous to add the asymptotic near-tip displacement field to the basis functions so that the stress singularity can be captured without having a very fine nodal mesh around the crack tip. Fleming et al. (1997) first proposed this for the Element Free Galerkin (EFG) method and called the resulting basis as enriched basis functions. We do this for the

MLPG method to study the LEFM problems. In two-dimensional LEFM, both mode-I and mode-II crack-tip fields should be considered. For mode-I deformations, the crack-tip displacements are (Anderson, 1991)

$$\begin{Bmatrix} u_1 \\ u_2 \end{Bmatrix} = \frac{K_I}{2\mu}\sqrt{\frac{r}{2\pi}} \begin{Bmatrix} \cos\frac{\theta}{2}\left[\kappa - 1 + 2\sin^2\frac{\theta}{2}\right] \\ \sin\frac{\theta}{2}\left[\kappa + 1 - 2\cos^2\frac{\theta}{2}\right] \end{Bmatrix}, \tag{2.16a}$$

$$\begin{Bmatrix} \sigma_{11} \\ \sigma_{22} \\ \sigma_{12} \end{Bmatrix} = \frac{K_I}{\sqrt{2\pi r}}\cos\frac{\theta}{2} \begin{Bmatrix} 1 - \sin\frac{\theta}{2}\sin\frac{3\theta}{2} \\ 1 + \sin\frac{\theta}{2}\sin\frac{3\theta}{2} \\ \sin\frac{\theta}{2}\cos\frac{3\theta}{2} \end{Bmatrix}. \tag{2.16b}$$

For mode-II deformations, the asymptotic displacement fields near the crack-tip are (Anderson, 1991)

$$\begin{Bmatrix} u_1 \\ u_2 \end{Bmatrix} = \frac{K_{II}}{2\mu}\sqrt{\frac{r}{2\pi}} \begin{Bmatrix} \sin\frac{\theta}{2}\left[\kappa + 1 + 2\cos^2\frac{\theta}{2}\right] \\ -\cos\frac{\theta}{2}\left[\kappa - 1 - 2\sin^2\frac{\theta}{2}\right] \end{Bmatrix}, \tag{2.17a}$$

$$\begin{Bmatrix} \sigma_{11} \\ \sigma_{22} \\ \sigma_{12} \end{Bmatrix} = \frac{K_{II}}{\sqrt{2\pi r}}\cos\frac{\theta}{2} \begin{Bmatrix} -\sin\frac{\theta}{2}\left[2 + \cos\frac{\theta}{2}\cos\frac{3\theta}{2}\right] \\ \sin\frac{\theta}{2}\cos\frac{\theta}{2}\cos\frac{3\theta}{2} \\ \cos\frac{\theta}{2}\left[1 - \sin\frac{\theta}{2}\cos\frac{3\theta}{2}\right] \end{Bmatrix}. \tag{2.17b}$$

Here K_I and K_{II} are the stress intensity factors, and depend upon the crack length, the specimen geometry and the applied loading, and (r,θ) are the cylindrical coordinates of a point with the origin located at the crack-tip and the positive angle measured counterclockwise from the axis of the crack. The Kolosov constant κ is related to Poisson's ratio by

$$\kappa = \begin{cases} 3-4\nu & \text{for plane strain,} \\ \dfrac{3-\nu}{1+\nu} & \text{for plane stress,} \end{cases} \tag{2.18}$$

After using trigonometric identities, one can show that all of the functions in Eqs. (2.16) and (2.17) are spanned by the following four basis functions:

$$\left\{ \sqrt{r}\cos\frac{\theta}{2}, \sqrt{r}\sin\frac{\theta}{2}, \sqrt{r}\sin\frac{\theta}{2}\sin\theta, \sqrt{r}\cos\frac{\theta}{2}\sin\theta \right\}. \tag{2.19}$$

These four basis functions are added to the monomial basis functions in $\mathbf{p}(\mathbf{x})$ to form enriched basis functions. Thus, $\mathbf{p}(\mathbf{x})$ will have either seven or ten basis functions according as it has complete monomials of degree 1 or 2 respectively.

2.2.5 Visibility and diffraction criteria

The meshless methods usually provide a smooth approximation of a function and its spatial derivatives; however, the displacements are generally discontinuous across a crack. One way to introduce discontinuities in the MLPG approximation is to adopt the visibility criterion proposed by Belytschko et al. (1994). In this approach, a crack is considered to be opaque. When the domain of influence for a weight function is constructed, the line from a point to a node is viewed to be a ray of light. If the ray of light encounters this opaque crack, it is terminated and the point is not included in the domain of influence of the node. For example, consider a crack shown in Fig. 2.1a. The domain of influence for node *P* is truncated by this crack, and the shaded area on the opposite side of node *P* is not included in the domain of influence for node *P*. This truncation will create a discontinuity in the shape function for node *P* and thus result in discontinuous displacement fields across the crack. For a node near the crack tip, an additional discontinuity may be produced by the visibility method. For example, the domain of influence for node I is not only cut by the crack line *AC*, but also truncated by the line *AB*, which introduces discontinuous shape functions around the

crack tip. Even though the shape functions are discontinuous, Krysl and Belytschko (1997) have shown that the method gives convergent solutions.

Another technique to account for discontinuous fields across the crack is the diffraction method proposed by Organ et al. (1996). In this method, the domain of influence for a node near the crack tip is wrapped around its sharp corner. For example, in Fig. 2.1b, if the line joining a sampling point **x** and a node $\mathbf{x}_I$ intersects the crack line and the crack tip is within the domain of influence of the node, then the distance d_α in the expression (2.15) for the weight function is modified to

$$d_\alpha = \left(\frac{s_1 + s_2(\mathbf{x})}{s_0(\mathbf{x})} \right)^{\bar{\lambda}} s_0(\mathbf{x}), \tag{2.20}$$

where $s_1 = |\mathbf{x}_I - \mathbf{x}_c|$, $s_2 = |\mathbf{x} - \mathbf{x}_c|$, $s_0 = |\mathbf{x} - \mathbf{x}_I|$, and $\mathbf{x}_c$ is the position vector of the crack tip located at the point *C*. The parameter $\tilde{\lambda}$ is used to adjust the distance of the support of $w_\alpha(\mathbf{x})$ on the opposite side of the crack. Organ et al. (1996) found that $\tilde{\lambda} = 1 \text{ or } 2$ performs well in the EFG analysis. Here, we have taken $\tilde{\lambda} = 1$.

2.2.6 Computation of the stress intensity factors

Rice (1968) found that the component of Eshelby's (1956) energy momentum tensor along the axis of the crack can be used as a fracture parameter when the contour Γ of integration encloses the crack tip. He denoted this contour integral by *J*. For the crack along $x_1 - \text{axis}$

$$J = \int_\Gamma \left[W\delta_{1j} - \sigma_{ij} \frac{\partial u_i}{\partial x_1} \right] n_j d\Gamma, \tag{2.21}$$

where $W = \frac{1}{2}\sigma_{ij}\varepsilon_{ij}$ is the strain energy density. For a mixed-mode problem in LEFM, *J* is related to the stress intensity factors via Irwin's (1957) relation, i.e.,

$$J = G = \frac{1}{\overline{E}}\left(K_I^2 + K_{II}^2\right). \tag{2.22}$$

where $\overline{E} = E$ for plane stress, $\overline{E} = E/(1-\nu^2)$ for plane strain problems, E is Young's modulus. Yau et al. (1980) and Shih and Asaro (1988) have used an interaction integral to extract K_I and K_{II} from Eq. (2.22); the interaction integral is described below.

Consider two equilibrium states of a body with a crack: state 1 the actual state for the given boundary conditions and state 2 an auxiliary state. The interaction integral, $M^{(1,2)}$, for the two equilibrium states is given by

$$M^{(1,2)} = \int_\Gamma \left[W^{(1,2)}\delta_{1j} - \sigma_{ij}^{(1)}\frac{\partial u_i^{(2)}}{\partial x_1} - \sigma_{ij}^{(2)}\frac{\partial u_i^{(1)}}{\partial x_1} \right] n_j \, d\Gamma, \tag{2.23}$$

where

$$W^{(1,2)} = \frac{1}{2}\left(\sigma_{ij}^{(1)}\varepsilon_{ij}^{(2)} + \sigma_{ij}^{(2)}\varepsilon_{ij}^{(1)}\right), \tag{2.24}$$

is the mutual strain energy density. For the two superposed equilibrium states, Eq. (2.21) gives

$$J^{tot} = J^{(1)} + J^{(2)} + M^{(1,2)}, \tag{2.25}$$

Irwin's relation (2.22) implies that

$$\begin{aligned} J^{tot} &= \frac{1}{\overline{E}}\left[\left(K_I^{(1)} + K_I^{(2)}\right)^2 + \left(K_{II}^{(1)} + K_{II}^{(2)}\right)^2 \right], \\ &= \frac{1}{\overline{E}}\left[\left((K_I^{(1)})^2 + (K_{II}^{(1)})^2\right) + \left((K_I^{(2)})^2 + (K_{II}^{(2)})^2\right) + 2\left(K_I^{(1)}K_I^{(2)} + K_{II}^{(1)}K_{II}^{(2)}\right)\right], \\ &= J^{(1)} + J^{(2)} + \frac{2}{\overline{E}}\left(K_I^{(1)}K_I^{(2)} + K_{II}^{(1)}K_{II}^{(2)}\right). \end{aligned} \tag{2.26}$$

Equating the right hand sides of Eqs. (2.25) and (2.26) we conclude that

$$M^{(1,2)} = \frac{2}{\overline{E}}\left(K_I^{(1)}K_I^{(2)} + K_{II}^{(1)}K_{II}^{(2)}\right), \tag{2.27}$$

The choice (2.16) for the auxiliary field gives

$$M^{(1,2)} = \frac{2}{\overline{E}}K_I, \tag{2.28}$$

and the choice (2.17) for it yields

$$M^{(1,2)} = \frac{2}{\overline{E}}K_{II}. \tag{2.29}$$

Thus K_I and K_{II} can be computed from the interaction integral by appropriate choices of the auxiliary field. Further details on the use of the *M*-integrals for crack problems in isotropic media, as well as cracks at anisotropic bimaterial interfaces can be found in Atluri (1997), and Chow et al. (1995).

The line integrals (2.21) and (2.23) are often converted into equivalent domain forms for numerical evaluation. Let *q* be a differentiable function that equals 0 on the closed contour Γ and equals 1 at the crack tip. It can be shown that (e.g. see Nikishkov and Atluri (1987); Moran and Shih (1987); and Anderson (1991))

$$J = \int_A \left[\sigma_{ij}\frac{\partial u_i}{\partial x_1} - W\delta_{1j}\right]\frac{\partial q}{\partial x_j}d\Omega, \tag{2.30}$$

$$M^{(1,2)} = \int_A \left[\sigma_{ij}^{(1)}\frac{\partial u_i^{(2)}}{\partial x_1} + \sigma_{ij}^{(2)}\frac{\partial u_i^{(1)}}{\partial x_1} - W^{(1,2)}\delta_{1j}\right]\frac{\partial q}{\partial x_j}d\Omega, \tag{2.31}$$

where *A* is the area enclosed by the contour Γ. This approach of evaluating K_I and K_{II} is called the equivalent domain integral (EDI) method, is often used in the finite element work,

and has been employed by Lu et al. (1994) in the EFG method. It requires the discretization of the domain A into either fictitious cells or finite elements. However, the determination of K_I and K_{II} from Eqs. (2.23), (2.28) and (2.29) keeps the method purely meshless. Kim and Atluri (2000) use the EDI method in the context of the meshless MLPG formulation.

2.3 Computation and Discussion of Results

We have developed a computer code based on the aforestated equations. The code has been validated by comparing computed results with the analytical solution for the following three problems: a cantilever beam loaded by tangential tractions at the unclamped edge, an infinite plate with a circular hole subjected to uniformly distributed tensile tractions at infinity, and a circular hollow cylinder subjected to a pressure loading on the inner surface. In each case the computed solution was found to essentially coincide with the analytical solution of the problem. For the cantilever beam problem, as also pointed out by Atluri and Zhu (2000), the MLPG method gave exact results even for Poisson's ratio = 0.4999; the FE method exhibits locking phenomenon for this case and significantly underestimates the tip deflection of the cantilever beam. Here we describe results for five other problems. In each case, there is no body force, and the penalty function α defined on Γ_{su} in Eq. (2.5) is taken to be a constant, and is set equal to $10^5 E/l$ where l is a typical length in the problem. The test function $v(\mathbf{x})$ (cf. Eq. (2.8)) is set equal to the weight function $w_\alpha(\mathbf{x})$ of the MLS approximation, with the radius r_0 of the local domain Ω_s taken equal to the radius r_α of the support of the weight function. If the union of all local domains covers the global domain, i.e., $\bigcup \Omega_s \supset \Omega$, the equilibrium equations and the boundary conditions are satisfied respectively in Ω and on Γ. This is ensured by selecting an Ω_s for each node $\mathbf{x}_\alpha \in \Omega$ and taking r_0 large enough. While evaluating integrals on Ω_s and Γ_s, 8×8 and 8 Gauss points are employed respectively. The two linear algebraic equations resulting from Eq. (2.6) are assembled, and solved for $\hat{u}_i$. Displacements and hence strains and stresses at any point $\mathbf{x}\in\Omega$ can then be computed from Eqs. (2.9), (2.3) and (2.2) respectively. We use (i) the

quadratic (with and without the enriched) basis functions, (ii) either the visibility or the diffraction criterion, and (iii) Eq. (2.27) with the near crack tip solution as the auxiliary field to compute the stress intensity factors.

2.3.1 Near-tip mode-I stress fields

We analyze plane strain deformations of a single edge-cracked square plate of side *b* and crack length *a* with $b = 2a = 10$ units, E = 1000 units and $\nu = 0.3$. Both tangential and normal displacements given by Eq. (2.16a) and $K_I = 1$ are prescribed on the four bounding edges. Figure 2.2a shows a sketch of the problem studied and Fig. 2.2b displays the layout of the 590 nodes; the nodal mesh is fine near the crack tip. Rao and Raman (2000) have scrutinized this problem by the EFG method in conjunction with the enriched basis functions and the diffraction criterion, and employed uniformly spaced mesh of 175 nodes with 13 nodes on each side. They used weight functions based on the Student's *t*-distribution. For the weight functions, the values of $d_\alpha, c_\alpha, r_\alpha, k$ and $\overline{\lambda}$ used herein and the enriched basis functions, stresses near the crack-tip computed with the uniformly spaced mesh of 175 nodes deviated somewhat from the exact solution of the problem. However, with the nodal mesh of Fig. 2.2b and as shown in Fig. 2.3a, the variations of σ_{rr} and $\sigma_{\theta\theta}$ with the distance from the crack tip of points on the crack axis match very well with the analytical solution (2.16b) of the problem. Also, for $r/a = 0.1$, the variation with the angle, θ, of the computed values of $\sigma_{rr}, \sigma_{\theta\theta}$ and $\sigma_{r\theta}$ agree very well with those obtained from the analytical solution (2.16b). Here $\sigma_{rr}, \sigma_{\theta\theta}$ and $\sigma_{r\theta}$ are the radial, the circumferential (or the hoop) and the shear stresses respectively. Similar accuracy of the stresses was also demonstrated by Fleming et al. (1997) and Rao and Raman (2000) with the EFG method.

2.3.2 Edge-cracked plate loaded in tension

Plane strain deformations of an edge-cracked square plate, shown in Fig. 2.4a with *b* = 10, *a* = 5, *E* = 1000, $\overline{\nu} = 0.25$, and $\bar{t} = 1$ are analyzed. Due to the symmetry of the problem

about the horizontal centroidal axis, deformations of only the upper half of the plate with the nodal mesh of Fig. 2.2b are studied.

The expression for K_I given in Gdoutos (1993) is

$$K_I = \bar{t}\sqrt{\pi a}\left[1.12 - 0.23\frac{a}{b} + 10.55(\frac{a}{b})^2 - 21.72(\frac{a}{b})^3 + 30.39(\frac{a}{b})^4\right]. \qquad (2.32)$$

Thus, for the plate problem being studied, $K_I = 11.2$. We have listed in Table 2.1 computed values of the stress intensity factor K_I for different contours Γ and without using the enriched basis functions; the contour is shown in Fig. 2.4b. It is clear that the computed value of K_I is essentially independent of the contour, and it differs from the analytical value by less than 2.8%. The value of K_I computed with the contour integral is slightly closer to the analytical value than that obtained by the EDI method. In the evaluation of the domain integrals (2.30) and (2.31), we took

$$q(x_1, x_2) = (x_1 - a_2)(x_1 + a_1)(x_2 - b_2)(x_2 + b_1)/(a_1 a_2 b_1 b_2),$$

with the origin of the $x_1 - x_2$ coordinate axes at the crack tip; a_1, a_2, b_1 and b_2 are defined in Fig. 2.4b.

Although an accurate value of the stress intensity factor has been determined by using a fine nodal mesh near the crack tip and without using the enriched basis functions, the singular stress fields may not be accurately computed. As shown in Fig. 2.5a, the normal stress σ_{22} near the crack tip is finite and does not exhibit the $1/\sqrt{r}$ singularity. Therefore, we use the enriched basis functions, and model the entire edge-cracked plate because we adopt either the visibility or the diffraction criterion. Figure 2.5b evinces the variation of the normal stress σ_{22} along the horizontal line passing through the crack tip. The stress reaches very large values near the crack tip, and both the visibility and the diffraction criteria give virtually identical results. As was found by Belytschko et al. (1996) for the EFG method, the

solution computed with the visibility criterion in the MLPG formulation converges. Figure 2.6 exhibits the angular variation of the radial and the hoop stresses at points located at a radial distance of 0.5 $(r/a = 0.1)$ from the crack tip. We note that the stress distributions obtained with the visibility and the diffraction criteria are identical.

2.3.3 Double edge-cracked plate loaded in tension

We now study deformations of a square plate with cracks emanating from the vertical edges and subjected to the uniform tensile tractions $(\bar{t} = 1)$ at the upper and the lower horizontal surfaces; a schematic sketch of the problem studied is shown in Fig. 2.7a. We only give results for the stress intensity factor since the stress fields around the crack tip are similar to those of the example 2.3.2.

Due to the symmetry of the problem about the horizontal and the vertical centroidal axes, we consider a quarter of the plate. The nodal mesh used to analyze the problem is shown in Fig. 2.7b. We presume that a plane strain state of deformation prevails in the plate and set E = 1000, $\nu = 0.3$, b = 10 and a = 5. From the solution given in Gdoutos (1993) we obtain

$$K_I = \bar{t}\sqrt{\pi a}\left[1.12 + 0.2\frac{a}{b} - 1.2(\frac{a}{b})^2 + 1.93(\frac{a}{b})^3\right] = 4.65.$$

Values of K_I computed with the MLPG method without employing the quadratic polynomial enriched basis functions and by using different contours (a_1, a_2, b_1 and b_2 are defined in Fig. 2.4b) are summarized in Table 2.2. For the first seven contours considered, the value of K_I computed by the EDI method differs from its analytical value by less than 3.2%. The value of K_I computed with the contour integrals has an error of about 6%. For the contour of integration close to the crack tip, the EDI method has a larger error than the contour integral method. The value of K_I computed from the y-intercept of the plot of $ln\,\sigma_{22}(r,0)$ vs. $ln\,r$ with the solution obtained using the enriched basis functions was found to be 4.66 which differs from the analytical value by 0.2%.

2.3.4 Edge-cracked plate under mixed-mode loading

A schematic sketch of the problem studied is exhibited in Fig. 2.8a, and the nonuniform mesh of 621 nodes used to analyze the problem is shown in Fig. 2.8b. The bottom edge of the plate is rigidly clamped while the top edge is subjected to uniformly distributed tangential tractions, $\bar{t} = 1$. We set w = 7 units, h = 16 units, and the crack length a = 3.5 units. A plane strain state of deformation is assumed to prevail in the plate. The stress intensity factors K_I and K_{II} computed by using Eqs. (2.28) and (2.29) respectively, and the fully enriched quadratic basis functions in a region of radius 2, transition basis functions within an annular region of inner and outer radii of 2 and 4 respectively, and regular basis functions elsewhere are listed in Table 2.3; lengths a_1, a_2, b_1 and b_2 are illustrated in Fig. 2.4b. The reference values, $K_I = 34.0$ units and $K_{II} = 4.55$ units, taken from Wilson (1969), compare very well with those computed from Eqs. (2.28) and (2.29) with either the EDI method or the contour integrals. The results are virtually independent of the domain size and the difference between the computed and the reference values of K_I and K_{II} is less than 1.25%. Similar results have been obtained by Rao and Raman (2000) and Fleming et al. (1997) with the EFG method.

2.3.5 Double edge-notched plate with the edge between the notches loaded in compression

Kalthoff and Winkler (1987) studied transient deformations of a double edge-notched plate with the edge between the notches loaded by a fast moving cylindrical projectile. Here we analyze its quasistatic deformations. A schematic sketch of the problem is depicted in Fig. 2.9a. Figure 2.9b shows the shape of the notch tip; the major principal axis of the elliptic notch-tip is aligned with the axis of the notch and has length *a*, and the length of the minor principal axis equals *b*. The shape of the notch tip is taken to circular, and thus we set $a = b = 0.3mm$. We asume that a plane strain state of deformation prevails in the plate, and take E = 210GPa, $\nu = 0.29$, the applied normal traction $\bar{t} = 200$ MPa, and tangential

tractions on this surface = 0. The remaining bounding surfaces of the plate and of the notch are traction free. Deformations of only the upper half of the plate are analyzed with the symmetry boundary conditions imposed on the horizontal centerline of the plate and the rightmost point on this line rigidly clamped. Figure 2.9c exhibits the nonuniform nodal mesh of 3632 nodes with 25 nodes on the surface of the circular notch tip (cf. Fig. 2.9d). The visibility method is adopted to account for the discontinuous fields across the notch. Since the nature of the singular fields near the notch tip is unknown, enriched basis functions are not used.

The MLPG results are compared with the finite element (FE) solution computed with four node quadrilateral elements with the same nodes used in the two analyses. Figures 2.10a and 2.10b display respectively the undeformed and the deformed shapes of the notch and the circular notch tip. Because of the expanded scales used to plot the results, small differences between the FE and the MLPG solutions are greatly magnified. Figures 2.11a and 2.11b depict respectively the variation of σ_{22} and σ_{12} at points on the axis of the notch and lying ahead of the notch tip; the MLPG and the FE results virtually coincide. The maximum value of $|\sigma_{12}|$ occurs at a point slightly ahead of the notch tip. Note that the axial variation of σ_{12} exhibits a boundary layer like phenomenon near the notch tip. Figures 2.12a and 2.12b evince the angular variation of the maximum principal tensile stress and the maximum shear stress at points on the surface of the notch tip. It is clear that the MLPG and the FE solutions agree qualitatively but their magnitudes differ slightly; however, the two solutions predict the same angular locations (70^{o} and -57^{o} respectively) of the points where the maximum principal tensile stress and the maximum shear stress occur; these angular locations are virtually the same as those found by Batra and Gummalla (2000) in the transient analysis of the thermoviscoplastic problem. Once limiting values of these stresses are reached, a brittle failure will ensue from the point where the maximum principal tensile stress occurs and a ductile failure from the location of the maximum shear stress. The maximum principal tensile stress and the maximum shear stress at points on the surface of the notch tip equal approximately ten times the magnitude of the applied uniform normal traction.

We have plotted in Figs. 2.13a and 2.13b respectively, on the logarithmic scale, the variations, at points on the axis of the notch, of $|\sigma_{22}|$ and $|\sigma_{12}|$ with the distance, *r*, from the notch tip. The slopes of both curves equal $-1/2$ signifying the $1/\sqrt{r}$ singularity of the stress fields near the notch tip. Thus the deformation fields close to the tip of the circular notch of radius 0.15*mm* seem to behave as if the notch were a sharp crack. Values of the stress intensity factors computed from the *y*-intercepts of these curves and normalized by applied normal tractions of 200 MPa are $\overline{K}_I = -2.24\sqrt{mm}$ and $\overline{K}_{II} = -4.39\sqrt{mm}$. The mode-mixty parameter, $m^e = \frac{2}{\pi}\tan^{-1}(\frac{K_I}{K_{II}})$, at the notch tip equals 0.3 which is close to the analytical value of 0.25 found by Lee and Freund (1990) for the dynamic problem who took Poisson's ratio, $\nu = 0.25$. Lee and Freund showed that the mode mixity parameter stayed unchanged till a wave reflected from the right free edge arrived at the notch tip. Thus the deformations near the notch tip are K_{II} dominated. The three-dimensional analysis of the transient thermoviscoplastic problem by Batra and Ravisankar (2000) showed that there is a noticeable K_{III} deformation field adjacent to the front and the back faces of the plate. The plane strain state of deformation prevails in the middle 75% of the thickness of the plate. In Figs. 2.12a and 2.12b, we have also exhibited the stresses computed by taking $K_I = \overline{K}_I\bar{t}$ and $K_{II} = \overline{K}_{II}\bar{t}$ in Eqs. (2.16b) and (2.17b) respectively, and adding like components from the two stress fields. It is clear that the stress fields so obtained do not agree even qualitatively with those computed by the MLPG and the FE methods. It suggests that the stress fields near a notch tip can not be derived from those near a crack tip. However, the stress intensity factors K_I and K_{II} determined from Eqs. (2.28) and (2.29) with $M^{(1,2)}$ evaluated from Eq. (2.23) are found to be essentially independent of the contour Γ of integration, and their values equal -461 and $-904\,N/mm^{3/2}$, respectively, for a contour with $a_1 = a_2 = b_1 = b_2 = 1.5mm$. (cf. Fig. 2.4b). These values are close to those found by the stress extrapolation method, i.e., y-intercepts of straight lines in Figs. 2.13a and 2.13b. The energy release rate computed from Eq. (2.21) equals 4490 N/*mm*. We also summarize the computed values of stress intensity factors

K_I and K_{II}, and the *J*-integral in Table 2.4 for different contours. Whereas in Kalthoff's experimental set up and in the numerical simulations of the transient problem, the plate is free to move in the direction of impact, in the static problem studied herein the rigid motions are ruled out. Besides neglecting the effect of inertia forces in the static problem, boundary conditions are not identical in the static and the dynamic problems.

2.3.5.1 The effect of the shape of the notch tip

Batra et al. (2002) recently investigated the effect of the shape of the notch tip on the failure mode transition speed. They found that for circular and very blunt shape of notch tips the failure mode transitioned from the brittle to the ductile with an increase in the impact speed. However, for two very sharp elliptic notch tips, the ductile failure preceded the brittle failure for the six impact speeds studied. Here we use the MLPG method to analyze static deformations of the prenotched elastic plate to ascertain the mode-I and the mode-II stress intensity factors and the deformation fields near the elliptic notch tip.

We take $b = 0.3mm$ (cf. Fig. 2.9b), and set the aspect ratio $a/b = 0.2, 1, 2 \text{ and } 10$. Instead of using the visibility criteria, the diffraction method is adopted to account for the discontinuous deformation fields across the notch.

For $a/b = 0.2, 1, 2, \text{and } 10$, values of K_I and K_{II} computed by the EDI technique and normalized by the magnitude 200 MPa of the applied normal traction respectively equal (-2.34, -4.46), (-2.36, -4.43), (-2.37, -4.43) and (-2.37, -4.46) $\sqrt{mm}$ and the corresponding values of the energy release rate are 4420, 4399, 4402 and 4447 *N*/*mm*. Thus values of the stress intensity factors and the energy release rate are virtually independent of the shape of the notch tip. However, the angular distributions, depicted in Figs. 2.14a and 2.14b, of the normalized maximum principal tensile stress and the normalized maximum shear stress at points on the surface of the notch tip strongly depend upon the shape of the notch tip. For $a/b = 0.2,$ the peak value of the maximum principal tensile stress occurs at $\theta = +87^{o}$ and that of the maximum shear stress at $\theta = -87^{o}$ suggesting that the brittle and the ductile failures will

originate from these points. With an increase in the value of a/b, points on the notch surface where peak values of these two stresses occur shift towards the axis of the notch. For $a/b = 1, 2, \text{and} 10$, angular positions of the points where the maximum principal tensile stress and the maximum shear stress attain their peak values equal respectively (71°, -54°), (26°, -13°), (1°, -1°).

Figures 2.15a and 2.15b depict respectively the variations of the normalized σ_{22} and σ_{12} at points straight ahead of the notch tip; except for the axial variation of σ_{12} with $a/b = 10$, these stress distributions are essentially independent of the ratio a/b. With the exception of the case for $a/b = 10$, the maximum value of $|\sigma_{12}|$ occurs at a point slightly ahead of the notch tip. The axial variation of σ_{12} exhibits a boundary layer like phenomenon near the notch tip. We note that for a sharp crack loaded in mode-II, σ_{12} at $\theta = 0$ is not zero. In order to ensure that the results for the sharp notch tip (i.e. $a/b = 10$) are independent of the nodal locations, two different arrangements of nodes near the notch tip were tried. For each one of these three nodal meshes, the axial variation of σ_{12} was virtually the same (cf. Fig. 2.15c). It seems that an elliptic notch-tip with $a/b = 10$ behaves like a sharp crack. For transient thermomechanical deformations analyzed by Batra et al. (2002), qualitatively similar results were obtained for $a/b = 0.2$, 1, 2, and 10 and with the same nodes as used herein.

2.4 Conclusions

We have enriched the polynomial basis functions with the crack tip singular fields and incorporated the visibility and the diffraction criteria, respectively, of Belytschko et al. (1994) and Organ et al. (1996) into the MLPG approach of Atluri and Zhu (1998, 2000) to successfully compute singular fields by the MLPG method. The stress intensity factors computed by using either the contour integrals or the equivalent domain integral method in a single and a double edge-cracked square plate loaded by uniformly distributed either tangential or normal surface tractions on the edges parallel to the crack match well with their

reference values. The singular stress fields near the crack tip computed with the MLPG method and the enriched basis functions exhibit the $1/\sqrt{r}$ singularity, and agree well with those found from the analytical solution. The angular variations of the stress fields computed with the visibility and the diffraction criteria are found to be virtually indistinguishable from each other. For a double edge-notched plate with the edge between the two notches loaded by a uniformly distributed normal traction, the stress fields near the circular notch tip of radius 0.15 mm exhibit the $1/\sqrt{r}$ singularity. Here r is the distance from the notch tip of a point located on the axis of the notch. The mode I and mode II stress intensity factors normalized by the magnitude of the applied normal surface traction equal -2.24 and -4.39$\sqrt{mm}$ respectively. It is found that the values of K_I and K_{II} are independent of the ratio of the major to the minor principal axes of the elliptic notch tip. However, the angular distributions of the maximum principal tensile stress and the maximum shear stress at points on the surface of the notch tip strongly depend upon the aspect ratio of the notch tip. With an increase in the aspect ratio of the notch tip, points on the notch tip surface where peak values of these stresses occur move towards the axis of the notch. The variations of stresses at points directly ahead of the notch tip are essentially independent of the aspect ratio of the notch tip.

2.5 References

Anderson, T. L. (1991): *Fracture Mechanics: Fundamentals and Applications* (1st Ed.) CRC Press.

Atluri, S. N. (1997): *Structural Integrity and Durability*, Tech. Science Press, Forsyth, GA.

Atluri, S. N. and Zhu, T. (1998): A new Meshless Local Petrov-Galerkin (MLPG) approach in computational mechanics. *Computational Mechanics*, vol. 22, pp. 117-127.

Atluri, S. N., Kim, H. G. and Cho J. Y. (1999a): A critical assessment of the truly meshless local Petrov-Galerkin (MLPG) and local boundary integral equation (LBIE) methods. *Computational Mechanics*, vol 24, pp. 348-372.

Atluri, S. N., Cho, J. Y. and Kim, H. G. (1999b): Analysis of thin beams, using the meshless local Petrov-Galerkin method, with generalized moving least squares interpolants. *Computational Mechanics*, vol. 24, pp. 334-347.

Atluri, S. N. and Zhu, T. (2000): The Meshless Local Petrov-Galerkin (MLPG) approach for solving problems in elasto-statics. *Computational Mechanics*, vol. 25, pp. 169-179.

Batra, R. C. and Gummalla, R. R. (2000): Effect of material and geometric parameters on deformations near the notch tip of a dynamically loaded prenotched plate. *International Journal of Fracture*, vol. 101, pp. 99-140.

Batra, R. C., Jaber, N. A. and Malsbury, M. E. (2002): Analysis of failure modes in an impact loaded thermoviscoplastic prenotched plate. *International Journal of Plasticity*, (in press).

Batra, R. C. and Ravisankar, M. V. S. (2000): Three dimensional numerical simulation of the Kalthoff problem. *International Journal of Fracture*, vol. 105, pp. 161-186.

Belytschko, T., Lu, Y. Y. and Gu, L. (1994): Element-free Galerkin methods. *International Journal for Numerical Methods in Engineering*, vol. 37, pp. 229-256.

Belytschko, T., Krongauz, Y., Fleming, M., Organ, D. J. and Liu, W. K. (1996): Smoothing and accelerated computations in the element free Galerkin method. *Journal of Computational and Applied Mathematics*, vol. 74, pp. 111-126.

Belytschko, T., Krongauz, Y., Organ, D., Fleming, M. and Krysl, P. (1996): Meshless methods: An overview and recent developments. *Computer Methods in Applied Mechanics and Engineering*, vol. 139, pp. 3-47.

Chow, W. T., Beom, H. G. and Atluri, S. N. (1995): Calculation of stress intensity factors for an interfacial crack between dissimilar anisotropic media using a hybrid element method and the mutual integral. *Computational Mechanics*, vol. 15, pp. 546-557.

Eshelby, J. D. (1956): The continuum theory of lattice defects. *Solid State Physics*, vol. 3, pp. 79-141.

Fleming, M., Chu, Y., Moran, B. and Belytschko, T. (1997): Enriched element-free Galerkin methods for crack tip fields. *International Journal for Numerical Methods in Engineering*, vol. 40, pp. 1483-1504.

Gdoutos, E. E. (1993): *Fracture Mechanics: an Introduction*. Kluwer Academic Publishers.

Irwin, G. R. (1957): Analysis of stresses and strains near the end of a crack traversing a plate. *Journal of Applied Mechanics*, vol. 24, pp. 361-364.

Kalthoff, J. F. and Winkler, S. (1987): Failure mode transition at high strain rate of shear loading. in Chiem C.Y., Kunze H.D., Meyer L.W. editors, *Impact Loading and Dynamic Behavior of Materials*, vol. 1, pp. 185-195.

Kim, H. G. and Atluri, S. N. (2000): Arbitrary placement of secondary nodes, and error control in the meshless local Petrov-Galerkin (MLPG) method. *Computer Modeling in Engineering and Sciences*, vol. 1, pp. 11-32.

Krysl, P. and Belytschko, T. (1997): Element-free Galerkin: Convergence of the continuous and discontinuous shape functions. *Computer Methods in Applied Mechanics and Engineering*, vol. 148, pp. 257-277.

Lin, H. and Atluri, S. N. (2000): Meshless local Petrov-Galerkin (MLPG) method for convection-diffusion problems. *Computer Modeling in Engineering and Sciences*, vol. 1, pp. 45-60.

Lu, Y. Y., Belytschko, T. and Gu, L. (1994): A new implementation of the element free Galerkin method. *Computer Methods in Applied Mechanics and Engineering*, vol. 113, pp. 397-414.

Moran, B. and Shih, C. F. (1987): Crack tip and associated domain integrals from momentum and energy balance. *Engineering Fracture Mechanics*, vol. 27(6), pp. 615-641.

Nikishkov, G. P. and Atluri, S. N. (1987): Calculation of fracture mechanics parameters for an arbitrary 3-D crack by the equivalent domain integral method. *International Journal for Numerical Methods in Engineering*, vol. 24, pp. 1801-1822.

Organ, D. J., Fleming, M. and Belytschko, T. (1996): Continuous meshless approximations for nonconvex bodies by diffraction and transparency. *Computational Mechanics*, vol. 18, pp. 225-235.

Rao, B. N. and Rahman, S. (2000): An efficient meshless method for fracture analysis of cracks. *Computational Mechanics*, vol. 26, pp. 298-308.

Rice, J. R. (1968): A path independent integral and the approximate analysis of strain concentration by notches and cracks. *Journal of Applied Mechanics*, vol. 35, pp. 379-386.

Shih, C. F. and Asaro, R. J. (1988): Elastic-plastic analysis of cracks on bimaterial interfaces: Part I - small scale yielding. *Journal of Applied Mechanics*, vol. 55, pp. 299-316.

Wilson, W. K. (1969): *Combined-Mode Fracture Mechanics*. Ph.D. thesis, University of Pittsburgh.

Yau, J. F., Wang, S. S. and Corten, H. T. (1980): A mixed-mode crack analysis of isotropic solids using conservation laws of elasticity. *Journal of Applied Mechanics*, vol. 47, pp. 335-341.

Domain				$K_I^{\text{numerical}} / K_I^{\text{analytical}}$	
a_1	a_2	b_1	b_2	**EDI method**	**Contour**
3	3	3	3	0.9768	0.9804
2	2	2	2	0.9723	0.9821
2.5	2.5	2.5	2.5	0.9750	0.9795
2	2	3	3	0.9786	0.9830
2.5	2.5	3.6	3.6	0.9795	0.9821
1.5	1.5	2.2	2.2	0.9741	0.9848
3	3	4.5	4.5	0.9804	0.9821

Table 2.1 Comparison of analytical values of the stress intensity factor for a single edge-cracked plate loaded in tension with those computed by using the contour and equivalent domain integrals.

Domain				$K_I^{\text{numerical}} / K_I^{\text{analytical}}$	
a_1	a_2	b_1	b_2	**EDI method**	**Contour**
3	3	3	3	1.0194	1.0495
2	2	2	2	1.0108	1.0538
2.5	2.5	2.5	2.5	1.0172	1.0516
2	2	3	3	1.0280	1.0624
2.5	2.5	3.6	3.6	1.0323	1.0624
1.5	1.5	1.5	1.5	1.0001	1.0495
1.5	1.5	2.2	2.2	1.0194	1.0624
0.75	0.75	0.75	0.75	0.9591	1.0473

Table 2.2 Comparison of analytical values of the stress intensity factor for a double edge-cracked plate loaded in tension with those computed by using the contour and equivalent domain integrals.

Domain				$K_I^{\text{numerical}} / K_I^{\text{analytical}}$		$K_{II}^{\text{numerical}} / K_{II}^{\text{analytical}}$	
a_1	a_2	b_1	b_2	**EDI method**	**Contour**	**EDI method**	**Contour**
1	1	1	1	1.0089	1.0074	0.9978	0.9980
1.4	1.4	2	2	1.0068	1.0055	0.9974	0.9945
2	2	2	2	1.0065	1.0051	0.9969	0.9954
2.8	2.8	3	3	1.0064	1.0064	0.9965	0.9960
3	3	3	3	1.0064	1.0057	0.9965	0.9974
3.5	3.5	3.5	3.5	1.0065	1.0090	0.9963	0.9903
3.5	3.5	5	5	1.0067	1.0103	0.9960	0.9908
3.5	3.5	6.5	6.5	1.0067	1.0105	0.9960	0.9877

Table 2.3 Comparison of reference values of stress intensity factors for a single edge-cracked plate loaded by tangential tractions with those computed by using the contour and equivalent domain integrals.

Domain				K_I	K_{II}	K_I / K_{II}	J
a_1	a_2	b_1	b_2	$(\frac{N}{mm^{3/2}})$	$(\frac{N}{mm^{3/2}})$		$(\frac{N}{mm})$
1.5	1.5	1.5	1.5	-460.7	-904.0	0.51	4490
2.5	2.5	2.5	2.5	-462.7	-902.0	0.51	4482
3	3	3	3	-463.7	-901.4	0.51	4481
5	5	5	5	-466.5	-898.8	0.52	4472
7.5	7.5	7.5	7.5	-469.7	-896.5	0.52	4467
10	10	10	10	-472.7	-894.3	0.53	4462
15	15	15	15	-479.1	-890.2	0.54	4458

Table 2.4 Stress intensity factors and the *J*-integral computed by the contour integral for a double edge-notched plate with the edge between the notches loaded in compression.

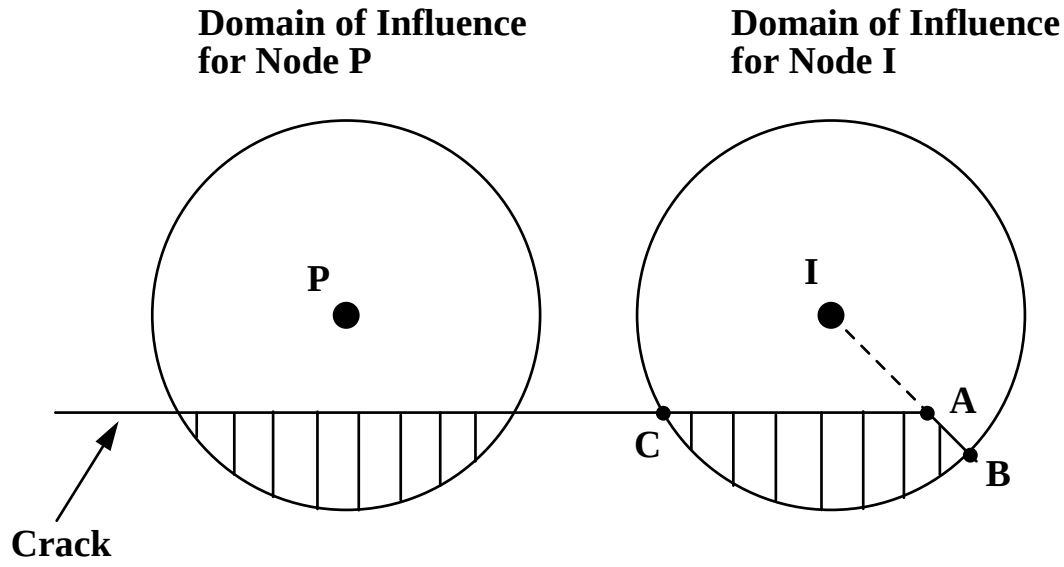

Fig. 2.1a Domain of influence near a crack tip for the visibility method

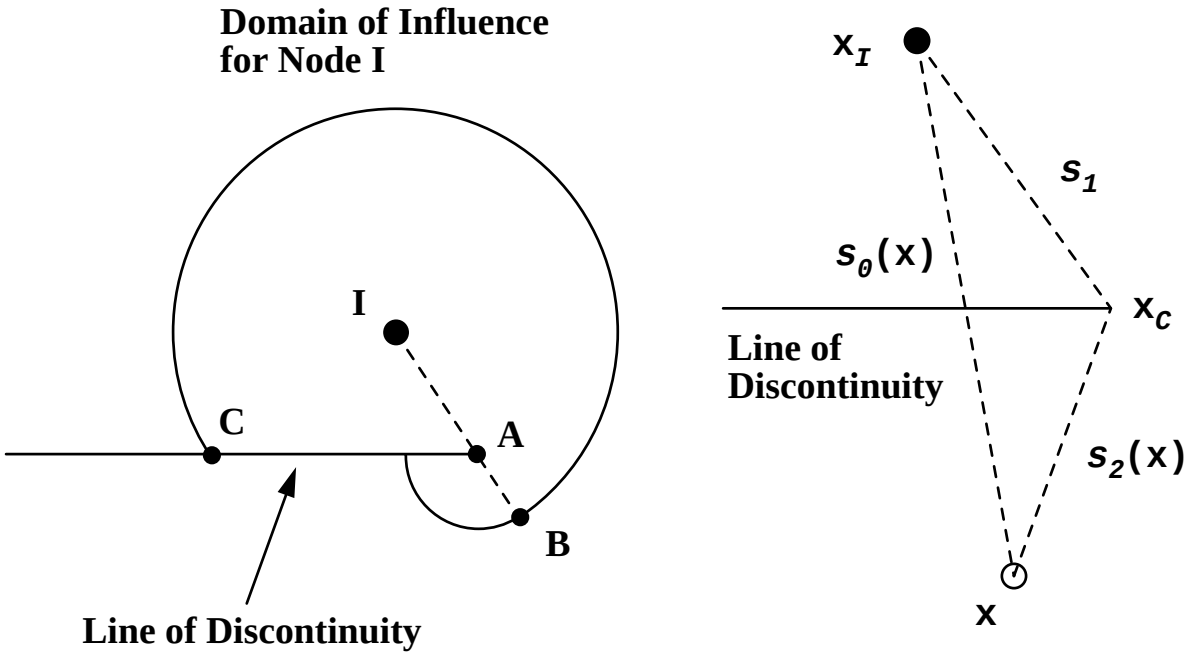

Fig. 2.1b Domain of influence near a crack tip for the diffraction method

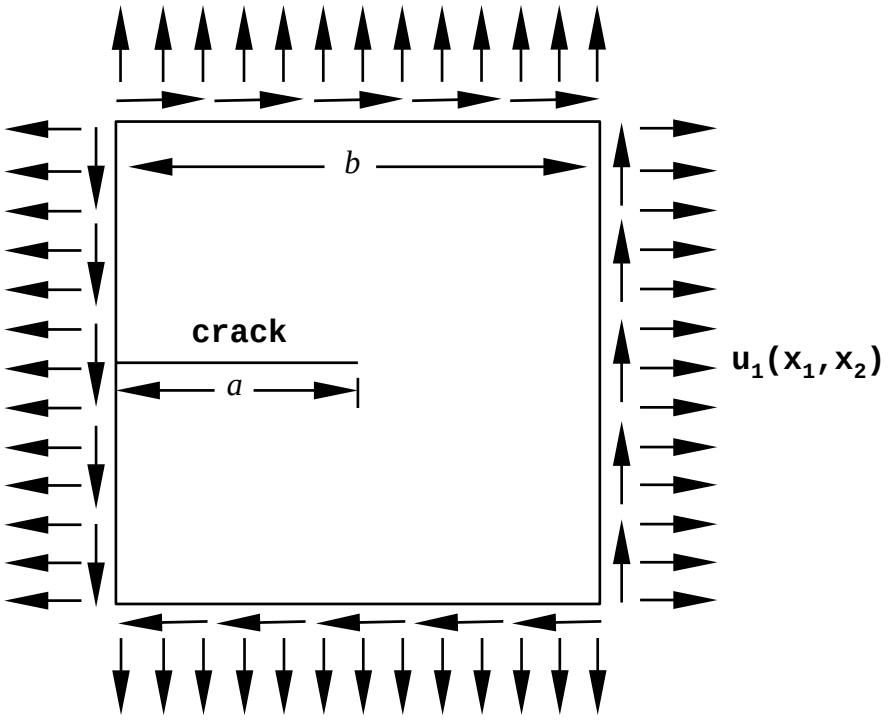

Fig. 2.2a A square plate subjected to mode−I displacement at its edges

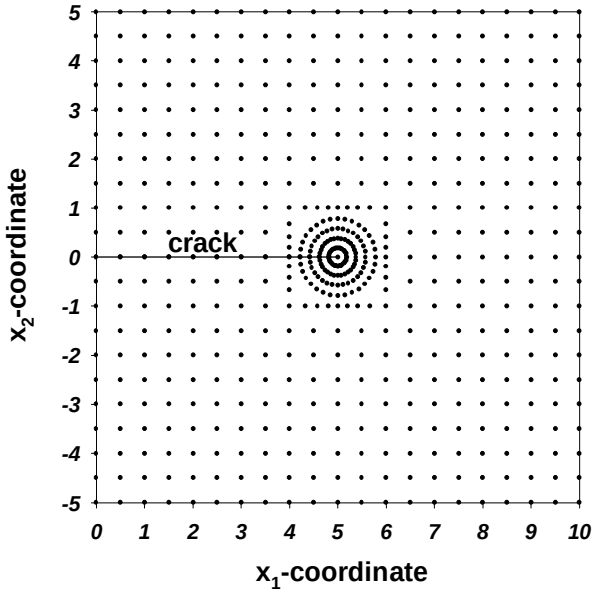

Fig. 2.2b The nodal mesh with 590 nodes

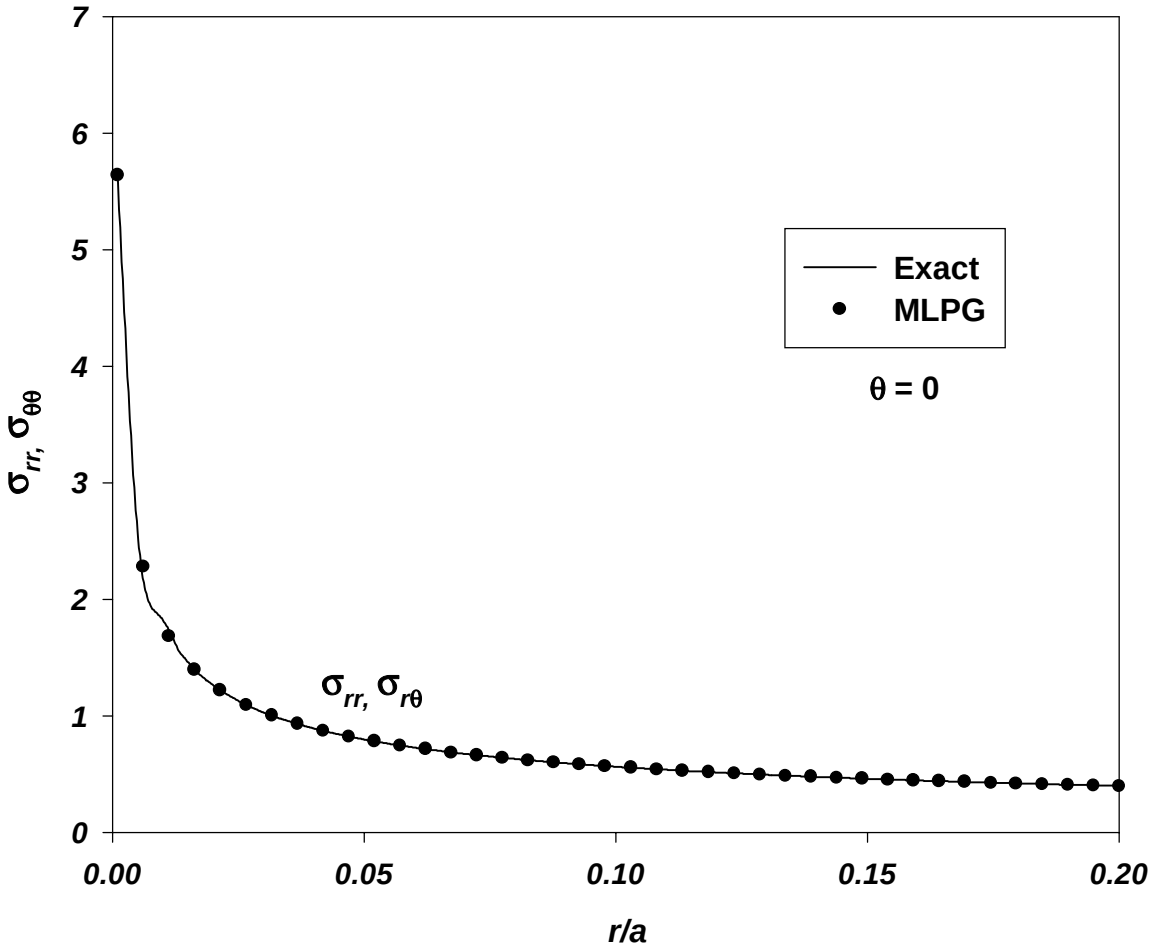

Fig. 2.3a Axial variations of σ_{rr} and $\sigma_{\theta\theta}$ ahead of the crack tip

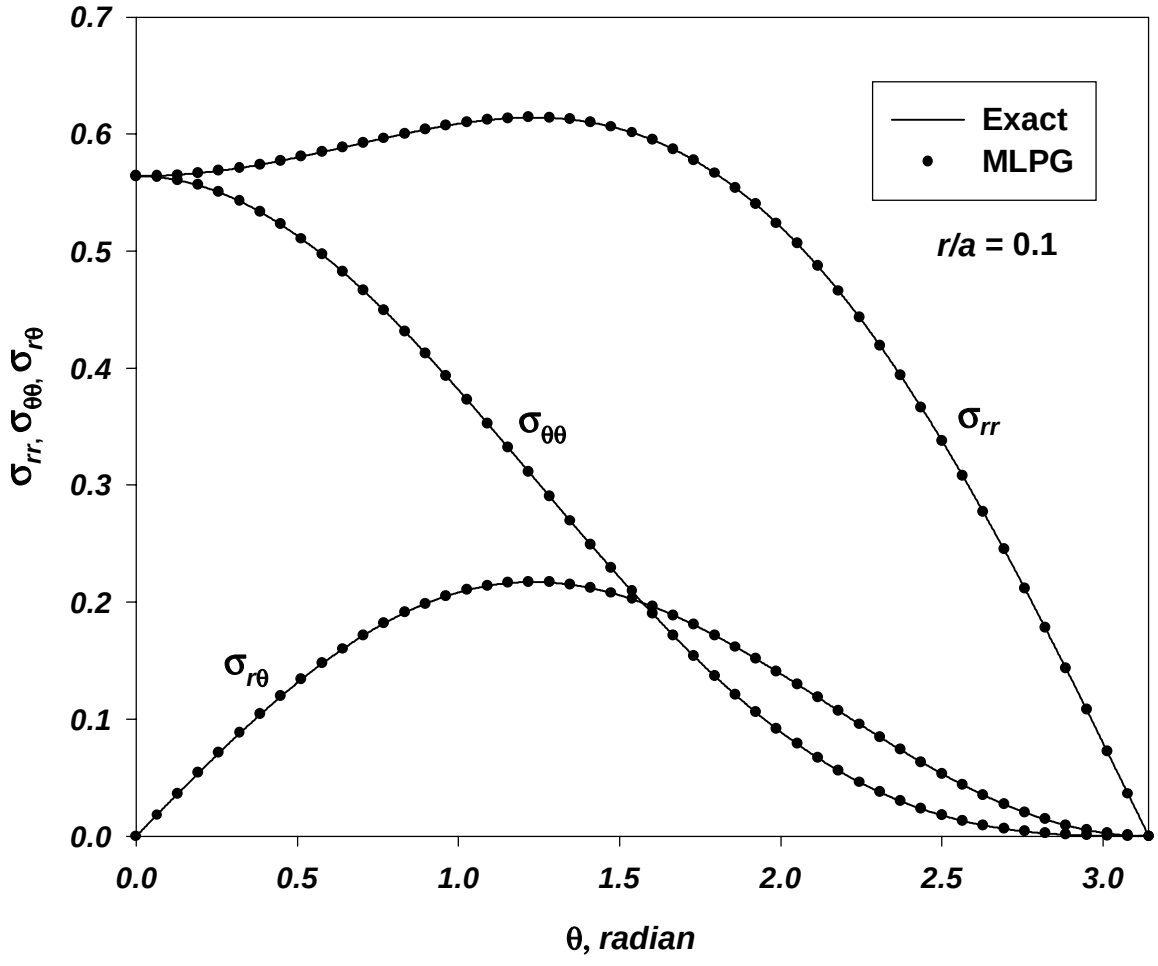

Fig. 2.3b Angular variation of stresses at $r/a = 0.1$

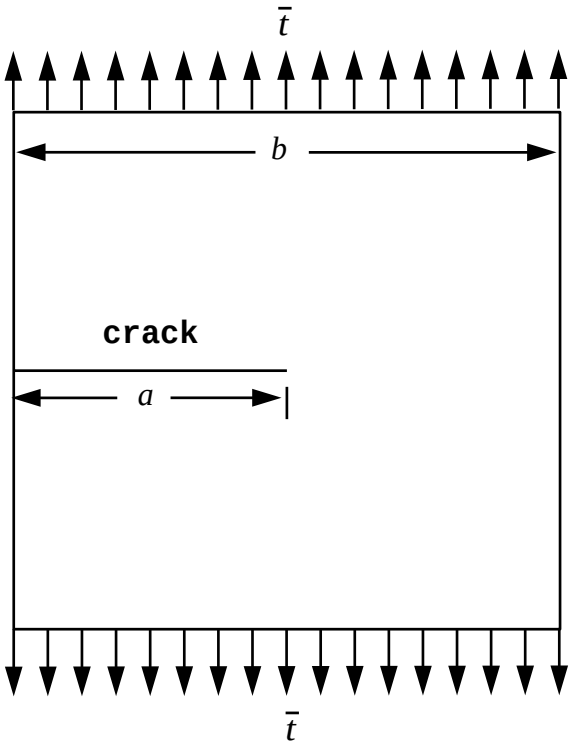

Fig. 2.4a An edge−cracked square plate loaded by uniformly distributed tensile surface tractions

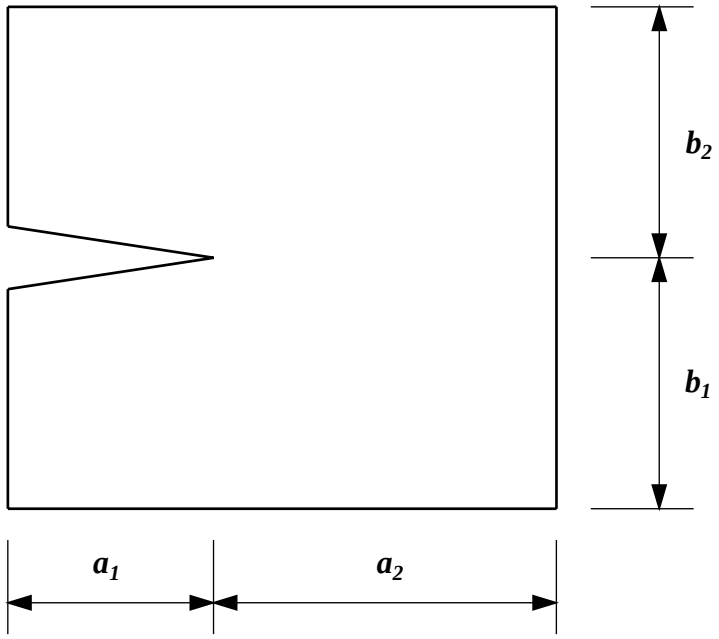

Fig. 2.4b The contour of integration for the evaluation of the *J*−integral and the interaction integral

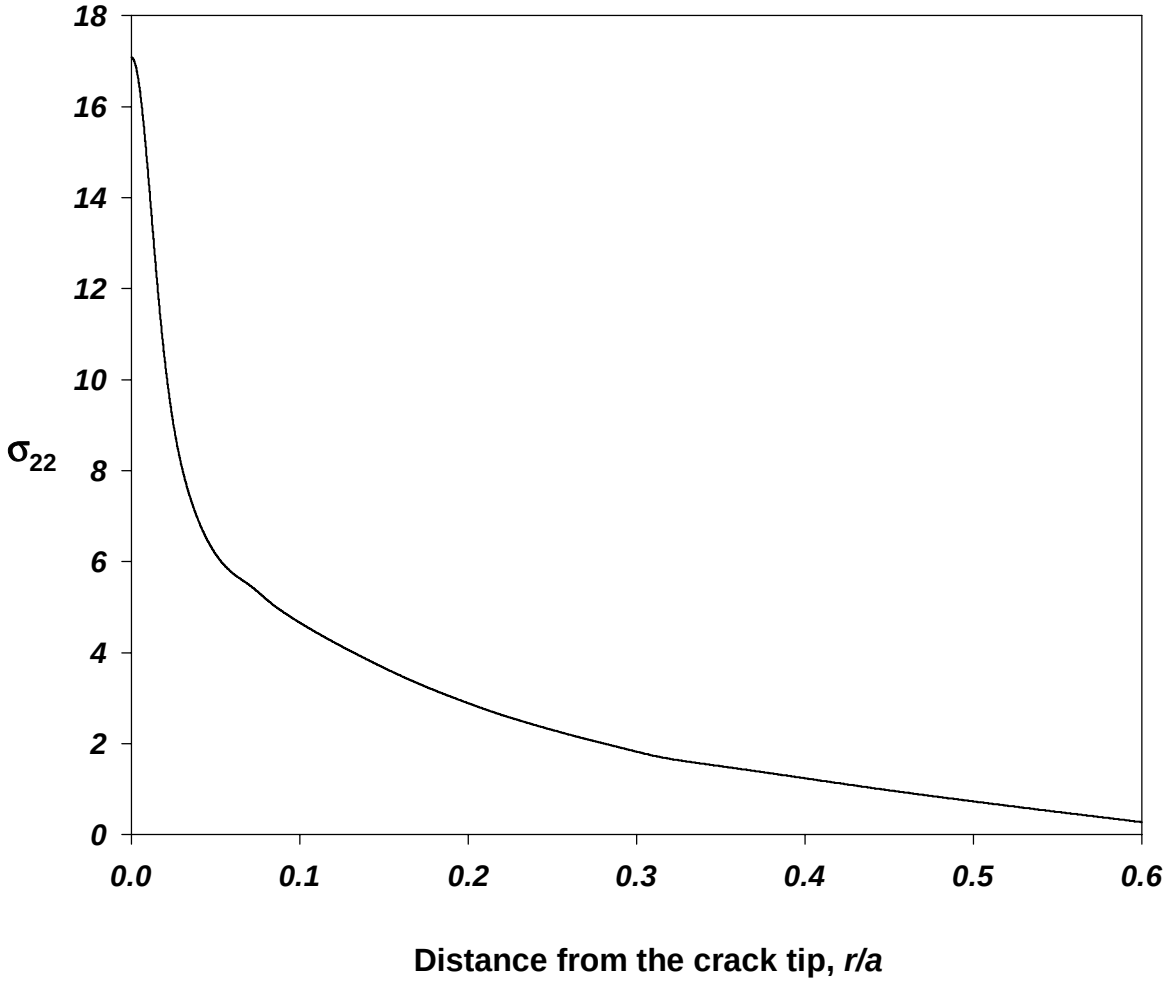

Fig. 2.5a Variation of σ_{22} at points on the axis of the crack with their distance from the crack tip computed without using enriched basis functions

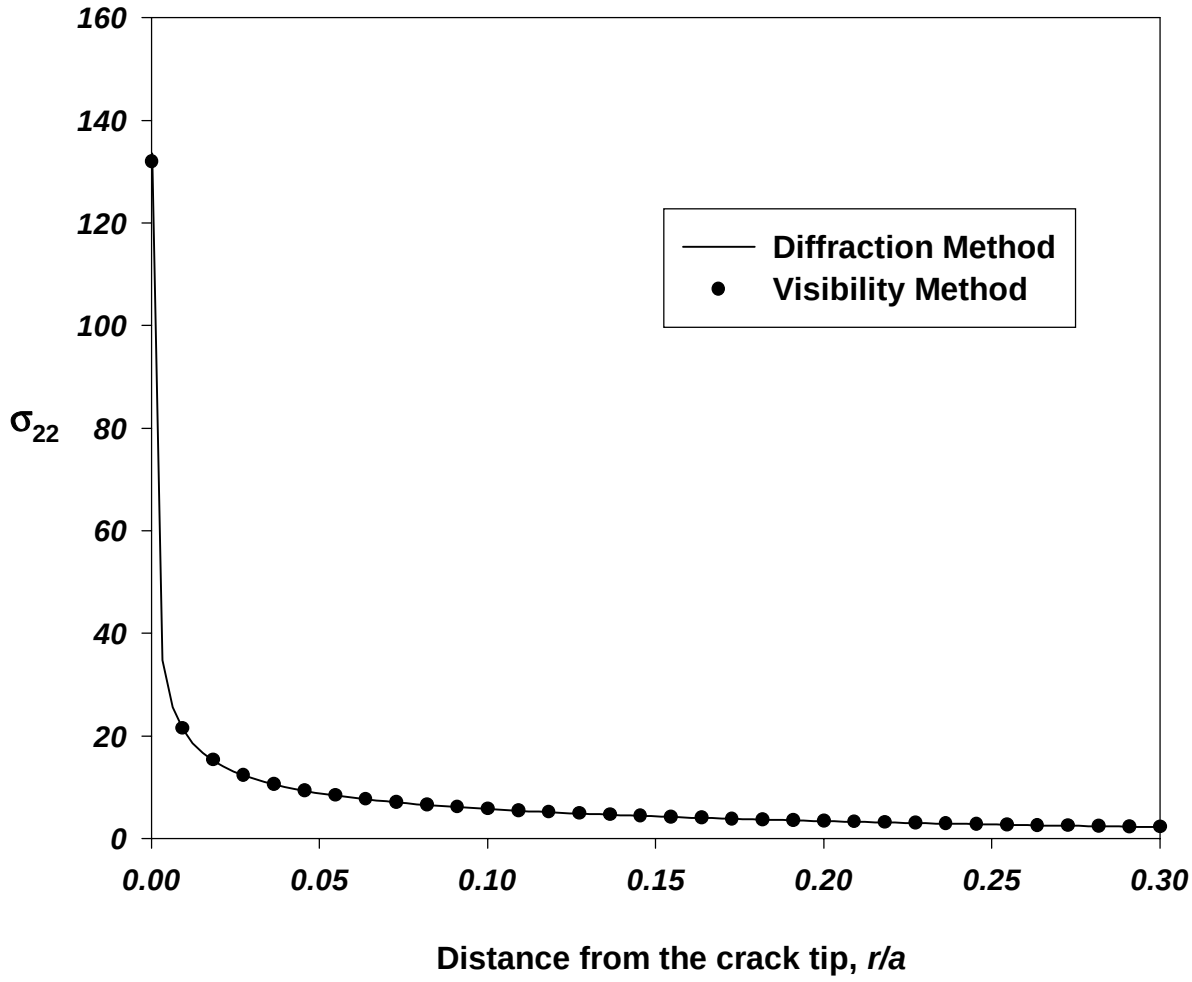

Fig. 2.5b Variation of σ_{22} at points on the axis of the crack with their distance from the crack tip computed with using enriched basis functions

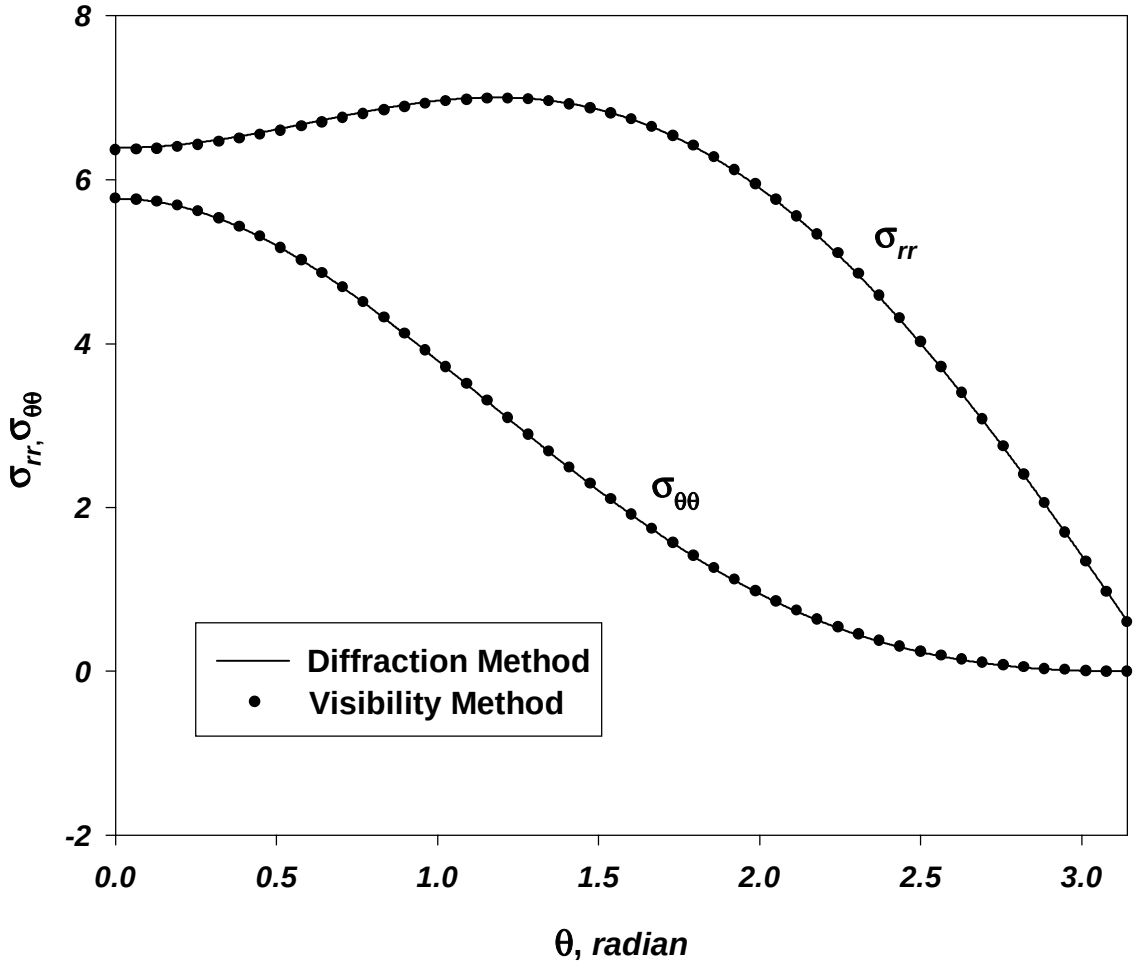

Fig. 2.6 Angular variation of the radial stress, σ_{rr}, and the hoop stress, $\sigma_{\theta\theta}$, around the crack tip obtained by using the visibility and diffraction methods; here r/a =1

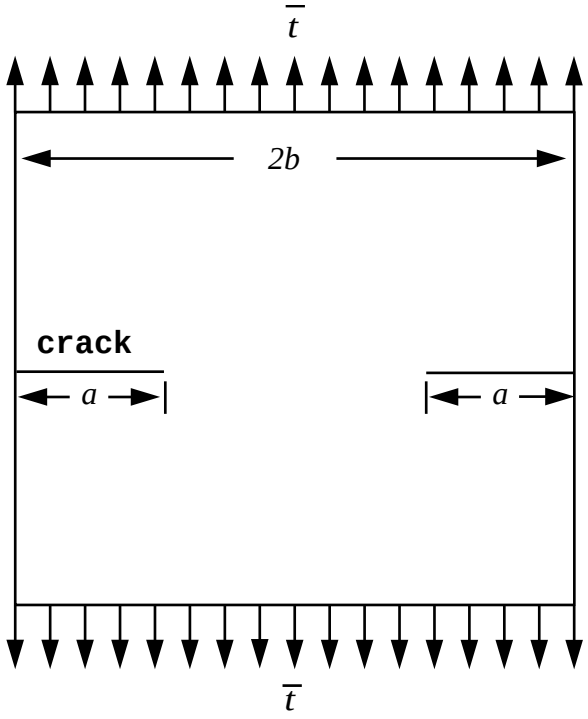

Fig. 2.7a A double edge−cracked square plate loaded by uniformly distributed tensile surface tractions

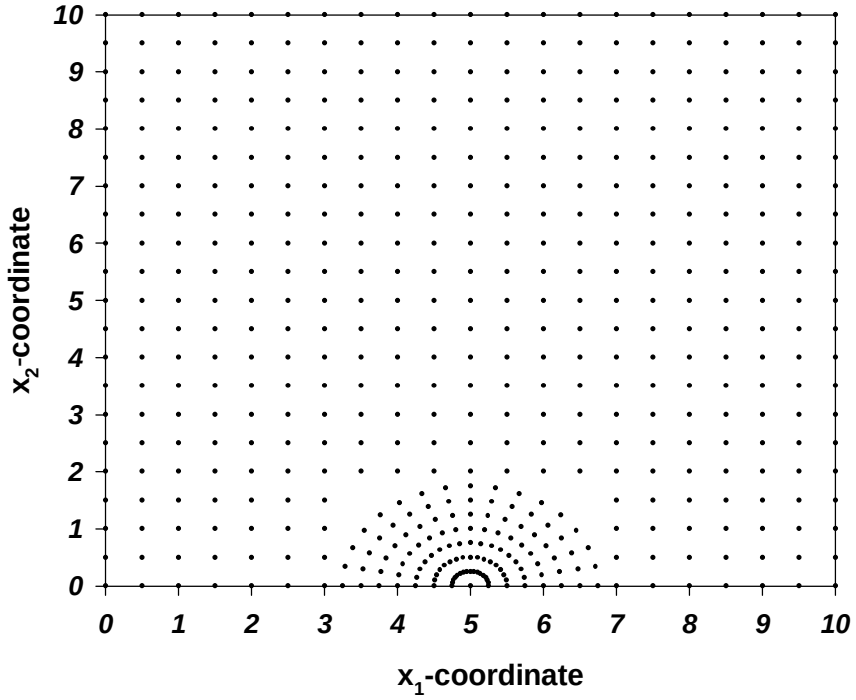

Fig. 2.7b The nodal mesh with 533 nodes for one quarter of double edge-cracked plate

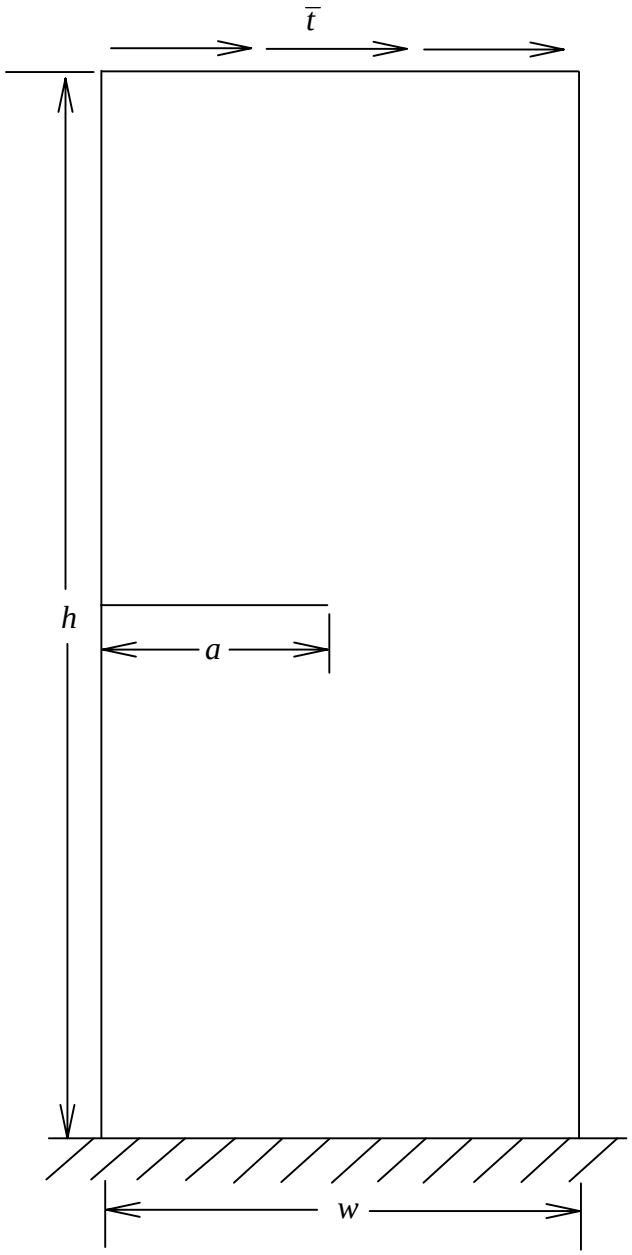

Fig. 2.8a An edge-cracked plate under mixed-mode loading

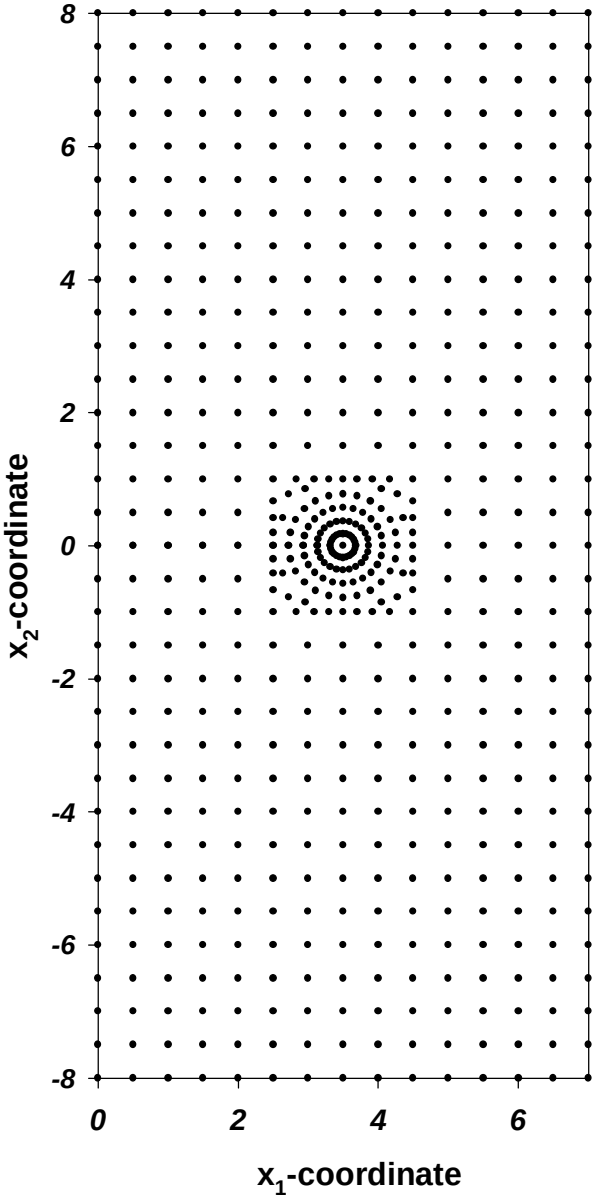

Fig. 2.8b The nodal mesh of 621 nodes

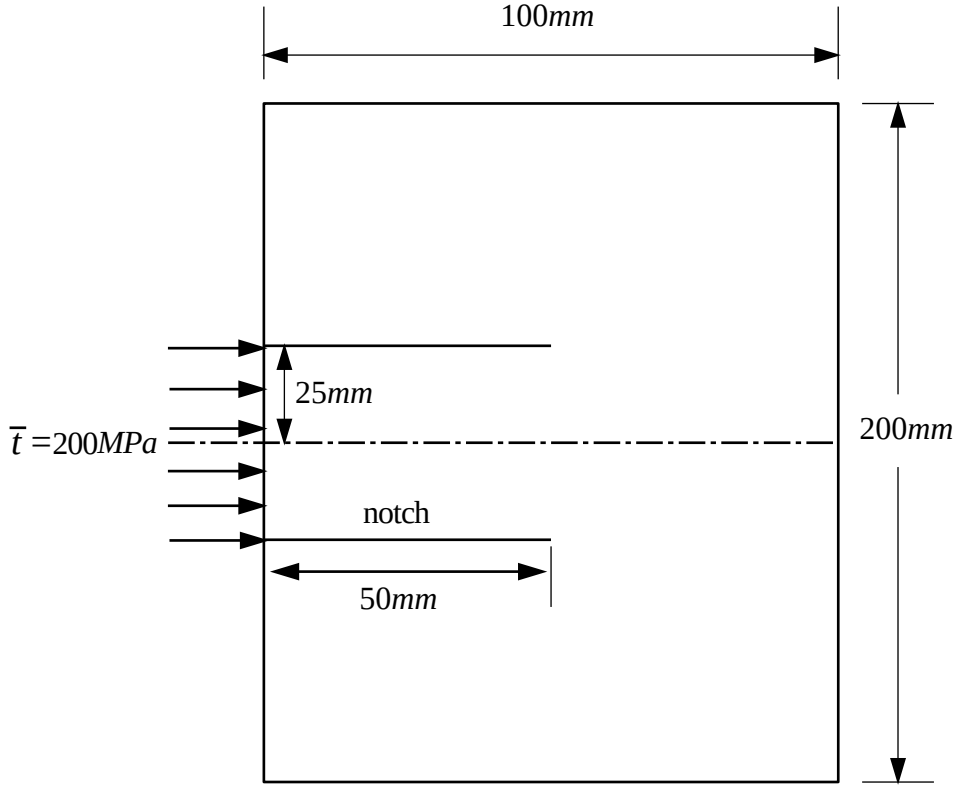

Fig. 2.9a A schematic sketch of the double edge−notched plate

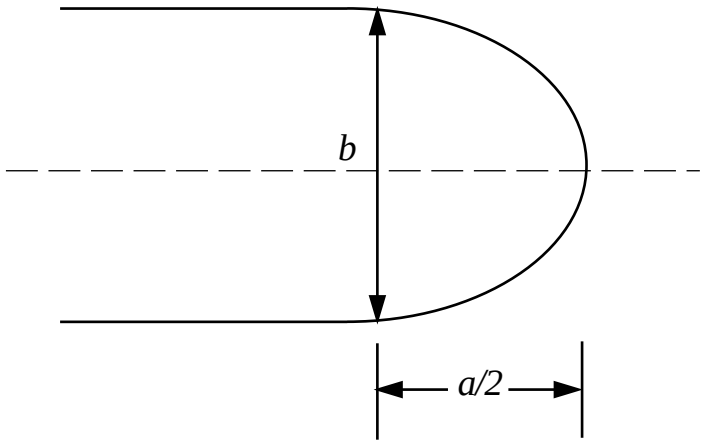

Fig. 2.9b The shape of the elliptic notch tip

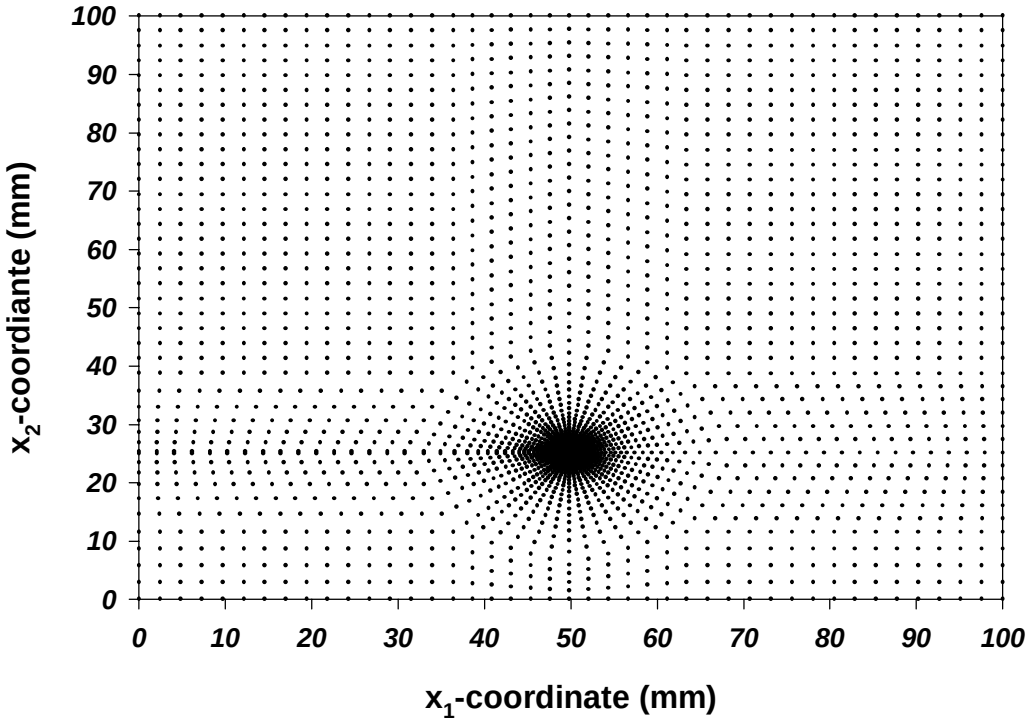

Fig. 2.9c The nodal mesh for the upper half of the double edge-notched plate

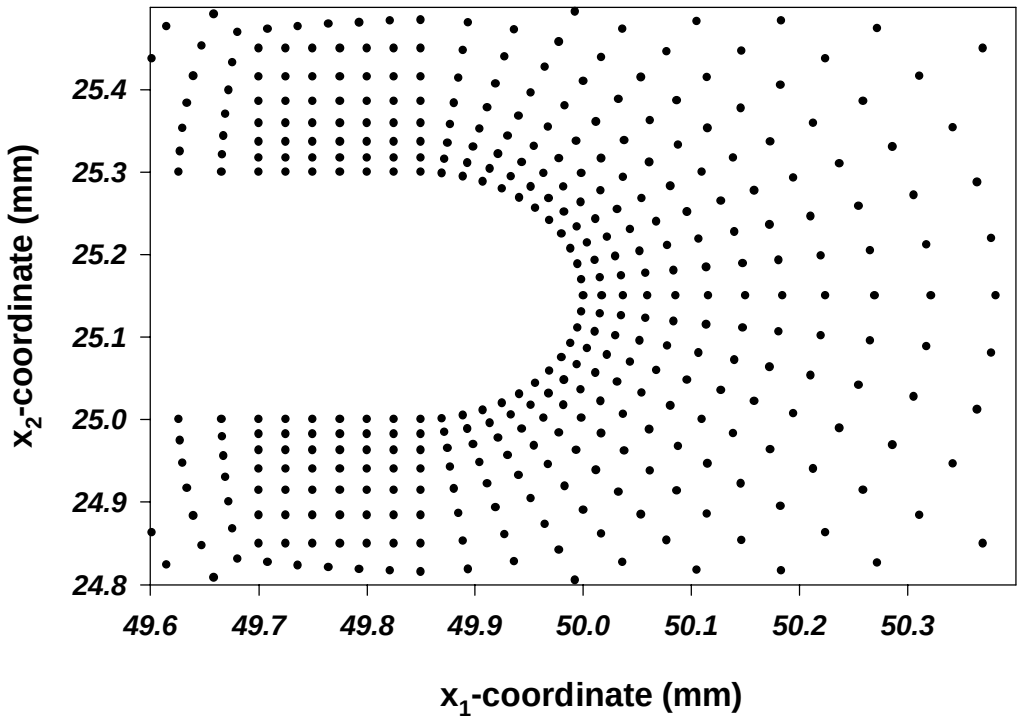

Fig. 2.9d The nodal mesh around the circular notch tip of radius 0.15*mm*

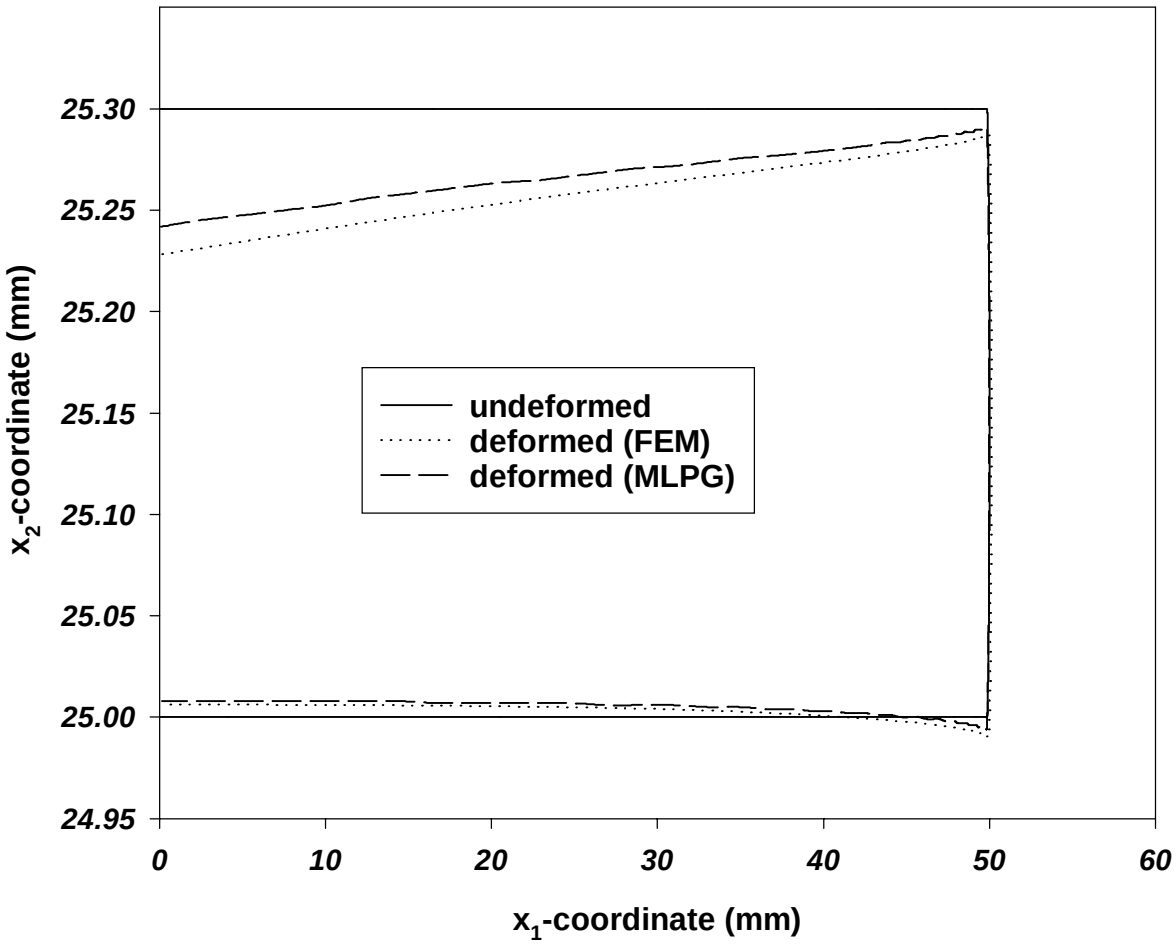

Fig. 2.10a Undeformed and deformed shapes of the notch

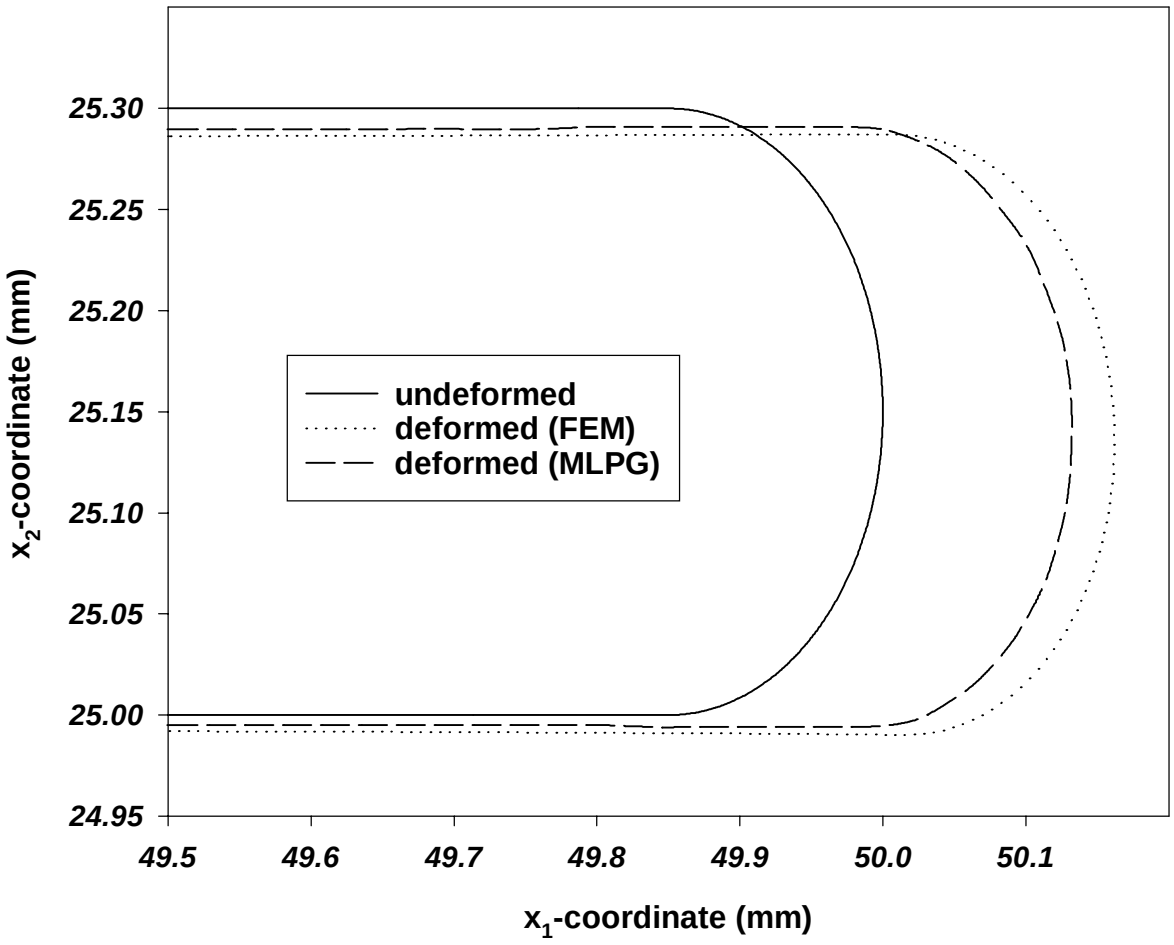

Fig. 2.10b Undeformed and deformed shapes of the circular notch tip

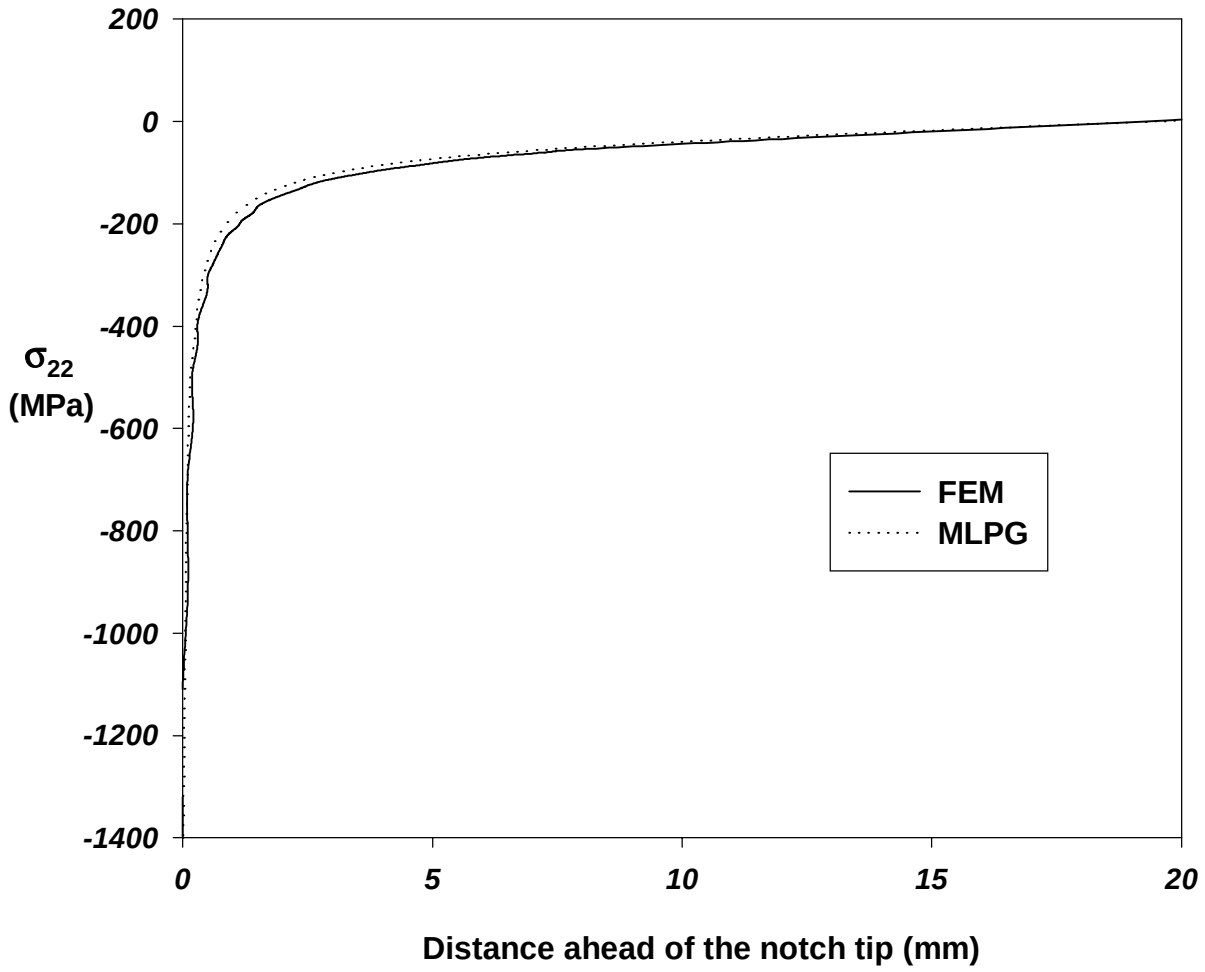

Fig. 2.11a Variations at points on the axis of the notch tip of σ_{22} with the distance from the notch tip

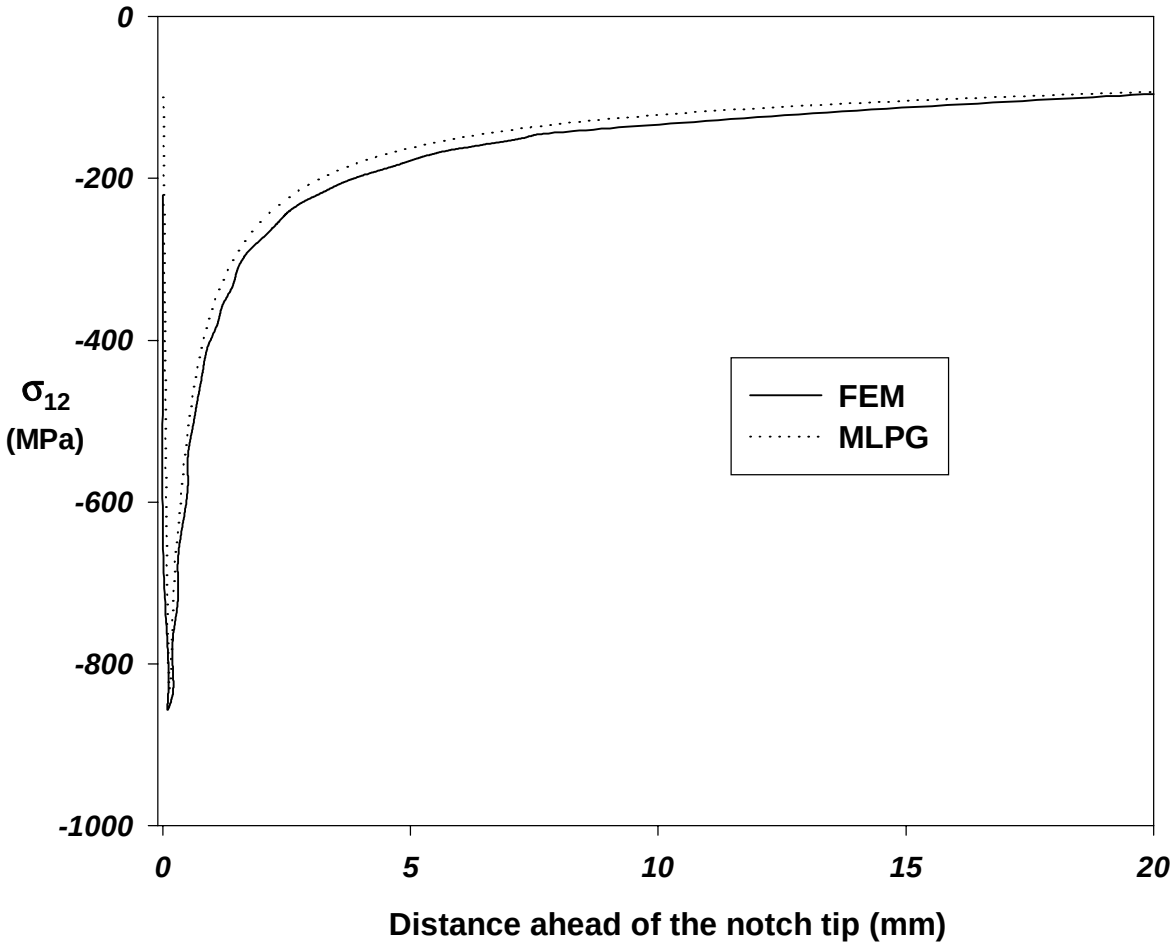

Fig. 2.11b Variations at points on the axis of the notch tip of σ_{12} with the distance from the notch tip

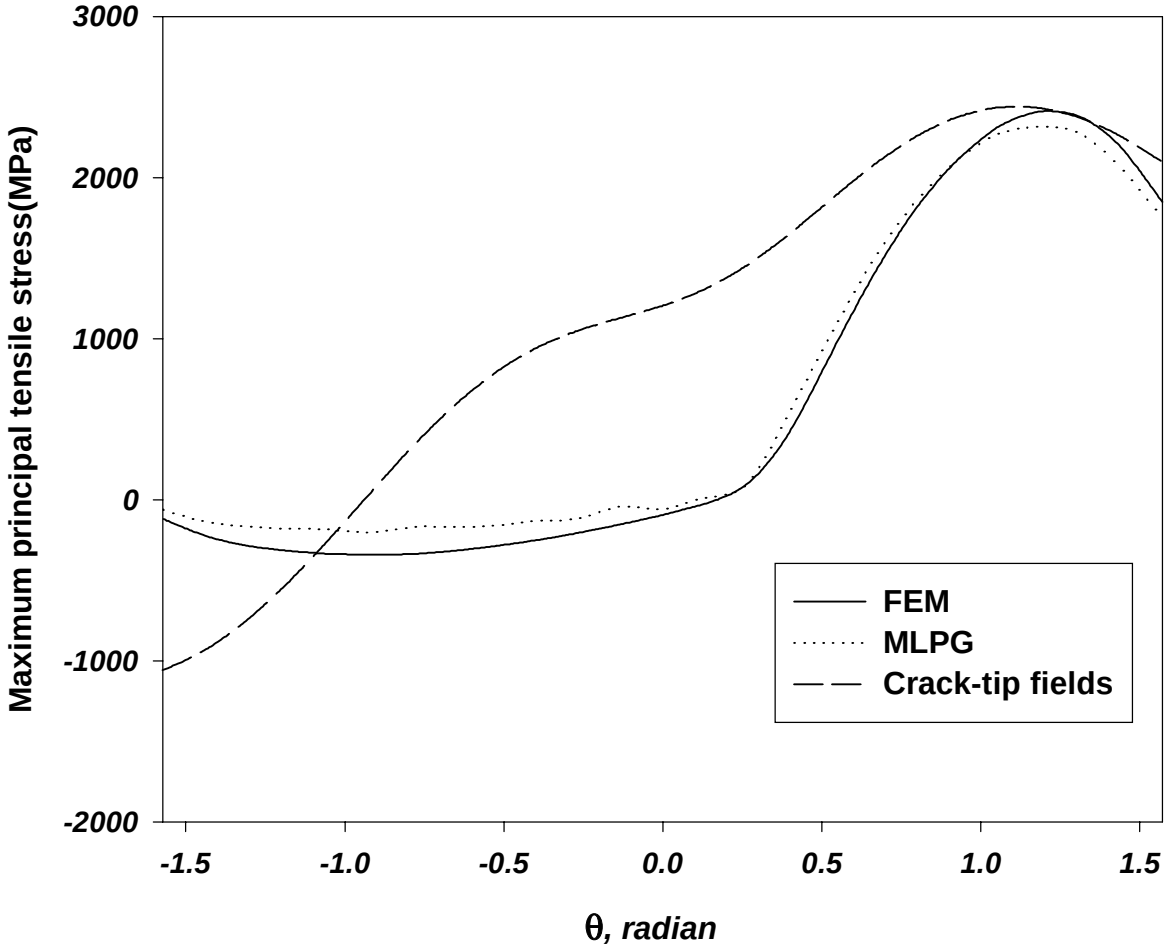

Fig. 2.12a Angular variation at points on the surface of the circular notch tip of the maximum principal tensile stress

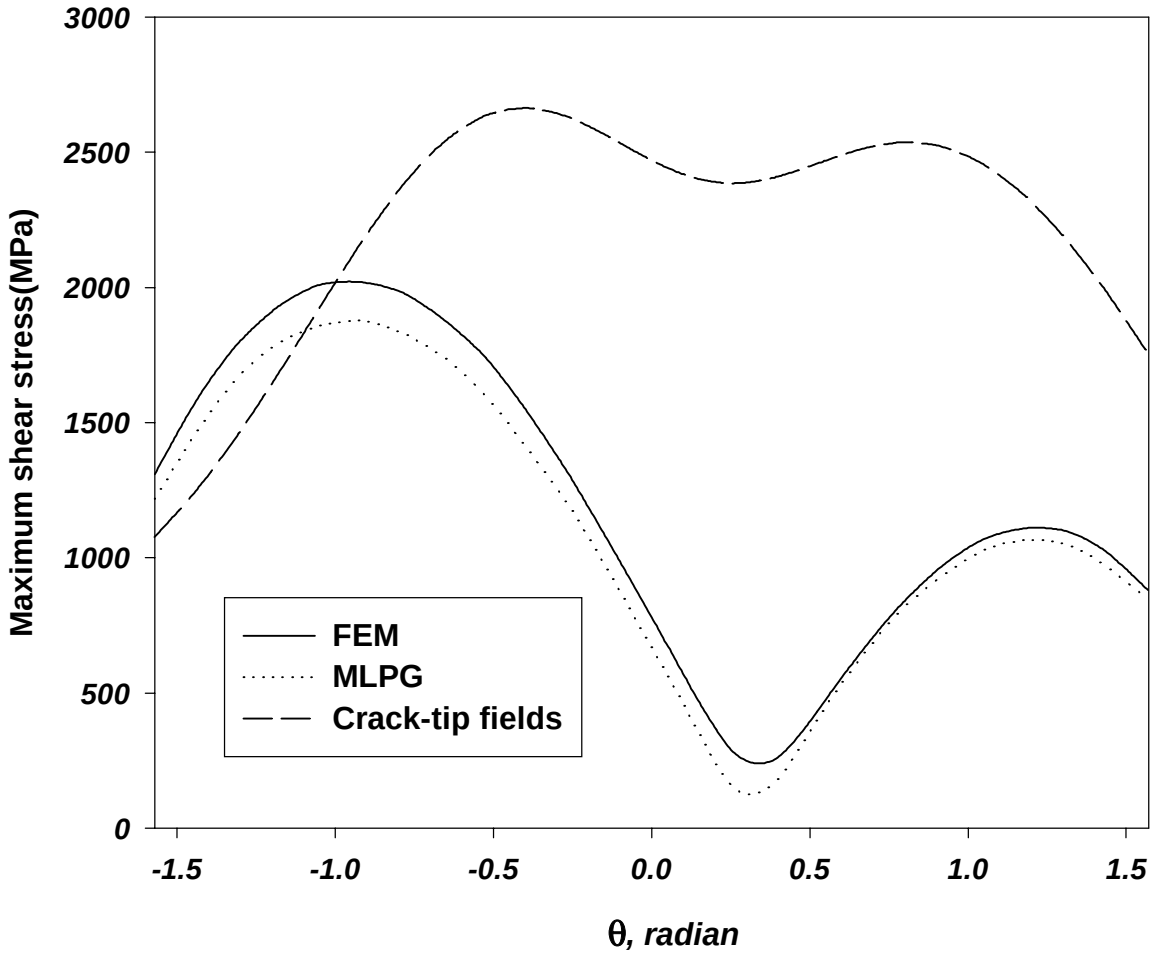

Fig. 2.12b Angular variation at points on the surface of the circular notch tip of the maximum shear stress

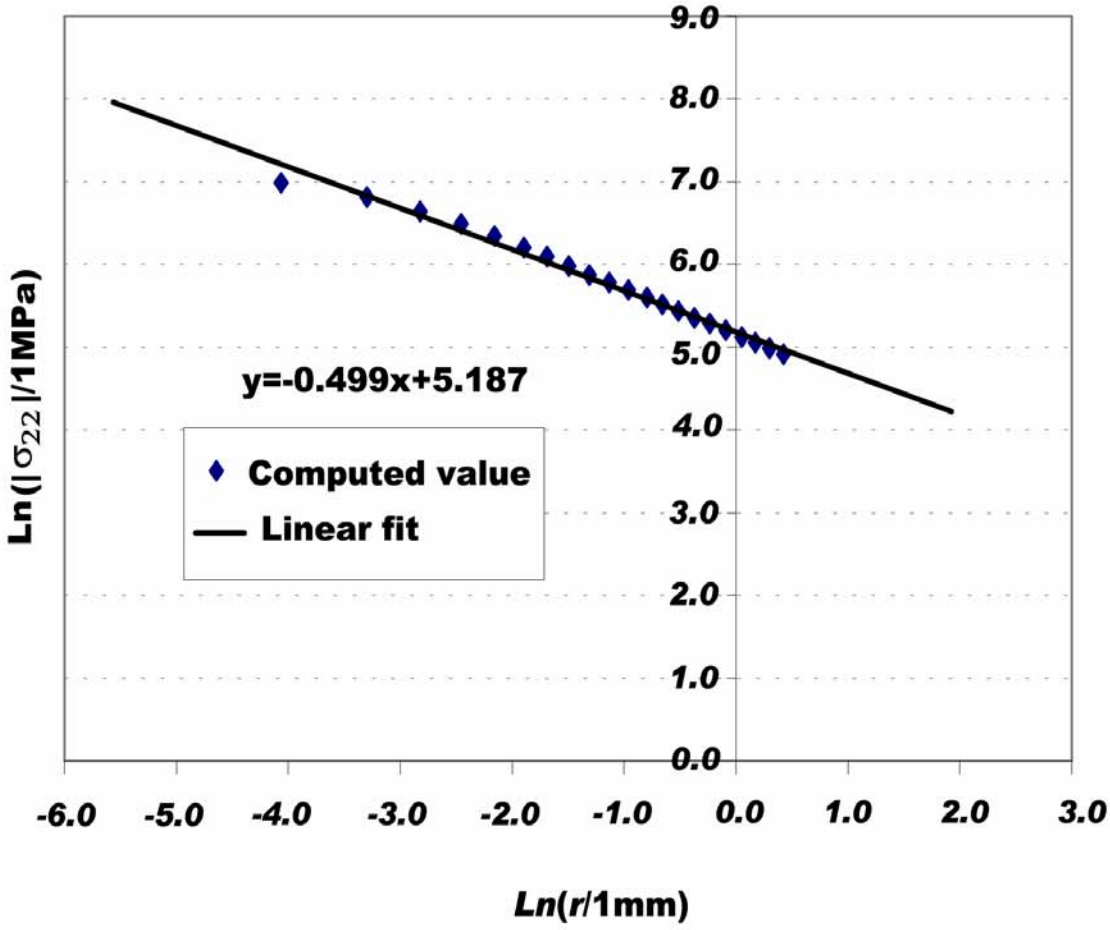

Fig. 2.13a A logarithmic plot of the variations at points on the axis of the notch of σ_{22} with the distance from the notch tip

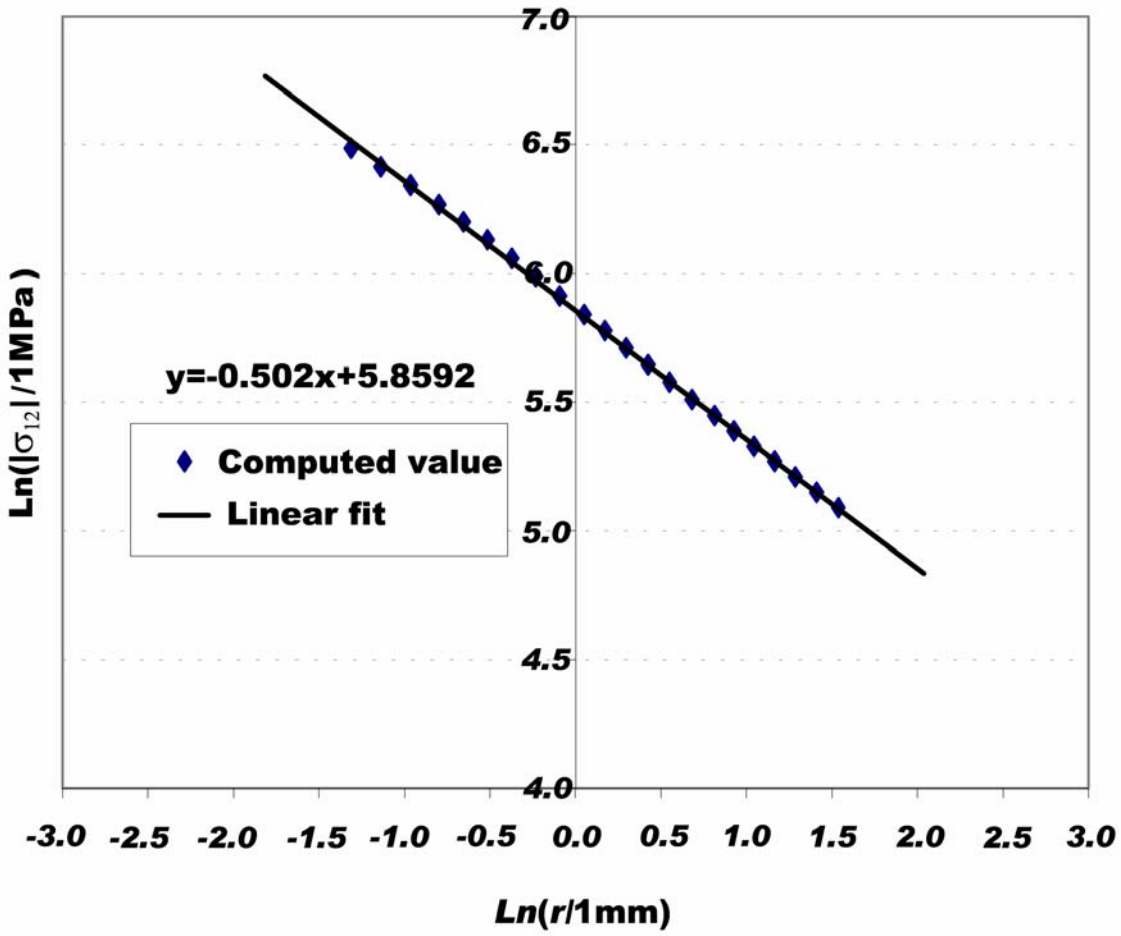

Fig. 2.13b A logarithmic plot of the variations at points on the axis of the notch of σ_{12} with the distance from the notch tip

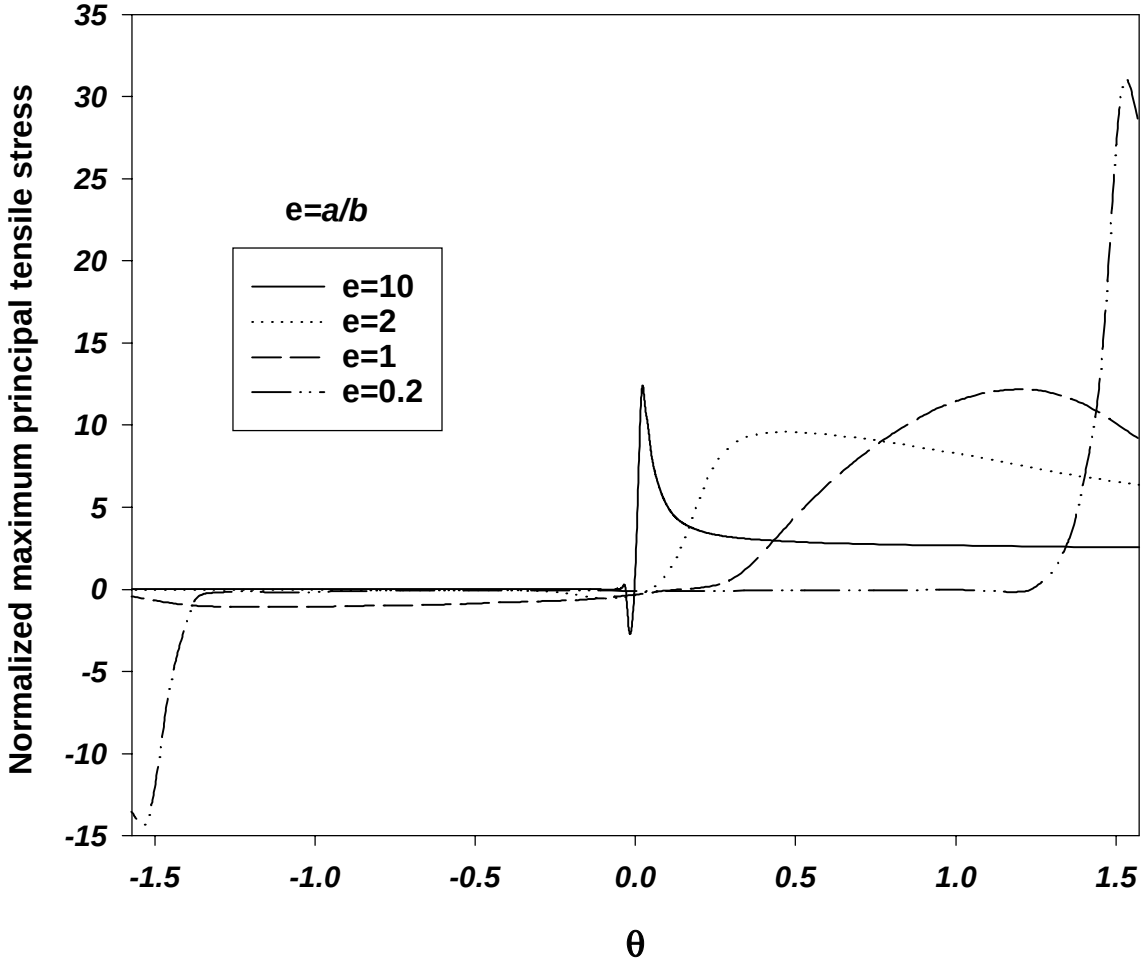

Fig. 2.14a Angular distribution of the normalized maximum principal tensile stress at points on the surface of the notch tip

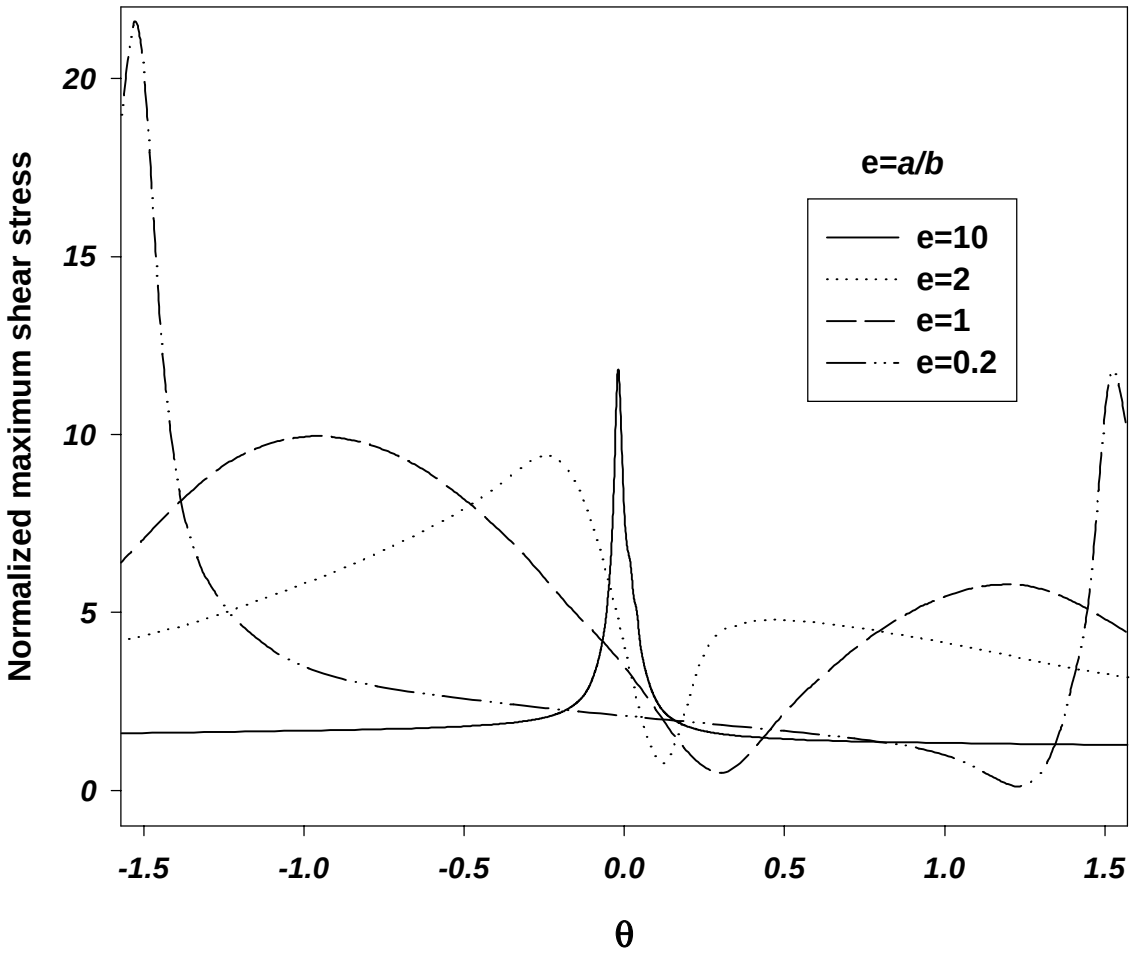

Fig. 2.14b Angular distribution of the normalized maximum shear stress at points on the surface of the notch tip

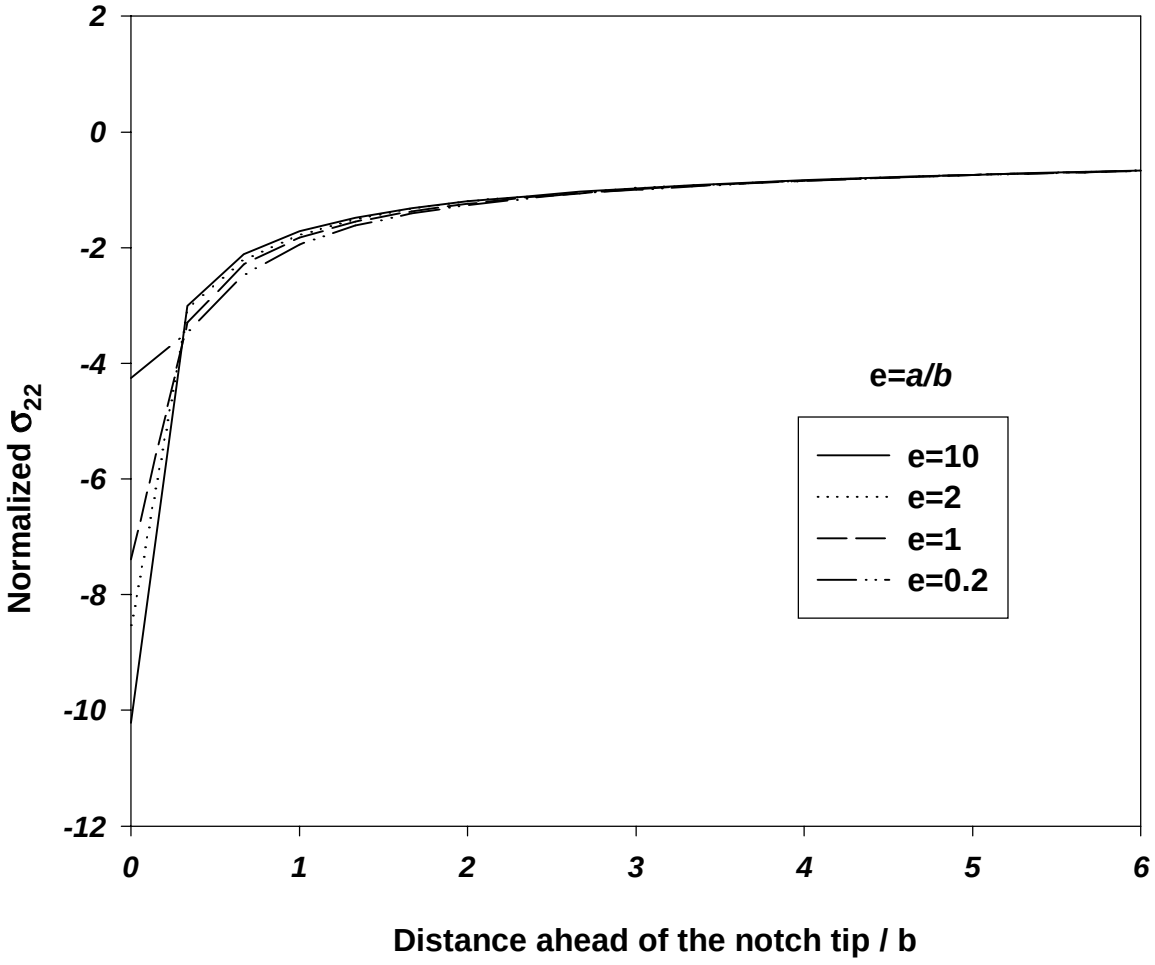

Fig. 2.15a Variation of the normalized σ_{22} at points directly ahead of the notch tip

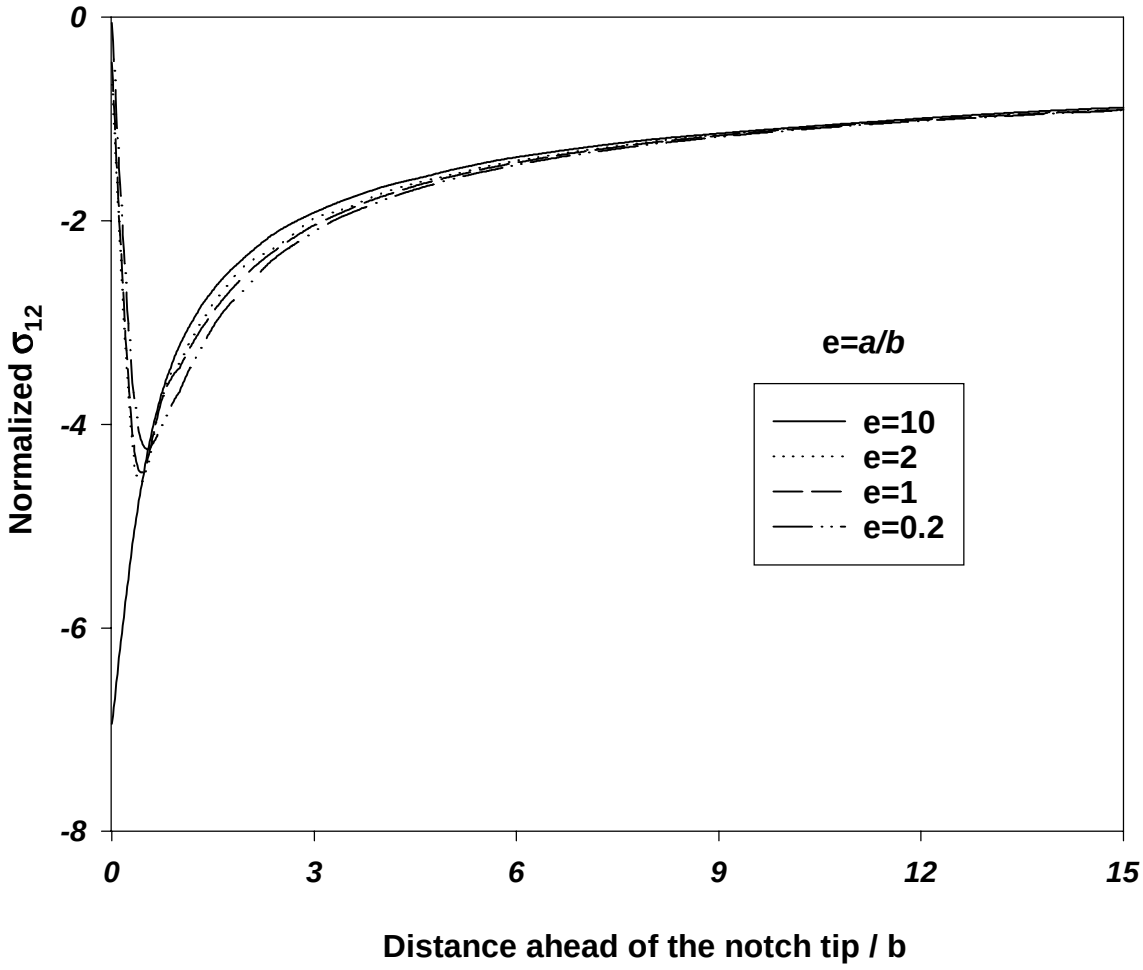

Fig. 2.15b Variation of the normalized σ_{12} at points directly ahead of the notch tip

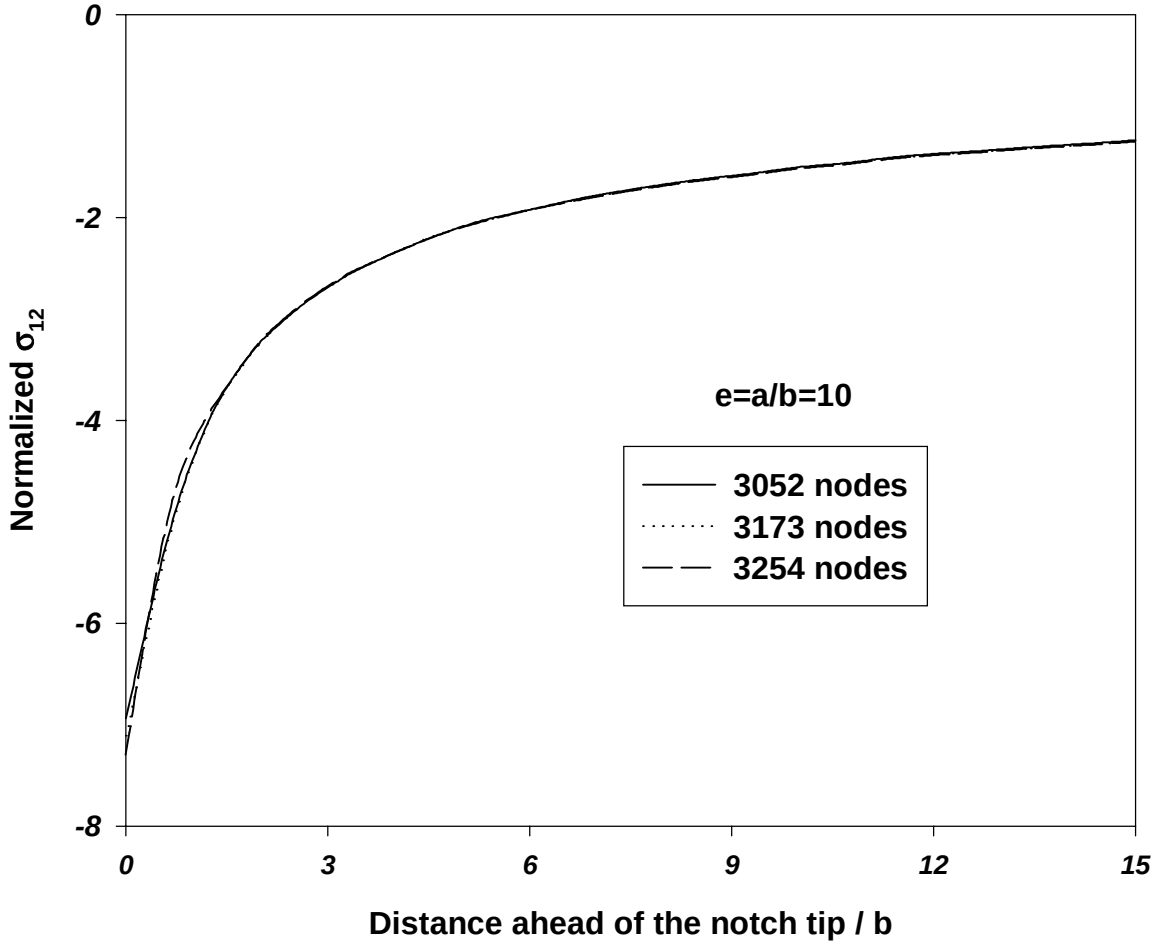

Fig. 2.15c For three different arrangements of nodes near the notch-tip, variation of the normalized σ_{12} at points directly ahead of notch tip

Chapter 3

Plane Strain Deformations of an Elastic Material Compressed in a Rough Rectangular Cavity

Abstract

Deformation and stress distributions in a linear elastic solid, confined to a rigid cavity with rough walls and subjected to uniform compression from one end, are examined. Wall roughness is modeled by Coulomb friction. At the rigid walls, one boundary condition involves deformation and the other stresses, and this renders the problem non-standard. A Laplace transformation solution is constructed for a semi-infinite cavity, and a computational solution for a cavity with finite length. Agreement between the two solutions is good, and improves with increasing cavity lengths and higher coefficients of friction. There exists a critical value of the coefficient of friction below which the axial displacements decay monotonically with distance from the loaded end and the material points stay in contact with the rough walls. For supercritical values of the coefficient of friction, displacements and stresses on the rough walls exhibit oscillatory behavior in the axial direction. The material loses contact with the walls, and the analytical solution presented here loses validity.

Key Words: Coulomb friction; Corner singularities; Analytical solution; Numerical solution.

A slightly modified version of this chapter has appeared in the *International Journal of Engineering Science*, Vol. 40, pp. 991-1010, 2002; authors are A. Warlock, H.-K. Ching, A. K. Kapila and R. C. Batra.

3.1 Introduction

Our interest in the problem under study stems from our recent treatment of a related but different problem, namely, the consolidation of a non-cohesive powder via compaction (Hill and Kapila, 1995; Warlock, 1997). Uniaxial pressing is a common technological process in which solid grains are placed in a cylindrical die into which two pistons are inserted. One of the pistons is generally held stationary while the other is pushed in to compact the powder. The compaction process is generally quite slow, and the major goal is to produce a specimen in which density distribution is as close to uniform as possible. Experimental data on explosive pressing (Elban and Chiarito, 1986) show that when a one-inch long cylindrical specimen of powdered explosive is pressed in a one-inch diameter tube of polished steel, statically, only 60% of the load applied at one face of the specimen is transmitted to the other face, the remaining 40% being supported by friction at the walls. A rather different application of compaction occurs in the so-called DDT (deflagration-to-detonation transition) tube tests on high-energy explosives (McAfee et al.,1989). The test apparatus consists of a sealed tube completely filled with lightly tamped explosive powder. The explosive is subjected to mechanical stimulus at one end of the tube by a moving piston. The piston drives a shock-like wave of compaction through the explosive bed, increasing the solid volume fraction from 70 - 75% to 90 - 95% and initiating ignition. Friction plays a role in this dynamic problem as well, the details of which were examined in recent studies of a rather simple fluid-like model of the powder, with the assumption of Coulomb friction at the walls (Hill and Kapila, 1995; Warlock, 1997). It was found, as expected, that friction causes the pressure at the piston face to rise with time if the piston is driven at a constant speed, and the speed of the piston to drop if the piston is driven at a constant pressure, with concomitant effects on the strength of the compaction shock and on the distribution of the state between the shock and the piston. We found, in particular, that for small values of the coefficient of friction the decay from the piston to the shock was monotonic, but at higher values oscillations crept in. The desire to discover whether a similar non-monotonicity of

deformation is exhibited by an elastic material at higher coefficients of friction led to the present study.

We consider only the static deformation of the material as it is compressed in a planar, rectangular, rigid cavity whose walls are rough. Under the assumption of plane strain, powerful analytical techniques based on the theories of complex variables and singular integral equations are available for construction of the solution (Muskhelishvili, 1963). What makes the problem non-standard, and the application of these techniques difficult, is the pair of boundary conditions on the rough wall, where rigidity leads to a condition on displacements and roughness to a condition on stresses. Expansion in terms of the eigenfunctions of the biharmonic equation is another possible approach, but questions of completeness and orthogonality for the boundary conditions at hand again lead to complexity. We opt for the Laplace transformation, which has the advantage that completeness and orthogonality are dealt with automatically, and the limitation that it only applies to a semi-infinite domain. However, the friction-induced decay suggests that results for the unbounded configuration may well provide a good approximation for those for the finite configuration. A comparison of the analytical results against those obtained numerically for a finite domain confirms that accuracy of the approximation is indeed good, and improves with increase in the coefficient of friction or the length of the cavity.

The paper begins by giving the formulation of the problem in Section 3.2. Section 3.3 gives an analytical solution of the problem by the Laplace transform method and discusses singularities at the corners. A weak formulation of the problem suitable for seeking a numerical solution by the Meshless Local Petrov-Galerkin method is given in Section 3.4. The deformation and the stress fields computed by the two methods are compared in Section 3.5. Effects on the deformation and stress distributions of varying the friction coefficient are examined. We find that for friction coefficients above a critical value oscillations appear, and necessitate a reconsideration of the Coulomb model.

3.2 Formulation of the Problem

A schematic sketch of the problem studied is shown in Fig. 3.1. We use rectangular Cartesian coordinates depicted in Fig. 1 to describe static deformations of the linear elastic material compressed in the rigid cavity with rough horizontal walls at $x_2 = \pm 1$ and smooth rigid vertical walls at $x_1 = 0$ and L. We presume that a plane strain state of deformation prevails; thus the dimension in $x_3 - \text{direction}$ is very large as compared to 2 and L. In the absence of body forces, equations governing the deformations of the body are

$$\sigma_{ij,j} = 0, \ i, j = 1, 2, \tag{3.1}$$

$$\sigma_{ij} = \lambda e_{kk} \delta_{ij} + 2\mu e_{ij}, \tag{3.2}$$

$$e_{ij} = (u_{i,j} + u_{j,i})/2, \tag{3.3}$$

$$u_1(L, x_2) = 0, \ \ \sigma_{21}(L, x_2) = 0, \ \ -1 \le x_2 \le 1, \tag{3.4a}$$

$$u_1(0, x_2) = u_0, \ \sigma_{21}(0, x_2) = 0, \ \ -1 \le x_2 \le 1, \tag{3.4b}$$

and for $0 < x_1 < L$,

$$u_2(x_1, \pm 1) = 0, \tag{3.4c$_1$}$$

and either

$$u_1(x_1, \pm 1) = 0, \text{ if } \sigma_{12}(x_1, \pm 1) < \mu_f \left|\sigma_{22}(x_1, \pm 1)\right| \text{ and } \sigma_{22}(x_1, \pm 1) < 0, \tag{3.4c$_2$}$$

or

$$\sigma_{12}(x_1, \pm 1) = -\mu_f \left|\sigma_{22}(x_1, \pm 1)\right| \frac{u_1(x_1, \pm 1)}{\left|u_1(x_1, \pm 1)\right|}, \ \sigma_{22}(x_1, \pm 1) < 0, \tag{3.4c$_3$}$$

or

$$\sigma_{12}(x_1, \pm 1) = 0, \ \sigma_{22}(x_1, \pm 1) \ge 0. \tag{3.4c$_4$}$$

Here σ is the stress tensor, **e** the infinitesimal strain tensor, **u** the displacement of a point, a comma followed by the index j indicates partial differentiation with respect to x_j, a repeated index implies summation over the range of the index, λ and μ are the Lame′

constants, and μ_f the coefficient of friction between the walls of the cavity and the deformable material. The boundary conditions (3.4a)-(3.4c$_4$) imply that a material point of the deformable body cannot penetrate through the rigid walls of the cavity. At the surfaces of the upper and lower rough walls, a material point of the deformable body can slide over the wall only if the tangential traction is sufficient to overcome the frictional force. Also, a material point may separate away from the wall in which case it is on a free surface. These three possibilities are listed in Eqs. (3.4c$_2$)-(3.4c$_4$), and make the problem quite challenging. Substitution from (3.3) into (3.2) and the result into (3.1) gives a set of second-order, linear, coupled partial differential equations (3.5) for the determination of the two components of the displacement $\mathbf{u}$:

$$(\lambda+\mu)u_{k,ki}+\mu u_{i,jj}=0. \tag{3.5}$$

In the absence of friction the problem has the following simple solution:

$$u_1(x_1,x_2)=u_0\left(1-\frac{x_1}{L}\right),\quad u_2(x_1,x_2)=0. \tag{3.6}$$

However, in the presence of friction, it is not easy to find an analytical solution of the problem, especially for finite values of L. Here we study in detail the case when the boundary condition (3.4c$_3$) holds and delimit the values of μ_f for which the solution is valid. In view of the axial displacements prescribed on the left end, we anticipate that the boundary condition (3.4c$_3$) applies; it will be verified a posteriori. We first give an analytical solution of the problem for $L=\infty$, and then a numerical solution of the problem for finite values of L. It is found that the numerical solution of the problem agrees well with the analytical solution except at points very close to the right smooth rigid wall. The rate of decay of the solution in the axial direction varies with the value assigned to the coefficient of friction. Thus the correlation between the analytical solution for $L=\infty$ and the numerical solution for a finite value of L depends also upon the coefficient of friction.

3.3 Analytical Solution for the Semi-infinite Cavity

It is anticipated that the solution of the problem for the semi-infinite cavity will provide a substantial amount of information about the behavior of the solution for the finite-strip. For the former geometry the boundary conditions (3.4a) are replaced by

$$\lim_{x\to\infty} u_1(x_1,x_2)=0,\quad \lim_{x\to\infty}\sigma_{21}(x_1,x_2)=0,\quad |x_2|<1. \tag{3.7}$$

By introducing the Airy stress function, the problem can of course be recast as a boundary – value problem for the biharmonic equation. In this formulation the semi-infinite elastostatic strip has attracted considerable attention, the primary emphasis having been on the construction of Fourier-series solutions in terms of the so-called Papkovich-Fadle eigenfunctions. Thus, algorithms have been derived for the computation of the Fourier coefficients (Smith, 1952; Johnson and Little, 1965), the question of completeness of eigenfunctions has been addressed and conditions stated for the convergence of the series (Gregory, 1980; Joseph, 1977; Spence, 1982), and the role played by possible corner singularities has been elucidated (Gregory and Gladwell, 1982). All of this work assumes stress-free boundary conditions on the walls, and is therefore not directly applicable to the present solution.

The problem can be solved by using Laplace transformation in x_1 if the functions involved are Laplace transformable, and u_1, $u_{1,1}$, u_2 and $u_{2,1}$ at $x_1=0$ are known. The first and the fourth of these quantities are given as boundary data. The other two are unknown but will be assumed to possess Fourier series in x_2 with the coefficients of the series determined as a part of the solution. Since u_i and $u_{i,j}$ are expected to be bounded within the body and to vanish at infinity, the only sources of difficulty in taking the Laplace transform are the possible singularities in $u_{i,j}$ at the corners $(0,\pm 1)$. For example, if $u_{1,1}(0,x_2)$ is unbounded as $x_2\to\pm 1$, then its singular behavior will need to be subtracted out before it can be Fourier

expanded for taking its Laplace transform (e.g., see Champeney, 1987). Such singularities are admissible since stresses and hence displacement gradients are only required to be integrable rather than bounded at the boundaries. We use similarity analysis at the corners to identify potential singularities there.

3.3.1 Corner solutions

In order to characterize the likely singularities in the solution at the corner (0,1), we introduce a polar coordinate system with the origin at (0,1). The coordinates of a point in the two coordinate systems are related as $x_2 - 1 = r\sin\theta,\ x_1 = r\cos\theta,$ with $-\pi/2 < \theta < 0.$ Note that the form of the singularity as $r \to 0$ should be independent of θ; thus we look for a product solution.

By eliminating $u_2(u_1)$ from the two partial differential equations (3.5), we obtain $\nabla^4 u_1 = 0$ ($\nabla^4 u_2 = 0$). Thus both u_1 and u_2 are biharmonic. However, not all biharmonic functions satisfy (3.5). Biharmonic functions of the product form that give bounded values of the displacements $\mathbf{u}$ but singular behavior of $\nabla\mathbf{u}$ as $r \to 0$ are of the following types:

$$\begin{aligned} &1.\ r(c_0\sin\theta + c_1\theta\sin\theta + c_2\cos\theta + c_3\theta\cos\theta) \\ &\quad + r\ln r(d_0\sin\theta + d_1\theta\sin\theta + d_2\cos\theta + d_3\theta\cos\theta), \\ &2.\ r^b(g_0\sin(b\theta) + g_1\sin((2-b)\theta) + g_2\cos(b\theta) + g_3\cos((2-b)\theta)). \end{aligned} \tag{3.8}$$

Here $c_0, c_1, c_2, c_3, d_0, d_1, d_2, d_3, g_0, g_1, g_2, g_3$ and b are constants. Warlock (1997) has shown that there are no solutions of the type (3.8) that give bounded values of $\mathbf{u}$ but unbounded values of $|\nabla\mathbf{u}|$ at the corners $(0,\pm1)$. However, there could be solutions with $|\nabla\nabla\mathbf{u}|$ unbounded.

3.3.2 The Laplace-transform solution

Due to the symmetry of the problem about the horizontal centroidal axis, u_2 is an odd and $u_{1,1}$ an even function of x_2. Thus at the edge $x_1 = 0,$ these can be assumed to have the forms

$$u_{1,1}(0, x_2) = a_0 + \sum_{n=1}^{\infty} a_n \cos(n\pi x_2), \tag{3.9a}$$

$$u_2(0, x_2) = \sum_{n=1}^{\infty} b_n \sin(n\pi x_2). \tag{3.9b}$$

We apply the Laplace transform

$$U_i(p, x_2) = \int_0^{\infty} e^{-px_1} u_i(x_1, x_2) dx_1, \quad i = 1, 2, \tag{3.10}$$

to Eq. (3.5) and the boundary conditions (3.4a)-(3.4c$_4$), and obtain

$$\begin{aligned} &(1-2\nu)U_1'' + 2p^2(1-\nu)U_1 + pU_2' \\ &= \sum_{n=1}^{\infty} n\pi b_n \cos(n\pi x_2) + 2(1-\nu)\left(pu_0 + a_0 + \sum_{n=1}^{\infty} a_n \cos(n\pi x_2)\right), \end{aligned} \tag{3.11a}$$

$$2(1-\nu)U_2'' + (1-2\nu)p^2 U_2 + pU_1' = (1-2\nu)p\sum_{n=1}^{\infty} b_n \sin(n\pi x_2), \tag{3.11b}$$

$$U_2(p, 1) = 0, \tag{3.12a}$$

$$U_2(p, -1) = 0, \tag{3.12b}$$

$$(1-2\nu)U_1' - 2\mu_f \nu p U_1 - 2\mu_f (1-\nu)U_2' = -2\mu_f \nu u_0 \quad \text{at } x_2 = 1, \tag{3.12c}$$

$$(1-2\nu)U_1' - 2\mu_f \nu p U_1 - 2\mu_f (1-\nu)U_2' = -2\mu_f \nu u_0 \quad \text{at } x_2 = -1. \tag{3.12d}$$

Here a prime indicates derivative with respect to $x_2,$ and $\nu = \lambda/2(\lambda + 2\mu)$ is the Poisson ratio. The far field condition (3.7) imposes two restrictions on U_1. Curbing of exponential

growth demands that there be no poles in the right-half plane, and the avoidance of algebraic growth requires that

$$\lim_{p\to 0} pU_1 = 0. \tag{3.13}$$

Eqs. (3.11a) and (3.11b) are a system of linear ordinary differential equations. We write these as a first order system of four equations in four unknowns: U_1, U_2, U_1', U_2'. We first find a homogeneous solution of these equations and then a particular solution by the method of undetermined coefficients. A general solution is

$$\begin{aligned} U_1 = {} & A\sin(px_2) + B\cos(px_2) + Cx_2\sin(px_2) + Dx_2\cos(px_2) \\ & + \frac{a_0}{p} + \frac{u_0}{p} + \sum_{n=1}^{\infty} A_n \cos(n\pi x_2), \end{aligned} \tag{3.14a}$$

$$\begin{aligned} U_2 = {} & A\cos(px_2) - B\sin(px_2) + Cx_2\cos(px_2) - C\frac{3-4\nu}{p}\sin(px_2) \\ & - Dx_2\sin(px_2) - D\frac{3-4\nu}{p}\cos(px_2) + \sum_{n=1}^{\infty} B_n \sin(n\pi x_2), \end{aligned} \tag{3.14b}$$

where *A, B, C, D* are constants of integration, and

$$A_n = \frac{((1-2\nu)p^2 - 2(1-\nu)(n\pi)^2)a_n - (n\pi)^3 b_n}{(1-2\nu)(p-n\pi)^2(p+n\pi)^2}, \tag{3.15a}$$

$$B_n = \frac{p((1-2\nu)p^2 + 2(n\pi)^2\nu)b_n + pn\pi a_n}{(1-2\nu)(p-n\pi)^2(p+n\pi)^2}. \tag{3.15b}$$

Substitution from (3.14a) and (3.14b) into the boundary conditions (3.12a)-(3.12d) gives four equations for the determination of A, B, C, D. Their solution gives

$$A = 0, \quad B = \frac{(p\cos p - (3-4\nu)\sin p)}{2(1-2\nu)ph(p)} J(p), \tag{3.16a}$$

$$D = 0, \quad C = \frac{\sin p}{2(1-2\nu)ph(p)} J(p), \tag{3.16b}$$

where

$$\begin{aligned} J(p) = {} & \frac{2\mu_f \nu}{p} a_0 + \sum_{n=1}^{\infty} \frac{(-1)^n 2\mu_f p}{(p^2 - n^2\pi^2)^2} (\nu p^2 + n^2\pi^2(1-\nu)) a_n \\ & + \sum_{n=1}^{\infty} \frac{(-1)^n 2u_f pn\pi}{(p^2 - n^2\pi^2)^2} ((1-\nu)p^2 + \nu n^2\pi^2) b_n, \end{aligned} \tag{3.17a}$$

$$h(p) = \mu_f p + 2(1-\nu)(\sin p)^2 - (1-2\nu)\mu_f \sin p \cos p. \tag{3.17b}$$

The coefficients a_n and b_n in Eqs. (3.9a) and (3.9b) are determined by requiring that the solution decay at infinity. Upon expanding various terms in the expression (3.14a) for U_1 in Taylor series about $p = 0,$ and using the condition (3.13), we obtain

$$\frac{(1-\nu)a_0}{\mu_f \nu} + u_0 = 0. \tag{3.18}$$

Curbing exponential growth at infinity requires the absence of singularities in the transformed solution in the right half plane. Thus we must set to zero the residues of any apparent poles there. There are two sets of apparent poles: $p_n = n\pi,$ and the roots p_k of $h(p_k) = 0$ with positive real parts. Straightforward algebraic calculations show that these requirements lead to

$$J(p_k) = 0. \tag{3.19}$$

Values of $a_0, a_1, a_2, \ldots$ and $b_0, b_1, b_2, \ldots$ are found by solving Eqs. (3.18) and (3.19).

3.3.3 Inverting the Laplace transform

We obtain displacements $u_i(x_1, x_2)$ by taking the inverse transforms of $U_i(x_1, x_2),$ i.e.,

$$u_i(x_1,x_2)=\frac{1}{2\pi i}\int_{r-i\infty}^{r+i\infty}e^{px_1}U_i(p,x_2)dp, \tag{3.20}$$

where $\gamma>0$. There are no branch points, and completion of contour in the left-half plane in the usual way yields

$$u_1(x_1,x_2)=\sum_{p_k}e^{p_kx_1}\frac{\overline{B}(p_k,x_2)J(p_k)}{2(1-2\nu)p_k\dfrac{\partial h(p_k)}{\partial p_k}}, \tag{3.21a}$$

$$u_2(x_1,x_2)=\sum_{p_k}e^{p_kx_1}\frac{\overline{C}(p_k,x_2)J(p_k)}{2(1-2\nu)p_k\dfrac{\partial h(p_k)}{\partial p_k}}, \tag{3.21b}$$

where the p_k are the roots of $h(p)=0$ with negative real parts, and

$$\overline{B}(p,x_2)=(p\cos p-(3-4\nu)\sin p)\cos(px_2)+px_2\sin p\sin(px_2),$$
$$\overline{C}(p,x_2)=px_2\sin p\cos(px_2)-p\cos p\sin(px_2).$$

3.4 Numerical Solution of the Problem

We use the meshless local Petrov-Galerkin (MLPG) method to find a numerical solution of the problem defined by Eqs. (3.1)-(3.4c$_4$). We first derive the local symmetric weak form.

Let Ω denote the rectangular region $[0,L]\times[-1,1]$ shown in Fig. 1 and occupied by the linear elastic body, and $\Gamma=\partial\Omega$. We write the boundary conditions (3.4a) - (3.4c$_4$) as

$$u_i=\overline{u}_i \quad \text{on } \Gamma, \tag{3.22a}$$

$$t_i\equiv\sigma_{ij}n_j=\overline{t}_i \quad \text{on } \Gamma, \tag{3.22b}$$

with the understanding that only linearly independent components of u_i and t_i can be prescribed at a point. The equation corresponding to the unprescribed component of u_i and t_i is written as $0 = 0$. Here $\mathbf{n}$ is an outward unit normal to the boundary Γ. We write the boundary condition $(3.4c_4)$ as

$$\mathbf{p}(\sigma) = \mathbf{A}\sigma = \mathbf{0} \quad \text{on } \Gamma_c, \tag{3.22c}$$

where

$$\mathbf{A} = \begin{bmatrix} 0 & \pm\mu_f & 1 \\ 0 & 0 & 0 \end{bmatrix}, \quad \sigma = \begin{Bmatrix} \sigma_{11} \\ \sigma_{22} \\ \sigma_{12} \end{Bmatrix}, \tag{3.22d}$$

and $\Gamma_c = [0, L] \times \{\pm 1\}$. At points of Γ_c the natural boundary condition (3.22b) is replaced by (3.22c).

Select a set of discrete points $\{\mathbf{x}_1, \mathbf{x}_2, ..., \mathbf{x}_N\}$ in and on the boundary of Ω; these points will henceforth be called nodes. For $\mathbf{x} \in \Omega$, let $\Omega_{\mathbf{x}} \subset \Omega$ be the neighborhood of $\mathbf{x}$, and $\mathbf{v}$ be a test function defined on $\Omega_{\mathbf{x}}$. Taking the inner product of Eq. (3.1) with $\mathbf{v}$, of Eq. (3.22a) with $\alpha\mathbf{v}$, and of Eq. (3.22c) with $\beta\mathbf{v}$, integrating the resulting equations on $\Omega_{\mathbf{x}}$, $\Gamma_{\mathbf{x}} = \Gamma \cap \partial\Omega_{\mathbf{x}}$, and $\Gamma_{c\mathbf{x}} = \Gamma_c \cap \partial\Omega_{\mathbf{x}}$ respectively, adding them, and using the divergence theorem, we obtain

$$\int_{\Omega_{\mathbf{x}}} \sigma_{ij} v_{i,j} d\Omega + \int_{\Gamma_{\mathbf{x}}} \alpha v_i (u_i - \bar{u}_i) d\Gamma + \int_{\Gamma_{c\mathbf{x}}} \beta v_i p_i d\Gamma - \int_{\Gamma_{\mathbf{x}}} v_i t_i d\Gamma = 0. \tag{3.23}$$

Here α and β are scalar functions of $\mathbf{x}$ defined on $\Gamma_{\mathbf{x}}$ and can be viewed either as Lagrange multipliers in which case they are to be determined as a part of the solution of the problem or as preassigned penalty parameters; their dimensions are such as to make Eq. (3.23) dimensionally correct. In order to obtain two sets of equations for the two components of **u**,

we select two linearly independent functions $\mathbf{v}^{(1)}$ and $\mathbf{v}^{(2)}$ in Eq. (3.23). The function $\mathbf{v}$ could be different for each node point; we signify this by writing $\mathbf{v} = \mathbf{v}(\mathbf{x}, \mathbf{x}_A)$.

In order to find an approximate solution, we replace $\mathbf{u}(\mathbf{x})$ by $\mathbf{u}^h(\mathbf{x})$ in Eq. (3.23) and set

$$u_i^h(\mathbf{x}) = \phi_A(\mathbf{x})\hat{u}_{Ai} \qquad (A = 1,2,...,n;\ i = 1,2), \tag{3.24}$$

where $\phi_1(\mathbf{x}), \phi_2(\mathbf{x}), ...\phi_n(\mathbf{x})$ are linearly independent functions defined on $\hat{\Omega}_{\mathbf{x}}$, and $\hat{u}_{Ai}$ are 2n scalar quantities which are not necessarily associated with the values of $\mathbf{u}^h(\mathbf{x})$ at any point $\mathbf{x} \in \Omega_{\mathbf{x}}$. We use the moving least squares method to ascertain functions $\phi_1(\mathbf{x}), \phi_2(\mathbf{x}),$ $...\phi_n(\mathbf{x})$. We refer the reader to Atluri and Zhu (1998) for details of finding the basis functions $\phi_l(\mathbf{x})$ and the definition of $\hat{\Omega}_{\mathbf{x}}$. However, we note that in a two-dimensional problem $\Omega_{\mathbf{x}}$ is usually a circle but $\hat{\Omega}_{\mathbf{x}}$ is an irregular shaped region.

Substituting for $\mathbf{u}^h(\mathbf{x})$ from Eq. (3.24) into Eq. (3.23) we arrive at two linear equations in 2*n* unknowns $\hat{u}_{Ai}$. Repeating this process for $\mathbf{x}$ located at each one of the *N* nodes and assembling them, we arrive at the following system of 2*N* equations in 2*N* unknowns:

$$\mathbf{K}\mathbf{u}^h = \mathbf{f}, \tag{3.25}$$

where

$$\begin{aligned}\mathbf{K}_{LM} = \sum_{\mathbf{x}} \Big[& \int_{\Omega_{\mathbf{x}}} \varepsilon_{\mathbf{v}}(\mathbf{x}, \mathbf{x}_L)\mathbf{D}\mathbf{B}_M \, d\Omega + \int_{\Gamma_{\mathbf{x}}} \alpha \mathbf{v}(\mathbf{x}, \mathbf{x}_L)\mathbf{S}\phi_M \, d\Gamma \\ & + \int_{\Gamma_{\mathbf{x}}} \mathbf{v}(\mathbf{x}, \mathbf{x}_L)\mathbf{N}\mathbf{D}\mathbf{B}_M \mathbf{S} d\Gamma + \int_{\Gamma_{c\mathbf{x}}} \beta \mathbf{v}(\mathbf{x}, \mathbf{x}_L)\mathbf{A}\mathbf{D}\mathbf{B}_M \, d\Gamma \Big],\end{aligned} \tag{3.26a}$$

$$\mathbf{f}_L = \sum_{\mathbf{x}} \Big[\int_{\Gamma_{\mathbf{x}}} \mathbf{v}(\mathbf{x}, \mathbf{x}_L)\bar{\mathbf{t}} d\Gamma + \int_{\Gamma_{\mathbf{x}}} \alpha \mathbf{v}(\mathbf{x}, \mathbf{x}_L)\mathbf{S}\bar{\mathbf{u}} d\Gamma \Big], \tag{3.26b}$$

$$\mathbf{N} = \begin{bmatrix} n_1 & 0 & n_2 \\ 0 & n_2 & n_1 \end{bmatrix}, \tag{3.26c}$$

$$\mathbf{B}_L = \begin{bmatrix} \phi_{L,1} & 0 \\ 0 & \phi_{L,2} \\ \phi_{L,2} & \phi_{L,1} \end{bmatrix}, \tag{3.26d}$$

$$\mathbf{D} = \begin{bmatrix} \lambda+\mu & \mu & 0 \\ \mu & \lambda+\mu & 0 \\ 0 & 0 & \mu \end{bmatrix}, \tag{3.26e}$$

$$\sigma^T = [\sigma_{11}, \sigma_{22}, \sigma_{12}], \quad \varepsilon^T = [\varepsilon_{11}, \varepsilon_{22}, \varepsilon_{12}], \tag{3.26f}$$

$$\mathbf{S} = \begin{bmatrix} S_1 & 0 \\ 0 & S_2 \end{bmatrix}, \quad S_i = \begin{cases} 1 & \text{if } u_i \text{ is prescribed on } \Gamma_{\mathbf{x}}, \\ 0 & \text{if } u_i \text{ is not prescribed on } \Gamma_{\mathbf{x}}. \end{cases} \tag{3.26g}$$

The approximate displacement field is computed from Eq. (3.24), and then strains and stresses can be evaluated at any point. In the solution of the problem we took α and β as penalty parameters and set their magnitudes equal to 10^8.

3.5 Results

Both the numerical and the analytical solutions have been computed for $\nu = 0.25$, $u_0 = 1$, and for a broad range of values of the coefficient of friction, μ_f. The analytical solution is for a semi-infinite strip, and the numerical solution, unless otherwise specified, for L=15. A regular mesh of 1089 nodes is used over the analysis domain. The roots of $h(p) = 0$ were found by using the bisection method for the real roots and Newton's method for the complex ones. The series were summed by retaining enough terms to ensure that $|s_{n+1} - s_n| / |s_n| < 0.001$ where s_n is the n_{th} partial sum. It was found that there exists a critical value of the friction coefficient, $\mu_{f_{crit}} \cong 1.4$, that separates two distinct types of deformations of the elastic medium.

For subcritical μ_f, boundary condition $(3.4c_3)$ applies and was verified a posteriori by the computed solution. A typical observation is that increasing μ_f magnifies the effect of

friction without any qualitative change. Results for $\mu_f = 1$ are typical, and are discussed below.

Figures 3.2a and 3.2b exhibit the variation of the horizontal displacement u_1 with the vertical coordinate x_2 for several values of x_1, and the variation of u_1 with x_1 for five values of x_2. On a cross-section (i.e. the plane $x_1 = \text{constant}$) the horizontal displacement is uniform except for slightly smaller values near the top and bottom walls. (Due to the symmetry of the problem about the horizontal centroidal axis, results for only the upper half of the strip are displayed.) However, the horizontal displacement decays quite rapidly in the x_1-direction. These plots suggest that the horizontal displacement is greatest at the surface $x_1 = 0$, and for a fixed x_1 is greatest on the centerline $x_2 = 0$. Because $u_1(x_1, 0.99) > 0$, the frictional force on the top wall always acts in the negative x_1-direction. An excellent agreement between the numerical and the analytical results implies that *L*=15 is sufficient for computing numerical results with $\mu_f = 1$. Figures 3.3a and 3.3b exhibit the through-the-thickness distribution of the vertical displacement, u_2, for several values of x_1, and the variation of u_2 along the domain length, x_1, with fixed x_2. It is clear that the vertical displacement also decays in the x_1-direction. Observe that $u_2(x_1, x_2)$ is negative for small x_1 but positive for large x_1. Thus the material moves towards the centerline of the strip near the left edge but towards the top and the bottom walls in the interior. The maximum value of $|u_2(x_1, x_2)|$ is of the order of 10^{-2} whereas that of $|u_1(x_1, x_2)|$ is 1.

Figures 3.4a-c depict the variation on different horizontal planes of the stresses σ_{11}, σ_{22}, and σ_{12} scaled by the Lame′ constant λ. Note that all of the stresses decay to zero with an increase in x_1. All three stress components change rapidly in the x_1-direction near the corner $x_1 = 0,\ x_2 = 1$. Recall that the conclusion from the corner analysis was that there were no solutions of the field equations with regular displacements and singular but integrable stress fields. However, there may be solutions in which the second derivatives of

the displacement are unbounded as the corner is approached. Thus the stresses are bounded at the corner but may have infinite slopes. Note that $\sigma_{12}(0,1)=0$ is required by the boundary condition $(3.4b)_2$. Thus $\sigma_{12}(x_1,1)$ increases rapidly from 0 at $x_1=0$ to a finite value a short distance away from the edge $x_1=0$. The variation σ_{11} and σ_{22} at the corner in the x_1-direction is also quite sharp. Since $\sigma_{11}/\lambda=\mathrm{O}(1)$, the presumed value of $u_0=1$ is too large and the computed solution is outside the range of validity of the linear theory. Because the problem being studied is linear, the qualitative nature of the solution is preserved and the magnitude of the computed displacements and stresses will scale down linearly with a change in the value of u_0.

From the variation of stresses on several vertical planes plotted in Figs. 3.5a-d, it is evident that through-the-thickness distributions of σ_{11} and σ_{22} on vertical planes $x_1\geq 0$ are nearly uniform. However, on the plane $x_1=0$, σ_{11} varies sharply near the top wall and the same holds for σ_{22} on vertical planes $x_1=0.2$ and 0.4. The shear stress σ_{12} essentially vanishes on the vertical plane $x_1=10$, varies nearly linearly on vertical planes $1\leq x_1\leq 9$, and rapidly on the vertical planes $0.2\leq x_1\leq 0.8$. In order to see if the differences between the values of σ_{12} on the left edge computed from the numerical and the analytical solutions were caused by the discretization of the domain, we refined the nodal mesh. Results from the refined mesh are exhibited in Fig. 3.6 and show that $\sigma_{12}(0,0)=0$ is well satisfied, and that σ_{12} exhibits a boundary-layer effect near the top wall. The boundary condition $\sigma_{12}(0,1)=0$ at the corner is not satisfied even for the finer mesh. It is due to the conflicting requirements at the corner since the boundary condition $(3.4c_3)$ necessitates that $\sigma_{12}(0,1)\neq 0$ for the material point to stay in contact with the wall, unless $\sigma_{22}(0,1)=0$.

Figure 3.7 displays the variation of $u_1(x_1,0)$ on the centerline of the strip for four different values of the domain length L and the coefficient of friction, $\mu_f=0.5$. It is clear that the decay rate of $u_1(x_1,0)$ near the left edge is unaffected by increasing L from 15 to 30

but the decay rate $u_1(x_1, 0)$ away from the left edge is slower for $L = 30$ as compared to that for $L = 15$. However, the decay rate of $u_1(x_1, 0)$ near the left edge increases noticeably as L is decreased from 10 to 5. Within the region $0 \le x_1 \le 1.5$ where sharp variations in σ_{11} σ_{22}, and σ_{12} occur, the two solutions computed with $L = 15$ and 30 are virtually identical.

Solutions for other values of μ_f between 0 and 1.4 reveal that the qualitative behaviors of the displacements and the stresses are unaffected by the value of μ_f but the rate of decay of the solution in the x_1 direction changes with μ_f. The horizontal displacements on the centerline plotted in Fig. 3.8a for $\mu_f = 0.5,\ 1.0, 1.4$ reveal that their decay rate increases with an increase in the value of μ_f. The discrepancy between the analytically and the numerically computed values of σ_{22} at the point (1, 0.99) (cf. Fig. 3.8b) for $\mu_f = 0.1$ disappears when the length of the domain is increased (cf. Fig. 3.7) from 15 to 30. The values of σ_{12} at the point (1, 0.99) computed from the numerical solution for the four values of μ_f agree well with their respective analytical values. Figure 3.9 displays the axial location x_1^* at which the analytical value of $u_1(x_1^*, 0) = 0.01$ or 1% of its value at $x_1 = 0$. It suggests that the solution for the infinite strip provides a good approximation to the solution for the finite strip provided that it is long enough. On each vertical plane, the magnitude of the three stresses at a point adjacent to the top wall increases with an increase in the magnitude of μ_f; this is illustrated in Figs. 3.8b and 3.8c wherein σ_{12} and σ_{22} at the point (1, 0.99) vs. μ_f are plotted.

For values of the coefficient of friction $\mu_f > 1.4$, the deformations of the material points are quite different from those for $\mu_f < 1.4$. This is seen readily by examining Figs. 3.10a-10d, which are for $\mu_f = 5.0$ and display the archetypal variation of the horizontal displacement u_1 on three horizontal planes. While the magnitude of the displacement continues to decay with x_1, the profiles are now oscillatory rather than monotonic. Also,

through-the-thickness variation of u_1 on the four vertical planes $x_1 = 1,\ 2,\ 3$ and 4 is not alike; cf. Fig. 3.10b. The variation shown in Fig. 3.10c of the shear stress on each one of the three horizontal planes is also oscillatory with a decreasing amplitude of the oscillations. In order to understand the mathematical origin of this behavior, we recall that away from $x_1 = 0$, the character of the solution is determined predominantly by those poles in the transform plane that are closest to the imaginary axis. The location of the first six poles as a function of μ_f is exhibited in Figs. 3.11a-c. Figures 3.11a and 11b depict, respectively, the dependence of the real and the imaginary parts of the pole location on μ_f, and Fig. 3.11c shows the locations of the poles in the complex plane for a number of values of μ_f. The rightmost pair of poles are both real for small enough μ_f. As μ_f increases, one pole moves towards the origin while the other moves away from it until they meet and then become a complex conjugate pair. The real part of this complex conjugate pair then decreases with an increase in μ_f while the imaginary part increases. This behavior is also seen in each successive pair of poles, however the value of μ_f at which the two real poles change to a complex pair is smaller for the poles with more negative real parts. Recalling that the solution has the form $\sum_{p_k} e^{p_k x_1} f(p_k, x_2),$ at the critical value of $\mu_f \cong 1.4,$ the two largest terms in the expansion make the transition from having an exponential decay in x_1 to having a sinusoidal behavior with exponentially decaying amplitude. Furthermore, an increase in μ_f decreases the amplitude of the exponential decay and the oscillations become more pronounced.

3.6 Conclusions

We have analyzed plane strain static deformations of a homogeneous, isotropic linear elastic body enclosed within a rigid rectangular cavity with rough side walls but a smooth right end. The material is compressed by prescribing uniform axial displacements at the left end. The problem is solved both analytically by the Laplace transform technique and

numerically by the moving least squares Petrov-Galerkin method which requires only the locations of the nodes. The analytical solution is for an infinite length of the cavity and the numerical solution is for the finite cavity. Coulomb's friction law is assumed to apply at the two rigid walls.

It is found that there is a critical value of the coefficient of friction, $\mu_{f_{crit}} \cong 1.4$. For $\mu_f < \mu_{f_{crit}}$, the axial displacements of points decay monotonically with distance from the left edge and the material points stay in contact with the rough walls. Also, the rate of decay of the solution variables in the axial direction increases with an increase in the value of μ_f. The analytical solution for the infinite cavity represents well the deformations of the material compressed in the finite cavity for large values of μ_f.

For $\mu_f > \mu_{f_{crit}}$, the axial displacements and the stresses on the rough walls exhibit oscillatory behavior in the axial direction, with the amplitude of the oscillations decaying with increasing axial distance from the left end. The shear stress undergoes changes in sign and the material separates from the wall, so that the analytical solution presented here can no longer be deemed physically relevant. The solution is analogous to what had been observed in the earlier study on powders sliding in rough tubes (Hill and Kapila, 1995), which had motivated the present investigation. The implication is that at high levels of roughness the Coulomb friction model is no longer adequate, as it fails to capture faithfully the complex interaction between the now larger asperities and imperfections in the sliding surfaces. It is possible that the boundary conditions $(3.4c_2) - (3.4c_4)$ then apply on different (and a priori unknown) segments of the walls, but that is a difficult problem which we have not examined.

3.7 References

Hill L. G. and Kapila A. K. (1995): *Dynamic compaction of granular materials in a tube with wall friction, applied to DDT*, in B. Sturtevant, J. E. Shepherd and H. G. Hornung (Eds.), Proceedings of the 20th International Symposium on Shock Waves, World Scientific, 1413-1418.

Warlock A. W. (1997): *Effect of wall friction on compaction and compression*, Ph.D. Thesis, Rensselaer Polytechnic Institute.

Elban W. L. and Chiarito M. A. (1986): The strain-rate behavior of course HMX porous bed compaction. *Powder Technology*, 46, 181-187.

McAfee J. M., Asay B. W. and Cambell A. W. (1989): *Deflagration to detonation transition in granular HMX*, Proceedings of the Ninth Symposium (International) on Detonations, Portland, OR, 265-278.

Muskhelishvili N. I. (1963): *Some basic problems of the mathematical theory of elasticity*, Noordhoff. Ltd.

Smith R. C. T. (1952): The bending of a semi-infinite strip. *J. Sci. Res*., 5, 227-237.

Johnson Jr. M. W. and Little R. W. (1965): The semi-infinite elastic strip. *Quart. Appl. Math.,* 22, 335-344.

Gregory R. D. (1980): The traction boundary-value problem for the elastic semi-infinite strip, existence of solutions and completeness of the Papkovich-Fadle eigen functions. *Journal of Elasticity*, 10, 295-327.

Joseph D. D. (1977): The convergence of biorthogonal series for biharmonic and Stokes flow edge problems. *SIAM J. Appl. Math*., 33, 337-347.

Spence D. A. (1982): A note on the eigenfunction expansions for the elastic strip. *SIAM J. Appl. Math.*, 42, 155-173.

Gregory R. D. and Gladwell I. J. (1982): The cantilever beam under tension, bending or flexure at infinity. *Journal of Elasticity*, 12, 317-343.

Champeney D. C. (1987): A handbook of Fourier Theorems. *Cambridge University Press*, Cambridge.

Atluri S. N. and Zhu T. (1998): A new Meshless Local Petrov-Galerkin (MLPG) approach in computational mechanics. *Computational Mechanics*, 22, 117-127.

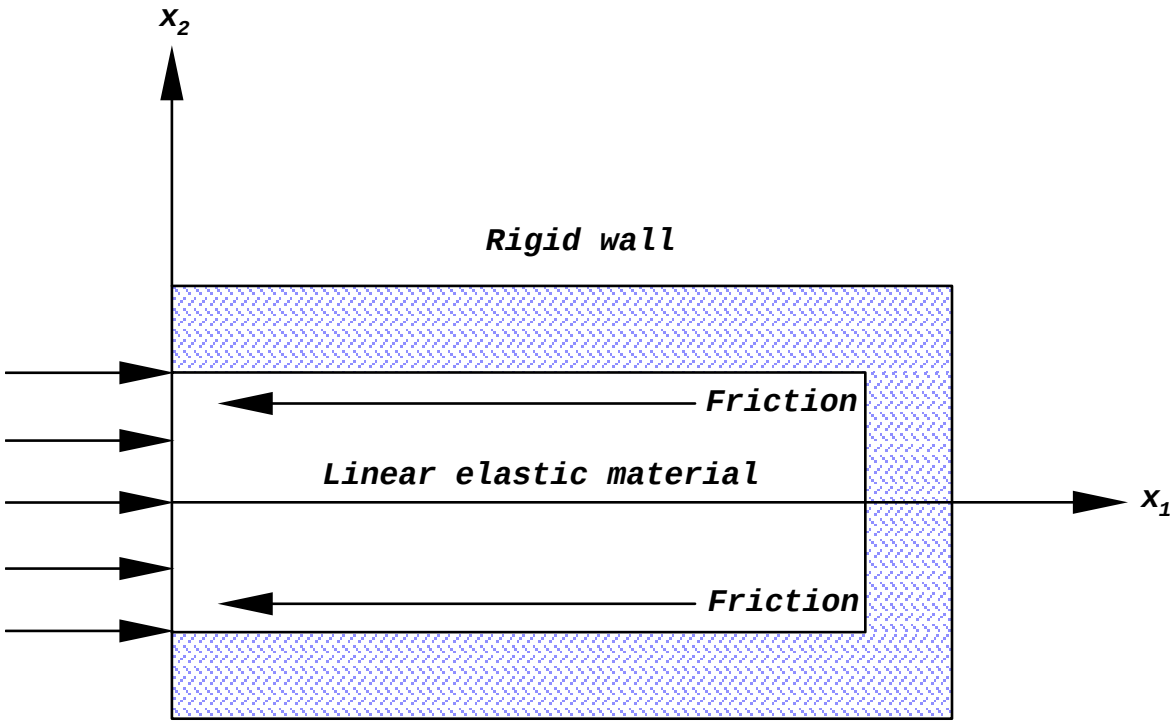

Fig. 3.1 A rectangular rigid cavity enclosing a linear elastic material

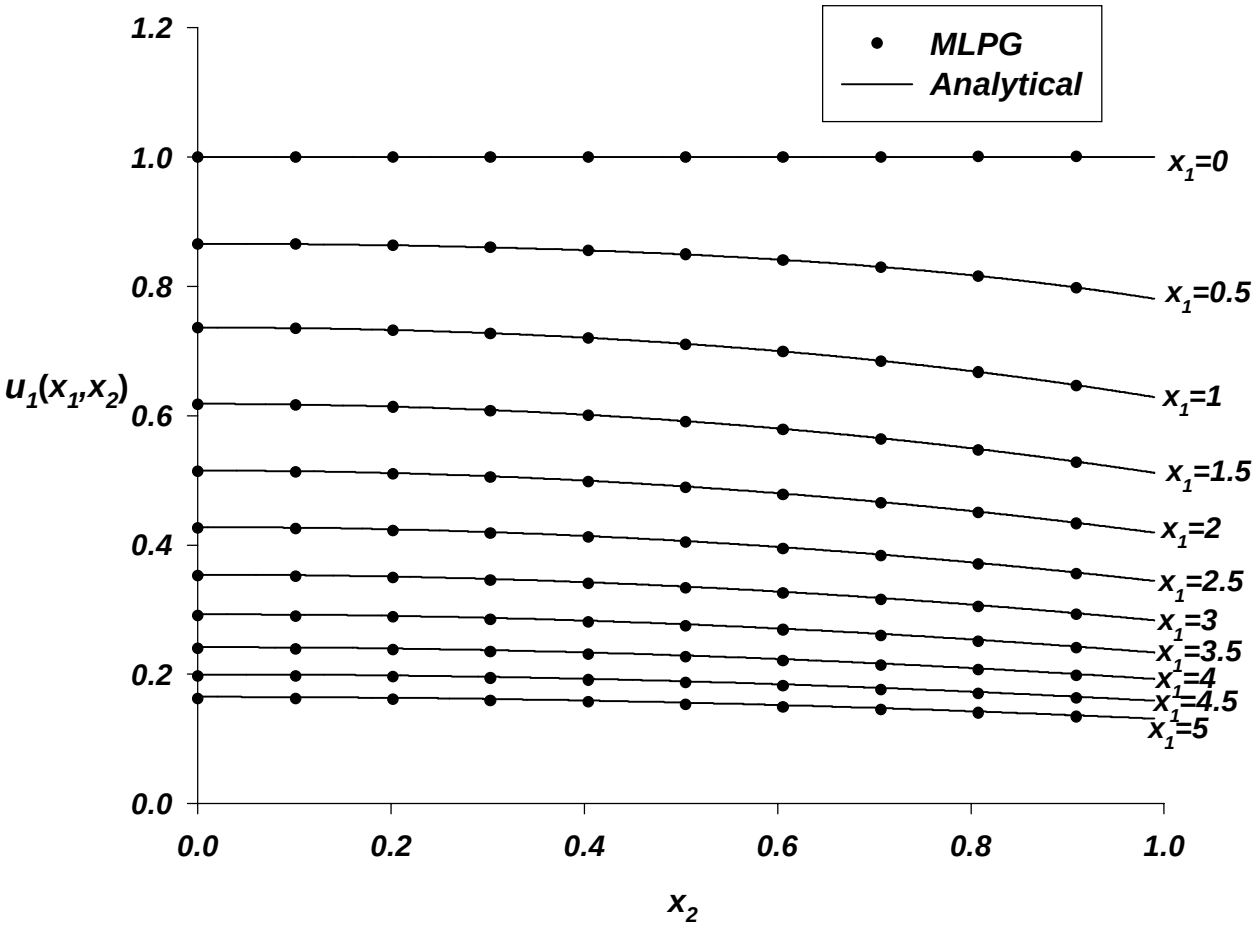

Fig. 3.2a Variation of the horizontal displacement on several vertical planes

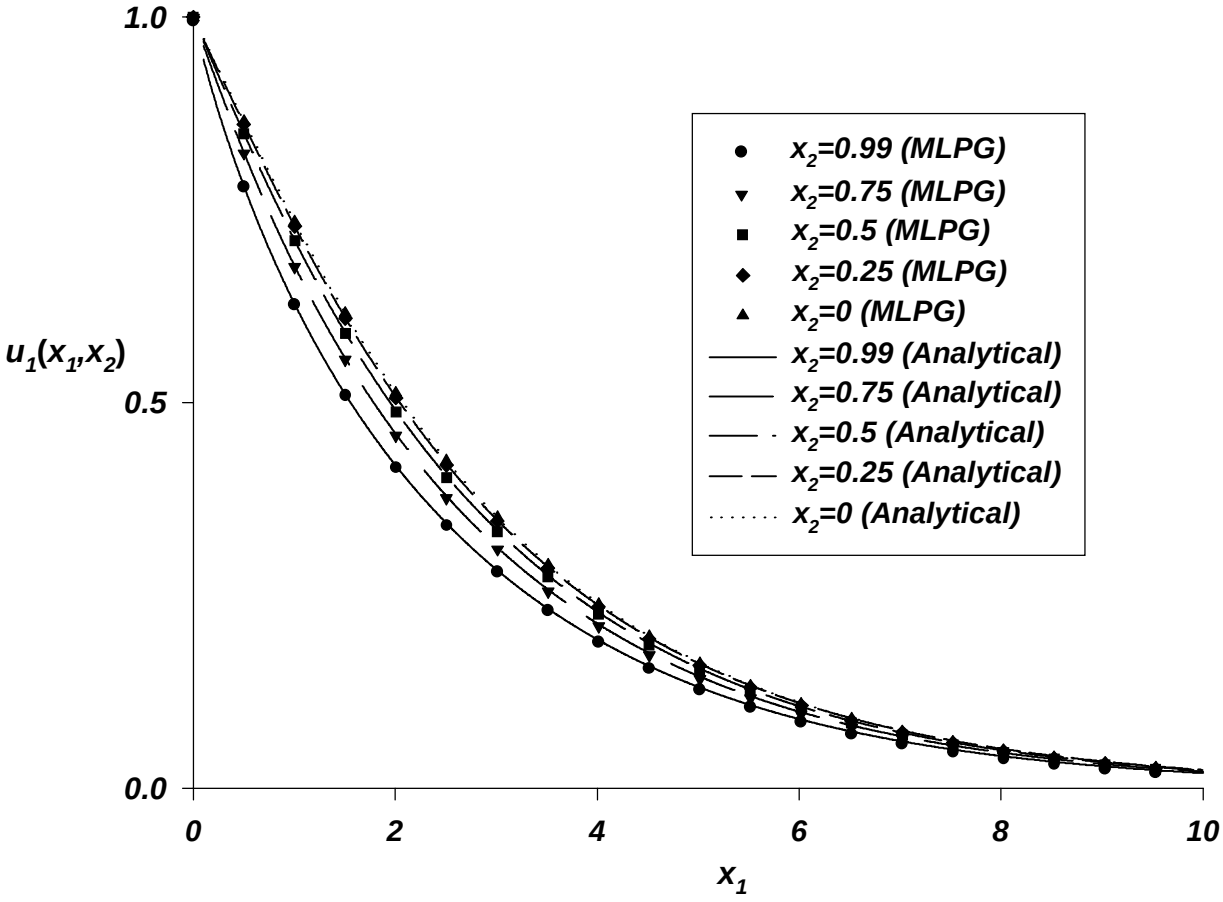

Fig. 3.2b Variation of the axial displacement on five horizontal planes

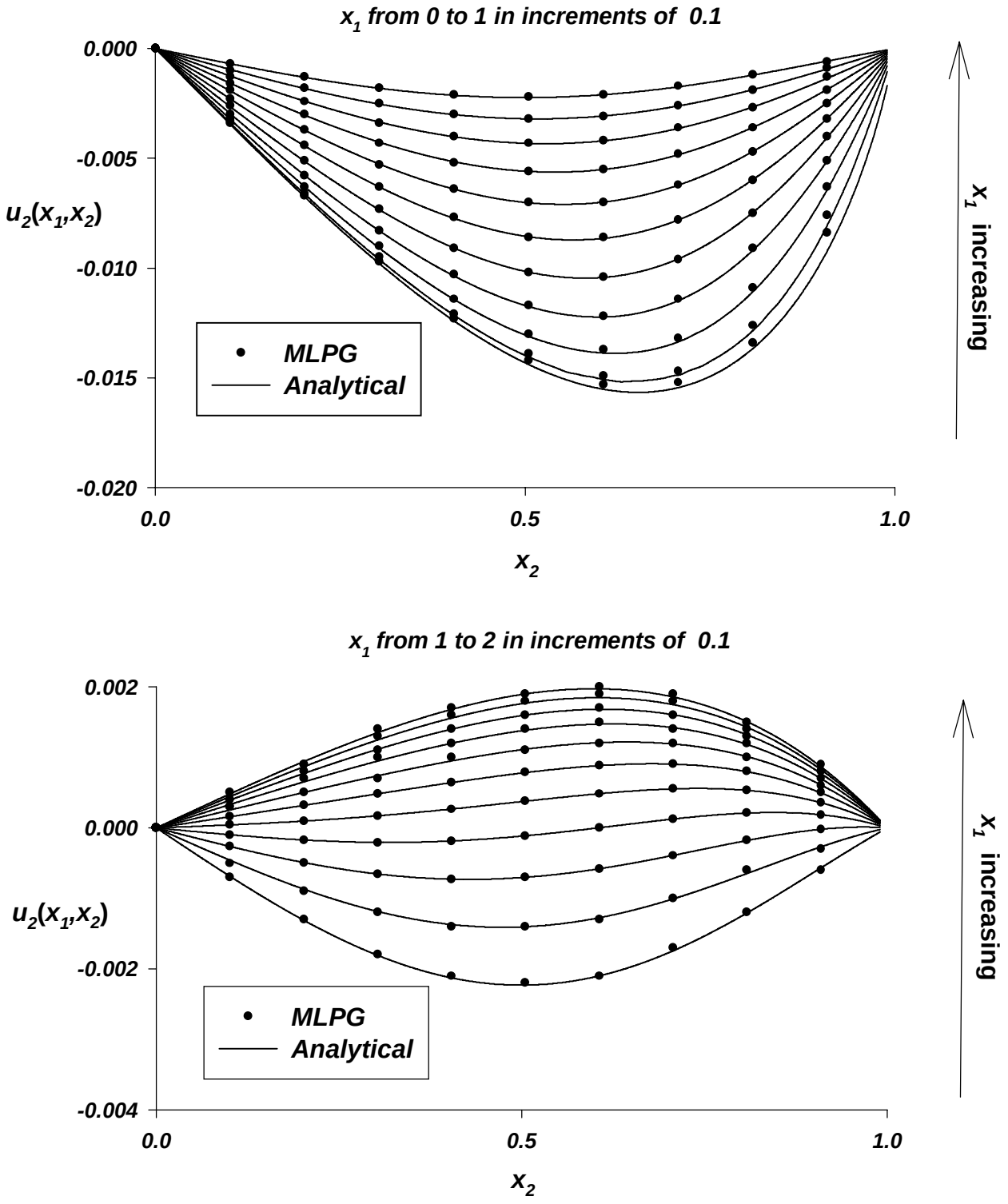

Fig. 3.3a Through-the-thickness distribution of the vertical displacement u_2 on several vertical planes

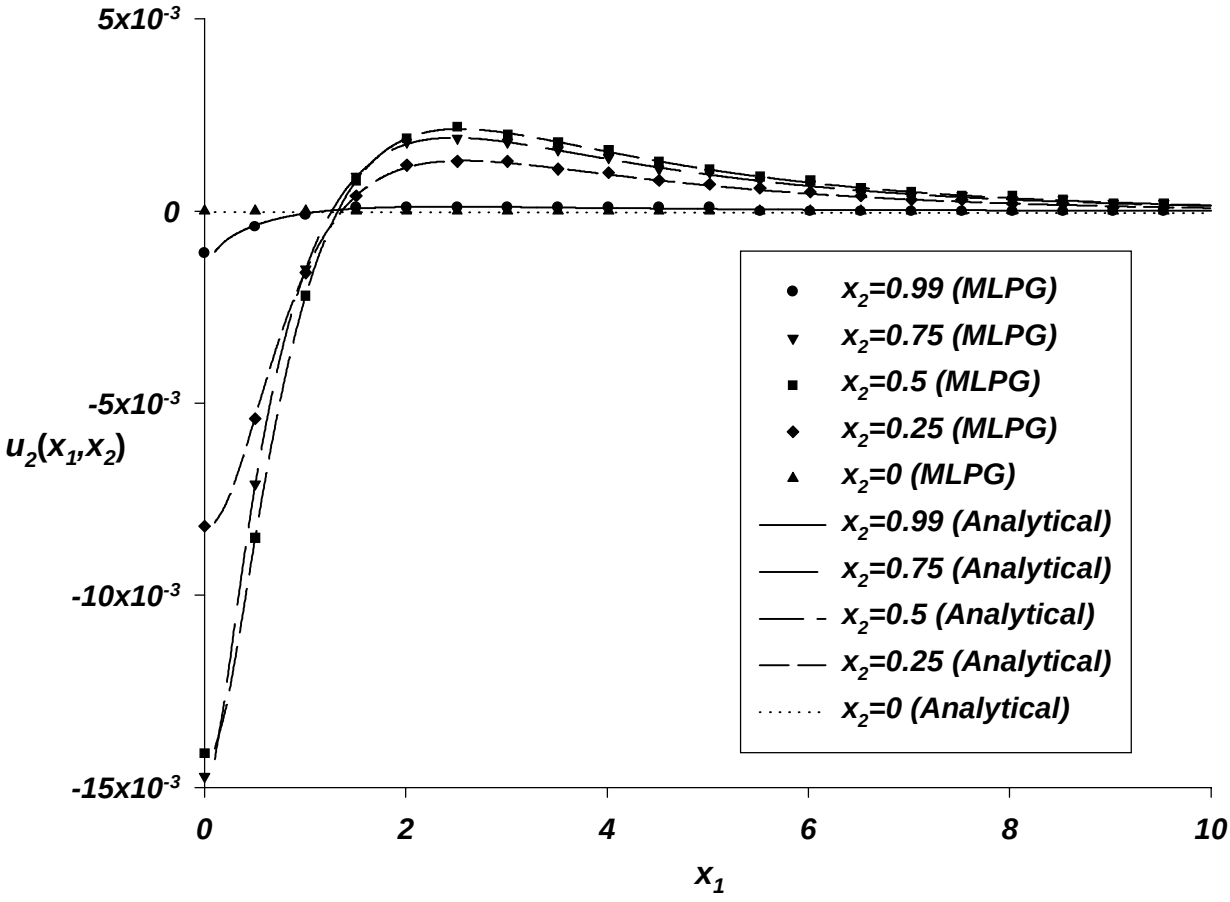

Fig. 3.3b Variation of the vertical displacement u_2 on different horizontal planes

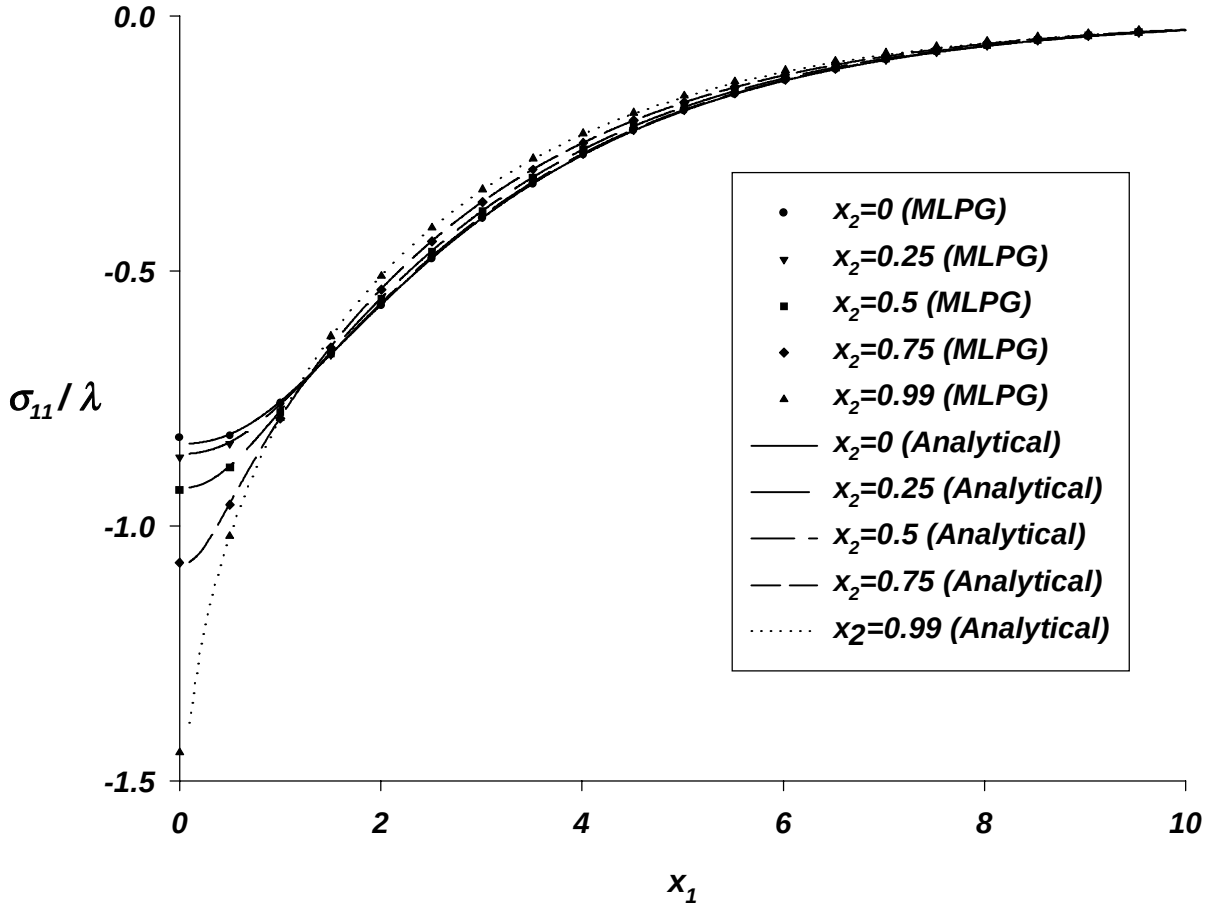

Fig. 3.4a Variation of the normalized axial stress σ_{11} on five horizontal planes

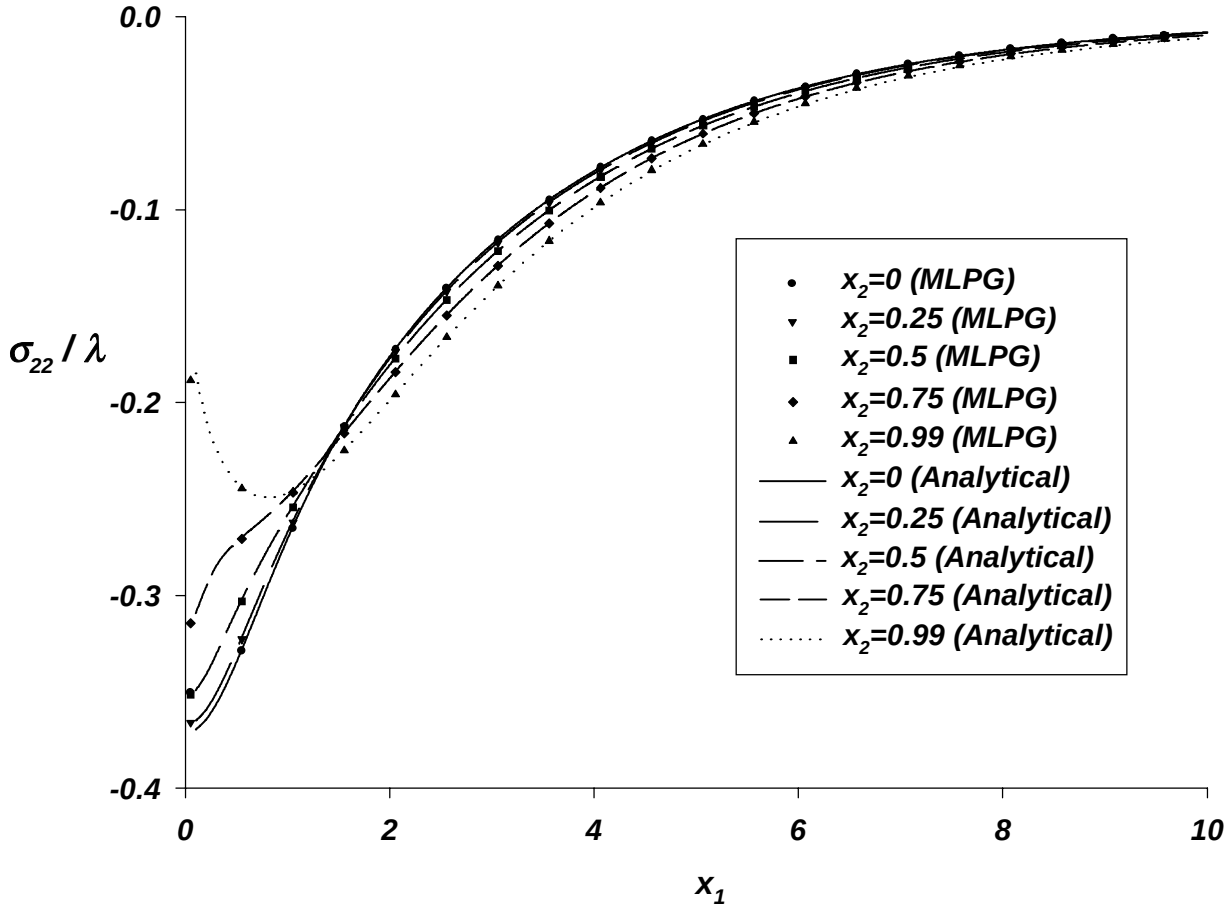

Fig. 3.4b Variation of the normalized transverse normal stress σ_{22} on five horizontal planes

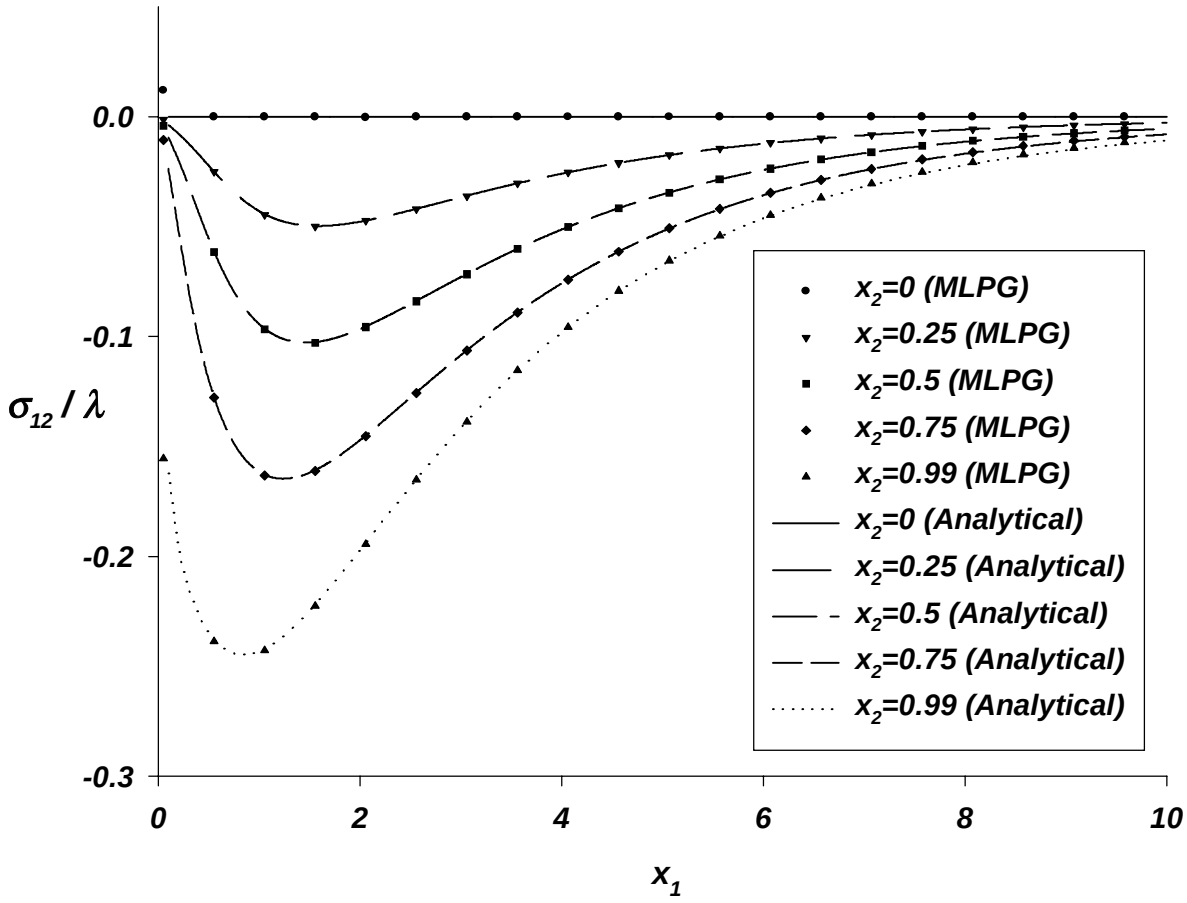

Fig. 3.4c Variation of the normalized shear stress σ_{12} on five horizontal planes

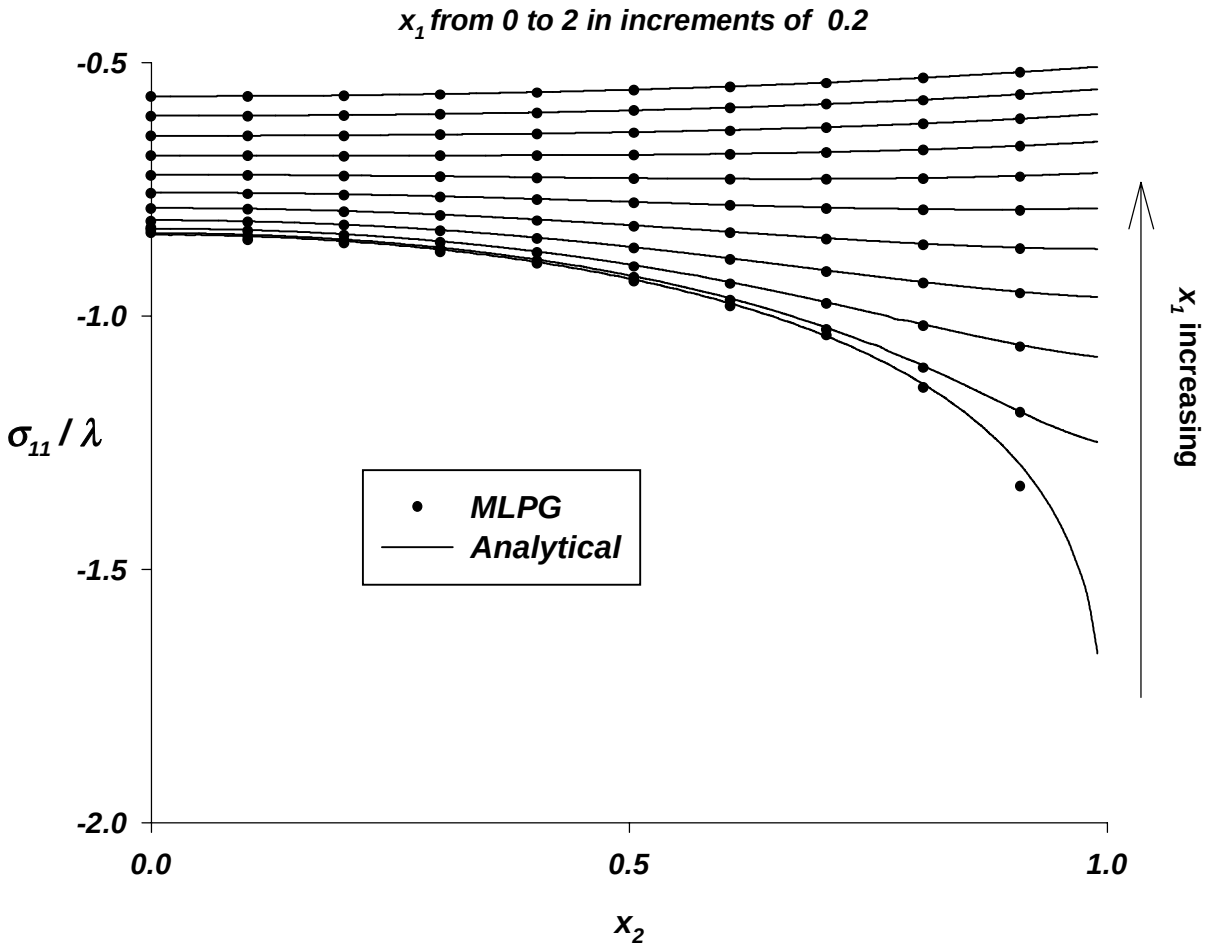

Fig. 3.5a Through-the-thickness distribution of the normalized axial stress σ_{11} on several vertical planes

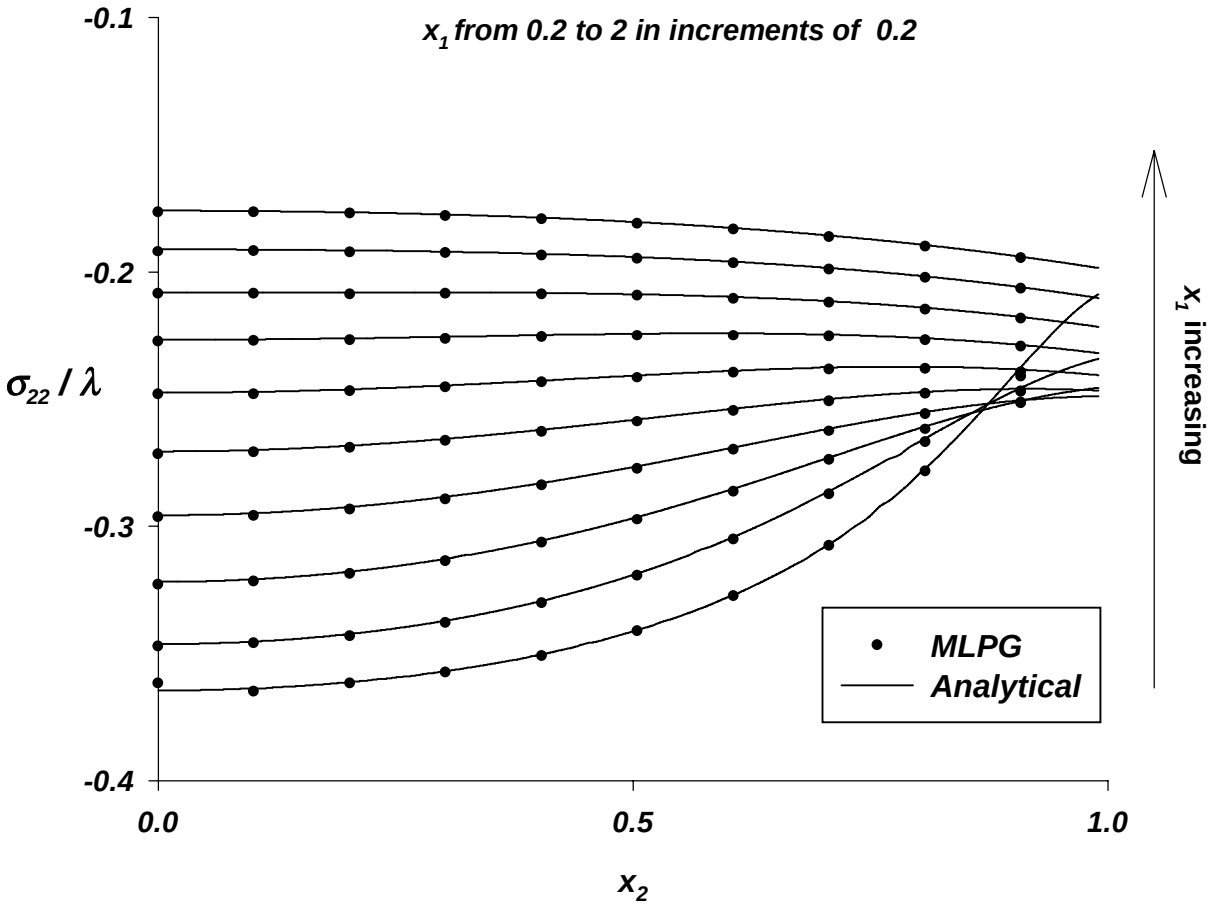

Fig. 3.5b Through-the-thickness distribution of the normalized transvese normal stress σ_{22} on several vertical planes

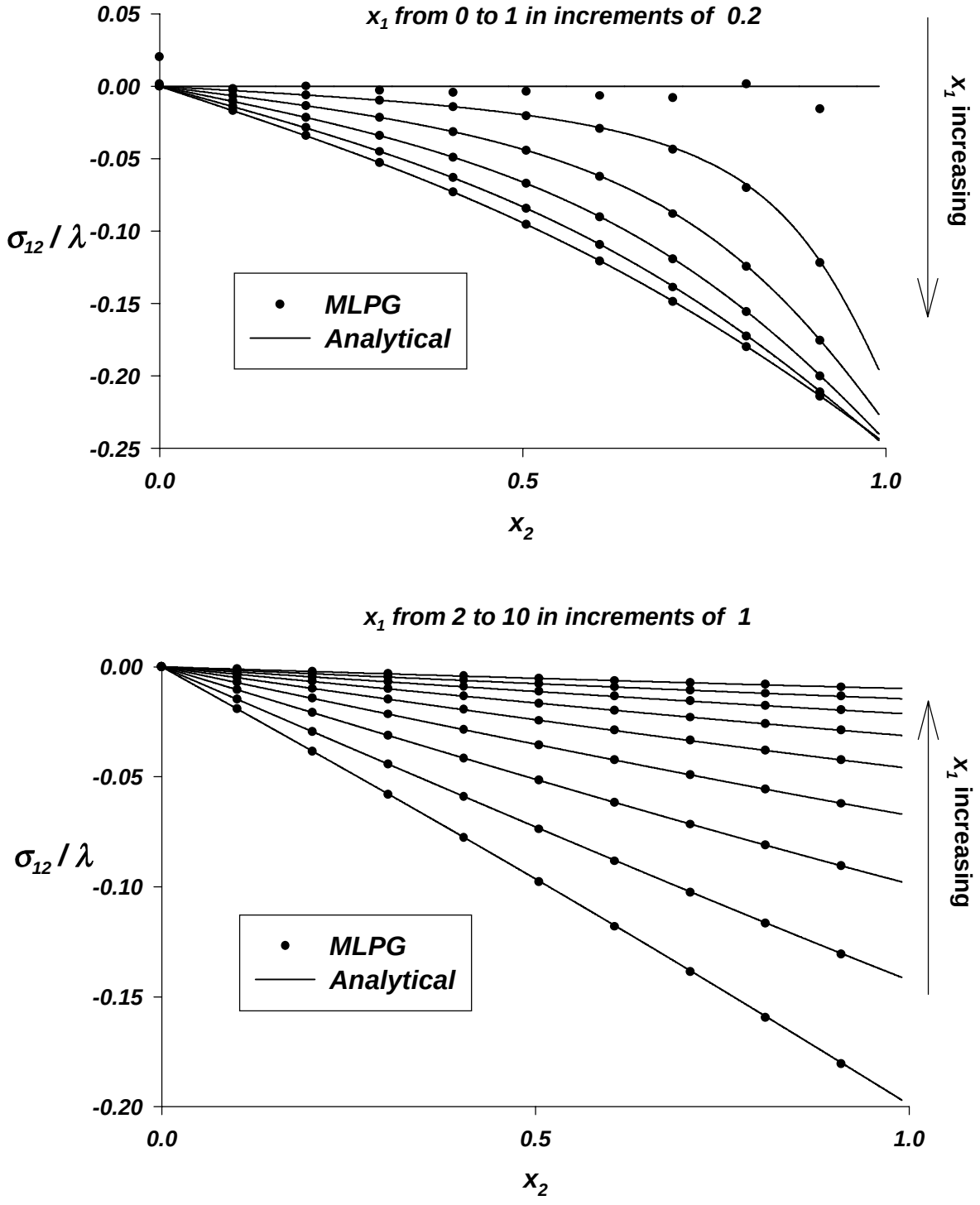

Fig. 3.5c Through-the-thickness distribution of the normalized shear stress σ_{12} on several vertical planes

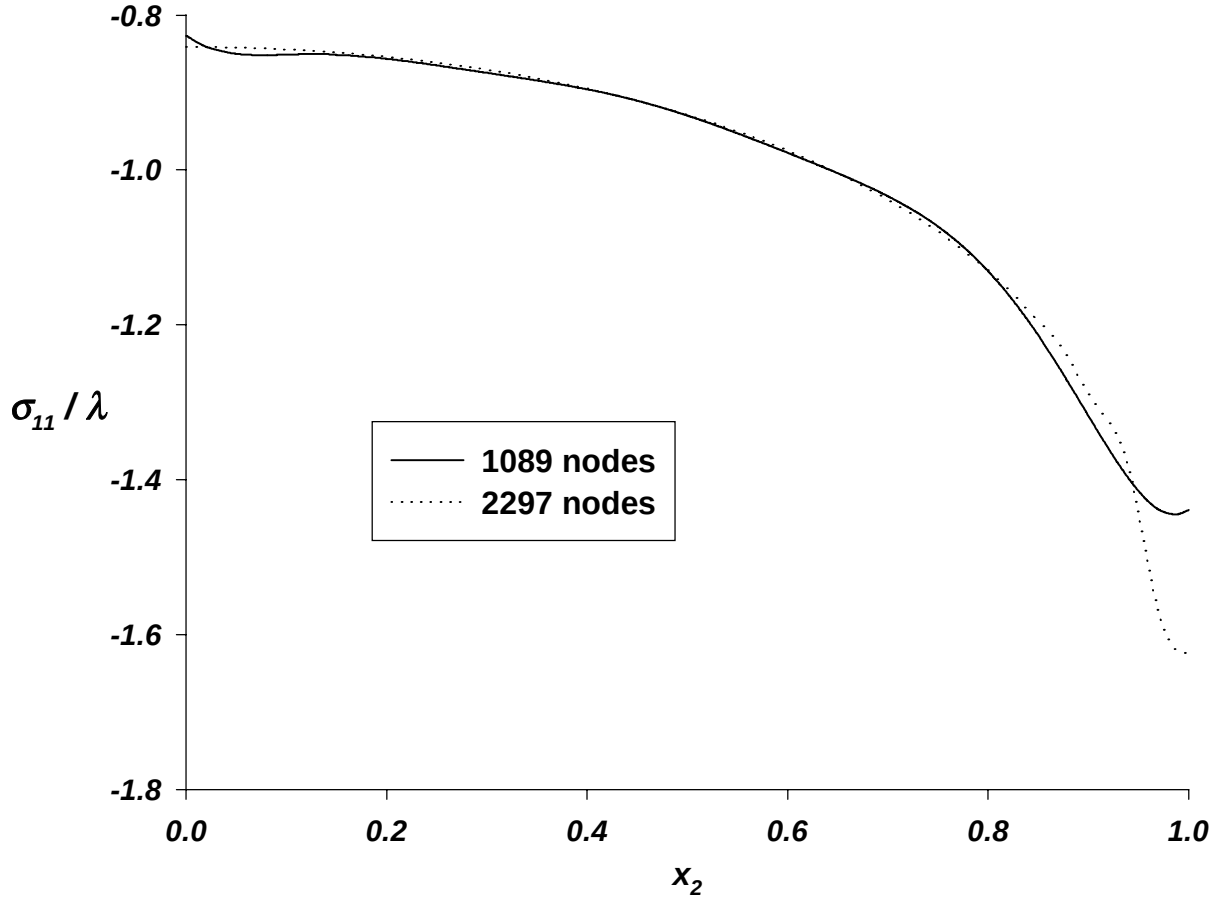

Fig. 3.6a Comparsion of through-the-thickness distribution of the normalized axial stress σ_{11} on the left edge computed with two nodal meshes

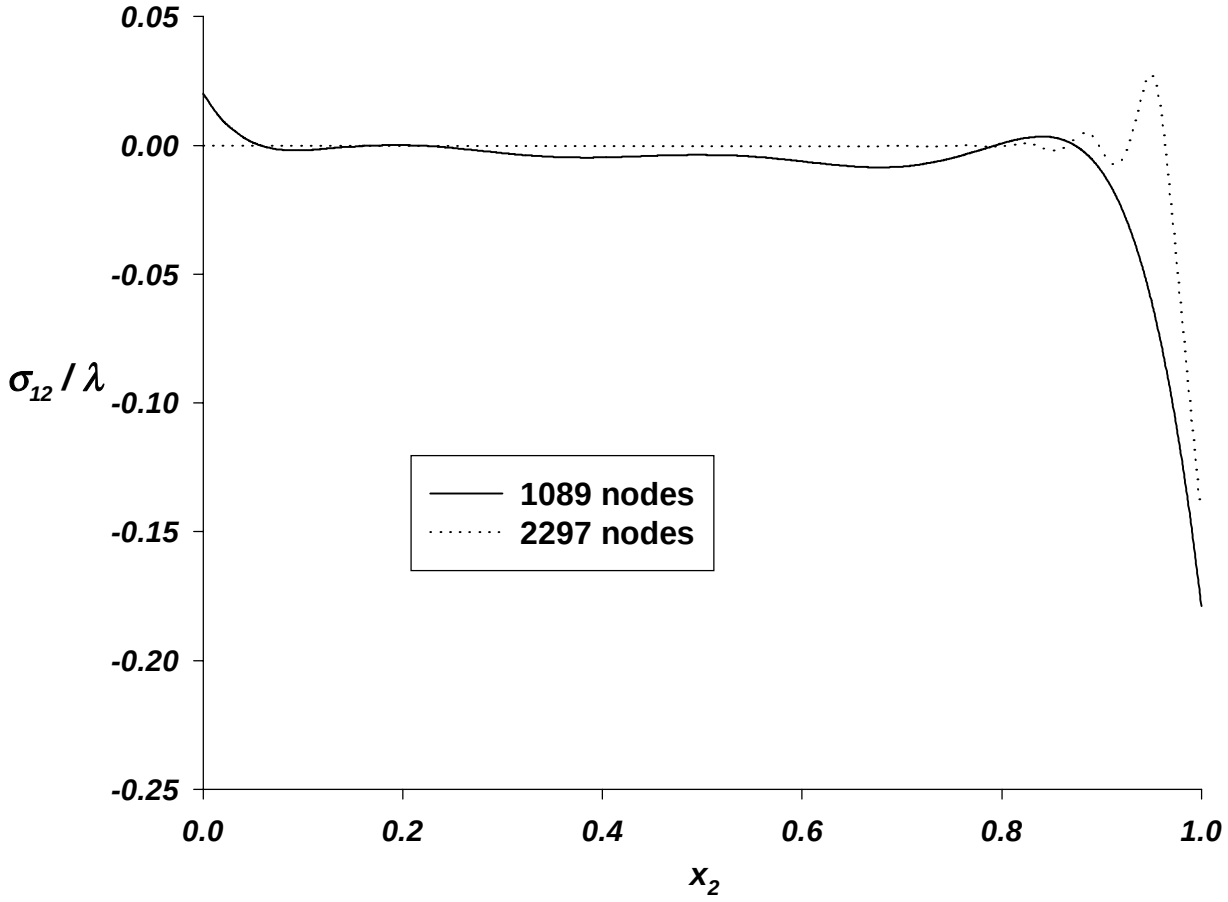

Fig. 3.6b Comparsion of through-the-thickness distribution of the normalized shear stress σ_{12} on the left edge computed with two nodal meshes

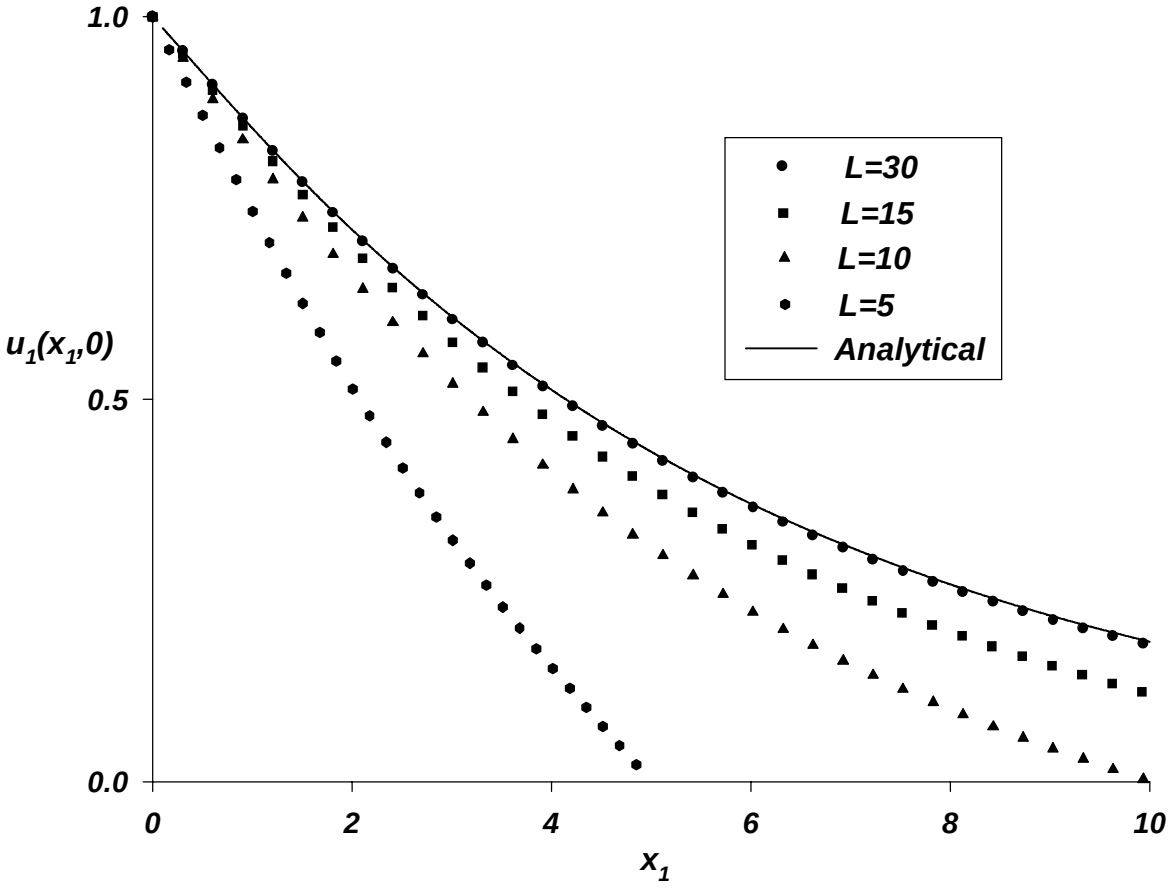

Fig. 3.7 Variation of the axial displacement u_1 on the centerline for four lengths of the domain

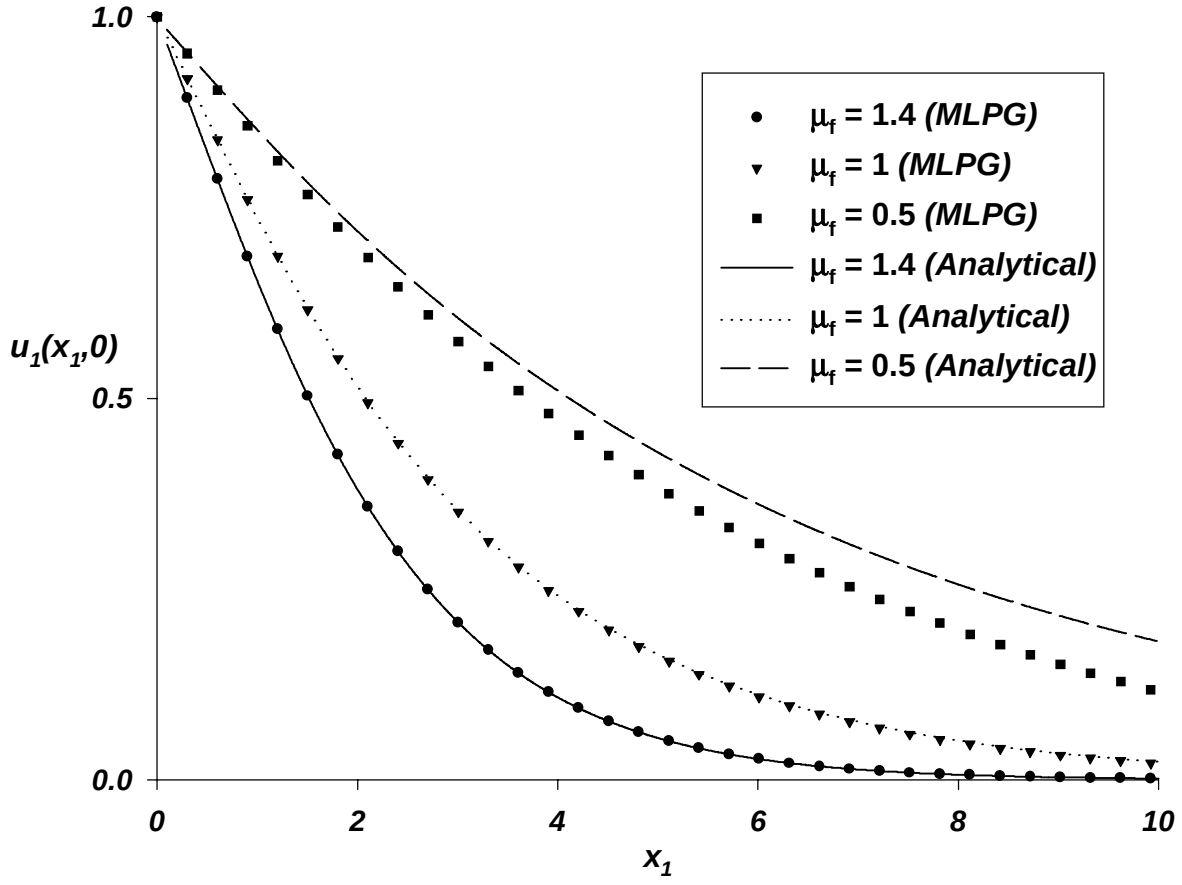

Fig. 3.8a Variation of the axial displacement u_1 on the centerline for three values of the coefficient of friction

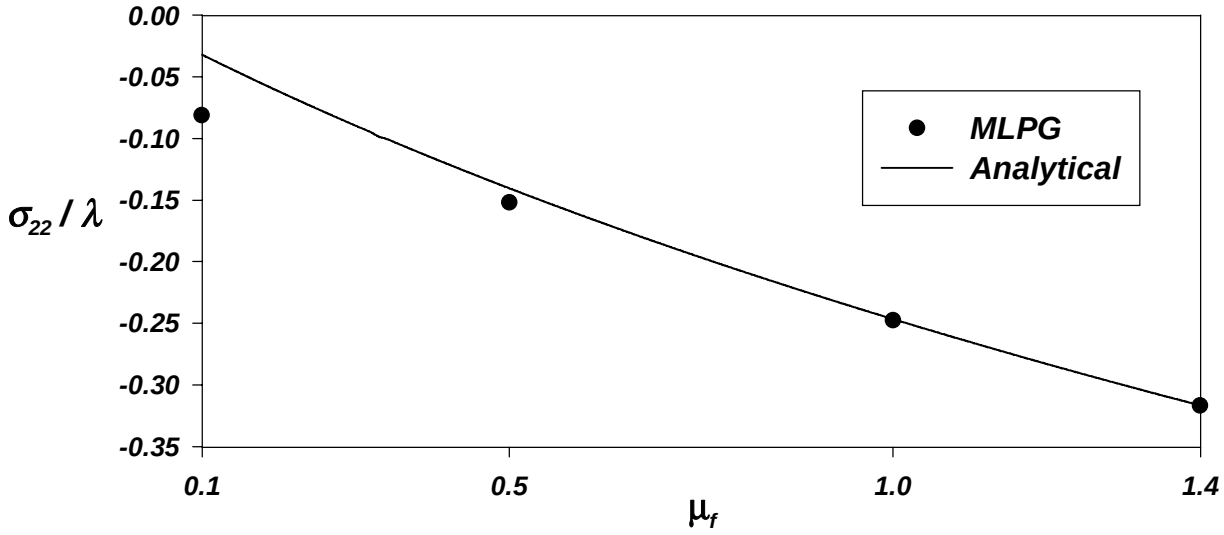

Fig. 3.8b Variation with the friction coefficient μ_f of the normalized transverse normal stress at the point (1, 0.99) on the top wall

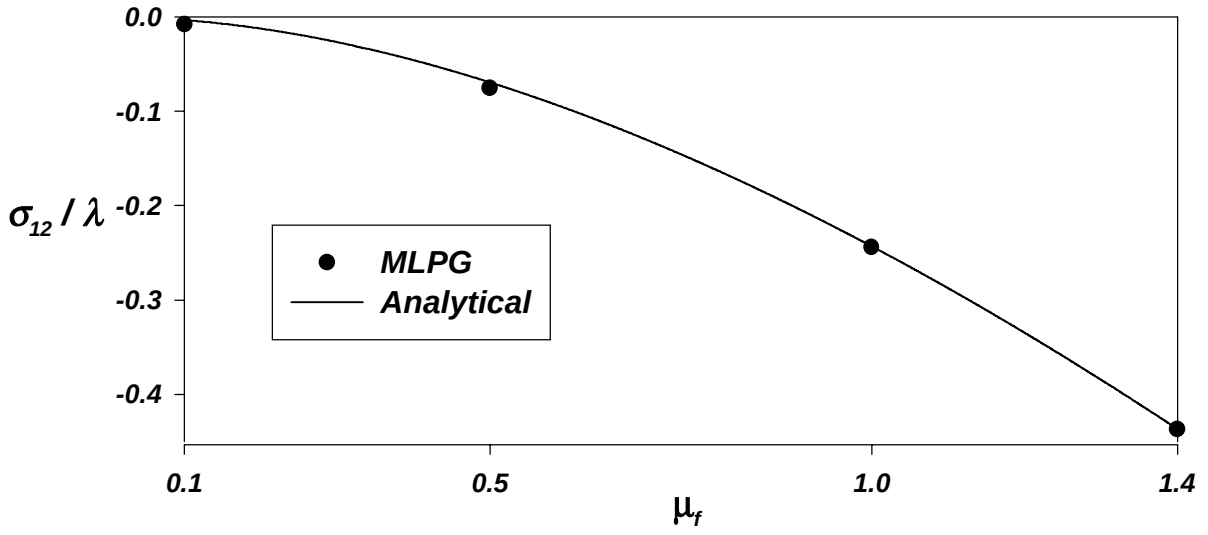

Fig. 3.8c Variation with the friction coefficient μ_f of the normalized shear stress at the point (1, 0.99) on the top wall

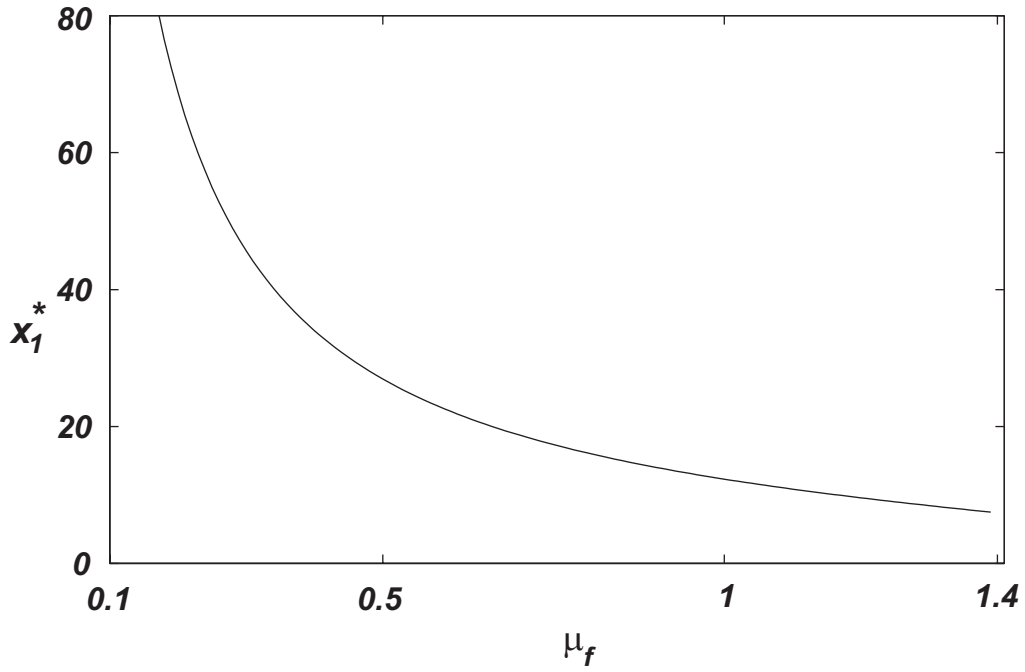

Fig. 3.9 Value of x_1^* at which $u_1(x_1^*, 0) = 0.01 u_1(0,0)$ versus μ_f

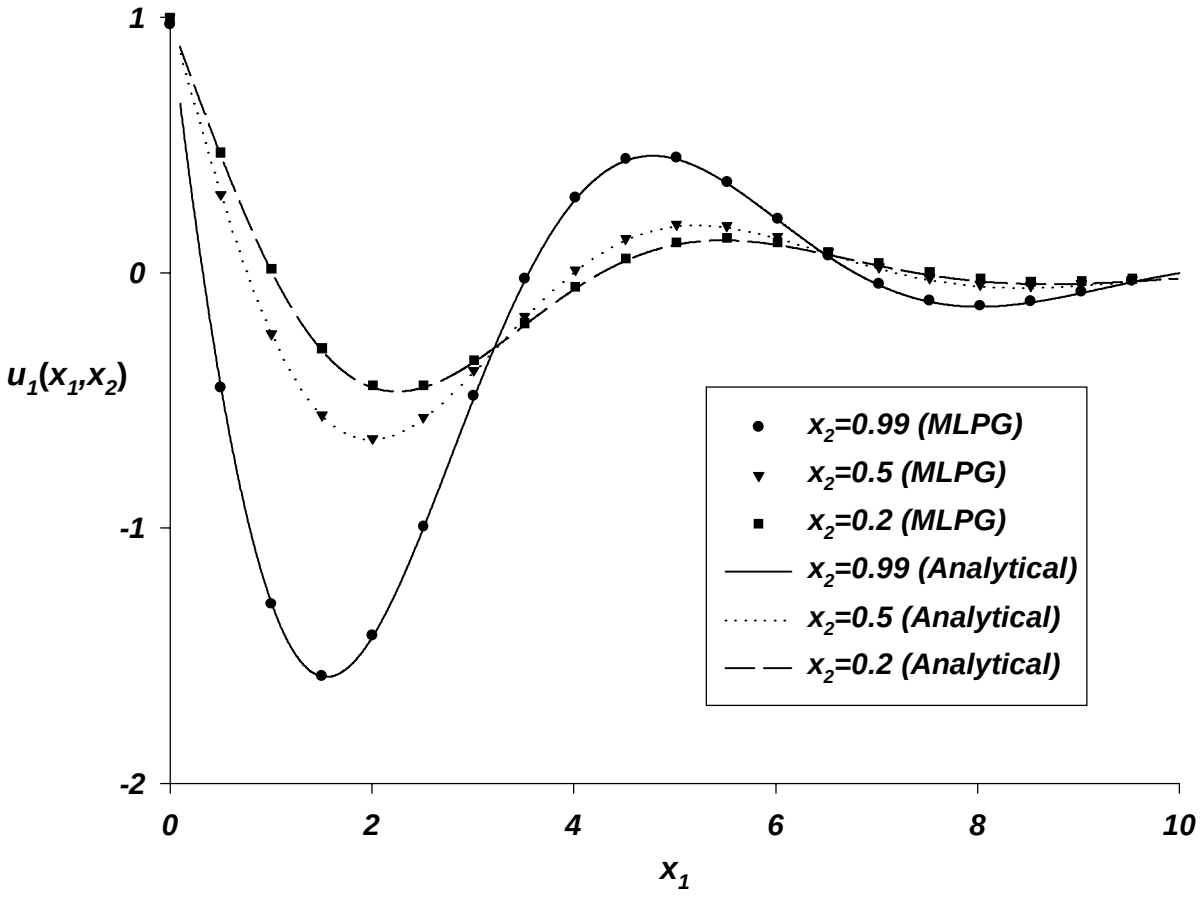

Fig. 3.10a For the friction coefficient = 5, variation of the axial displacement u_1 on three horizontal planes

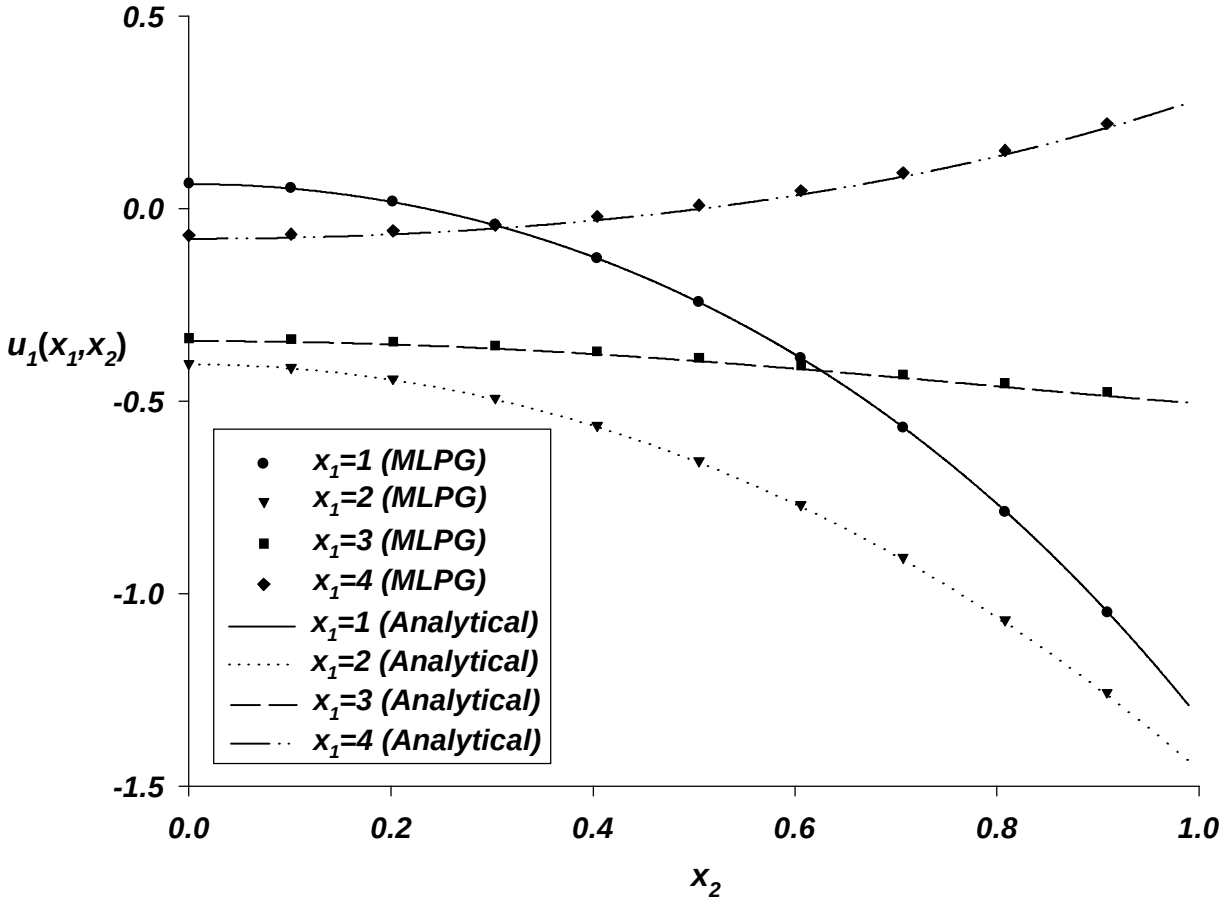

Fig. 3.10b For the friction coefficient = 5, variation of the axial displacement u_1 on four vertical planes

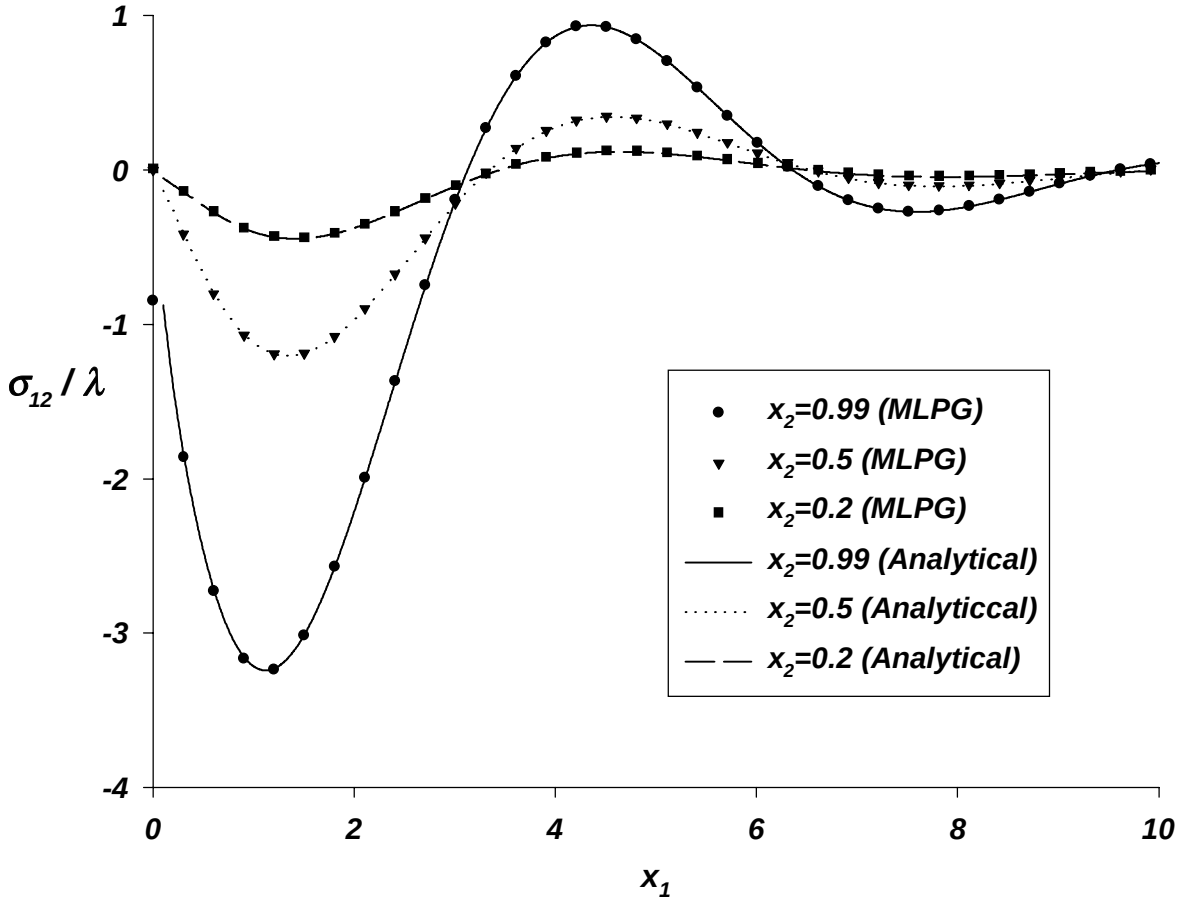

Fig. 3.10c For the friction coefficient = 5, variation of the normalized shear stress on three horizontal planes

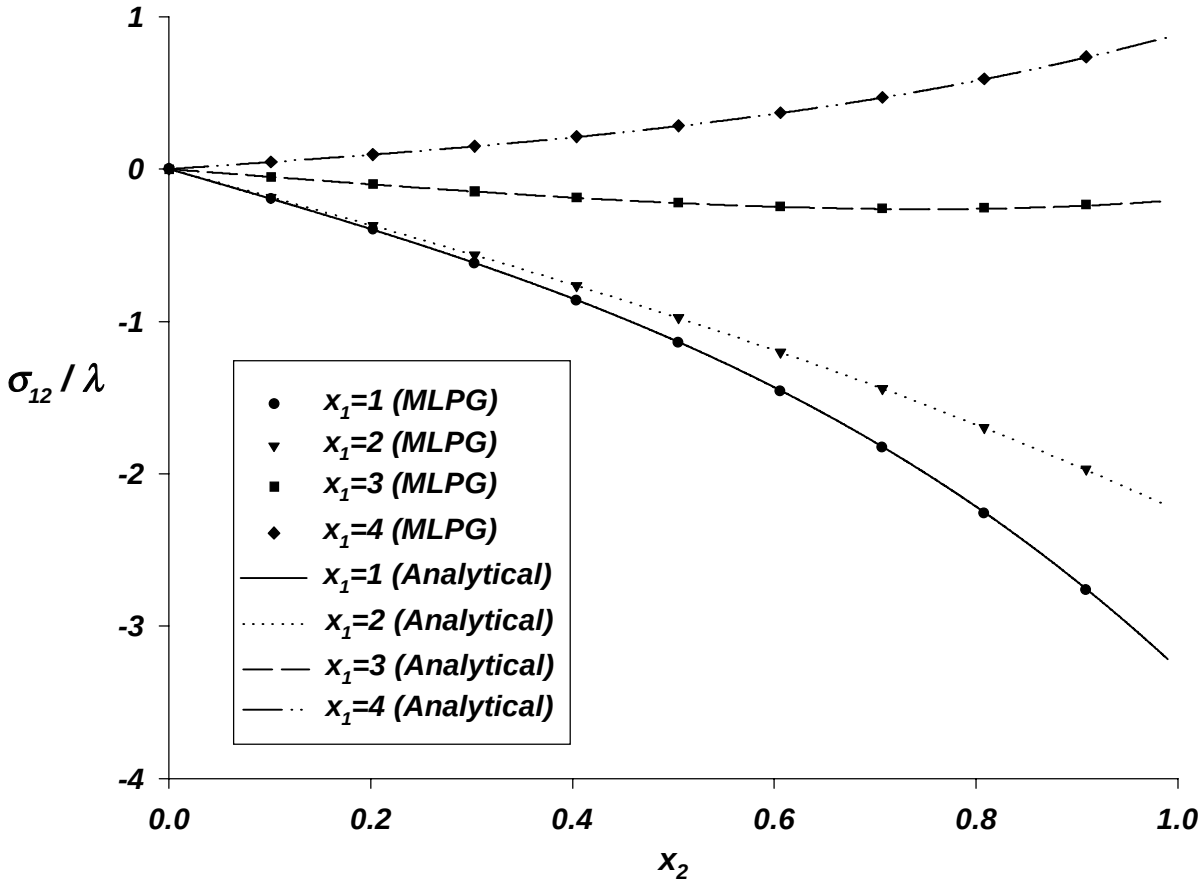

Fig. 3.10d For the friction coefficient = 5, variation of the normalized shear stress on four vertical planes

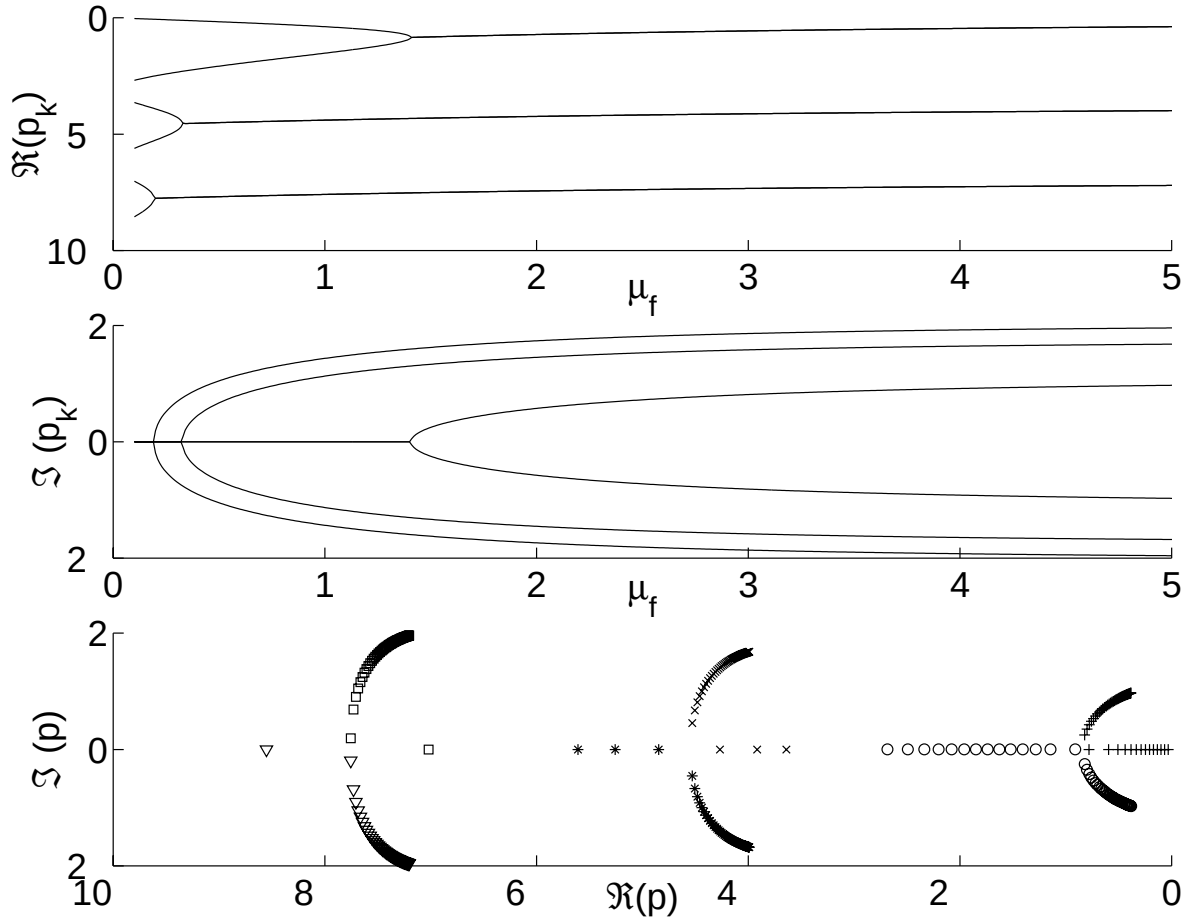

Fig. 3.11 Dependence of the pole location on μ_f

Chapter 4

Analysis of Elastodynamic Deformations near a Crack/Notch Tip by the Meshless Local Petrov-Galerkin (MLPG) Method

Abstract

The Meshless Local Petrov-Galerkin (MLPG) method is utilized to analyze transient deformations of either the crack or notch tip in an elastic plate. The local weak formulation is derived from the dynamic partial differential equation. The Newmark family of methods is used for the time integration scheme. The validity and accuracy of the present MLPG solution are illustrated by the 1D wave propagation of the rod. Two numerical examples, namely, a rectangular plate with a central crack with plate edges parallel to the crack axis loaded in tension and a double edge-notched plate with the edge between the notches loaded by compressive tractions, are solved for the elastodynamic deformations of the crack/notch tip. The MLPG results show that the stresses near the crack/notch tip agree well with those obtained from the analytical or the finite element solution, and the index of stress singularity can be ascertained by the present method. Time histories of the Mode I and Mode II dynamic stress intensity factors (DSIF) are determined from the computed stress fields.

Key Words: Singular fields; Dynamic stress intensity factors; Mixed-mode deformations; Edge-cracked plates; Edge-notched plates.

A slightly modified version of this chapter will appear in the *Computer Modeling in Engineering & Sciences*.

4.1 Introduction

The meshless method has attracted considerable attention in the past two decades due to the flexibility of locating nodes. Atluri and Zhu (1998) proposed a meshless method which requires no background mesh to integrate the weak formulation. Atluri et al. (1999) have pointed out that the Galerkin approximation can also be adopted that leads to a symmetric stiffness matrix. Atluri and Zhu (2000) solved elastostatic problems by the MLPG method, and Lin and Atluri (2000) introduced upwinding schemes to analyze steady convection-diffusion problems. Ching and Batra (2001) enriched the polynomial basis functions with those appropriate to describe singular deformation fields near a crack tip and used the diffraction criterion to find stress intensity factors, the *J*-integrals and singular stress fields near a crack tip. Gu and Liu (2001) used the Newmark family of methods to study forced vibrations of a beam. The problem of bending of a thin plate has been studied by Long and Atluri (2002). Warlock et al. (2002) have analyzed elastostatic deformations of a material compressed in a rough rectangular cavity analytically by the Laplace transformation technique and numerically by the MLPG method.

In this chapter, the application of the MLPG method to infinitesimal elastodynamic deformations is described. Section 2 gives the MLPG formulation including the local weak form, the moving least squares approximation, the discrete governing equations and the time integration scheme. Calculations of the dynamic stress intensity factors from the near-tip stress fields are also described. Numerical examples and discussion are presented in Section 3. The MLPG results are compared to either analytical or finite element solutions. The chapter ends with conclusions in Section 4.

4.2 Formulation of the Problem

4.2.1 Governing equations

For a linear elastodynamic problem on domain Ω bounded by the boundary Γ, governing equations are

$$\sigma_{ij,j} + b_i = \rho \ddot{u}_i, \ \text{in}\,\Omega, \ (i,j=1,2,3), \tag{4.1}$$

$$\sigma_{ij} = \lambda \varepsilon_{kk} \delta_{ij} + 2\mu \varepsilon_{ij}, \ \text{in}\,\Omega, \tag{4.2}$$

$$\varepsilon_{ij} = (u_{i,j} + u_{j,i})/2, \ \text{in}\,\Omega. \tag{4.3}$$

Here ρ is the mass density, $\ddot{u}_i = \partial^2 u_i / \partial t^2$ the acceleration, u_i the displacement, t the time, σ_{ij} the stress tensor, ε_{ij} the infinitesimal strain tensor, b_i the body force vector, λ and μ are Lame′ constants for material of the body, and a comma followed by the index j denotes partial differentiation with respect to x_j. Equations (4.1)-(4.3) are supplemented with the following initial and boundary conditions:

$$\mathbf{u}(\mathbf{x}, t_0) = \mathbf{u}_0(\mathbf{x}), \quad \mathbf{x} \in \Omega, \tag{4.4a}$$

$$\dot{\mathbf{u}}(\mathbf{x}, t_0) = \mathbf{v}_0(\mathbf{x}), \quad \mathbf{x} \in \Omega, \tag{4.4b}$$

$$u_i = \bar{u}_i, \ \text{on}\,\Gamma_u, \tag{4.4c}$$

$$t_i \equiv \sigma_{ij} n_j = \bar{t}_i, \ \text{on}\,\Gamma_t, \tag{4.4d}$$

where $\bar{u}_i$, $\bar{t}_i$, $\mathbf{u}_0$ and $\mathbf{v}_0$ denote the prescribed displacements, tractions, initial displacements and initial velocities, respectively, n_j is the unit outward normal to Γ, and Γ_u and Γ_t are complementary parts of Γ where essential and natural boundary conditions are prescribed.

4.2.2 Implementation of the MLPG method

Taking the inner product of Eq. (4.1) with **v** and of (4.4c) with $\alpha\mathbf{v}$, and integrating the resulting equations over Ω_s and Γ_{su} respectively, we obtain

$$\int_{\Omega_s}(\sigma_{ij,j}-\rho\ddot{u}_i+b_i)v_i d\Omega-\alpha\int_{\Gamma_{su}}(u_i-\bar{u}_i)v_i d\Gamma=0, \tag{4.5}$$

where $\Gamma_{su}=\Gamma_s\bigcap\Gamma_u$, Γ_s is the boundary of the local domain Ω_s and α is a penalty parameter used to satisfy the essential boundary conditions.

The first term on the left side of Eq. (4.5) is integrated by parts, and natural boundary condition (4.4d) is used. The result is

$$\begin{aligned}\int_{\Omega_s}\rho v_i\ddot{u}_i d\Omega+\int_{\Omega_s}v_{i,j}\sigma_{ij}d\Omega+\alpha\int_{\Gamma_{su}}v_i u_i d\Gamma-\int_{\Gamma_{su}}v_i t_i d\Gamma\\ =\int_{\Gamma_{st}}v_i\bar{t}_i d\Gamma+\alpha\int_{\Gamma_{su}}v_i\bar{u}_i d\Gamma+\int_{\Omega_s}v_i b_i d\Omega,\end{aligned} \tag{4.6}$$

where $\Gamma_{st}=\Gamma_s\bigcap\Gamma_t$, and v_i is taken to vanish on $\partial\Omega_s-\Gamma_{su}-\Gamma_{st}$.

In the MLPG method, the displacement is approximated by the moving least squares method (MLS). Details about the MLS approximation can be found in the paper by Lancaster and Salkauskas (1981). For the sake of completeness, the MLS approximation is briefly described here. We consider the trial function $\mathbf{u}^h(\mathbf{x},t)$ over the domain Ω defined by

$$u_k^h(\mathbf{x},t)=\sum_j^m p_j(\mathbf{x})a_{jk}(\mathbf{x},t)\equiv\mathbf{p}^T(\mathbf{x})\mathbf{a}(\mathbf{x},t), \tag{4.7}$$

where $\mathbf{a}(\mathbf{x},t)$ are the unknown coefficients and are functions of the space coordinates $\mathbf{x}^T=[x^1,x^2]$ and time *t*, and $\mathbf{p}(\mathbf{x})$ is a complete monomial basis functions of degree m. The quadratic basis functions in two-dimensions are

$$\mathbf{p}^T(\mathbf{x}) = [1, x^1, x^2, (x^1)^2, x^1x^2, (x^2)^2]; \quad m = 6. \tag{4.8}$$

For each component of **u**, the coefficients $\mathbf{a}(\mathbf{x},t)$ in Eq. (4.7) are obtained by minimizing the following:

$$J = \sum_{i=1}^{n} w(\mathbf{x}-\mathbf{x}_i)[\mathbf{p}^T(\mathbf{x}_i)\mathbf{a}(\mathbf{x},t) - \hat{u}_i(t)]^2. \tag{4.9}$$

Here $\hat{u}_i$ is the fictitious value of a component of $\mathbf{u}^h$ at $\mathbf{x} = \mathbf{x}_i$, and n is the number of nodes in the domain of influence of $\mathbf{x}$ for which the weight functions $w(\mathbf{x}-\mathbf{x}_i) \neq 0$. Several different weight functions can be found in Atluri and Shen (2002); in this paper, the Gaussian weight function is chosen.

The support of $w(\mathbf{x}-\mathbf{x}_i)$ is also called the domain of influence of node *i*, since node *i* affects the approximation within this domain but not outside this domain. The domain of influence is usually a circle, but it does not extend outside of the boundary of domain Ω. The effect of a crack is represented by changes in the domains of influence of the nodes surrounding the crack. Diffraction criterion proposed by Organ et al. (1996) has been used by Ching and Batra (2001) to account for changes in the domain of influence caused by discontinuous fields across a crack.

The stationary value of J in Eq. (4.9) with respect to $\mathbf{a}(\mathbf{x},t)$ leads to

$$\mathbf{a}(\mathbf{x},t) = \mathbf{A}^{-1}(\mathbf{x})\mathbf{B}(\mathbf{x})\hat{\mathbf{u}}(t), \tag{4.10}$$

with matrices $\mathbf{A}(\mathbf{x})$ and $\mathbf{B}(\mathbf{x})$ defined by

$$\mathbf{A}(\mathbf{x}) = \sum_{i=1}^{n} w(\mathbf{x}-\mathbf{x}_i)\mathbf{p}(\mathbf{x}_i)\mathbf{p}^T(\mathbf{x}_i), \tag{4.11a}$$

$$\mathbf{B}(\mathbf{x}) = [w(\mathbf{x}-\mathbf{x}_1)\mathbf{p}(\mathbf{x}_1), w(\mathbf{x}-\mathbf{x}_2)\mathbf{p}(\mathbf{x}_2), ..., w(\mathbf{x}-\mathbf{x}_n)\mathbf{p}(\mathbf{x}_n)]. \tag{4.11b}$$

By substituting from Eq. (4.10) into Eq. (4.7), we obtain the MLS approximants as

$$u^h(\mathbf{x},t)=\sum_{i=1}^{n}\sum_{j=1}^{m}p_j(\mathbf{x})[\mathbf{A}^{-1}(\mathbf{x})\mathbf{B}(\mathbf{x})]_{ji}\,\hat{u}_i(t)=\sum_{i=1}^{n}\phi_i(\mathbf{x})\,\hat{u}_i(t). \tag{4.12}$$

$\phi_i(\mathbf{x})$ is usually called the MLS shape function corresponding to node *i*. Substituting Eq. (4.12) into the local weak form (4.6) for each node and summing over all nodes give the following discrete equations:

$$\mathbf{M}\ddot{\hat{\mathbf{u}}}(t)+\mathbf{K}\hat{\mathbf{u}}(t)=\mathbf{f}(t), \tag{4.13}$$

where the "mass" matrix $\mathbf{M}$, the "stiffness" matrix $\mathbf{K}$ and the "load" vector $\mathbf{f}$ are given by

$$\mathbf{M}_{ij}=\int_{\Omega_s}\rho\phi_j\mathbf{v}(\mathbf{x},\mathbf{x}_i)d\Omega, \tag{4.14a}$$

$$\begin{aligned}\mathbf{K}_{ij}=&\int_{\Omega_s}\varepsilon_v(\mathbf{x},\mathbf{x}_i)\mathbf{D}\mathbf{B}_j d\Omega+\alpha\int_{\Gamma_{su}}\mathbf{v}(\mathbf{x},\mathbf{x}_i)\mathbf{S}\phi_j d\Gamma\\&-\int_{\Gamma_{su}}\mathbf{v}(\mathbf{x},\mathbf{x}_i)\mathbf{N}\mathbf{D}\mathbf{B}_j\mathbf{S}d\Gamma,\end{aligned} \tag{4.14b}$$

$$\mathbf{f}_i=\int_{\Gamma_{st}}\mathbf{v}(\mathbf{x},\mathbf{x}_i)\bar{\mathbf{t}}d\Gamma+\alpha\int_{\Gamma_{su}}\mathbf{v}(\mathbf{x},\mathbf{x}_i)\mathbf{S}\bar{\mathbf{u}}d\Gamma+\int_{\Omega_s}\mathbf{v}(\mathbf{x},\mathbf{x}_i)\mathbf{b}d\Omega. \tag{4.14c}$$

The matrices ε_v, $\mathbf{B}_j$, $\mathbf{S}$, $\mathbf{N}$ in the above equations are defined in Chapter 1. Note that the "mass" matrix is not symmetric. We diagonalize it by the row-sum technique to obtain

$$\begin{aligned}&\mathbf{M}_{ii}=\sum_{j=1}^{n}\int_{\Omega_s}\rho\phi_j\mathbf{v}(\mathbf{x},\mathbf{x}_i)d\Omega, \qquad \text{(no sum on } i\text{)},\\&\mathbf{M}_{ij}=0, \quad i\neq j.\end{aligned} \tag{4.15}$$

Initial values of $\hat{\mathbf{u}}_i$ and $\dot{\hat{\mathbf{u}}}_i$ are derived from Eqs. (4.4a) and (4.4b) as follows. The function $\mathbf{u}(\mathbf{x},t_0)$ is replaced by $\mathbf{u}^h(\mathbf{x},t_0)$, the inner product of both sides is taken with the function $\mathbf{v}(\mathbf{x},\mathbf{x}_i)$, and the resulting equations are integrated over the local domain Ω_s. The result is

$$\mathbf{M}_{ij}\hat{\mathbf{u}}_j(0) = \mathbf{F}_i^0, \tag{4.16a}$$

$$\mathbf{M}_{ij}\dot{\hat{\mathbf{u}}}_j(0) = \mathbf{G}_i^0, \tag{4.16b}$$

where

$$\mathbf{F}_i^0 = \int_{\Omega_s} \mathbf{u}_0(\mathbf{x})\mathbf{v}(\mathbf{x},\mathbf{x}_i)\phi_j(\mathbf{x})d\Omega, \tag{4.17a}$$

$$\mathbf{G}_i^0 = \int_{\Omega_s} \mathbf{v}_0(\mathbf{x})\mathbf{v}(\mathbf{x},\mathbf{x}_i)\phi_j(\mathbf{x})d\Omega. \tag{4.17b}$$

For null initial conditions, i.e., $\mathbf{u}_0 = \mathbf{0}$ and $\mathbf{v}_0 = \mathbf{0}$, Eqs. (4.16a) and (4.16b) give $\hat{\mathbf{u}}(0) = \mathbf{0}$, $\dot{\hat{\mathbf{u}}}(0) = \mathbf{0}$.

4.2.3 The time integration scheme

We use the Newmark family of methods to integrate equation (4.13). The recursive relations for displacements and velocities at times t_n and t_{n+1} are

$$\hat{\mathbf{u}}_{n+1} = \hat{\mathbf{u}}_n + \Delta t\dot{\hat{\mathbf{u}}}_n + \frac{(\Delta t)^2}{2}\left\{(1-2\beta)\ddot{\hat{\mathbf{u}}}_n + 2\beta\ddot{\hat{\mathbf{u}}}_{n+1}\right\}, \tag{4.18}$$

$$\dot{\hat{\mathbf{u}}}_{n+1} = \dot{\hat{\mathbf{u}}}_n + \Delta t\left\{(1-\gamma)\ddot{\hat{\mathbf{u}}}_n + \gamma\ddot{\hat{\mathbf{u}}}_{n+1}\right\}, \tag{4.19}$$

where $\hat{\mathbf{u}}_n, \dot{\hat{\mathbf{u}}}_n,$ and $\ddot{\hat{\mathbf{u}}}_n$ denote the displacements, velocities and accelerations, respectively, at time $t_n = n\Delta t$ and Δt is the uniform time interval between two time steps. β and γ are the parameters which control the stability and the accuracy of the time integration scheme. Values of β and γ for different methods are listed below:

$$\gamma = \frac{1}{2},\ \beta = \frac{1}{6}, \quad \text{Linear Acceleration Method;} \tag{4.20a}$$

$$\gamma = \frac{1}{2},\ \beta = \frac{1}{4}, \quad \text{Constant Average Acceleration Method;} \tag{4.20b}$$

$$\gamma = \frac{3}{2},\ \beta = \frac{4}{5}, \quad \text{Galerkin Method;} \tag{4.20c}$$

$$\gamma = \frac{3}{2},\ \beta = 1, \quad \text{Backward Difference Method.} \tag{4.20d}$$

The Newmark family of methods is unconditionally stable if

$$\gamma \geq \frac{1}{2} \quad \text{and} \quad \beta \geq \frac{1}{4}(\frac{1}{2}+\gamma). \tag{4.21}$$

Thus the linear acceleration method is conditionally stable and the other three methods are unconditionally stable. The methods are second-order accurate and nondissipative for $\gamma = \frac{1}{2}$ and first-order accurate and dissipative for $\gamma \neq \frac{1}{2}$.

Writing Eq. (4.13) at time $t_{n+1} = (n+1)\Delta t,$ and substituting from (4.18) and (4.19) into (4.13) yield the following system of equations:

$$\hat{\mathbf{K}}_{n+1}\hat{\mathbf{u}}_{n+1} = \hat{\mathbf{F}}_{n+1}, \tag{4.22}$$

where

$$\hat{\mathbf{K}}_{n+1} = \mathbf{K}_{n+1} + a_1\mathbf{M}_{n+1}, \tag{4.23a}$$

$$\hat{\mathbf{F}}_{n+1} = \mathbf{f}_{n+1} + \mathbf{M}_{n+1}\left\{a_1\hat{\mathbf{u}}_n + a_2\dot{\hat{\mathbf{u}}}_n + a_3\ddot{\hat{\mathbf{u}}}_n\right\}, \tag{4.23b}$$

$$a_1 = \frac{1}{\beta(\Delta t)^2}, \quad a_2 = \frac{1}{\beta\Delta t}, \qquad a_3 = \frac{1}{2\beta} - 1. \tag{4.23c}$$

Once $\hat{\mathbf{u}}_{n+1}$ has been computed from Eq. (4.20), $\ddot{\hat{\mathbf{u}}}_{n+1}$ and $\dot{\hat{\mathbf{u}}}_{n+1}$ can be obtained from

$$\ddot{\hat{\mathbf{u}}}_{n+1} = a_1\left\{\hat{\mathbf{u}}_{n+1} - \hat{\mathbf{u}}_n\right\} - a_2\dot{\hat{\mathbf{u}}}_n - a_3\ddot{\hat{\mathbf{u}}}_n, \tag{4.24a}$$

$$\dot{\hat{\mathbf{u}}}_{n+1} = \dot{\hat{\mathbf{u}}}_n + (1-\gamma)\Delta t\ddot{\hat{\mathbf{u}}}_n + \gamma\Delta t\ddot{\hat{\mathbf{u}}}_{n+1}. \tag{4.24b}$$

4.2.4 Determination of the stress intensity factors

It has been shown by Ching and Batra (2001) that the stress intensity factors in linear elastic fracture mechanics can be determined from the plots on logarithmic scales of stresses computed from the MLPG solution versus distance from the crack tip. We determine here the

dynamic stress intensity factors based on the near-tip stress fields. For elastodynamic deformations of a body containing a stationary crack, the mode-I and the mode-II stress intensity factors can be determined from $K_I = \sqrt{2\pi r}\sigma_{22}(r,0,t)$ and $K_{II} = \sqrt{2\pi r}\sigma_{12}(r,0,t)$ (Miannay, 2001) where r is the distance straight ahead of the crack tip and should be taken within the singular-deformations dominated zone. In the computations, the distance r is taken within 2% of the crack length. At each time step, we plotted $\ln|\sigma_{22}(r,0,t)|$ vs. $\ln r$ and $\ln|\sigma_{12}(r,0,t)|$ vs. $\ln r$, fitted straight lines through the data by the least squares method, and computed K_I and K_{II} from the intercepts of these lines with the ordinates. Theoretically, the slope (index of r) of each line should equal $-1/2$, signifying the $1/\sqrt{r}$ singularity of the stress fields near the crack tip.

4.3 Computation and Discussion of Results

4.3.1 One dimensional wave propagation

We have developed a computer code in Fortran based on the aforestated equations. To demonstrate the validity and accuracy of the code, the problem of wave propagation in a rod is studied first. Wave propagation in the rod is modeled as a one-dimensional problem.

The problem studied is sketched in Fig. 4.1, and governing equations are

$$EA\frac{\partial^2 u}{\partial x^2} = \rho A\frac{\partial^2 u}{\partial t^2}, \qquad 0 < x < L\ ;\ 0 < t < \infty, \tag{4.25}$$

$$EA\frac{\partial u}{\partial x}(0,t) = -Ap(t),\ u(L,t) = 0, \tag{4.26a,b}$$

$$u(x,0) = 0, \qquad \frac{\partial u}{\partial t}(x,0) = 0, \tag{4.26c,d}$$

where L denotes the length of the rod, E the Young's modulus, ρ and A the mass density and the cross section of the rod, respectively, and $p(t)$ the applied pressure. An analytical solution of equations (4.25) and (4.26) is

$$u(x,t)=\frac{8pL}{E\pi^2}\left[\sum_{n=0}^{\infty}\frac{1}{(2n+1)^2}\cos\frac{(n+\frac{1}{2})\pi ct}{L}\cos\frac{(n+\frac{1}{2})\pi x}{L}\right]+\frac{p}{E}x-\frac{pL}{E}, \tag{4.27}$$

where $c=\sqrt{E/\rho}$ is the wave speed.

When solving the problem by the MLPG method, we took $L=20in$, $E=30\times10^6\ psi$, $\rho=7.4\times10^{-4}\ lb\sec^2/in^4$, $A=1in^2$, and $p(t)=100H(t)psi$ where $H(t)$ is the Heaviside step function. The bar was divided into 41 equally spaced nodes. Unless otherwise specified, the penalty parameter is taken to be $\alpha=10^9\ lb/in^3$, and the time step $\Delta t=1\mu s$. All entries in the lumped mass matrix obtained from Eq. (4.15) were found to be positive.

Figure 4.2 shows the comparison with the analytical solution of the time histories of the axial stress at the midpoint ($x=L/2$) computed with different time integration schemes. The analytical value of the wave speed for the assumed material properties is $c=\sqrt{E/\rho}=0.20135in/\mu s$. It is clear that according to each one of the four integration methods, the wave arrives at the midpoint prior to the theoretical value of $49.66\mu s$. This is to be expected because of the coupling among motions of different nodes induced by the stiffness matrix. Here a diagonal mass matrix is used; otherwise the mass matrix will also couple the motion of different nodes. The average acceleration and the linear acceleration methods predict identical values of the axial stress, and the same is true for the Galerkin and the backward difference methods. Values of $\gamma>1/2$ introduce damping into the computed solution; this is evident from the absence of oscillations in the solutions obtained with the Galerkin and the backward difference methods for which $\gamma=3/2$. Each integration scheme correctly predicts doubling of the axial compressive stress when the wave reflected from the clamped end

$(x = L)$ arrives at the midpoint. In order to see if decreasing the time step size will improve the accuracy of the computed results, we have plotted in Fig. 4.3 time histories of the axial stress at the midpoint obtained by taking $\Delta t = 0.4\mu s$ and $1.0\mu s$ and the backward difference method. These results indicate that, at least for the backward difference method, $\Delta t = 1\mu s$ is adequate. Figure 4.4 depicts time histories of the axial stress at four locations along the length of the bar. The computed stress wave seems to travel a little faster as it approaches the fixed end of the bar. In Fig. 4.5 we have compared at two locations time histories of the axial velocity obtained from the analytical solution with those computed with the backward difference method. The computed velocity time histories exhibit oscillations of smaller amplitude than the stress histories. At $x = 0.25L$, oscillations die out and the computed axial velocity matches with the analytical value. It was found that the essential boundary condition prescribed at $x = L$ was very well satisfied. Time histories of the axial stress at $x = L/2$ computed with the lumped and the consistent mass matrices are compared in Fig. 4.6. In each case, the backward difference scheme is used to integrate the governing equations. It is clear that two computed time histories coincide with each other. In Fig. 4.7, we have plotted the evolution of the axial stress at $x = L/2$ computed with two uniform arrangements of nodes. In each case, the lumped mass matrix and the backward difference scheme were used. The close agreement between two sets of results suggests that the nodal mesh of 41 nodes uniformly placed nodes is adequate.

4.3.2 Rectangular plate with a central crack loaded in tension

We now analyze deformations of a rectangular plate with a centrally located crack, shown in Fig. 4.8, and loaded by axial tensile tractions applied at the top and the bottom surfaces. We set $\bar{t} = 0.4H(t)Gpa,\ L = 52mm,\ D = 20mm,\ a = 12mm,\ \mu = 29.4Gpa,\ \rho = 2450\ Kg/m^3$, and $\nu = 0.286$. A plane strain state of deformation is assumed to prevail in the plate. Due to the symmetry of the problem about the two centroidal axes, only a quadrant of the plate is modeled and discretized using 2534 nodes (see Fig. 4.9a) with a fine nodal mesh

around the crack tip (cf. Fig. 4.9b). We use the backward difference method with $\Delta t = 4\times 10^{-2}\,\mu s$ and compute results till $t = 20\mu s$.

Figure 4.10 displays, at three different instants of time, the deformed crack surface obtained by both the MLPG and the finite element (FE) methods. In computing the FE solution with ABAQUS the same nodal mesh as that in the MLPG method is employed. The two sets of computed results agree well with each other. It is worth pointing out that the material point located at the crack tip moves horizontal first to the right and then to the left while the upper and the lower boundaries are being pulled axially by the tensile tractions. The time history of the stress intensity factor $K_I(t)$ normalized by $\bar{t}\sqrt{\pi a}$ is shown in Fig. 4.11. The MLPG solution is compared with the analytical solution of Baker (1962) for an infinite plate, the singular finite element solution of Nishioka and Atluri (1980) and the dual boundary element solution of Fedelinski et al. (1994) for a finite plate identical to the one studied here. The stress intensity factor K_I remains zero until the dilatational wave reaches the crack tip at approximately $t = 2.5\mu s$. K_I attains the maximum value at $t = 11\mu s$ and decreases subsequently. It can be seen that there is a good agreement between the present numerical result and the available solutions. The time history of the order of singularity of the stress field near the crack tip is found to equal –0.48 which is close to the analytical value of –0.5. Figures 4.12-14 exhibit contours of the maximum principal stress normalized by $\bar{t}$ around the crack tip at $t = 6,\ 13,\ 20\mu s$ for both the MLPG and the FE solutions. The two sets of solutions agree well with each other. At $t = 13\mu s$, the maximum principal stress at the crack tip equals $45\bar{t}$.

4.3.3 Double edge-notched plate with the edge between the notches loaded in compression

Kalthoff and Winkler (1987) proposed an experiment to study transient mode-II dominated deformations. It involves a double edge-notched plate with the edge between the two notches impacted by a fast moving cylindrical projectile of diameter equal to the distance

between the notches. Here, we use the MLPG method to simulate this problem and approximate the action of the impactor by applying uniformly distributed compressive tractions on the impacted surface. Figure 4.15 shows a schematic sketch of the problem studied. We assume that a plane strain state of deformation prevails in the plate, and take Young's modulus $E = 210GPa$, Poisson's ratio $\nu = 0.29,$ mass density $\rho = 7833kg/m^3,$ the radius of the circular notch tip = $0.15mm$, the applied normal traction $\bar{t} = 200H(t)MPa,$ and tangential traction on the impacted surface = 0. Because of the symmetry of the problem about the horizontal centroidal plane, deformations of only the upper half of the plate are analyzed. Figure 4.16 exhibits the nonuniform nodal mesh of 3632 nodes with 25 nodes on the surface of the circular notch tip. The diffraction criterion is used to account for the discontinuous deformation fields across the notch surface. Coupled ordinary differential equations obtained from the local symmetric weak formulation of the governing partial differential equations are integrated by the backward difference method. We take time step $\Delta t = 0.0625\mu s$ in order to obtain accurate results. The two approximate solutions obtained by the MLPG and the FE methods are compared; the code ABAQUS was used to compute the FE solution. The same nodal mesh was used in the two analyses.

Figure 4.17 displays the undeformed and the deformed shapes of the notch tip. Due to the compressive tractions applied on the edge between the two notches, the notch faces move upwards. It is clear that the two sets of results agree well with each other. The time histories of normal stresses σ_{11} and σ_{22} at the notch tip are plotted in Fig. 4.18. The dilatational wave arrives at the notch tip at about $7\mu s.$ Soon after the arrival of the wave, stresses at the notch tip increase with σ_{22} being significantly larger in magnitude than σ_{11}. For time $t = 14\mu s$ and $24\mu s,$ Figs. 4.19a and 4.19b evince, respectively, the variations of σ_{22} and σ_{12} at points directly ahead of the notch tip. We note that the axial variation of $|\sigma_{12}|$ exhibits a boundary layer like phenomenon near the notch tip; the thickness of the boundary layer equals 0.2% of the length of the notch. The angular distributions of the principal tensile stress and the maximum shear stress at $t = 14\mu s$ and $24\mu s$ are exhibited in Figs. 4.20a and 4.20b. The

angular locations, θ, of points where these stresses attain their maximum values are essentially the same at $t = 14\mu s$ and $24\mu s$. Whereas the maximum principal tensile stress occurs at $\theta = 70^{o}$, the maximum shear stress attains its peak value at $\theta = -60^{o}$. These angular positions are close to those found by Batra and Gummalla (2000) in the transient FE analysis of the thermoviscoplastic problem. The angular distributions of the hoop stress $\sigma_{\theta\theta}$ and the shear stress $\sigma_{r\theta}$ are plotted in Figs. 4.21a and 4.21b respectively. Maximum values of $\sigma_{r\theta}$ occur at the extremities of the circular surface of the notch tip.

It is clear from the results plotted in Fig. 4.22a that indeed K_I and K_{II} are proportional to $\sqrt{r}$ during the time interval considered herein. The time histories of the stress intensity factors are depicted in Fig. 4.22b. Significantly larger values of K_{II} relative to those of K_I imply that the mode-II deformations near the notch tip are dominant.

We now assume that the prenotched plate is made of an orthotropic material with material axes of symmetry coincident with the coordinate axes. Two orthotropic materials, namely orthotropic (1) and orthotropic (2), are considered with the following material properties: orthotropic (1), $E_{11} = 210GPa, E_{22} = E_{33} = 0.5E_{11}, \nu_{12} = \nu_{23} = \nu_{31} = 0.29$, $G_{12} = 0.4E_{11}$; orthotropic (2), $E_{11} = 210GPa, E_{22} = E_{33} = 0.2E_{11}$, $\nu_{12} = \nu_{23} = \nu_{31} = 0.29$, $G_{12} = 0.4 E_{11}$. As can be seen from Fig. 4.23a, subsequent to the arrival of the dilatational wave at the notch tip, the magnitude of the stress intensity factor $K_I(t)$ for orthotropic materials is less than that for the isotropic material. The decrease in the magnitude of $K_I(t)$ is due to the reduction of the Young's moduli of the orthotropic materials in the x_2- direction. However, the time histories of the stress intensity factor $K_{II}(t)$ for isotropic and orthotropic materials in Fig. 4.23b are almost coincident with each other since the shear modus G_{12} in each has the same value. Thus the mode mixity of the deformation field near the notch tip in an orthotropic plate can be adjusted by suitably modifying the material moduli in the x_1- and x_2- directions

4.4 Conclusions

We have developed a computer code to analyze transient infinitesimal plane strain/stress deformations of an elastic body. The code has been validated by comparing computed results with the analytical solutions for two problems, namely, wave propagation in a bar, and a rectangular plate with a central crack with plate edges parallel to the crack axis loaded in tension. The computed time histories of the stress intensity factors were found to agree with those available in the literature for the same problem. The code is then used to analyze transient deformations of a double edge prenotched plate with the smooth edge between the two notches loaded by uniformly distributed compressive tractions. The deformations and stress fields near the notch tip computed by the MLPG method agree well with those obtained from the finite element solution. It is found that deformations near the crack/notch tip exhibit the $1/\sqrt{r}$ singularity.

4.5 References

Atluri S. N. and Zhu T. (1998): A New Meshless Local Petrov-Galerkin (MLPG) Approach in Computational Mechanics. *Computational Mechanics*, Vol. 22, pp. 117-127.

Atluri S. N., Kim H. G. and Cho J. Y. (1999): A Critical Assessment of the Truly Meshless Local Petrov-Galerkin (MLPG), and Local Boundary Integral Equation (LBIE) Methods. *Computational Mechanics*, Vol. 24, pp. 348-372.

Atluri S. N. and Zhu T. (2000): The meshless local Petrov-Galerkin (MLPG) approach for solving problems in elasto-statics. *Computational Mechanics*, Vol. 25, pp. 169-179.

Atluri S. N. and Shen S. P. (2002): The Meshless Local Petrov-Galerkin (MLPG) method : A simple & less-costly alternative to the finite element methods. *Computer Modeling in Engineering & Sciences*, 3(1), 11-51.

Baker B. R. (1962): Dynamic Stresses Created by a Moving Crack. *Journal of Applied Mechanics,* Vol. 29, pp. 449-545.

Batra R. C. and Gummalla R. R. (2000): Effect of Material and Geometric Parameters on Deformations near the Notch Tip of a Dynamically Loaded Prenotched Plate. *International Journal of Fracture*, Vol. 101, pp. 99-140.

Ching H. K. and Batra R. C. (2001): Determination of Crack Tip Fields in Linear Elastostatics by the Meshless Local Petrov-Galerkin (MLPG) Method. *Computer Modeling in Engineering & Sciences*, Vol. 2(2), pp. 273-289.

Fedelinski P., Aliabadi M. H. and Rooke D. P. (1994): The dual boundary method: *J*-integral for dynamic stress intensity factors. *International Journal of Fracture*, Vol. 65, pp. 369-381.

Gu Y. T. and Liu G. R. (2001): A Meshless Local Petrov-Galerkin (MLPG) Method for Free and Forced Vibration Analyses for Solids. *Computational Mechanics*, Vol. 27, pp. 188-198.

Kalthoff J. F. and Winkler S. (1987): Failure Mode Transition at High Rates of Shear Loading, in Chiem C.Y., Kunze H.D., and Meyer L.W. (eds.). *Impact Loading and Dynamic Behavior of Materials*, Verlag, Vol. 1, pp. 185-195.

Lancaster P. and Salkauskas K. (1981): Surfaces generated by moving least squares methods. *Mathematics of Computation 37*, 141-158.

Lin H. and Atluri S. N. (2000): Meshless Local Petrov-Galerkin (MLPG) Method for Convection-diffusion Problems. *Computer Modeling in Engineering & Sciences*, Vol. 1(2), pp 45-60.

Long S. and Atluri S. N. (2002): A Meshless Local Petrov-Galerkin Method for Solving the Bending Problem of a Thin Plate. *Computer Modeling in Engineering & Sciences* Vol. 3(1), pp. 53-64.

Miannay D. P. (2001): Time-Dependent Fracture mechanics. Springer-Verlag Inc., New York.

Newmark N. M. (1959): A method of Computation for Structural Dynamics. *J. Eng. Mech. Div., Proc*. *ASCE*, Vol. 85, No. EM3, pp. 67-94.

Nishioka T. and Atluri S. N. (1980): Numerical Modeling of Dynamic Crack Propagation in Finite Bodies by Moving Singular Elements, Part II. *Journal of Applied Mechanics*, Vol. 47, pp. 577-582.

Organ D. J., Fleming M. and Belytschko T. (1996): Continuous Meshless Approximations for Nonconvex Bodies by Diffraction and Transparency. *Computational Mechanics*, Vol. 18, pp. 225-235.

Warlock A., Ching H. K., Kapila A. K. and Batra R. C. (2002): Plane Strain Deformations of an Elastic Material Compressed in a Rough Rectangular Cavity. *International Journal of Engineering Science*, Vol. 40, pp. 991-1010.

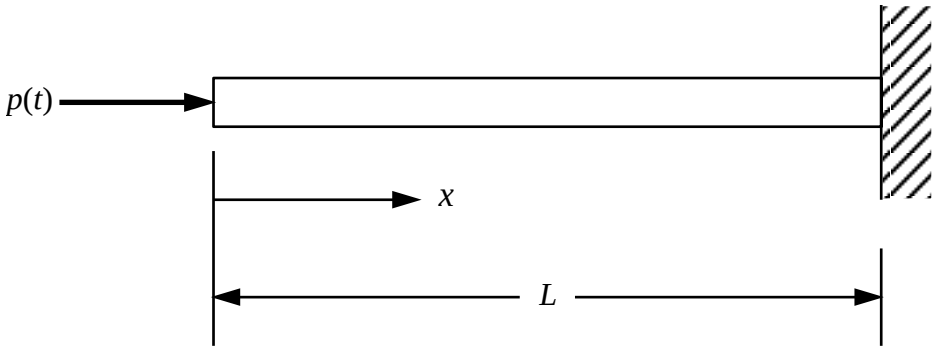

Fig. 4.1 A bar subjected to an impact force

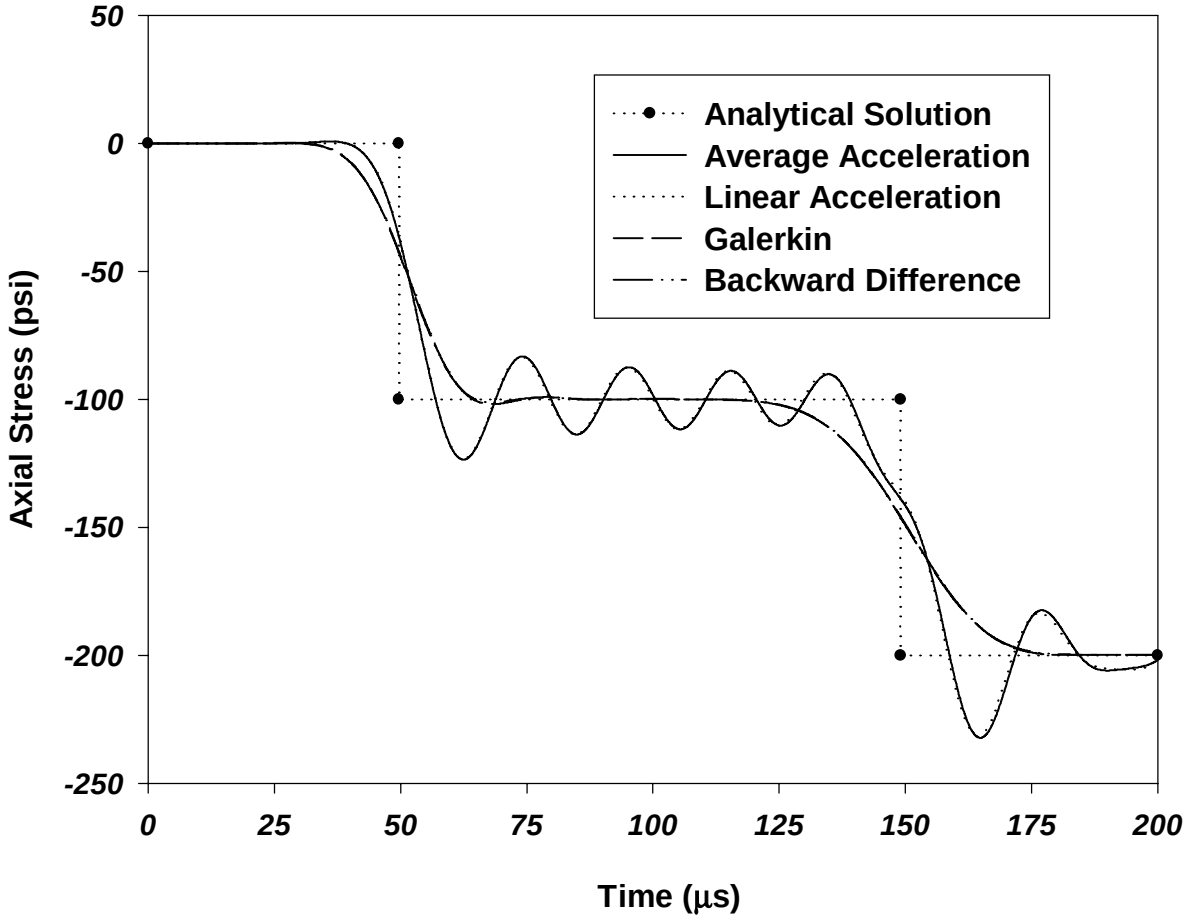

Fig. 4.2 Comparison with the analytical solution of the time history of the axial stress at the midpoint ($x=L/2$) obtained by usnig the four different integration methods

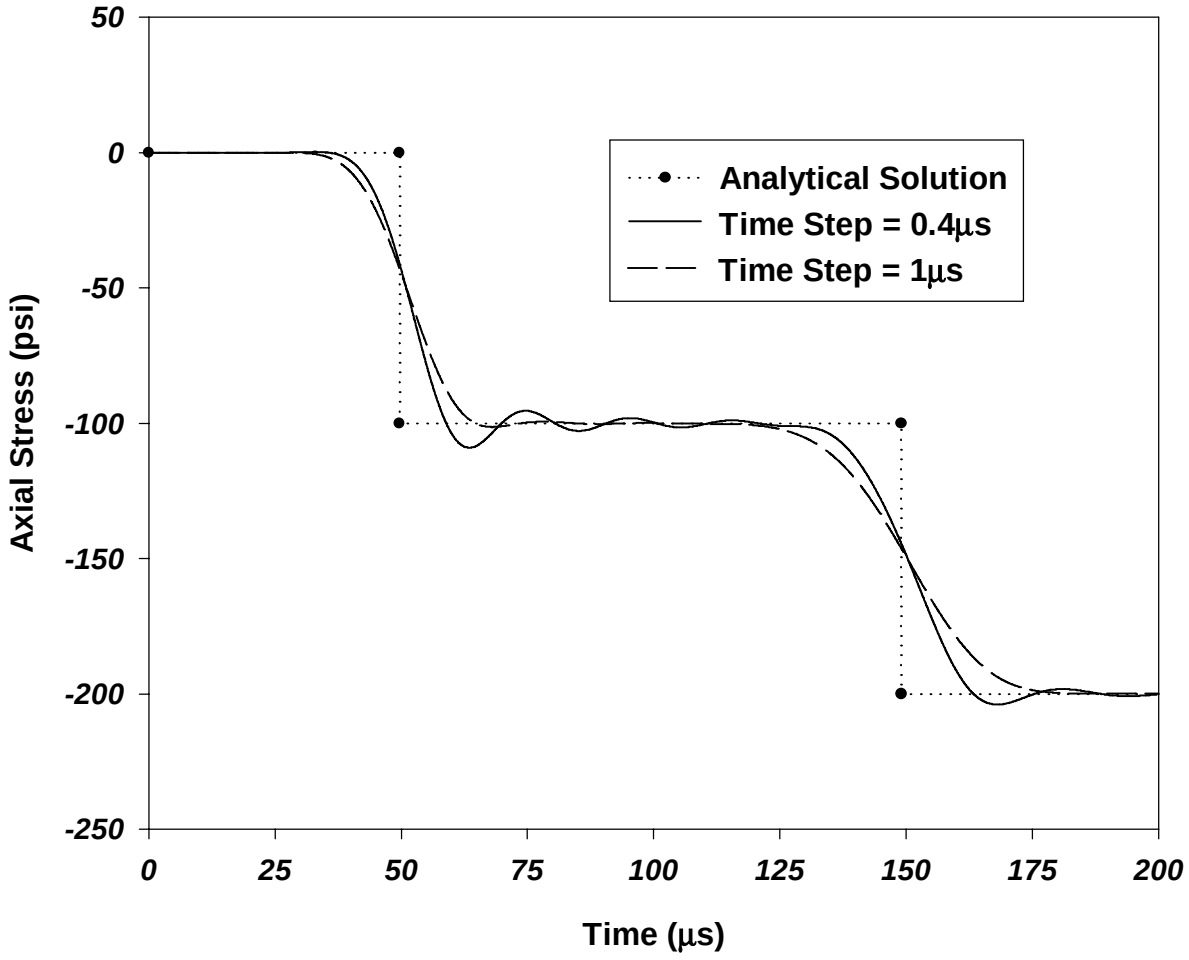

Fig. 4.3 Comparison with the analytical solution of the time history of the axial stress at the midpoint of the bar computed with two different time steps and by using the backward difference method

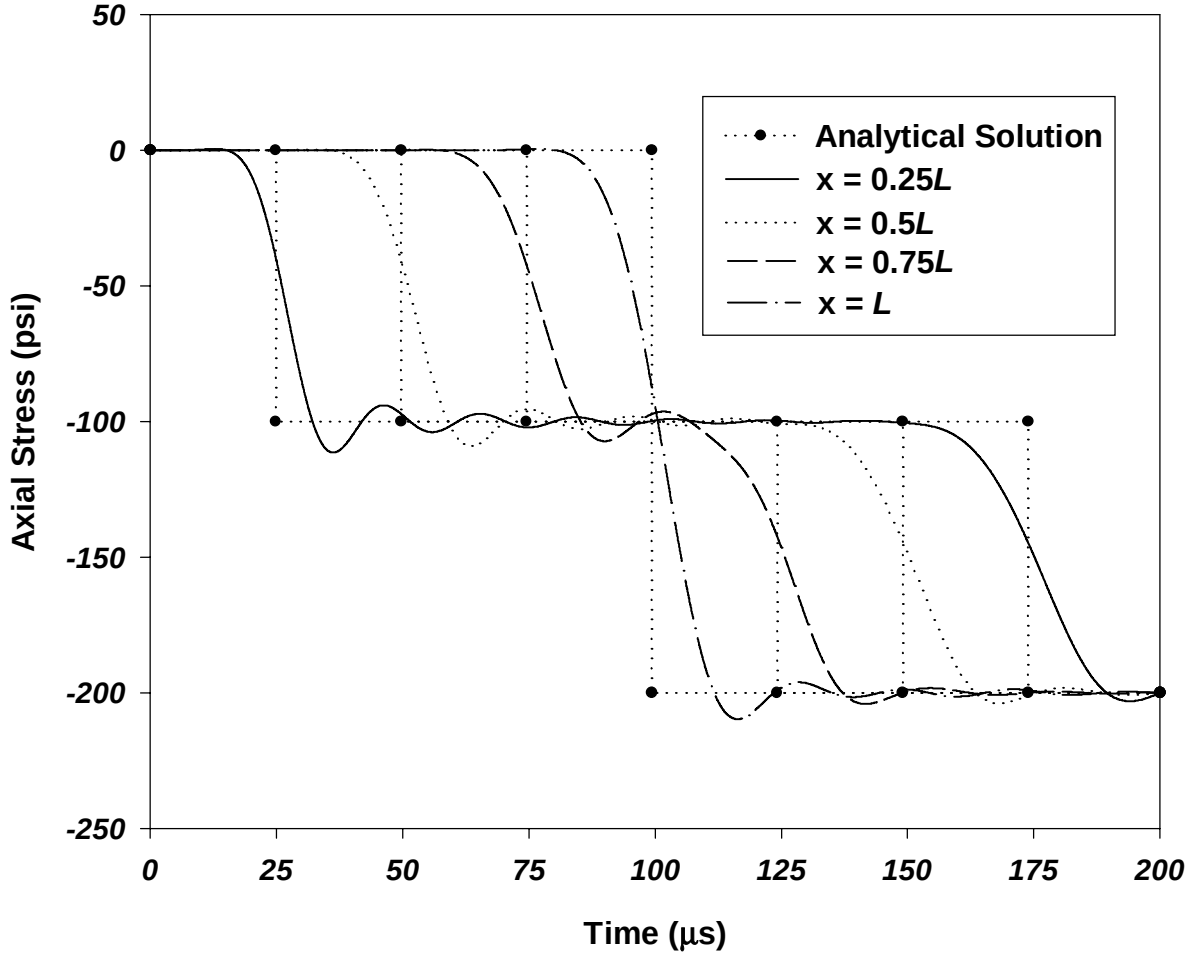

Fig. 4.4 Comparison with the analytical solution of the time history of the axial stress at four different locations obtained by using the backward difference method

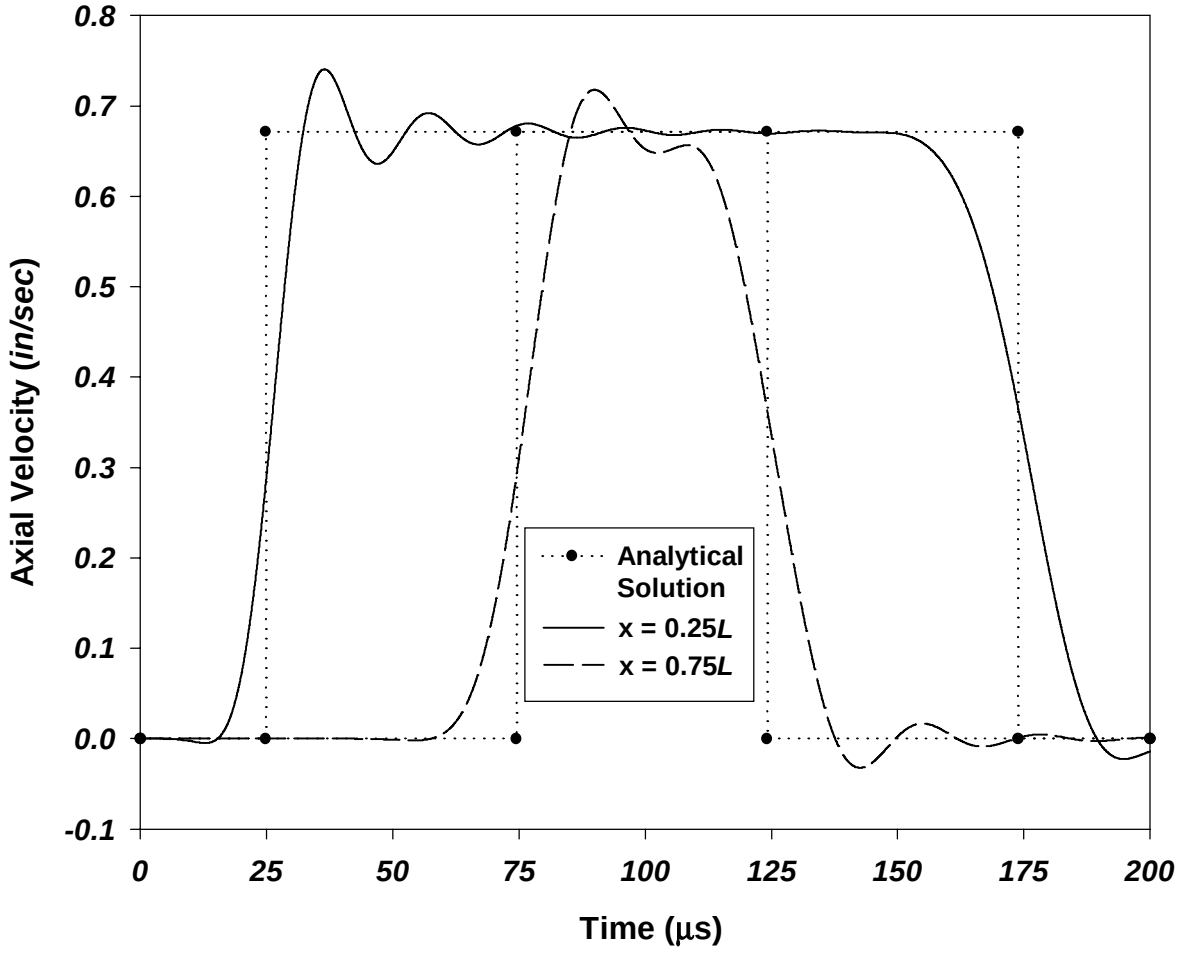

Fig. 4.5 Comparison with the analytical solution of the time history of the axial velocity at two different locations computed with the backward difference method

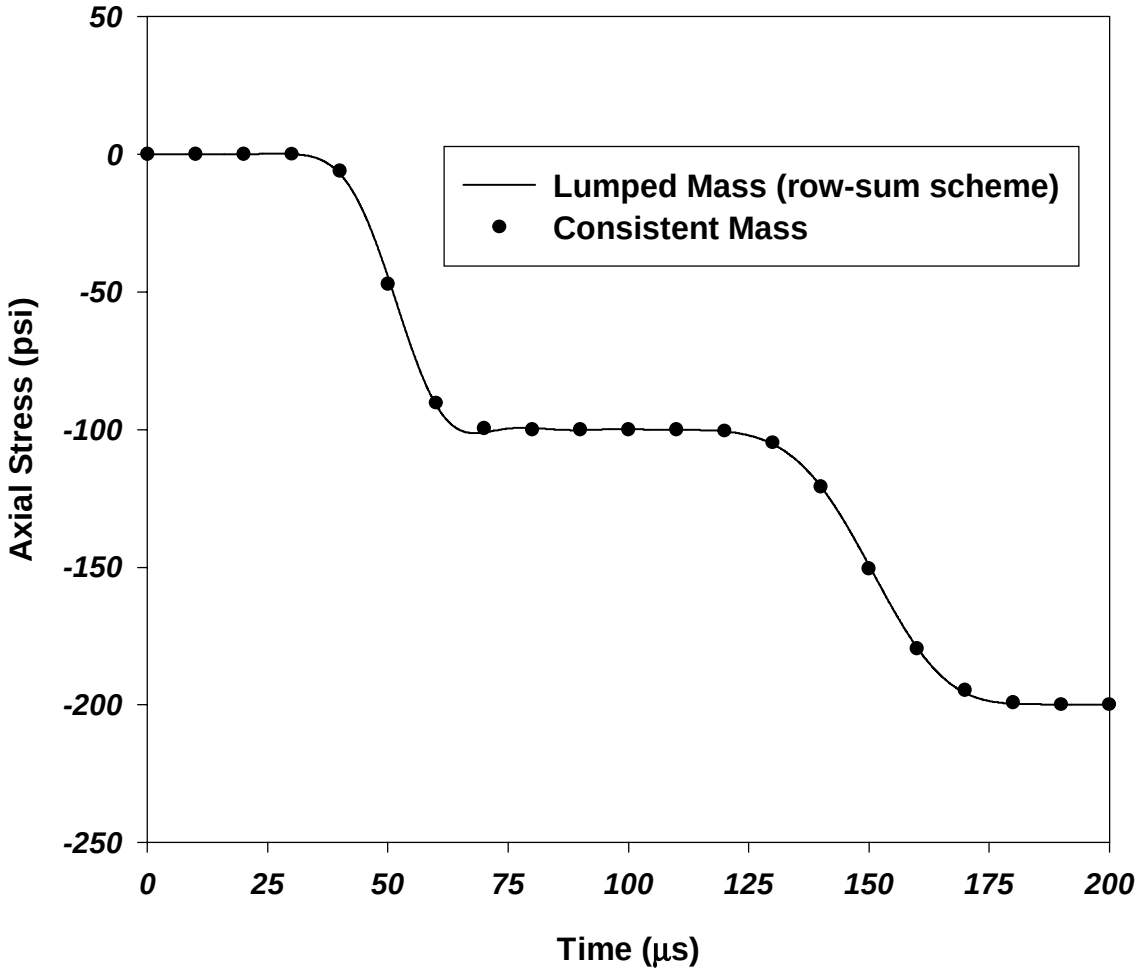

Fig. 4.6 Time histories of the axial stress at the midpoint computed with the lumped and the consistent mass matrices

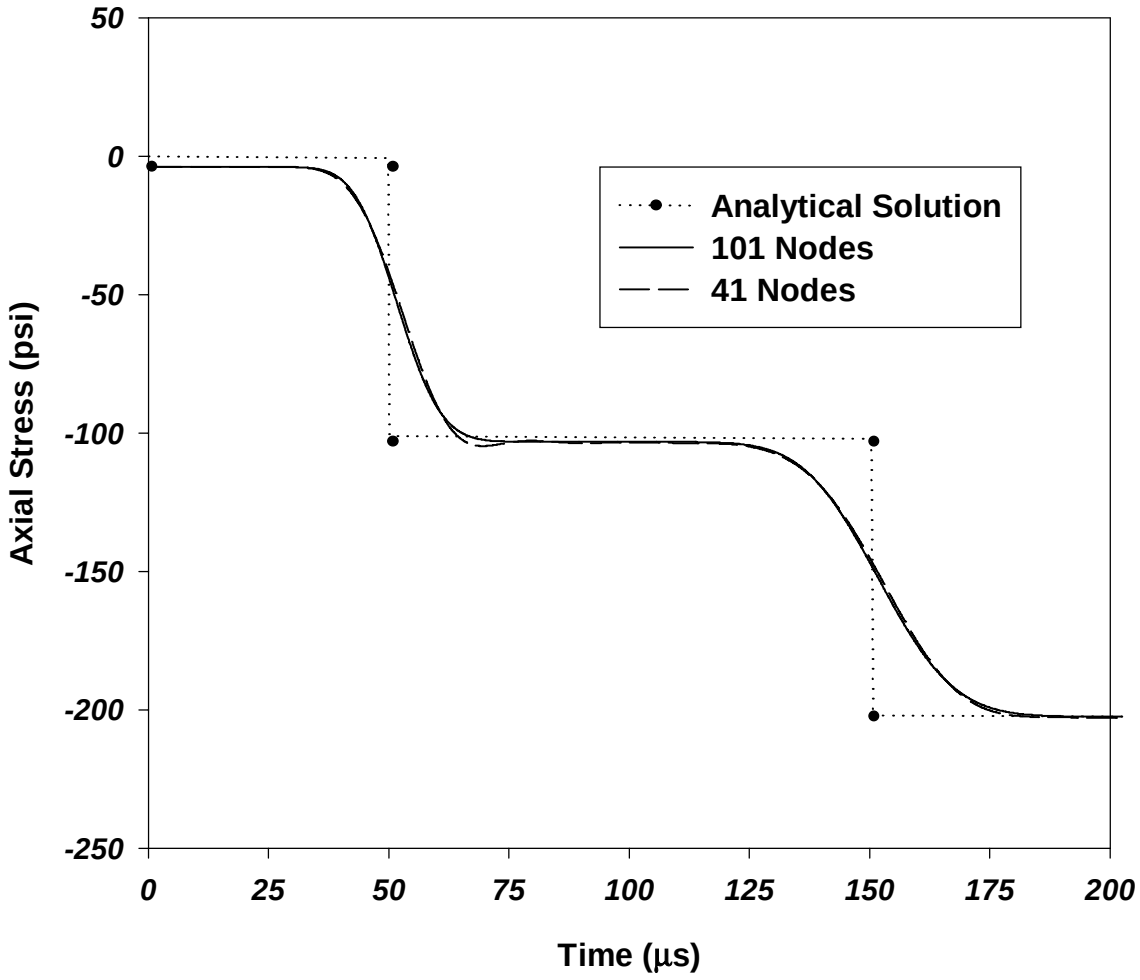

Fig. 4.7 Comparison of the time histories of the axial stress at the midpoint computed with two different arrangements of nodes

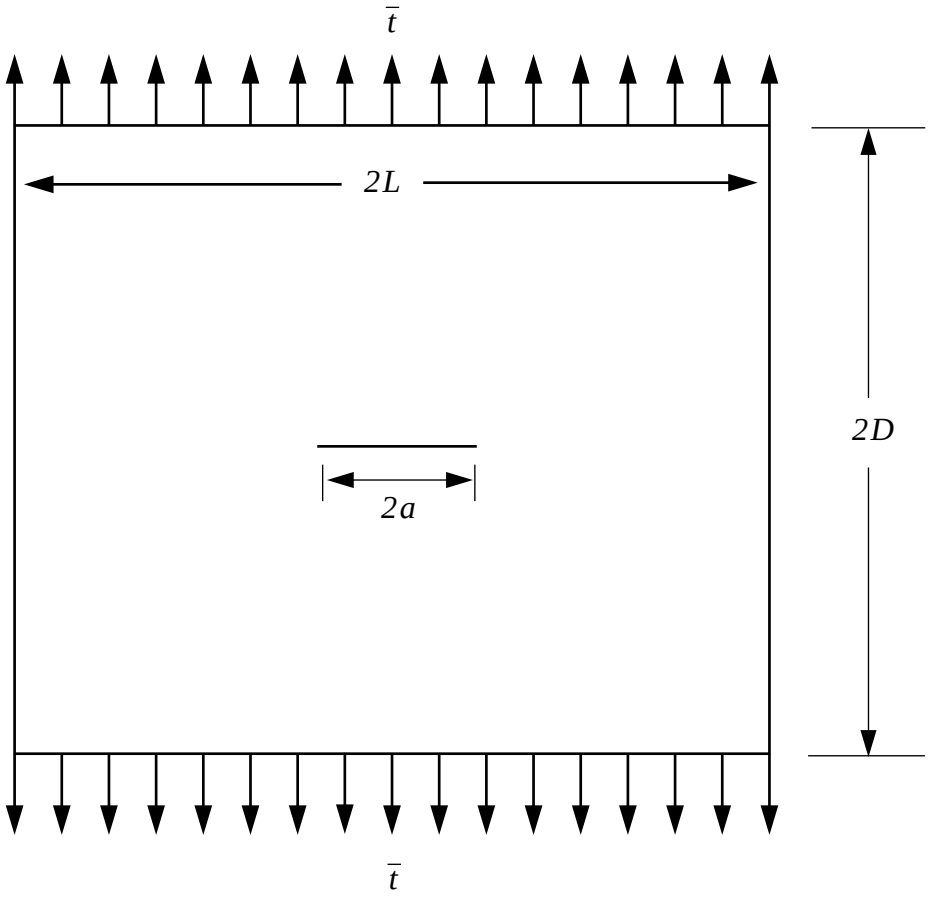

Fig. 4.8 A schematic sketch of the centrally cracked plate

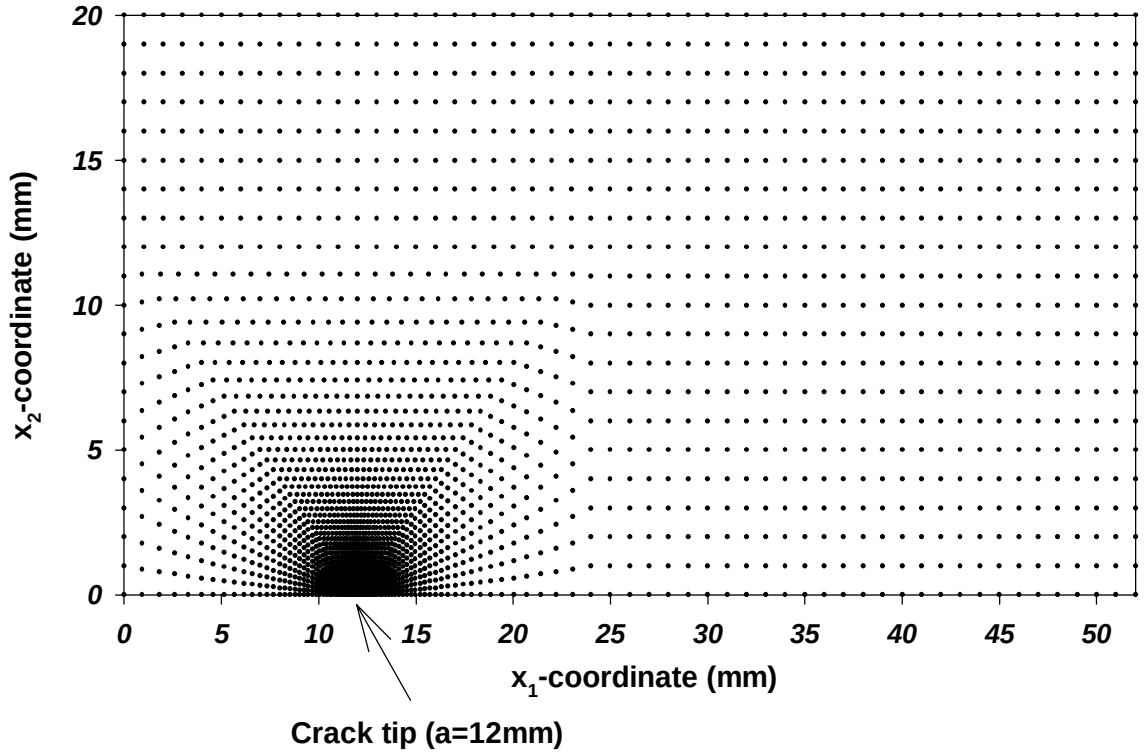

Fig. 4.9a The nodal mesh for one quarter of the centrally cracked plate

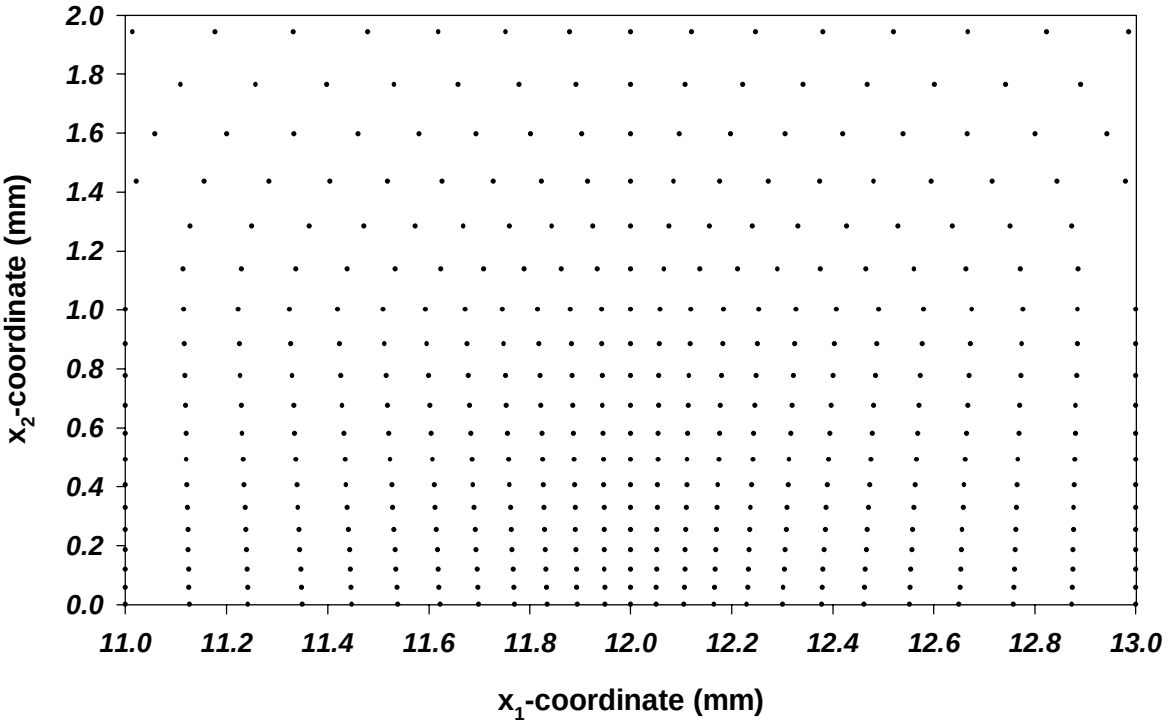

Fig. 4.9b The nodal mesh near the crack tip

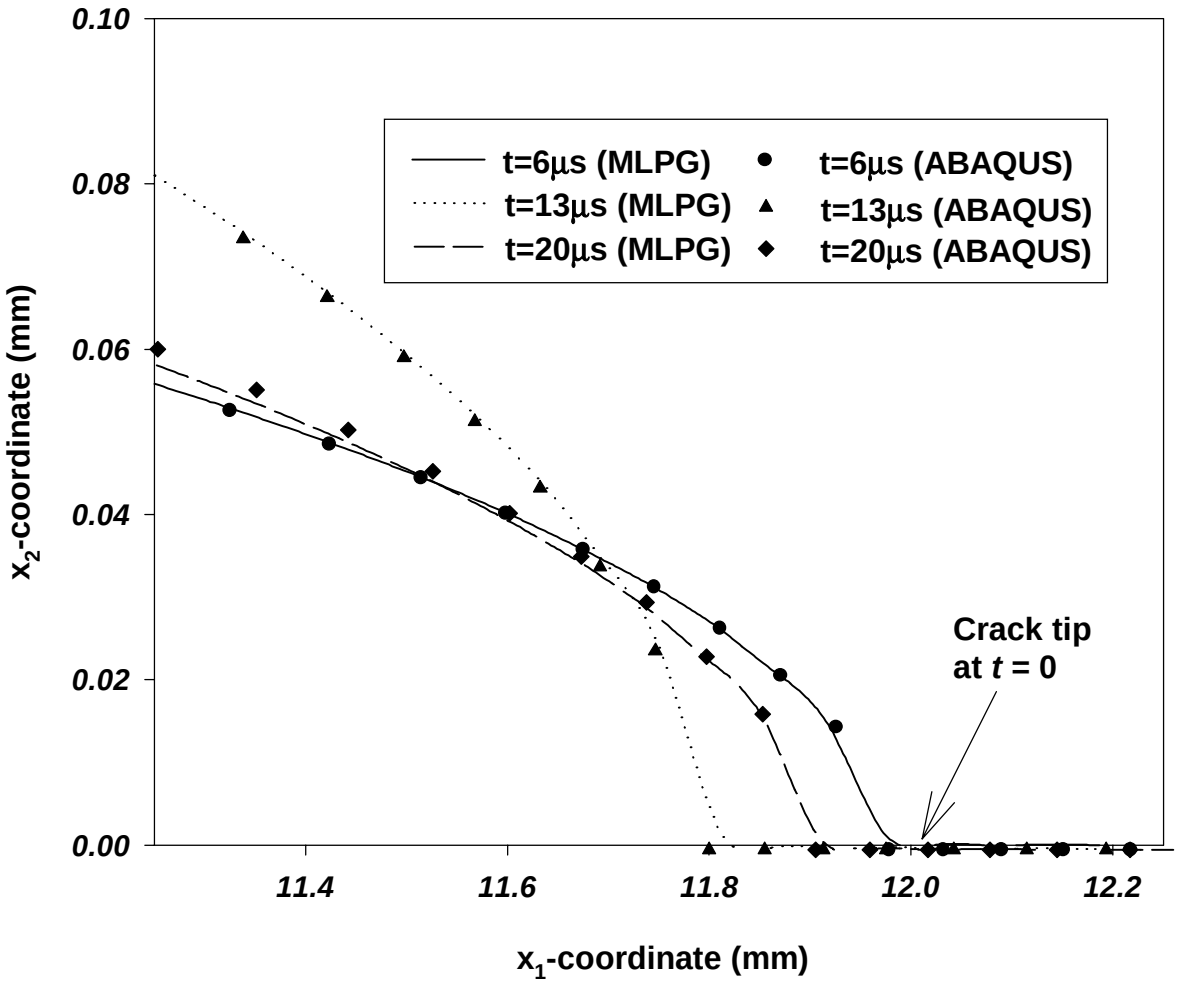

Fig. 4.10 Deformations of the crack tip at three different instants of time

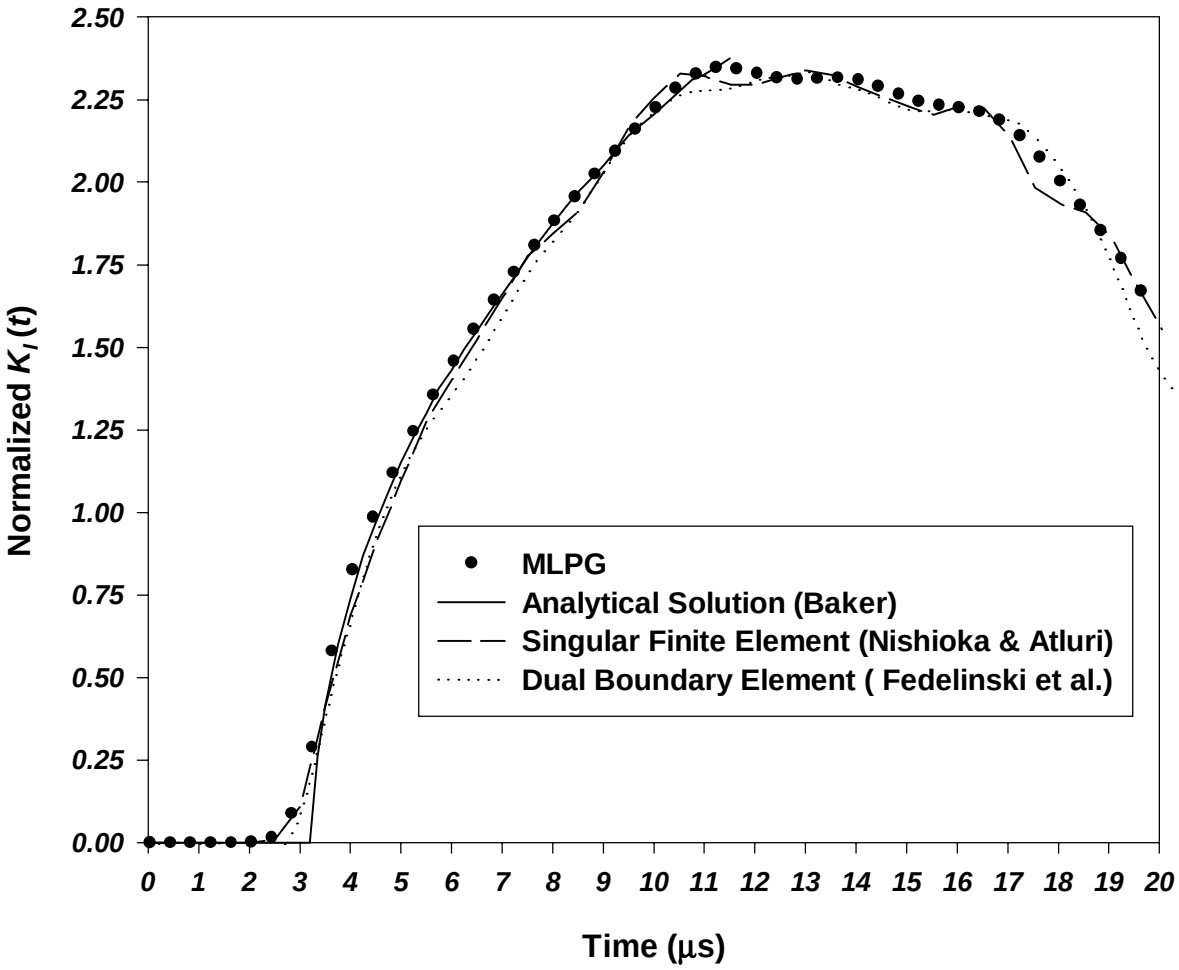

Fig. 4.11 The time history of the normalized stress intensity factor $K_I(t)$

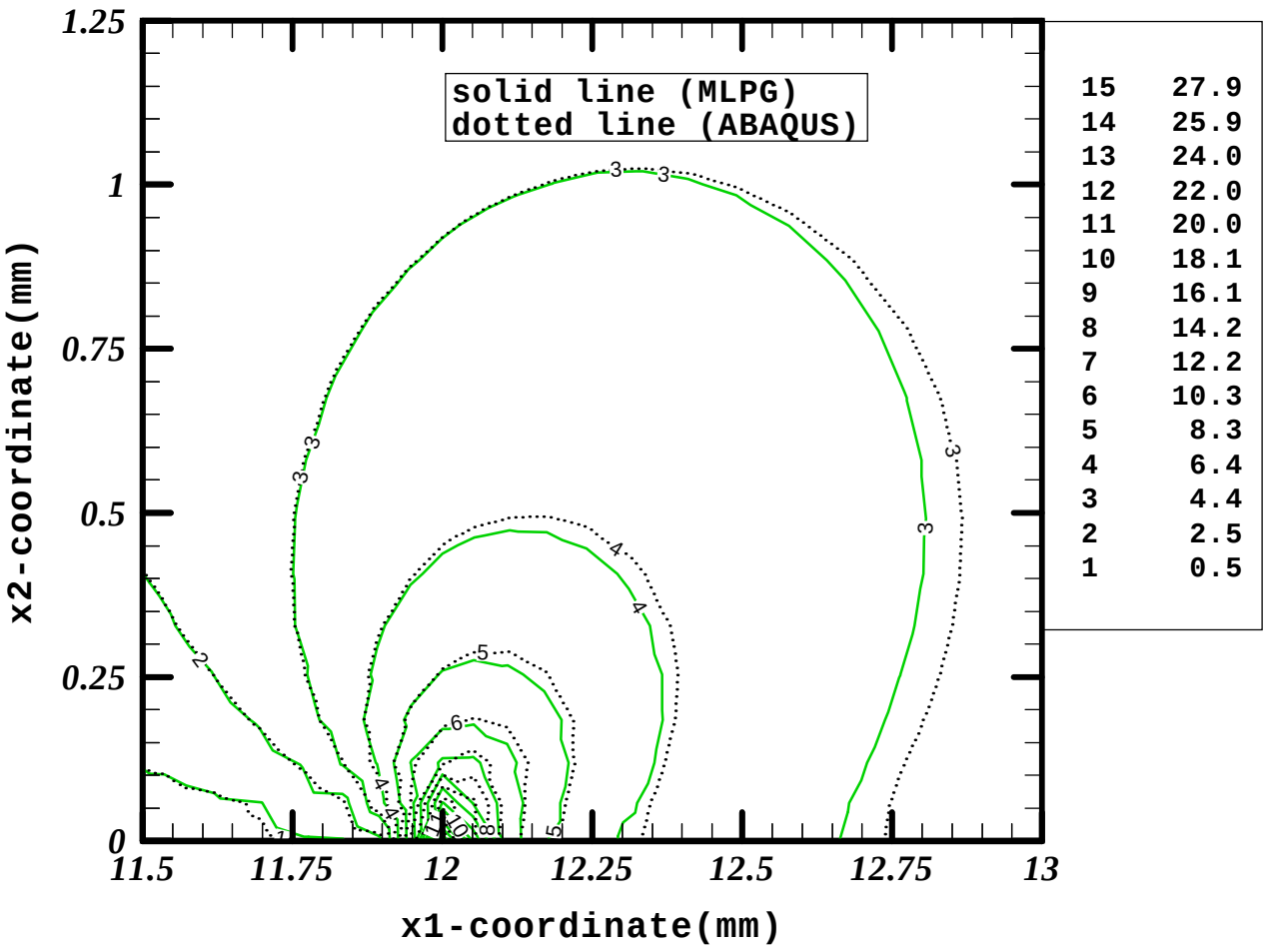

Fig. 4.12a Contours of the normalized maximum principal stress around the crack tip at t = 6μs

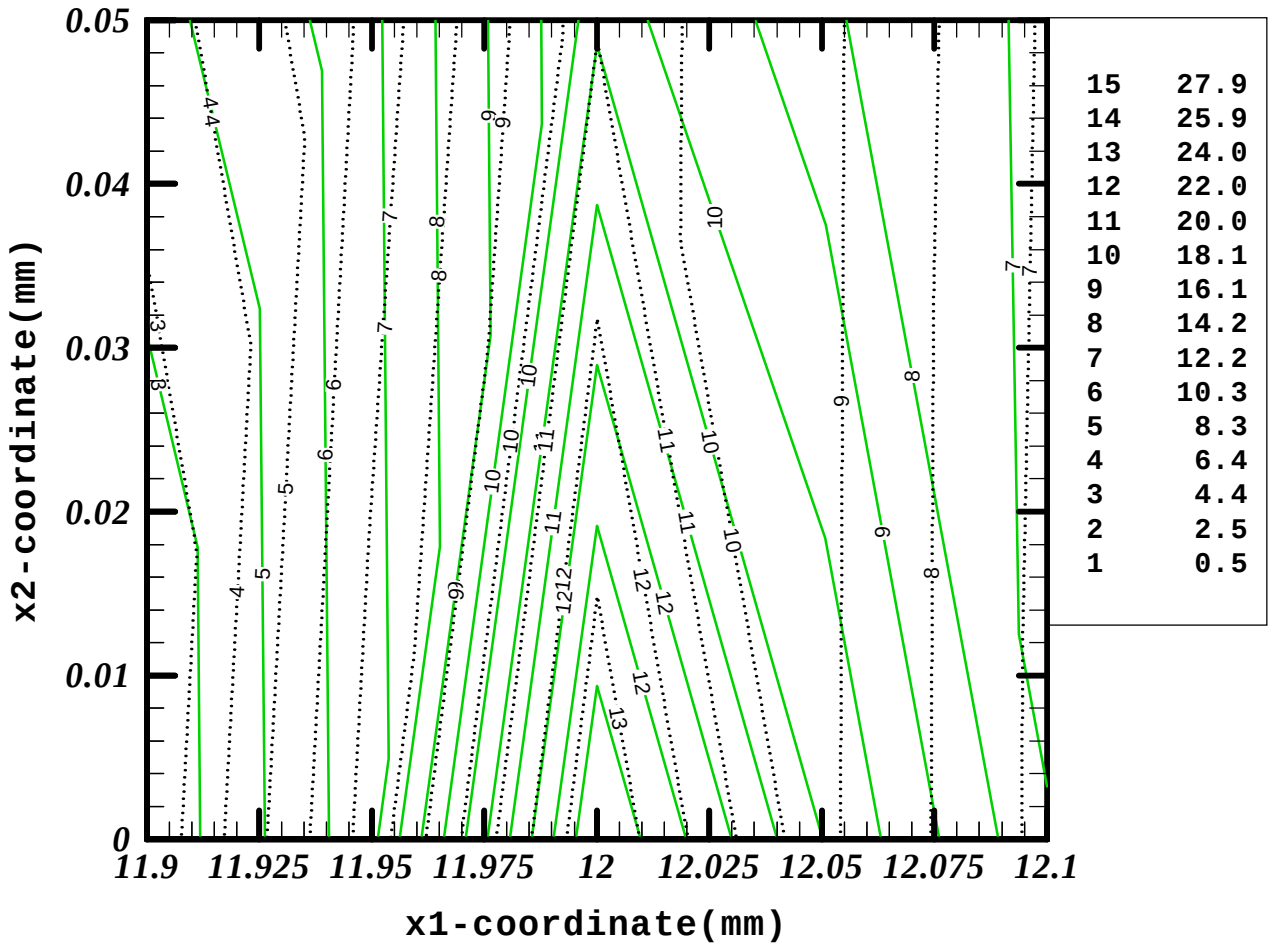

Fig. 4.12b Contours of the normalized maximum principal stress in a 0.2×0.05 region around the crack tip at t = 6μs; solid line (MLPG), dotted line (ABAQUS)

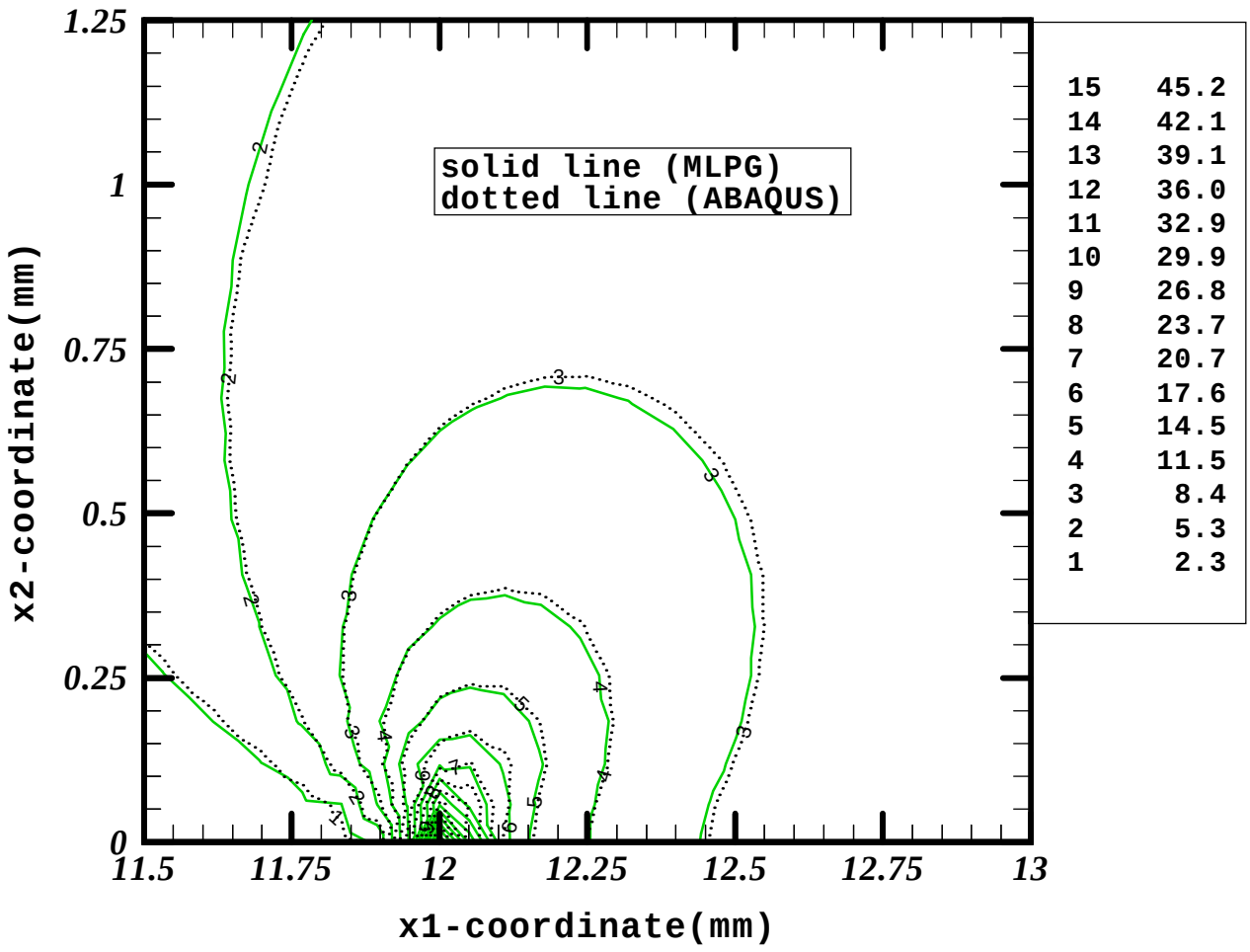

Fig. 4.13a Contours of the normalized maximum principal stress around the crack tip at t = 13μs

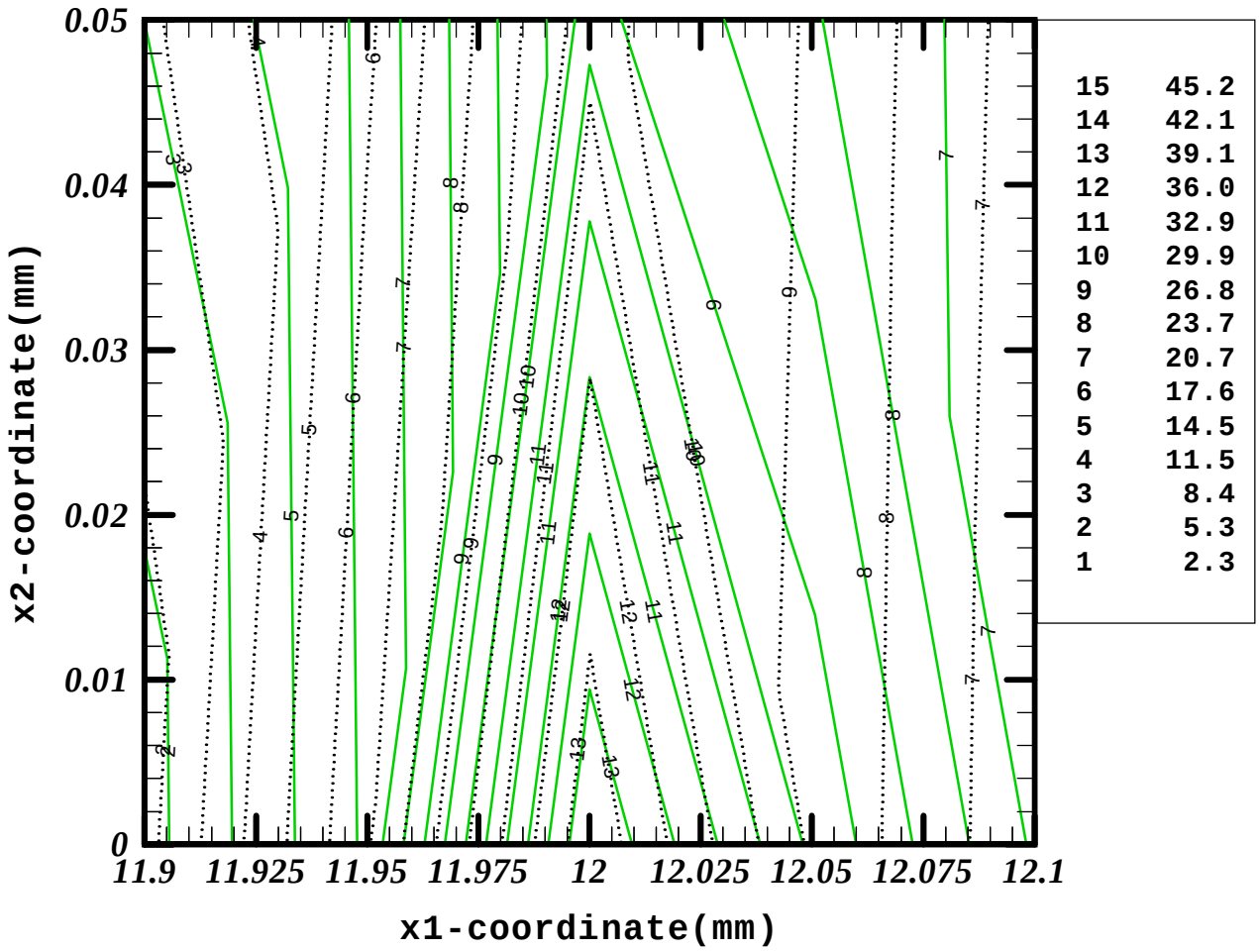

Fig. 4.13b Contours of the normalized maximum principal stress in a 0.2×0.05 region around the crack tip at t = 13μs; solid line (MLPG), dotted line (ABAQUS)

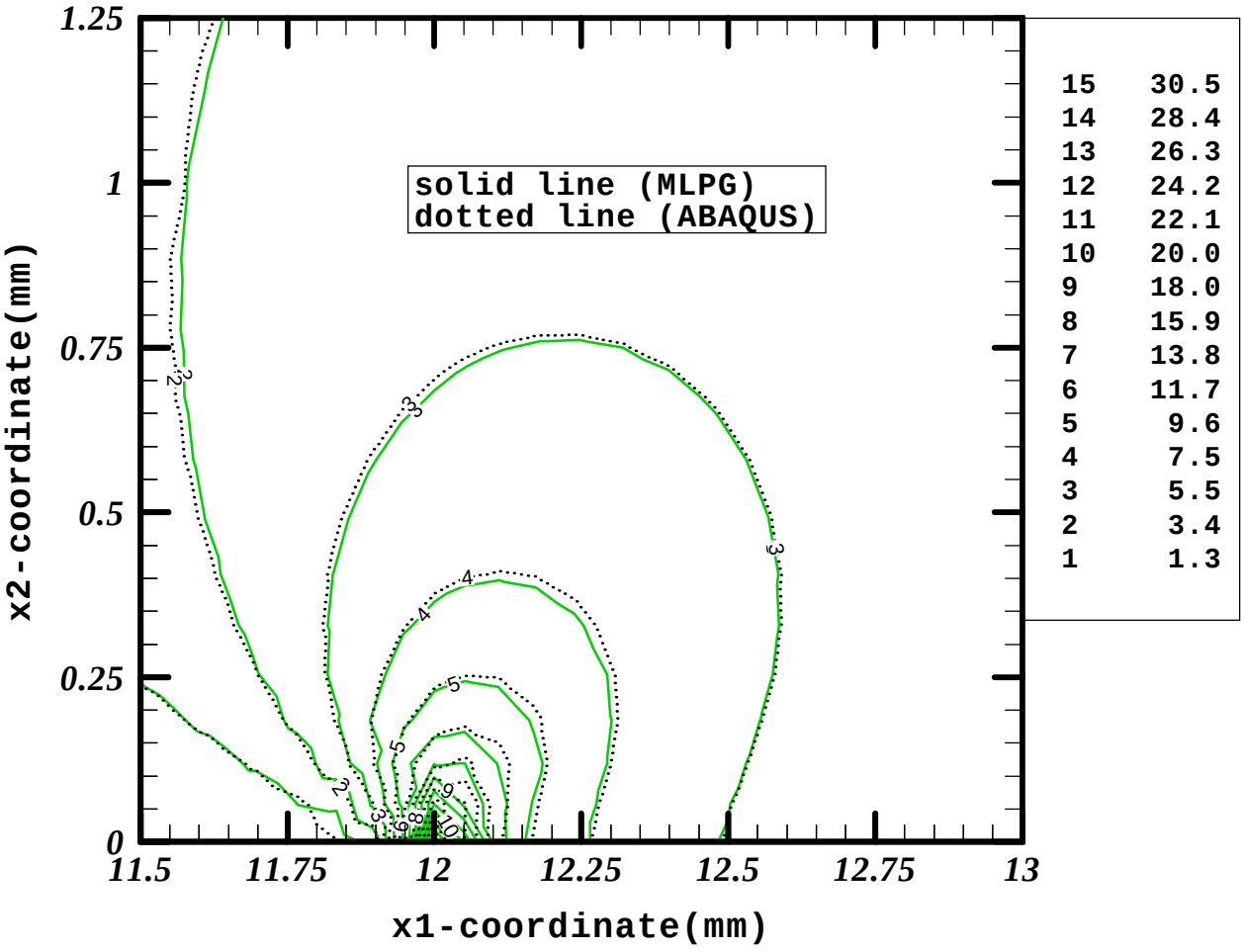

Fig. 4.14a Contours of the normalized maximum principal stress around the crack tip at t = 20μs

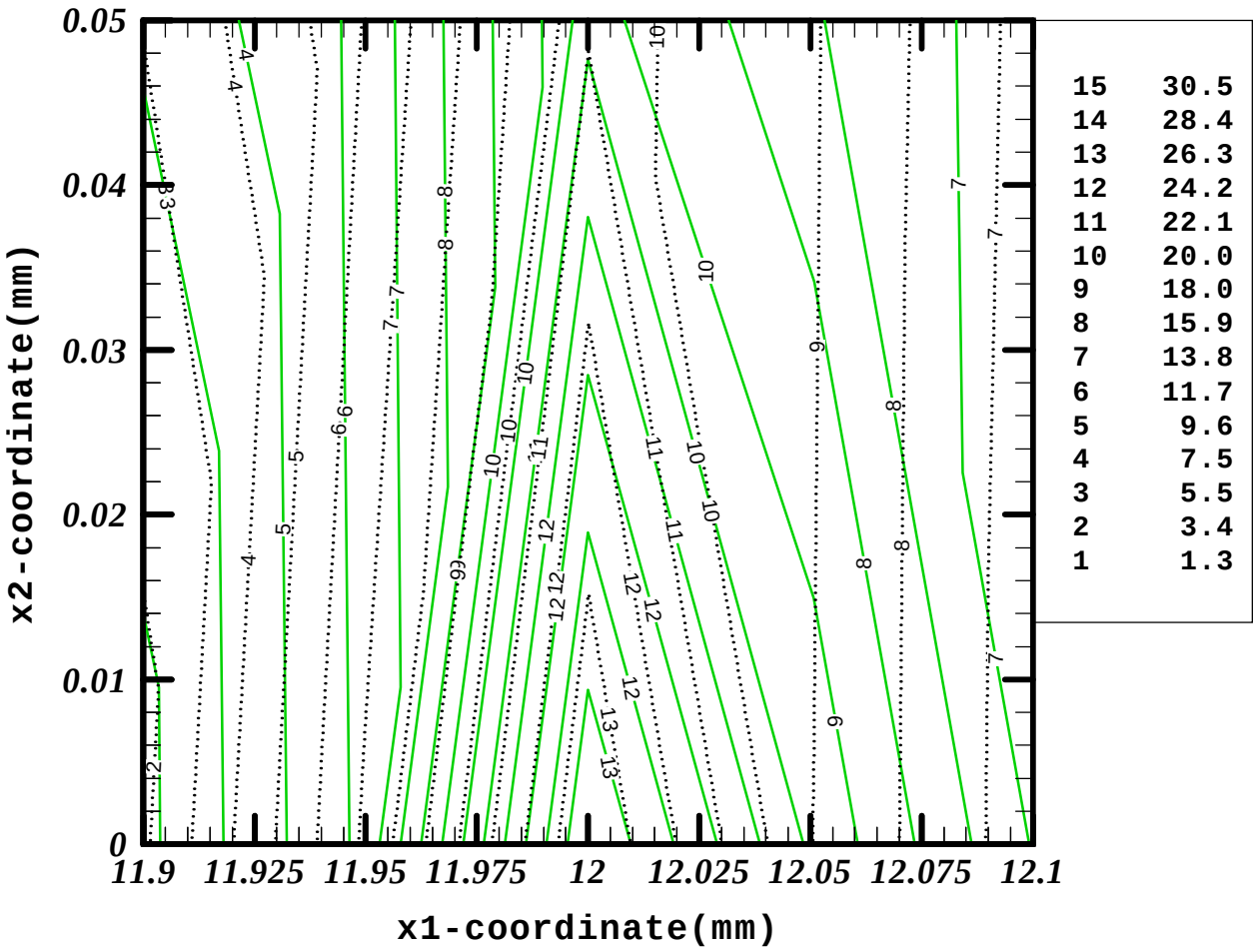

Fig. 4.14b Contours of the normalized maximum principal stress in a 0.2×0.05 region around the crack tip at t = 20μs; solid line (MLPG), dotted line (ABAQUS)

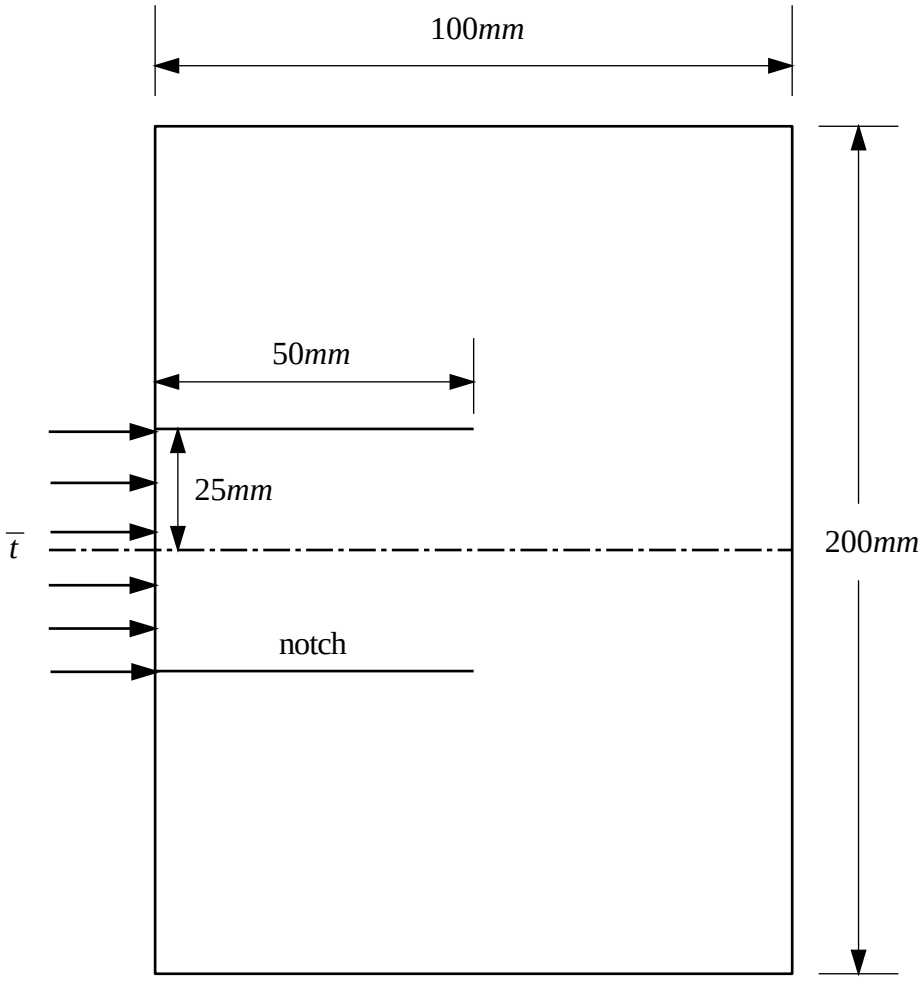

Fig. 4.15 A schematic sketch of the double edge−notched plate

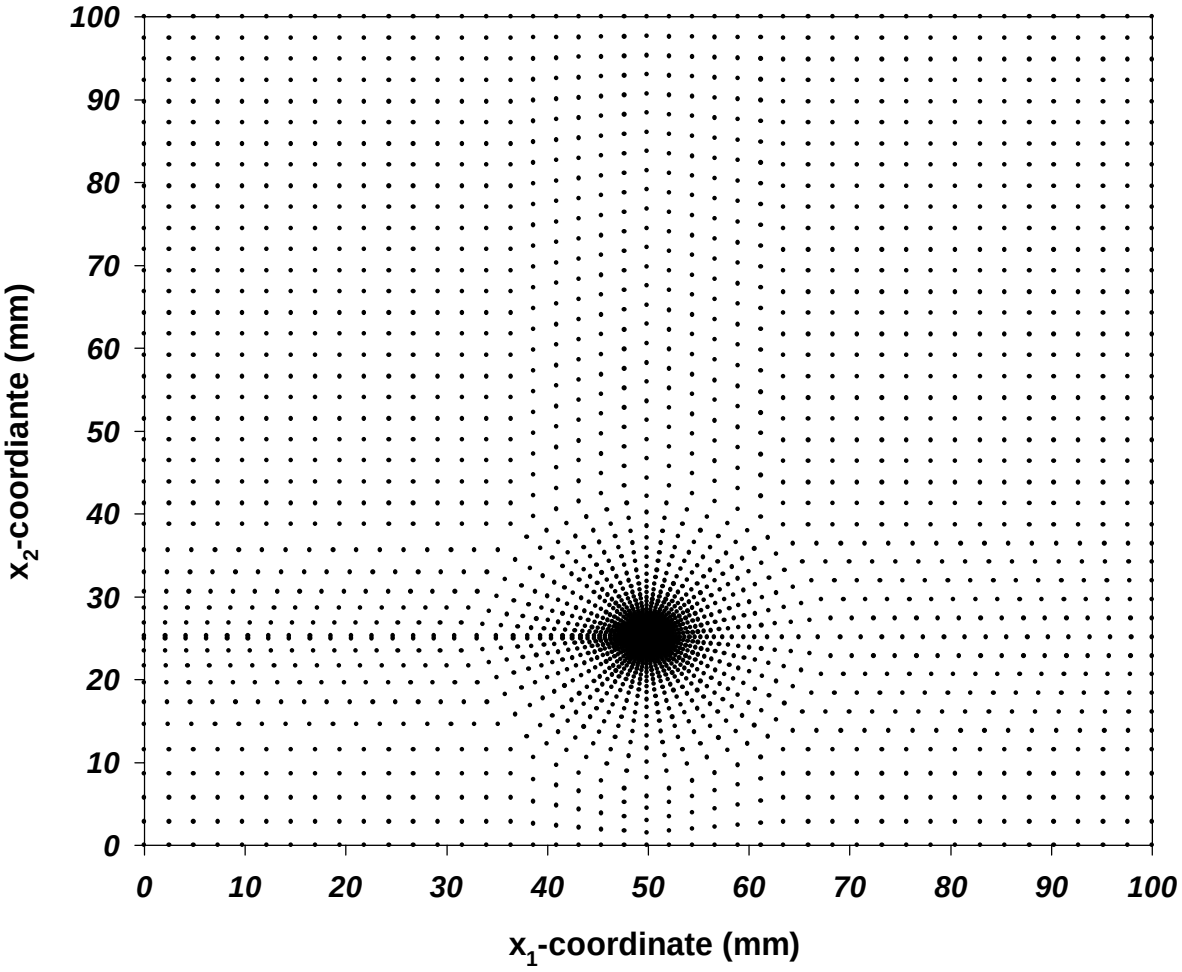

Fig. 4.16 The nodal mesh for the upper half of the double edge-notched plate

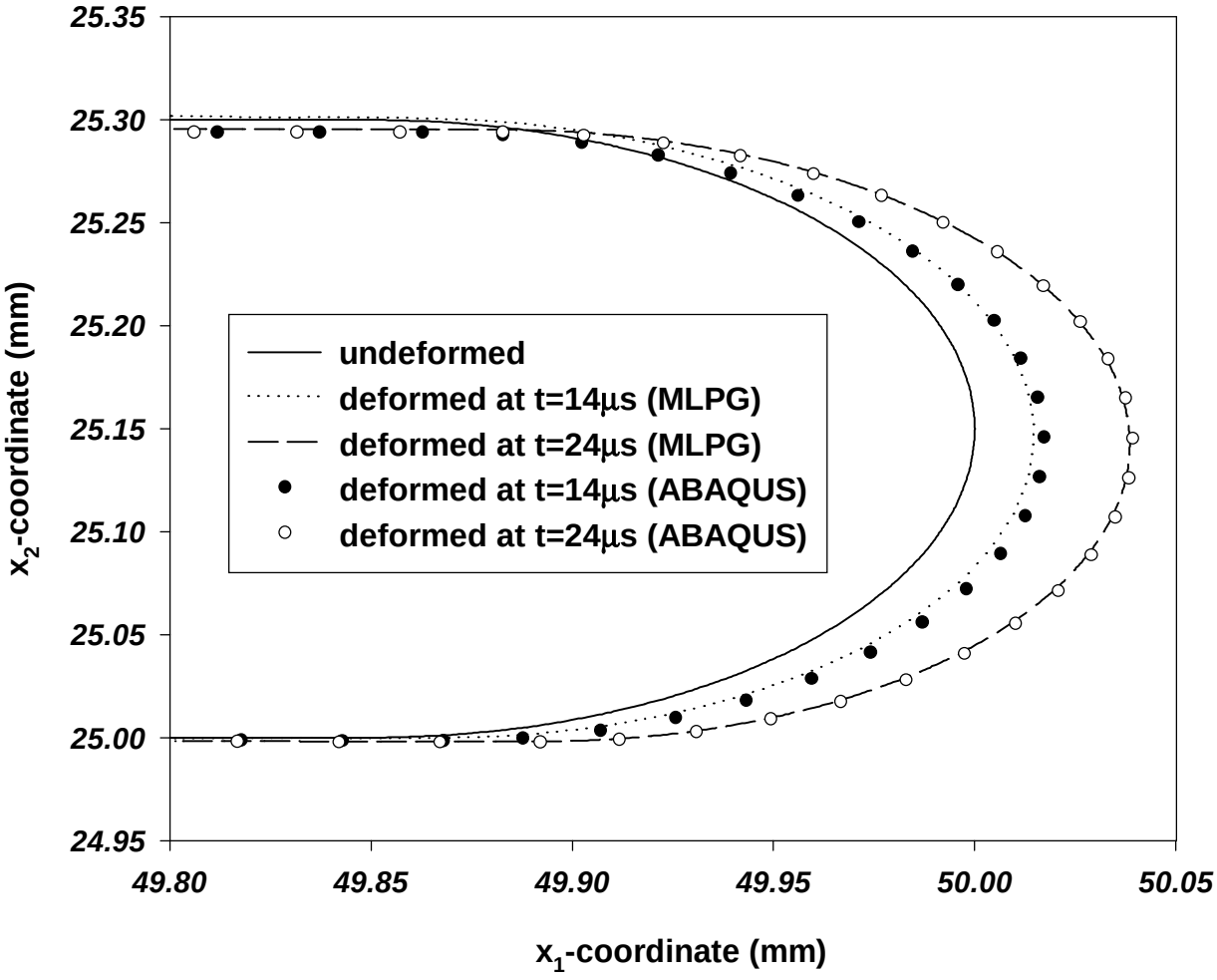

Fig. 4.17 Undeformed and deformed shapes of the circular notch surface

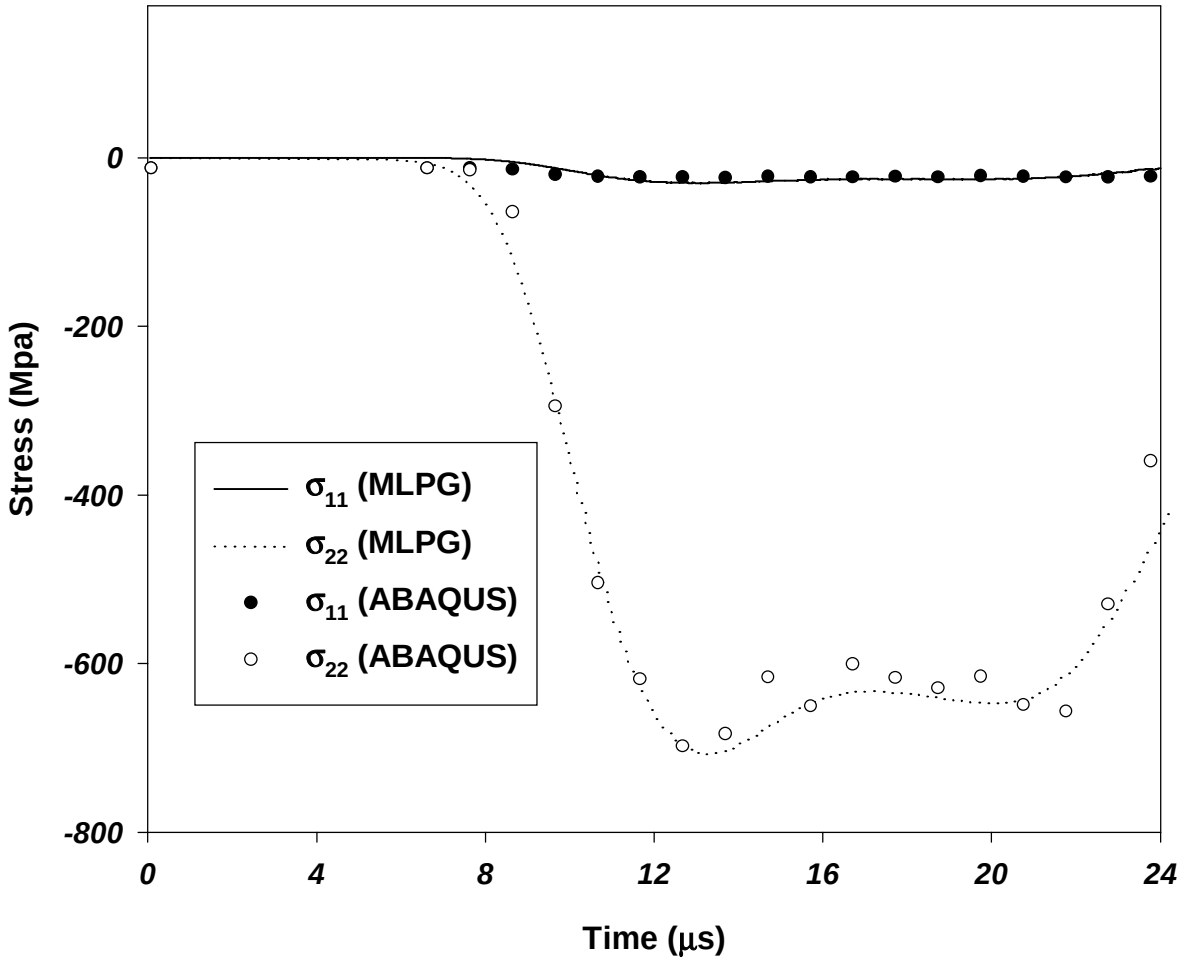

Fig. 4.18 Time histories of σ_{11} and σ_{22} at the notch tip

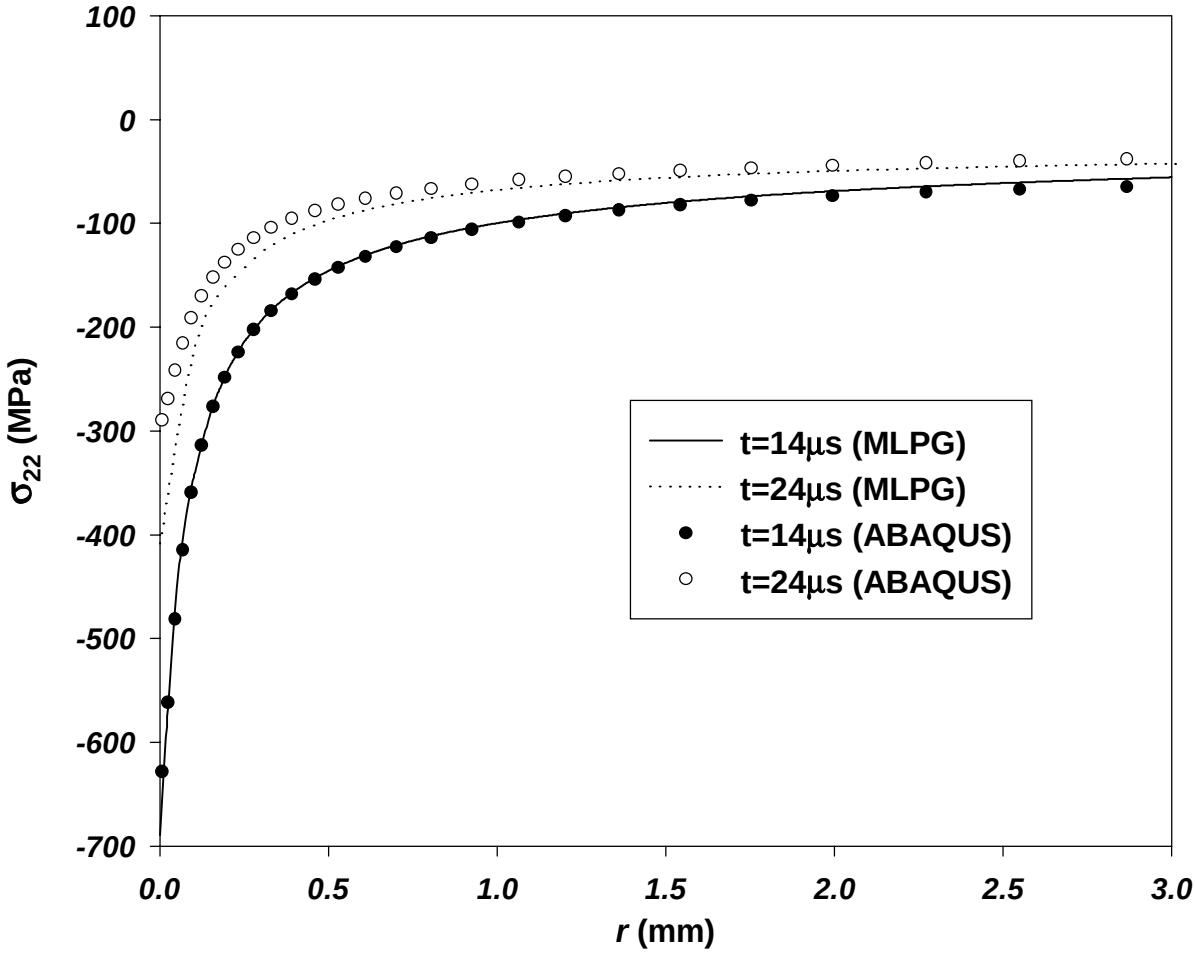

Fig. 4.19a Variations of σ_{22} with the distance directly ahead of the notch tip

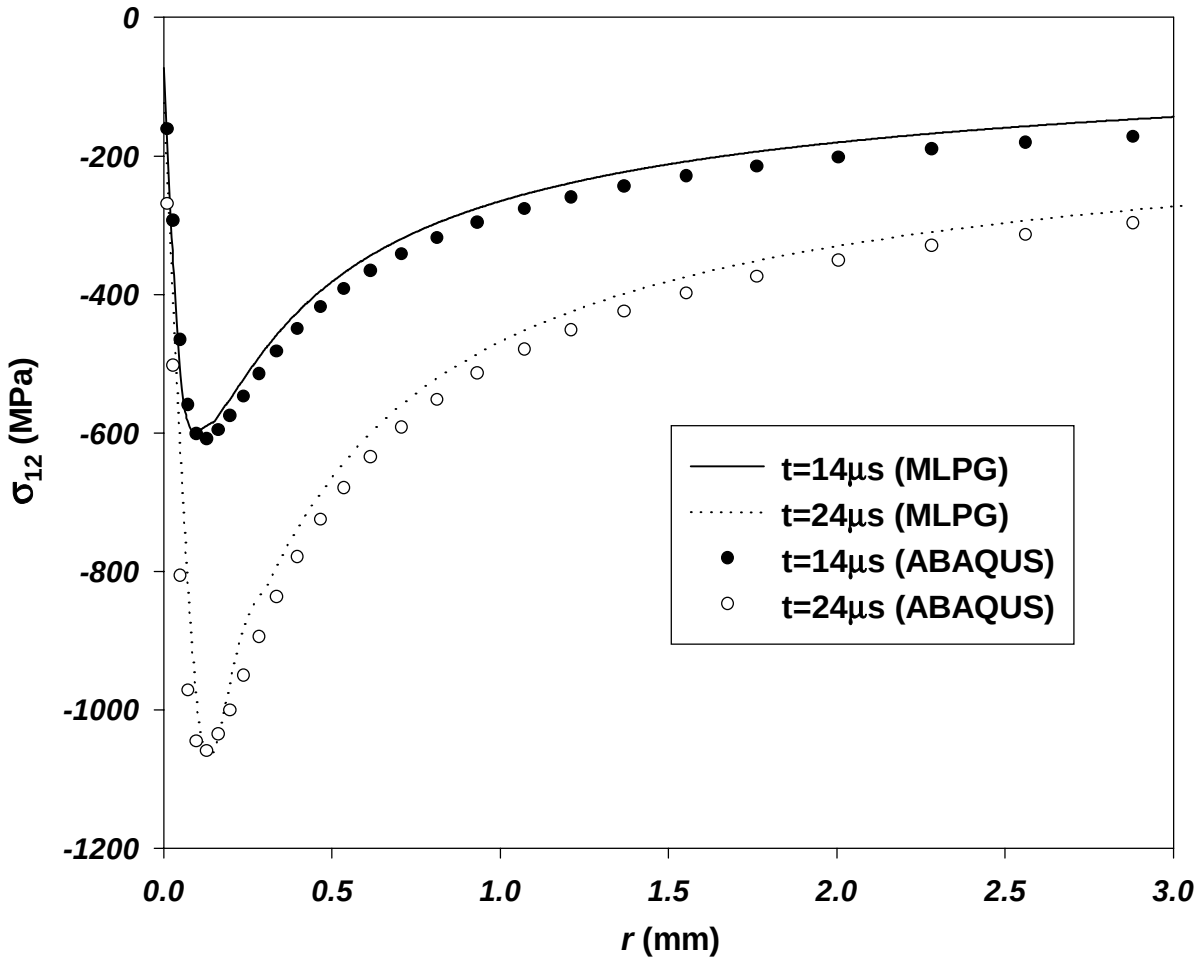

Fig. 4.19b Variations of σ_{12} with the distance directly ahead of the notch tip

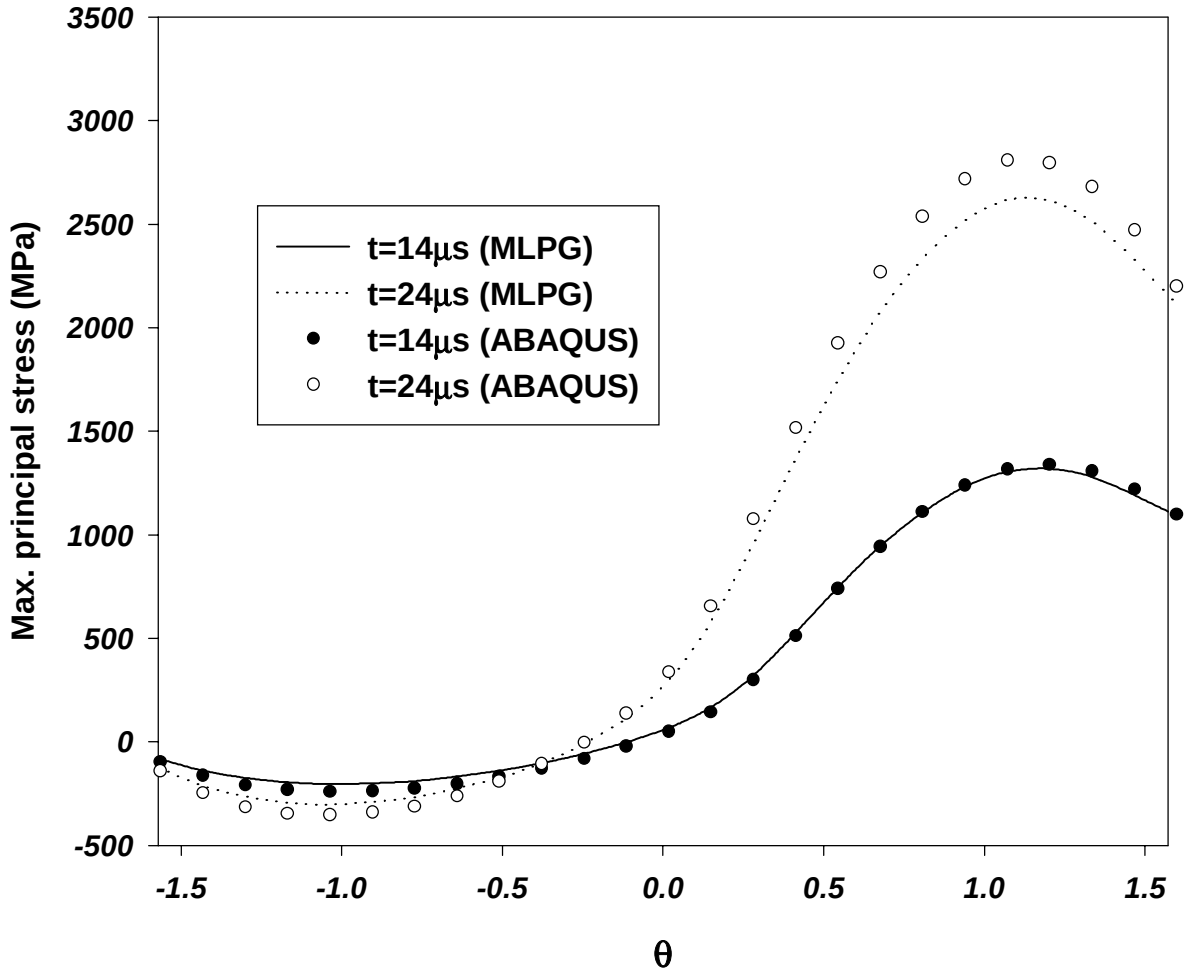

Fig. 4.20a Angular distribution of the maximum principal stress on the notch surface at two different times

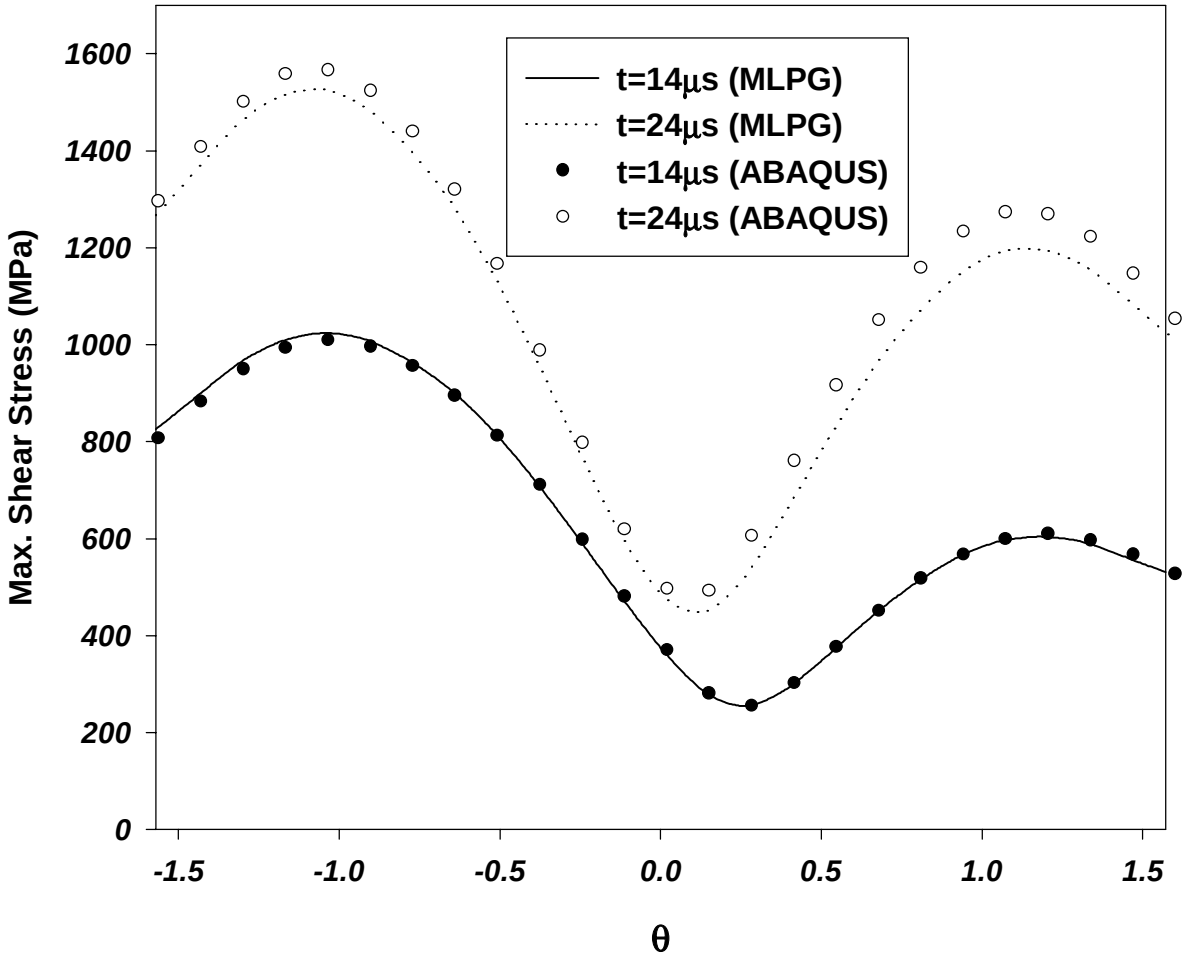

Fig. 4.20b Angular distribution of the maximum shear stress on the notch surface at two different times

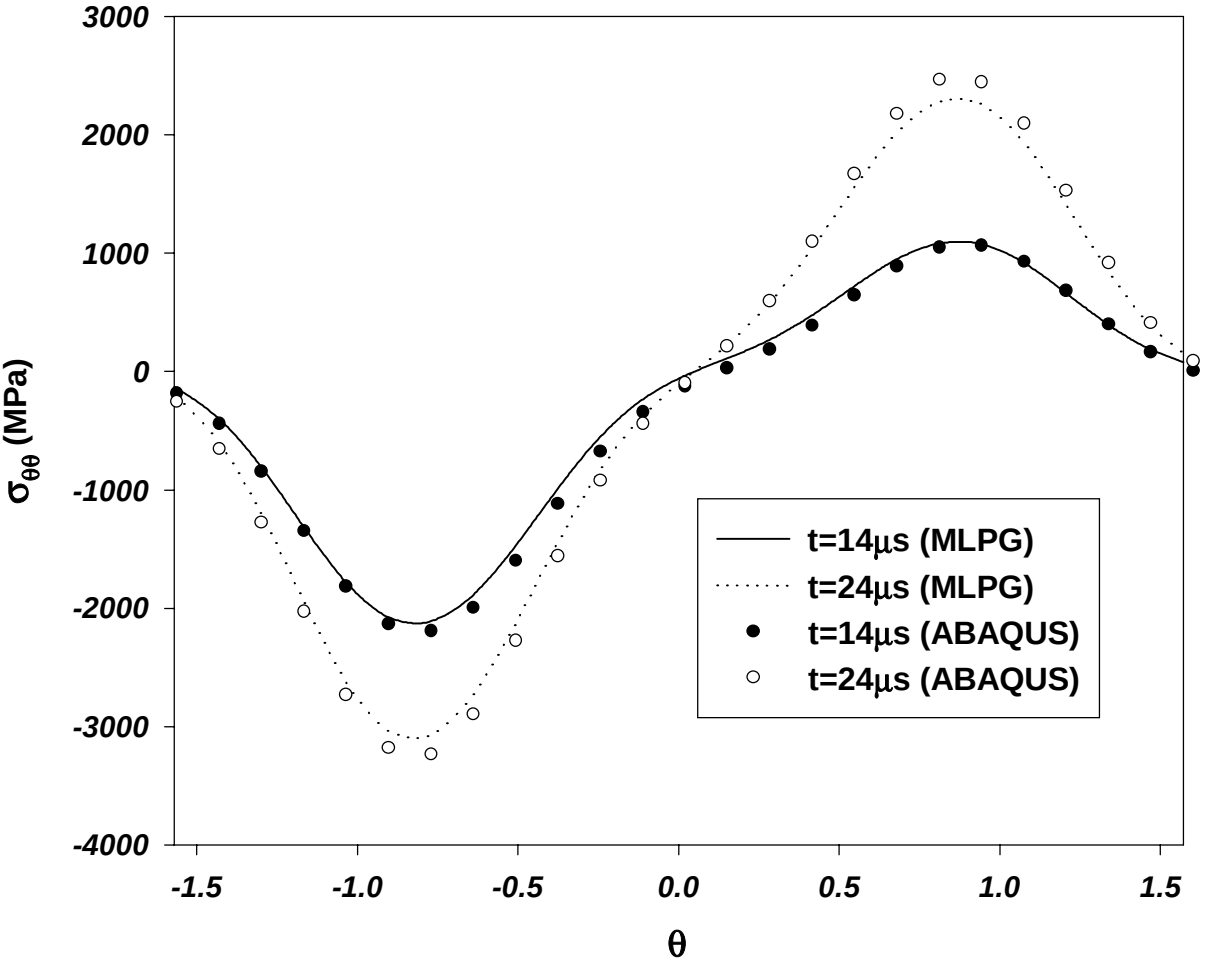

Fig. 4.21a Angular distribution of the hoop stress on the notch surface at two different times

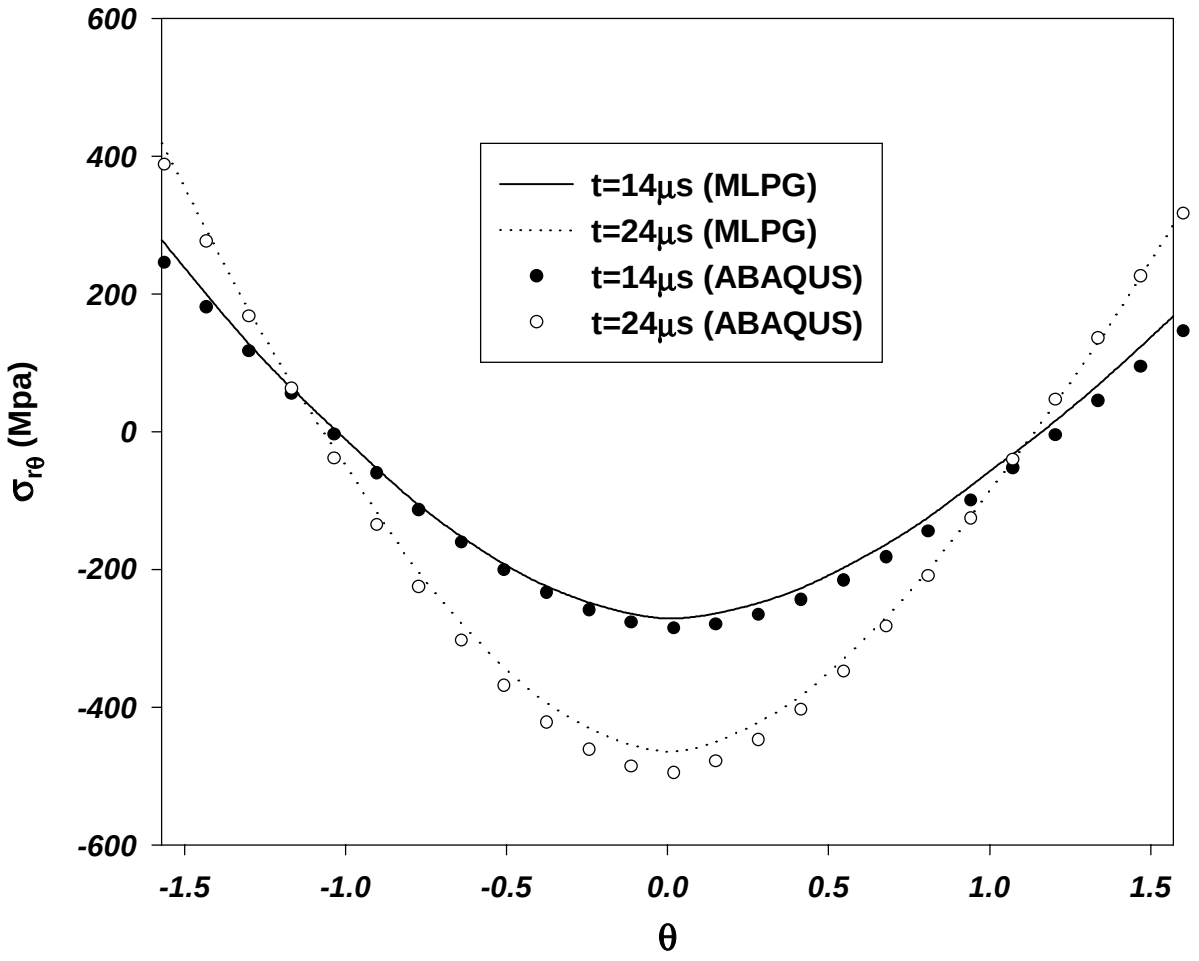

Fig. 4.21b Angular distribution of the shear stress on the notch surface at two different times

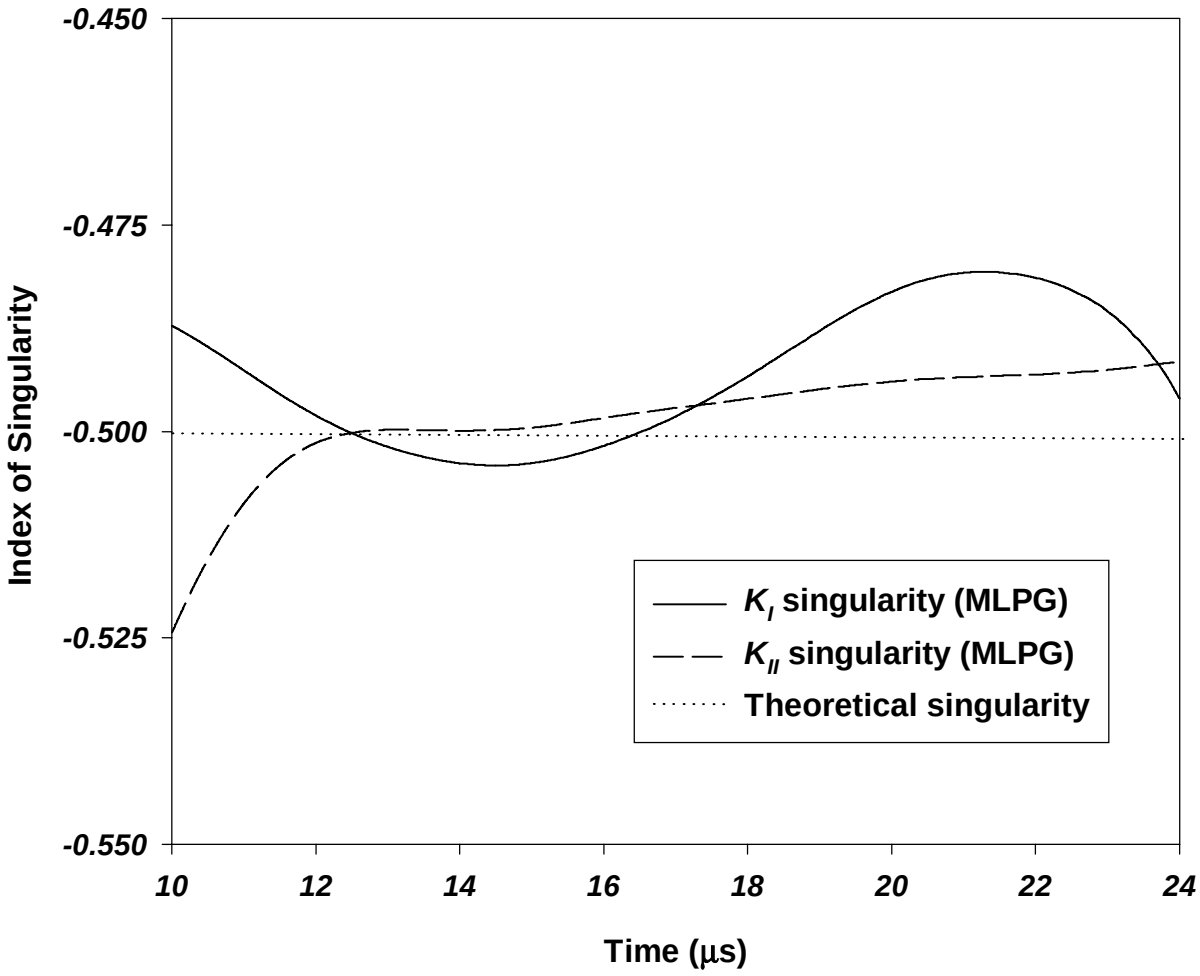

Fig. 4.22a The time history of the index of singularity for mode I and mode II deformations

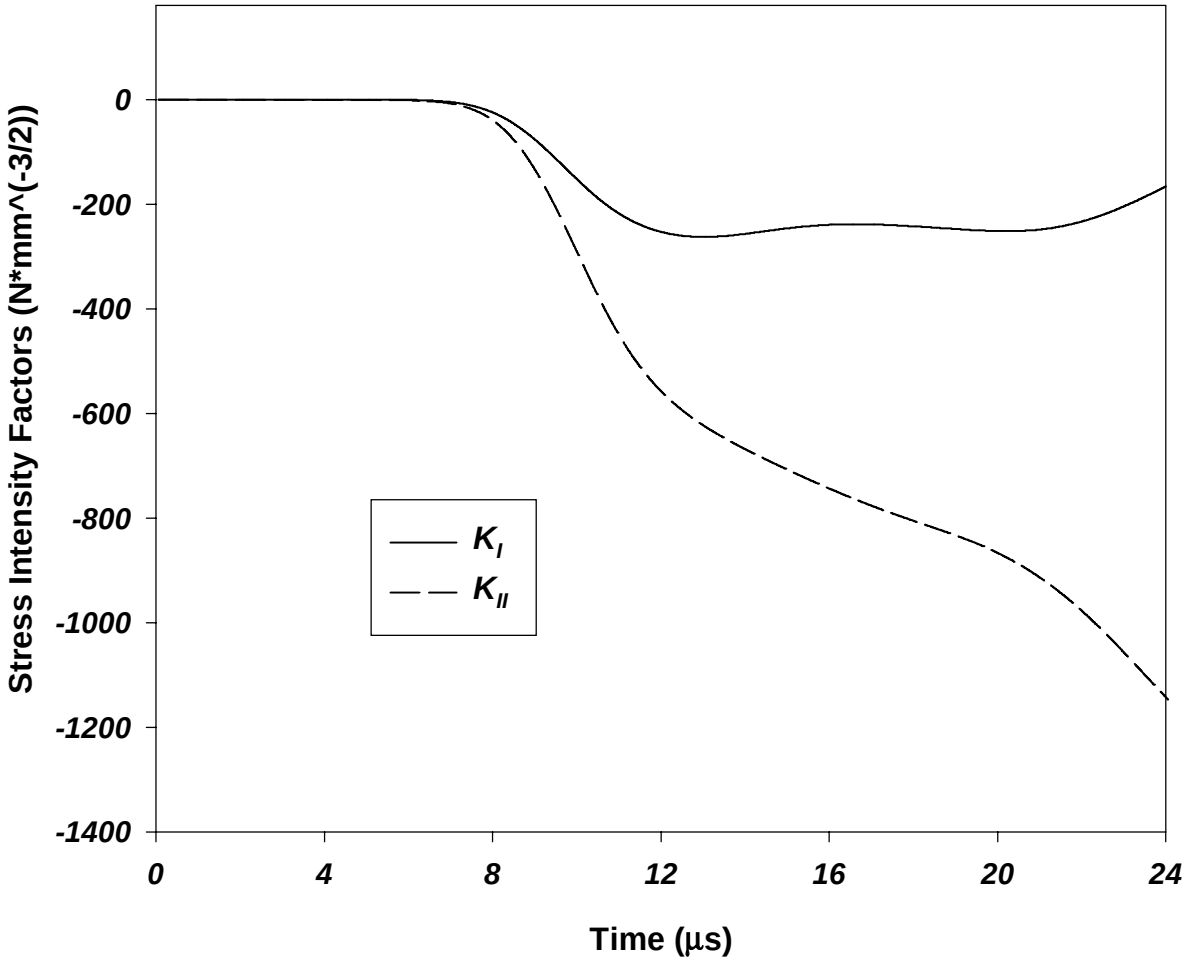

Fig. 4.22b The time history of the stress intensity factors K_I and K_{II}

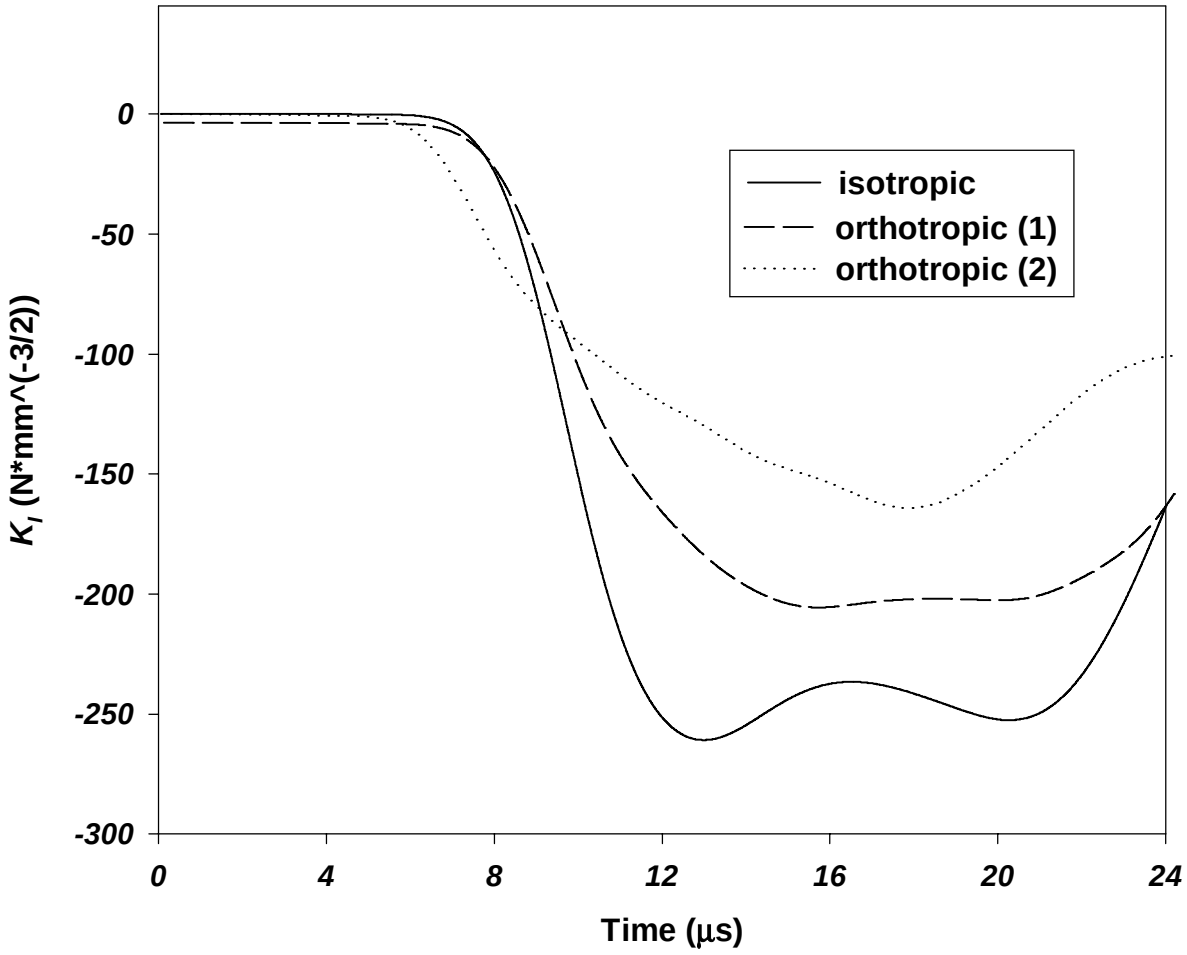

Fig. 4.23a The time history of the stress intensity factor K_I for three materials

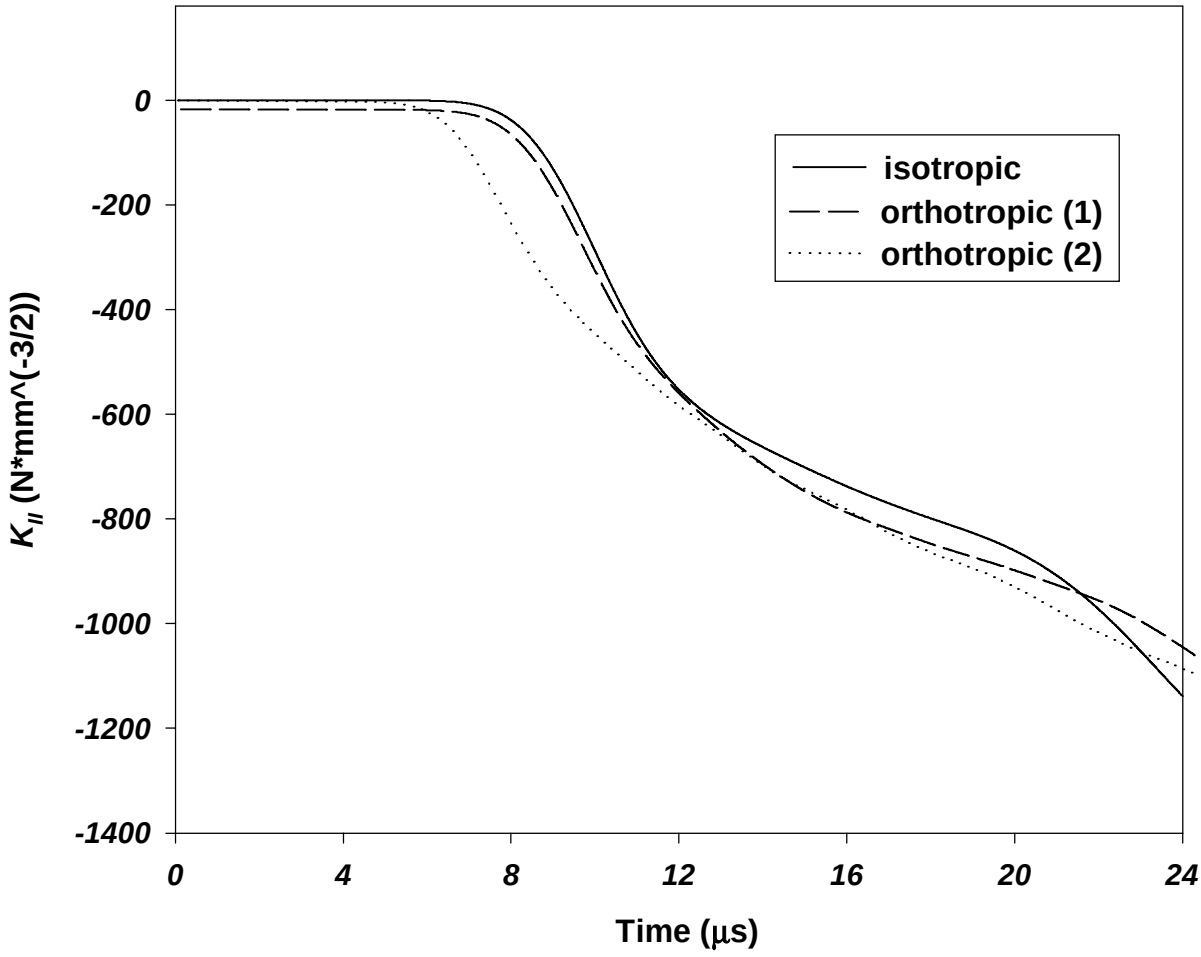

Fig. 4.23b The time history of the stress intensity factor K_{II} for three materials

Chapter 5

Contributions

We have developed a computer code in Fortran based on the meshless local Petrov-Galerkin (MLPG) formulation of plane strain/stress linear elastostatics and elastodynamic problems. The code has been validated by comparing computed results with the analytical solution of three static problems and a dynamic problem. It has then been used to analyze deformation fields near a crack tip in several problems. For this purpose, the monomial basis functions have been enriched with those describing the deformation fields near a crack tip in linear elastic fracture mechanics, and both diffraction and visibility criteria have been incorporated in the problem formulation and also implemented in the code. These criteria make the displacement field discontinuous across the crack faces.

Furthermore, the application of the MLPG formulation to solve a contact problem has been demonstrated. These problems differ from the traditional boundary-value problems since a normal component of the displacement and a relation between the tangential and the normal tractions is given on the same part of the boundary.

Appendix

Energy Release Rates in a Constrained Epoxy Disc with Hookean and Mooney-Rivlin Materials

Abstract

Assuming that the disc material can be modeled either as Mooney-Rivlin or as Hookean and the steel ring enclosing the disc as Hookean, the energy release rates as a function of the crack length are evaluated and compared. Two loadings are considered - one in which the surface of the star shape hole in the disc is loaded by a uniform pressure and the other in which the temperature of the composite body is uniformly raised. It is found that the linear and the nonlinear analyses give qualitatively similar results for the two loadings. For each load, the energy release rate increases with an increase in the starter crack length, reaches a maximum value and then decreases gradually.

Key Words: Energy release rate; Mechanical and thermal loads; Finite element solution; Linear and nonlinear analyses.

A slightly modified version of this appendix has appeared in the *Journal of Theoretical and Applied Fracture Mechanics*, Vol. 38, pp. 165-175, 2002.

1 Introduction

A common problem in industry is to design a part based on the test data for a simple loading condition such as an uniaxial tension test or a torsion test. Whereas test data from a tension test suffices to determine uniquely the two material parameters for an isotropic linear elastic material, it is usually insufficient for the determination of the constitutive relation for a nonlinear elastic material. Here such a problem for an epoxy is analyzed. Assuming that the epoxy can be modeled as a Mooney-Rivlin material, values of the two material parameters from the uniaxial tension test data are found, and then used to compute the energy release rate as a function of the starter crack length in a circular polymeric disc enclosed in a thin steel ring and having a star shaped hole with six symmetrical leaflets at its center. Two loadings, namely, a uniform pressure on the surface of the hole and a uniform temperature rise of the composite body are considered. The steel ring is modeled as a Hookean material. Computed results are compared with those obtained by modeling the epoxy as a Hookean material. It is found that for both loadings and for each one of the twelve crack lengths considered, the analysis of the nonlinear problem gives a smaller value of the energy release rate than that for the linear problem. Results for the Hookean material vary significantly with values of Poisson's ratio in the range 0.49 to 0.4999.

Since a structure has numerous cracks of varying lengths, this type of analysis will help estimate its useful life.

Many investigations [1-6] on crack-tip fields have considered linear strain-displacement relations but nonlinear stress-strain ones. The emphasis has been to derive a path independent integral whose value is a measure of deformation near a crack tip. The often used *J*-integral was given in [2] and it was stated that this is a special case of the energy momentum tensor introduced in [1]. The energy momentum tensor characterizes generalized forces of dislocations in an elastic field. It is shown in [7] that the energy momentum tensor appropriate for finding the force on a disclination in a nematic liquid crystal is, to within an

unimportant hydrostatic pressure, the same as the Ericksen stress tensor [8]. This implies that the so called configurational force on a disclination in a nematic liquid crystal is in fact a real force exerted on the core of the disclination by the surrounding medium; a similar result is proved in [9] for a nonlinear hyperelastic material. For a straight crack propagating at a uniform speed in a linear or a nonlinear elastic material, a path independent integral was derived in [4] from the balance of total energy which for a mechanical problem is also the first law of thermodynamics. It was shown that this path independent integral equals the energy release rate. Whereas the work employed a nonlinear stress-strain relation, strains were linearly related to displacement gradients. It should be mentioned that path independent integrals were used by Gunter in 1934 although not in the same context.

The work reported in [10] seems to be the first to analyze the problem within the framework of nonlinear elasticity for a neo-Hookean material. The problem of a crack in an infinite, thin and incompressible sheet subjected to biaxial tension at infinity was studied by the method of successive approximations which required that deformations be large throughout the entire sheet. An asymptotic plane strain analysis [11,12] of a symmetrically loaded traction free crack in a slab of compressible hyperelastic material showed that the singular field near the crack tip depends strongly on the behavior of the stored energy at large strains. It has been shown [13] that for a generalized Mooney-Rivlin material, the crack opens up in the neighborhood of its tip even if the applied load is antisymmetric with respect to the crack plane. The non-existence of an antisymmetric mode due to the nonlinearity of the global crack problems is also exhibited in [13]. An asymptotic analysis of the plane deformation crack problem for compressible rubberlike materials with Ogden-Ball stored energy function that satisfies the polyconvexity and certain growth conditions was performed in [14]. It showed that the degree of singularity and the leading terms of the local deformation field were exactly the same as those obtained in [11,12] even though the constitutive relations in the two studies were different. For the Ogden-Ball materials the opening angle between the crack faces becomes 180° at the crack tip. The coefficient of the canonical field, which is called the stress intensity factor, can be found only after the global crack problem has been solved.

Mode-I and mixed mode deformations of a crack in a homogeneous sheet made of a generalized neo-Hookean material, analyzed in [15], showed that there exists more than one singular term and the leading singularity is stronger than that predicted by the linearized theory. Whereas these studies considered traction free crack surfaces, the effect of non-conservative surface tractions applied to the crack faces on the energy release rate for 2-dimensional problems was scrutinized in [16]. This work discussed the modification to be made in the usual expression for the energy release rate and also demonstrated that the energy release rate depends upon the constitutive relation used to model the material response. For the problem studied here, numerical solutions indicate that the orders of singularity for the linear and the nonlinear analyses are the same. At a point near the crack tip, the normal strains predicted by the two analyses are nearly the same.

2 Formulation of the Problem

Figure A.1 shows a cross-section of the composite cylindrical body whose length is very large as compared to its diameter. Thus a plane strain state of deformation is assumed to prevail in the body. The star shaped hole at the center has six symmetrically located leaflets; dimensions of different parts are shown in Fig. A.1. The epoxy and the steel casing are modeled as isotropic and homogeneous materials. Initially the body is stress free and at a uniform temperature. Deformations of the body under two types of loads, namely, a uniform pressure on the inner surface of the hole and a uniform temperature rise of the entire body are studied. In each case, the outer surface of the steel ring is taken to be traction free. Because of the symmetry of the geometry and the loading conditions, deformations of only a 30^{o} sector of the body are investigated. Points on the bounding surfaces $\theta = 0^{o}$ and $\theta = 30^{o}$ are constrained to move radially, and tangential tractions on these surfaces are set equal to zero. The epoxy disc is assumed to be perfectly bonded to the steel ring so that displacements and surface tractions are continuous across their common interface.

The referential description of motion is employed to describe deformations of the body, and analyze the static problem. Displacements of a material point are found from the balance of linear momentum and the moment of momentum subject to the aforestated boundary conditions and the following constitutive relations. Deformations of the steel ring are assumed to be infinitesimal and its isotropic material modeled by Hooke's law with Young's modulus = 29 Mpsi, Poisson's ratio = 0.3, and the coefficient of thermal expansion = $6.5\times10^{-6}/{}^{\circ}\mathrm{F}$.

The epoxy is modeled either as a Mooney-Rivlin material or as a Hookean material. For the Mooney-Rivlin material

$$W = C_{10}(\bar{I}_1 - 3) + C_{01}(\bar{I}_2 - 3) + \frac{1}{D_1}(J^{el} - 1)^2, \tag{A.1}$$

where W is the strain energy per unit volume in the reference configuration; C_{10}, C_{01}, and D_1 are temperature dependent material parameters; $\bar{I}_1$ and $\bar{I}_2$ are the first and the second invariants of the deviatoric strain tensor, and are defined as

$$\bar{I}_1 = \bar{\lambda}_1^2 + \bar{\lambda}_2^2 + \bar{\lambda}_3^2, \quad \bar{I}_2 = 1/\bar{\lambda}_1^2 + 1/\bar{\lambda}_2^2 + 1/\bar{\lambda}_3^2. \tag{A.2}$$

Here $\bar{\lambda}_i = J^{-1/3}\lambda_i$; J equals the determinant of the deformation gradient and $\lambda_1, \lambda_2,$ and λ_3 are principal stretches. The shear modulus μ_0 and the bulk modulus K_0 at zero strain are given by

$$\mu_0 = 2(C_{10} + C_{01}), \quad K_0 = 2/D_1. \tag{A.3}$$

The elastic volume ratio, J^{el}, is related to J by

$$J^{el} = J/(1 + \alpha\Delta T)^3, \tag{A.4}$$

where α is the coefficient of thermal expansion and ΔT the change in temperature. For purely mechanical deformations, $\Delta T = 0,\ J^{el} = J,$ and D_1 is assigned a very large value as compared to C_{10} and C_{01} so that deformations are essentially isochoric.

Values of the two material parameters in the Mooney-Rivlin relation found from the uniaxial test data by using the finite element code ABAQUS are

$$C_{10} = 1550 \text{ psi},\ C_{01} = -811.1 \text{ psi}. \tag{A.5}$$

ABAQUS determines material constants through a least-squares-fit procedure which minimizes the relative error in the nominal stress. For *n* nominal axial stress vs. nominal axial strain data pairs, the error

$$\mathrm{E_r} = \sum_{i=1}^{n} (1 - T_i^{\text{com}} / T_i^{\text{test}})^2 \tag{A.6}$$

is minimized. Here T_i^{test} is a stress value from the test data, and T_i^{com} is the corresponding computed value. Computed values of the axial component of the first Piola-Kirchhoff stress tensor vs. the nominal axial strain which equals the change in length/length are compared with the experimental data in Fig. A.2. It is clear that the two sets of data are very close to each other implying thereby that values given in (A.5) of C_{10} and C_{01} are very good. Comparisons of computed results with test data for different loading configurations are needed to ensure that the Mooney-Rivlin relation models well the epoxy material with values (A.5) of C_{10} and C_{01}.

In order to delineate effects of material and geometric nonlinearities, the epoxy was also modeled as Hookean with Poisson's ratio varying from 0.49 to 0.4999 and the shear modulus = 1477.8 psi. As Poisson's ratio approaches 0.5, the material becomes essentially incompressible and is incompressible for Poisson's ratio = 0.5. As shown below, the energy release rate strongly depends upon Poisson's ratio for the Hookean material. The axial stress

vs. the axial strain curve for the Hookean material is also depicted in Fig. A.2. For both linear and nonlinear analyses, the coefficient of thermal expansion for the epoxy material equaled $5.6\times10^{-5}/{}^{\circ}\mathrm{F}$ which is a little less than nine times that for the steel.

With the goal of ascertaining the failure characteristics of the epoxy, the energy release rate as a function of the initial crack length was determined. When the inner surface of the hole and the surface of the starter crack aligned with the $x_1-\text{axis}$ are loaded by a uniform pressure *q*, the energy release rate *G,* for a linear elastic material is given by

$$G=\int_{\Gamma}\left(Wn_1-T_{ij}n_j\frac{\partial u_i}{\partial x_1}ds\right)+\int_{\Gamma_c}q\frac{\partial u_2}{\partial x_1}dx_1, \tag{A.7}$$

where *W* is the strain energy density, **u** the displacement of a point, Γ a closed curve enclosing the crack tip, **n** the outward unit normal to Γ, T_{ij} the stress tensor, a repeated index implies summation over the range of the index, and Γ_c the two crack faces. Note that the last term on the right-hand side of (A.7) represents the work done by the pressure on the crack surfaces. For the thermal load, there is no surface traction on the crack surface and this term makes no contribution to the value of *G*. For homogeneous hyperelastic material, T_{ij} equals the first Piola-Kirchhoff stress tensor.

For the linear elastic problem, the value of the energy release rate will vary approximately as the reciprocal of Young's modulus for the epoxy because the epoxy disc is enclosed in a steel ring which will apply different tractions on the outer surface of the epoxy disc when it's Young's modulus is varied. Numerical experiments indicated that $G\ \alpha\ 1/E$ is valid for the present problem since the steel ring is located far from the crack tip. However, no such conclusion can be drawn for the Mooney-Rivlin material. Furthermore, for the Hookean material, $G\ \alpha\ q^2$, and this proportionality relation is not valid for the Mooney-Rivlin material. Values of material parameters for five nonlinear materials from the same tension test data were found in [16] and the variation of the computed value of the energy

release rate with the pressure q on the crack faces was found to be different for these materials.

3 Computation and Discussion of Results

Because of the complicated geometry and the nonlinearities considered, the problem was analyzed by the finite element method with the commercial code ABAQUS 6.11. The region in the 30^{o} sector was divided into 4824 CPE8H (8-node element with biquadratic interpolation for displacements and linear interpolation for the pressure field) quadrilateral elements with smaller elements near the crack tip. Since the order of singularity at the crack tip for the Mooney-Rivlin material is not well established, the node on a side of an actual element was located at the midpoint of the side. As shown in Fig. A.3, the element size increased gradually with the distance from the crack tip. Two different finite element meshes – one with 2412 elements and the other with 4824 elements - were used to decipher the effect of discretization of the domain on the computed results. No appreciable difference between the two sets of results was found; results reported herein are with the mesh of 4824 elements. For a starter crack of length 1 in., Fig. A.4 exhibits the finite element mesh around the crack tip and five contours used to compute the energy release rate. These contours are comprised of boundaries of consecutive elements in the neighborhood of the crack tip; the first contour starts from the edge of the first element with one node at the crack tip, the second one from the edge of the second element etc. Distances from the crack-tip along the positive x_1 – axis of these five contours equal 0.039, 0.081, 0.127, 0.178 and 0.232 in. respectively.

3.1 Effect of Poisson's ratio

For 1000 psi pressure applied on the surface of the hole and faces of 1-in. long crack, Fig. A.5 depicts the dependence of the energy release rate upon Poisson's ratio, ν, of the disc modeled as a Hookean material. It is clear that the value of the energy release rate depends strongly upon ν. A close examination of the computed stresses and strains indicated that the hydrostatic pressure,

$$p = \frac{2\mu_0 \nu}{(1-2\nu)} \varepsilon_{ii} \tag{A.8}$$

varied noticeably when ν was increased from 0.49 to 0.4999. In equation (A.8) ε_{ij} is the infinitesimal strain tensor. An increase in ν decreases the compressibility of the material which reduces significantly the opening between the crack faces created by the pressure acting on them. This is evident from the deformed shapes of the crack face plotted in Fig. A.6a for different values of ν; note that the vertical scale is much expanded. Vertical displacements in the direction of the applied pressure of points on the crack faces decrease with an increase in Poisson's ratio. The curvature of the deformed crack tip increases with an increase in Poisson's ratio. Higher values of the vertical displacement of points on the crack face result in larger values of the work done by the pressure *q* acting on the crack face and increase noticeably the contribution to the energy release rate made by the last term on the right-hand side of Eq. (A.7).

For a temperature increase of 85^{o}F, values of the energy release rate, plotted in Fig. A.5, do not vary much when ν is increased from 0.490 to 0.4999 mainly because the last term on the right-hand side of equation (A.7) makes null contribution to the energy release rate.

Figure A.6b evinces the variation of the infinitesimal shear strain $\varepsilon_{xy} = \varepsilon_{12}$ at points near the crack tip and lying on the axis of the crack; the abcissa *r* equals the distance of a point from the crack tip. It is clear that Poisson's ratio significantly influences the distribution of the shear strain at points in the vicinity of the crack tip and the order of singularity increases with a decrease in Poisson's ratio from 0.4999 to 0.49.

Variations of the values of the energy release rate with the length of the starter crack for Poisson's ratio = 0.49, 0.495, 0.499 and 0.4999 are depicted in Fig. A.6c. Results are qualitatively similar in that for every length of the starter crack, the value of the energy release rate diminishes with an increase in Poisson's ratio.

Recalling that the Mooney-Rivlin material is incompressible, ν is henceforth set equal to 0.4999 for the Hookean material in comparing results of linear and nonlinear analyses.

3.2 Pressure load

For an internal pressure of 1000 psi, Table A.1 lists values of the energy release rate for different starter crack lengths and the five contours. Except for the case of the very short starter crack of length 0.05 in., the five values of the energy release rate are within 2.5% of each other implying that the integral is path independent. Figure A.7 evinces for the linear and the nonlinear analyses the dependence of the energy release rate on the length of the starter crack. In each case the energy release rate initially increases with an increase in the crack length, reaches a maximum value at a crack length of about 1.0 in. for the linear analysis and about 0.8 in. for the nonlinear analysis and then gradually decreases with an increase in the crack length. The two analyses give qualitatively similar results and the linear analysis gives approximately 20% higher value of the energy release rate. Note that in the nonlinear problem, the tangent modulus decreases with an increase in the strain at a point and thus the material exhibits softening behavior. Recall that in the linear problem, $G \alpha 1/E$, intuititively one will expect that G for the nonlinear problem should be higher than that for the linear problem. However, such is not the case. Contributions for the two cases to the energy release rate made by the last term on the right-hand side of equation (A.7) are the same since as shown in Fig. A.6a the deformed shapes of the crack face coincide with each other. The difference in the values of the energy release rate in the two cases must come from the first term on the right-hand side of equation (A.7). In an attempt to delineate the order of singularity at the crack tip, for a 1-in. starter crack the variation with the distance from the crack tip of the components $\varepsilon_{xx}(E_{xx})$, $\varepsilon_{yy}(E_{yy})$ and $\varepsilon_{xy}(E_{xy})$ of the strain at points on the x_1-axis is plotted in Fig. A.8. Here E_{ij} are components of the Green-St. Venant strain tensor and differ from those of ε_{ij} in quadratic terms in the displacement gradients. It is clear that the magnitude of each strain component at the crack tip for the linear analysis is a little higher than that for the nonlinear analysis. However, at points on the x_1-axis whose distance ahead of the crack tip is more than 10% of the starter crack length, the two analyses

give nearly the same values of strains. As exhibited in Fig. A.6a, the crack tip is blunted for the two analyses. For a starter crack of length 1 in., the maximum in-plane principal stress induced at a point near the crack tip is compressive and it's magnitude equals 219.96 and 261.06 psi respectively for the linear and the nonlinear analyses; the corresponding values of the maximum in-plane principal strains are 0.1231 and 0.1229. It is clear that the limit of validity of infinitesimal deformations has been exceeded.

Figure A.9 exhibits contours of the maximum principal strain in a small region around the crack tip for the two analyses. In each case, only a small region around the crack-tip is intensely deformed, and contours of the principal strain look alike. Contour plots of the maximum in-plane principal stress for the two analyses are also very similar to each other and are therefore omitted.

For a starter crack of length 1 in., the variation of the value of the energy release rate with the pressure q applied on the surfaces of the hole and the crack is plotted in Fig. A.10. One can verify that for the Hookean material the value of the energy release rate is proportional to q^2. Plots of Fig. A.10 reveal that the value of the energy release rate for the Mooney-Rivlin material is smaller than that for the Hookean material and the difference between the two increases with an increase in the applied pressure q.

3.3 Thermal load

The temperature of the disk and the steel ring was increased by 85^{o}F, and the coefficients of thermal expansion for the epoxy and the steel were set equal to $5.6\times10^{-5}/\ ^{o}$F and $6.5\times10^{-6}/\ ^{o}$F respectively. For both linear and nonlinear analyses, values of the energy release rate for each one of the five contours depicted in Fig. A.4 were found to be essentially the same. Figure A.11 shows the variation of the energy release rate with the crack length for the two analyses. The two sets of results agree qualitatively and quantitatively also. For the two analyses the maximum value of the energy release rate occurs for a crack of length 1 in. after which it gradually decreases with an increase in the crack length. As for the thermal loading, the energy release rate for the nonlinear analysis is smaller than that for the linear

analysis but the difference between the two is perceptible only when the length of the starter crack is less than 4 in. For the two analyses, the variation of the energy release rate with the temperature rise is parabolic. For a starter crack of length 1 in. and 85°F temperature rise, the variation with the distance from the crack tip of different components of strain at points ahead of the crack tip and located on the x_1-axis is plotted in Fig. A.12. Whereas for the linear problem, all components of the in-plane strain tensor exhibit a singular behavior near the crack tip, for the nonlinear analysis E_{xy} and E_{yy} appear to be singular but E_{xy} is not. As for the pressure loading, large values of strain are confined to points whose distance from the crack tip is less than 10% of the length of the starter crack. The maximum value of ε_{xy} is nearly 3.5 times that of E_{xy}. However, at a point near the crack tip the magnitude of E_{xx} is about 1.5 times that of ε_{xx} and values of E_{yy} and ε_{yy} are the same. For a crack of length 1 in., the maximum in- plane principal stresses in the epoxy for the linear and the nonlinear analyses equal 2369 and 2276 psi respectively, and the corresponding values of the maximum in-plane principal strains are 0.367 and 0.4156. It is clear that the range of validity of the linear theory has been exceeded.

4 Conclusions

The variation of the energy release rate with the crack length for an epoxy disk with a star shape hole at its center and enclosed in a thin circular steel ring has been studied. Two loadings, namely an internal pressure of 1000 psi and a temperature increase of 85°F, are considered. The epoxy is modeled either as a Mooney-Rivlin material or as a Hookean material. The value of the energy release rate for a Hookean material strongly depends upon the value assigned to Poisson's ratio, ν. It is found that for $\nu = 0.4999$ the variation of computed values of the energy release rate with the crack length obtained from the linear and the nonlinear analyses agree qualitatively; the value from the linear analysis is about 20% higher than that from the nonlinear analysis. Thus the design based on the linear analysis is conservative. The maximum value of the energy release rate for the linear analysis occurs for

a crack of length 1.0 in. but for a crack of length 0.8 in. for the nonlinear analysis. For the thermal load, the two analyses give about the same value of the energy release rate and the maximum value of the energy release rate occurs for a crack length of nearly 1 in.

Even for the linear analysis, values of the energy release rate for the combined thermomechanical load can not be obtained by adding the energy release rates for the corresponding mechanical and thermal loads since the energy release rate is proportional to the square of the applied pressure and to the square of the temperature change.

It is important that the epoxy be characterized more carefully with the test data from different types of experiments. For the present problem, the linear analysis gives qualitatively correct information and provides a reasonably accurate value of the critical crack length for which the energy release rate is maximum. However, this is not true in general since for the simple shearing problem the linear analysis fails to predict the Poynting effect whereas the nonlinear analysis with a Mooney-Rivlin constitutive relation predicts it. Also, results for the nonlinear analysis will depend upon the constitutive relation used to model the material response since it strongly influences the deformation fields near the crack tip.

5 References

[1] J. D. Eshelby, The determination of the elastic field of an ellipsoidal inclusion and related problems, *Proc. of Royal Soc*., London, Ser. A, 241 (1957) 376-936.

[2] J. W. Hutchinson, Singular behavior at the end of a tensile crack in a hardening material, *J. Mech. Phys. Solids* 6 (1968) 13-31.

[3] J. R. Rice and G.F. Rosengren, Plane strain deformation near a crack tip in a power law hardening material, *J. Mech. Phys. Solids* 6 (1968) 1-12.

[4] G. C. Sih, Dynamic aspects of crack propagation: in *Inelastic Behavior of Solids*, edited by M.F. Kanninen, W. F. Adler, A. P. Rosenfield and R. I. Jaffee, McGraw-Hill, (1970) 607-639.

[5] C. F. Shih, Small-scale yielding analysis of mixed-mode plane strain crack problems, in *Fracture Analysis ASTM* 560 (1974) 187-210.

[6] S. M. Sharma and N. Aravas, Determination of higher-order terms in asymptotic elastoplastic crack tip solutions, *J. Mech. Phys. Solids* 39(8) (1991) 1043-1072.

[7] J. D. Eshelby, The force on a disclination in a liquid crystal, *Philosophical Magazine*, 42A (1980) 359-367.

[8] J. L. Ericksen, Equilibrium theory of liquid crystals, in *Advances in Liquid Crystals*, edited by G. Brown, Vol. 2, Academic Press, New York, (1976) 233-298.

[9] R. C. Batra, The force on a lattice defect in an elastic body, *J. Elasticity*, 17 (1987) 3-8.

[10] F. S. Wong and R. T. Shield, Large plane deformations of thin elastic sheets of neo-Hookean material, *Zeitschrift* für *angewandte Mathematik und Physik* 20 (1969) 176-199.

[11] J. K. Knowles and E. Sternberg, An asymptotic finite-deformation analysis of the elastostatic field near the tip of a crack, *J. Elasticity* 3 (1973) 67-107.

[12] J. K. Knowles and E. Sternberg, Finite-deformation analysis of the elastostatic field near the tip of a crack: reconsideration and higher order results, *J. Elasticity* 4 (1974) 201-233.

[13] R. A. Stephenson, The equilibrium field near the tip of a crack for finite plane strain of incompressible elastic materials, *J. Elasticity* 12 (1982) 65-99.

[14] K. Ch. Le and H. Stumpf, The singular elastostatic field due to a crack in rubberlike materials, *J. Elasticity* 32 (1993) 183-222.

[15] P. H. Geubelle and W. G. Knauss, Finite strains at the tip of a crack in a sheet of hyperelastic material: I. Homogeneous case, *J. Elasticity* 35 (1994) 61-98.

[16] J. H. Chang and E. B. Becker, Finite element calculation of energy release rate for 2-d rubbery material problems with non-conservative crack surface tractions, *Int. J. Num. Meth*. *Engng*., 33 (1992) 907-927.

Starter crack's length (*in*)	Analysis Type	Contour				
		1	2	3	4	5
0.05	Linear	0.4166	0.4277	0.4266	0.4268	0.5479
	Nonlinear	0.3563	0.3581	0.3606	0.3640	0.4099
0.1	Linear	0.8143	0.8262	0.8232	0.8234	0.8232
	Nonlinear	0.6883	0.6788	0.6816	0.6897	0.6911
0.2	Linear	1.498	1.525	1.518	1.518	1.518
	Nonlinear	1.209	1.166	1.163	1.175	1.182
0.4	Linear	2.490	2.529	2.518	2.519	2.519
	Nonlinear	2.086	2.026	2.021	2.045	2.055
0.6	Linear	3.006	3.115	3.113	3.114	3.114
	Nonlinear	2.415	2.354	2.350	2.371	2.381
0.8	Linear	3.360	3.429	3.418	3.420	3.420
	Nonlinear	2.761	2.640	2.616	2.636	2.642
1.0	Linear	3.423	3.549	3.546	3.546	3.547
	Nonlinear	2.724	2.609	2.584	2.596	2.602
2.0	Linear	3.211	3.276	3.264	3.265	3.264
	Nonlinear	2.704	2.593	2.560	2.569	2.568
4.0	Linear	2.354	2.384	2.374	2.375	2.375
	Nonlinear	2.148	2.126	2.119	2.136	2.143
5.0	Linear	1.996	2.054	2.045	2.045	2.045
	Nonlinear	1.731	1.704	1.689	1.696	1.697
10.0	Linear	1.063	1.091	1.086	1.086	1.086
	Nonlinear	0.9492	0.9506	0.9458	0.9500	0.9513
15.0	Linear	0.5633	0.5801	0.5774	0.5774	0.5774
	Nonlinear	0.5363	0.5387	0.5334	0.5332	0.5321

Table A.1 Values of the energy release rate computed with the five contours for an internal pressure of 1000 psi, and different starter crack lengths.

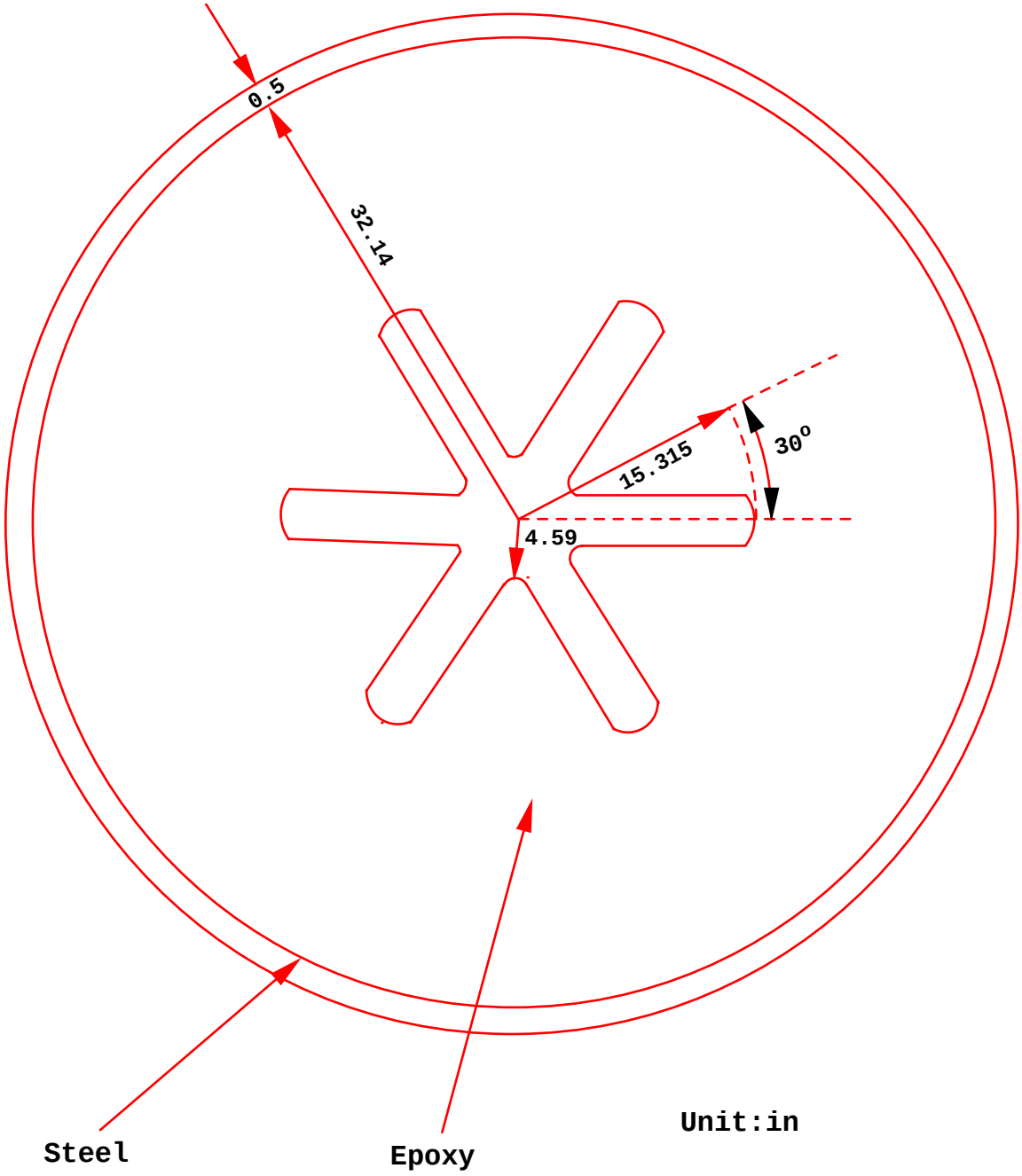

Fig. A.1 A cross−section of the composite cylindrical body whose plane strain deformations are studied

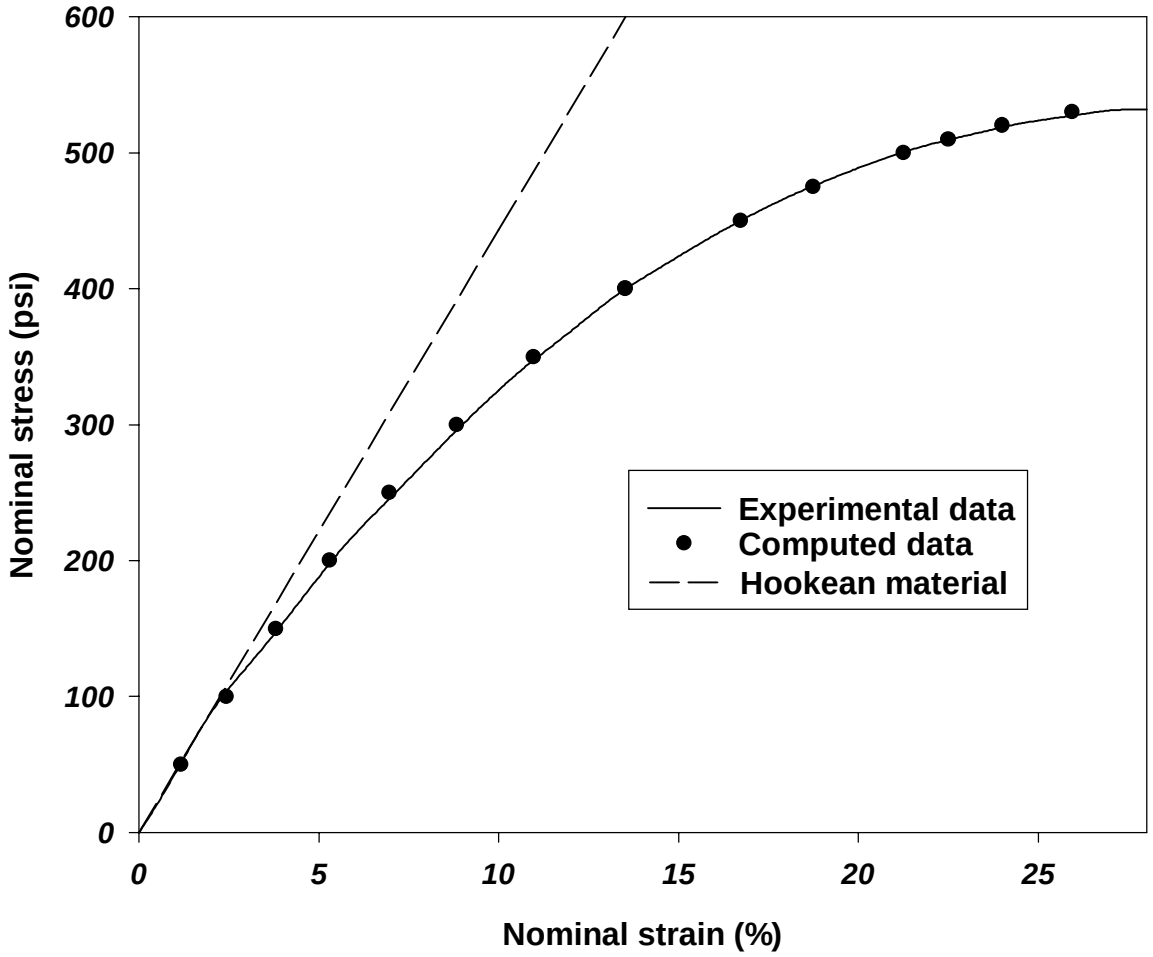

Fig. A.2 A comparison of the computed and the experimental axial nominal stress - axial engineering strain curves for the disk material

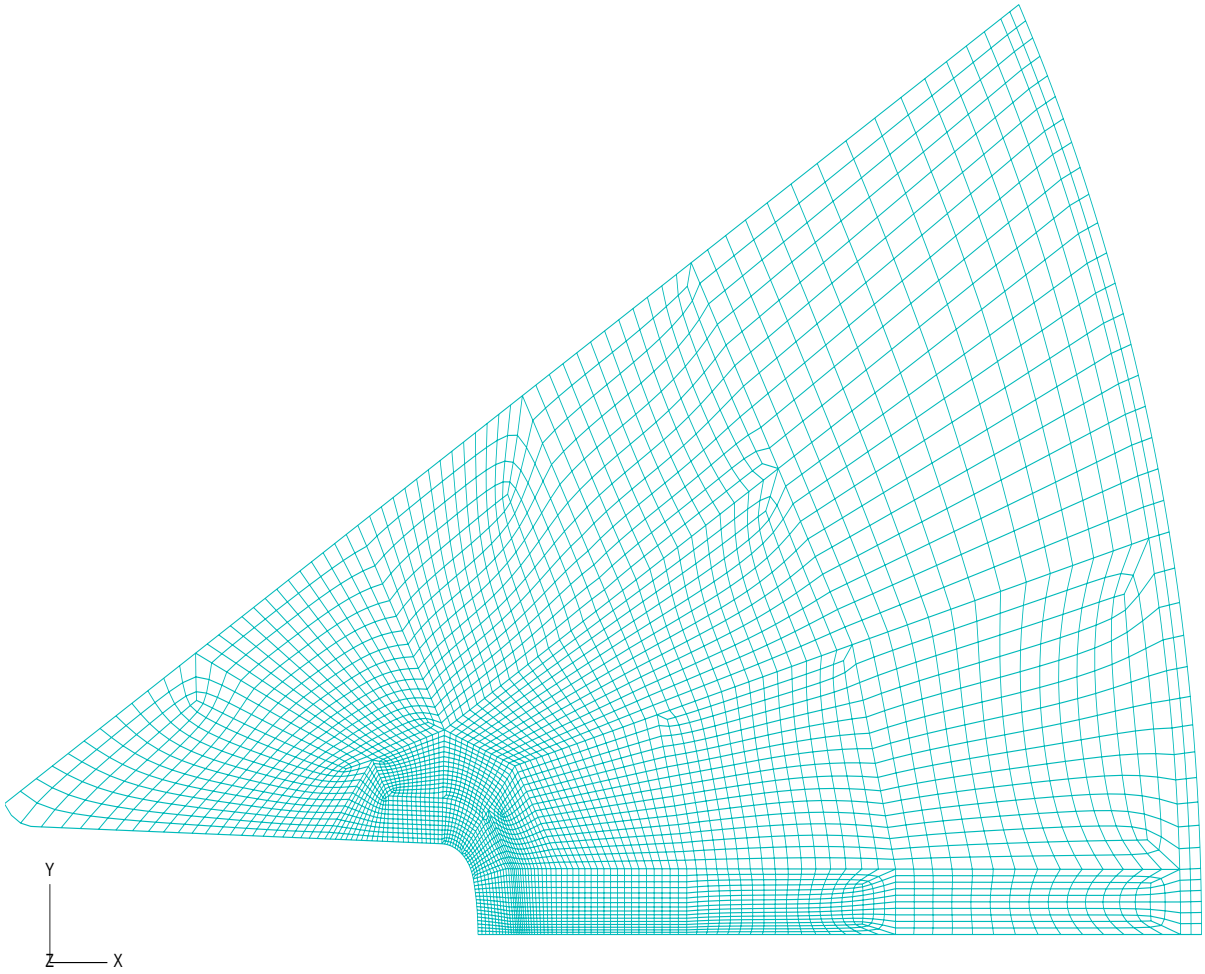

Fig. A.3 A finite element mesh with 4824 elements used for the analysis of the problem

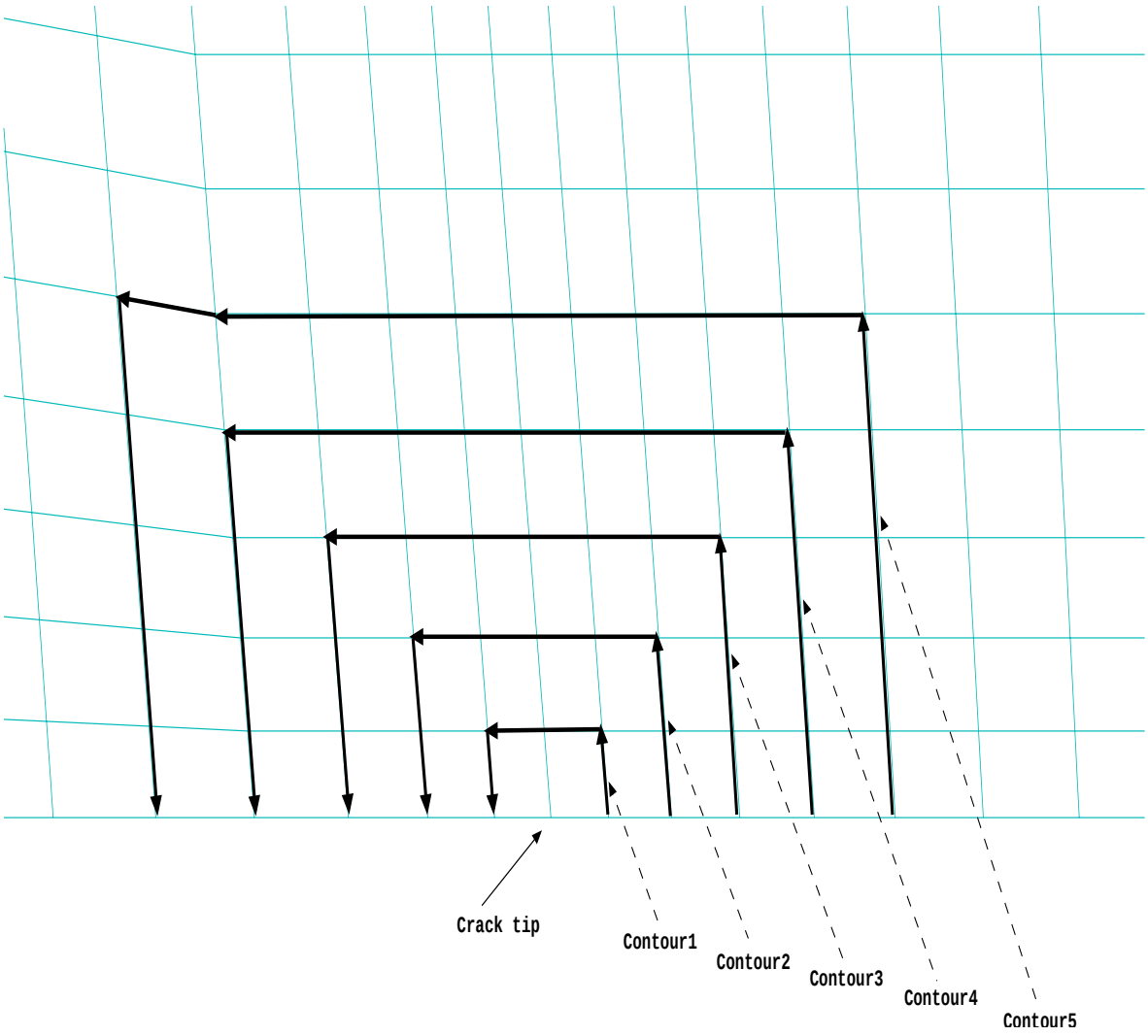

Fig. A.4 Finite element mesh around the crack tip, and five contours used to compute the energy release rate

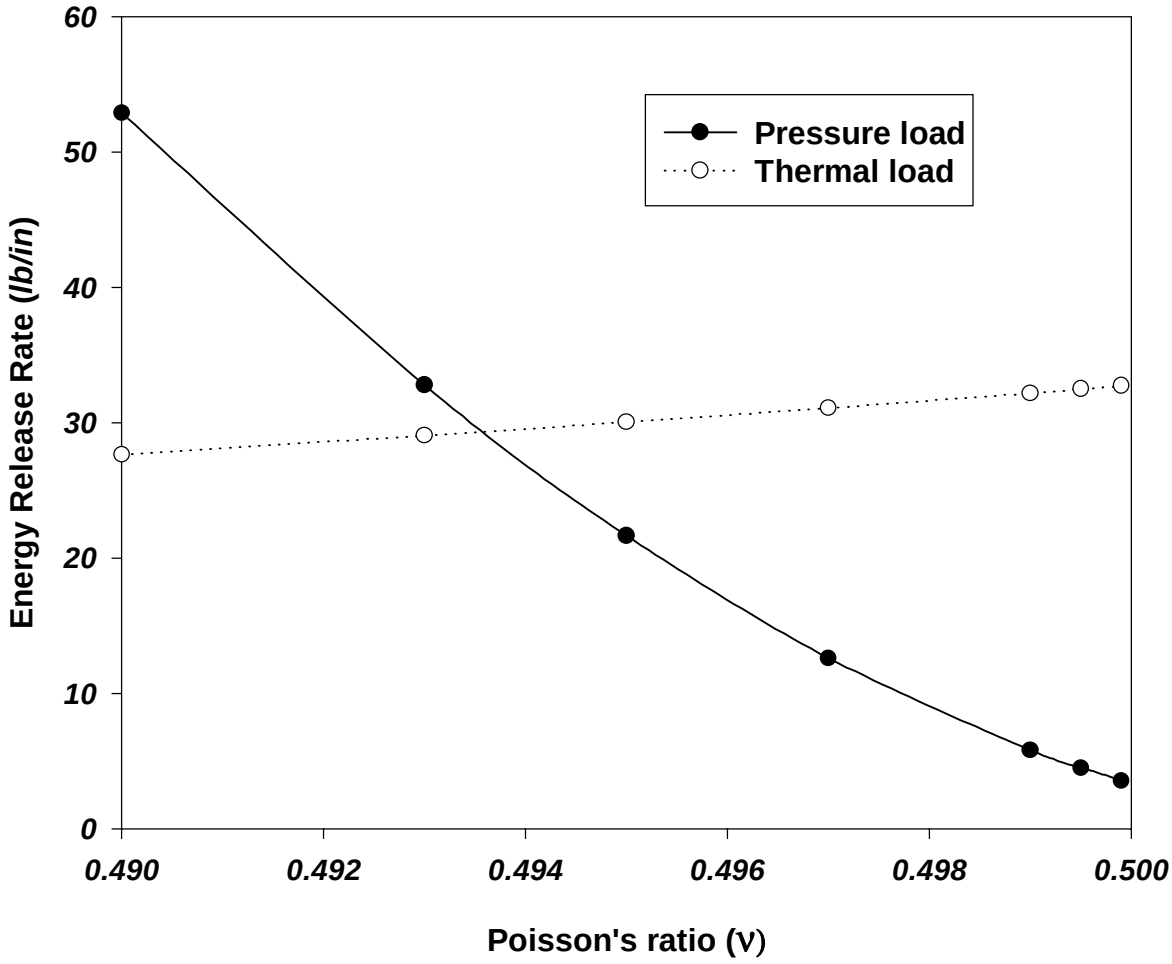

Fig. A.5 For 1000 psi pressure and initial crack length of 1 in., dependence of the value of the energy release rate upon Poisson's ratio, ν. The dependence of the energy release rate upon ν is also shown for a thermal load of 85^{o}F

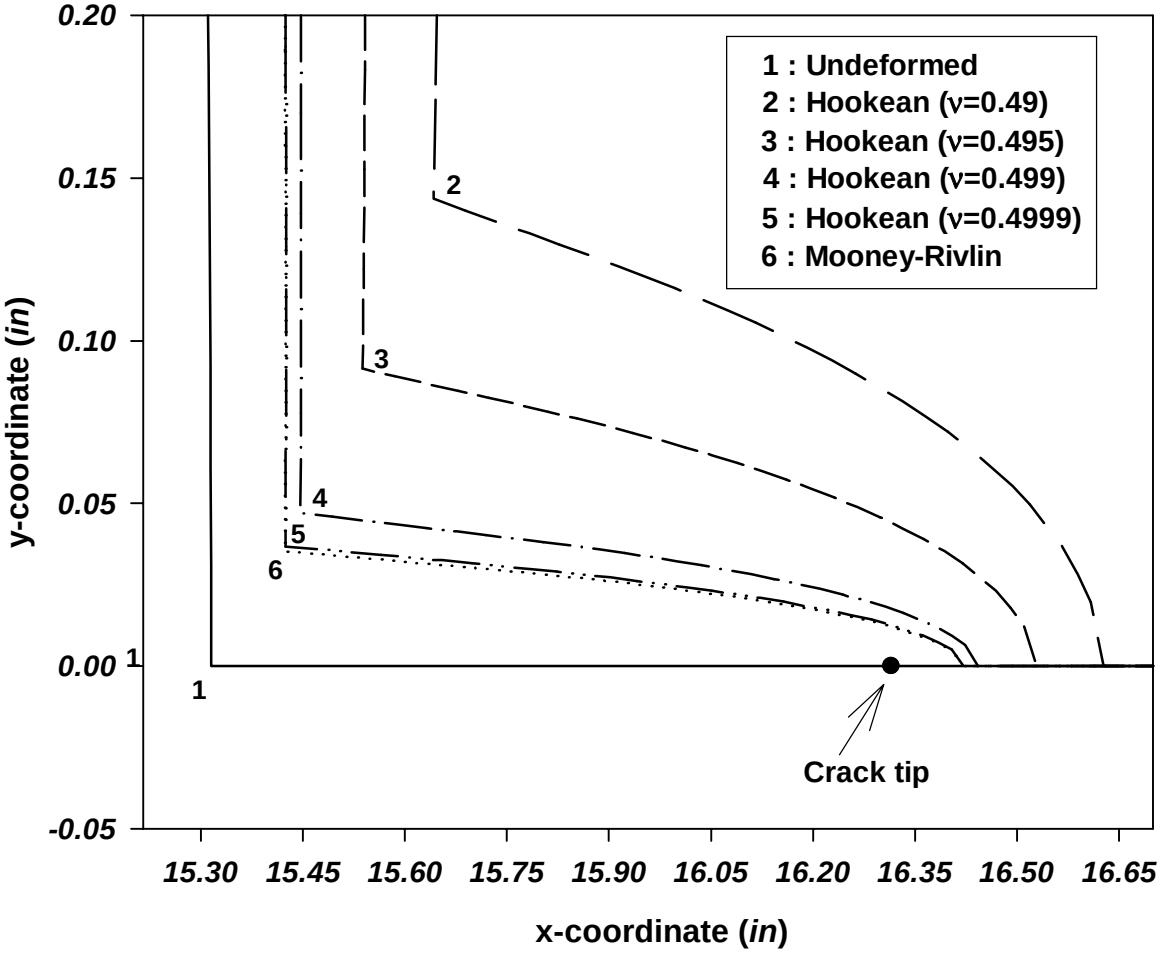

Fig. A.6a Deformed shapes of the crack face for different values of Poisson's ratio

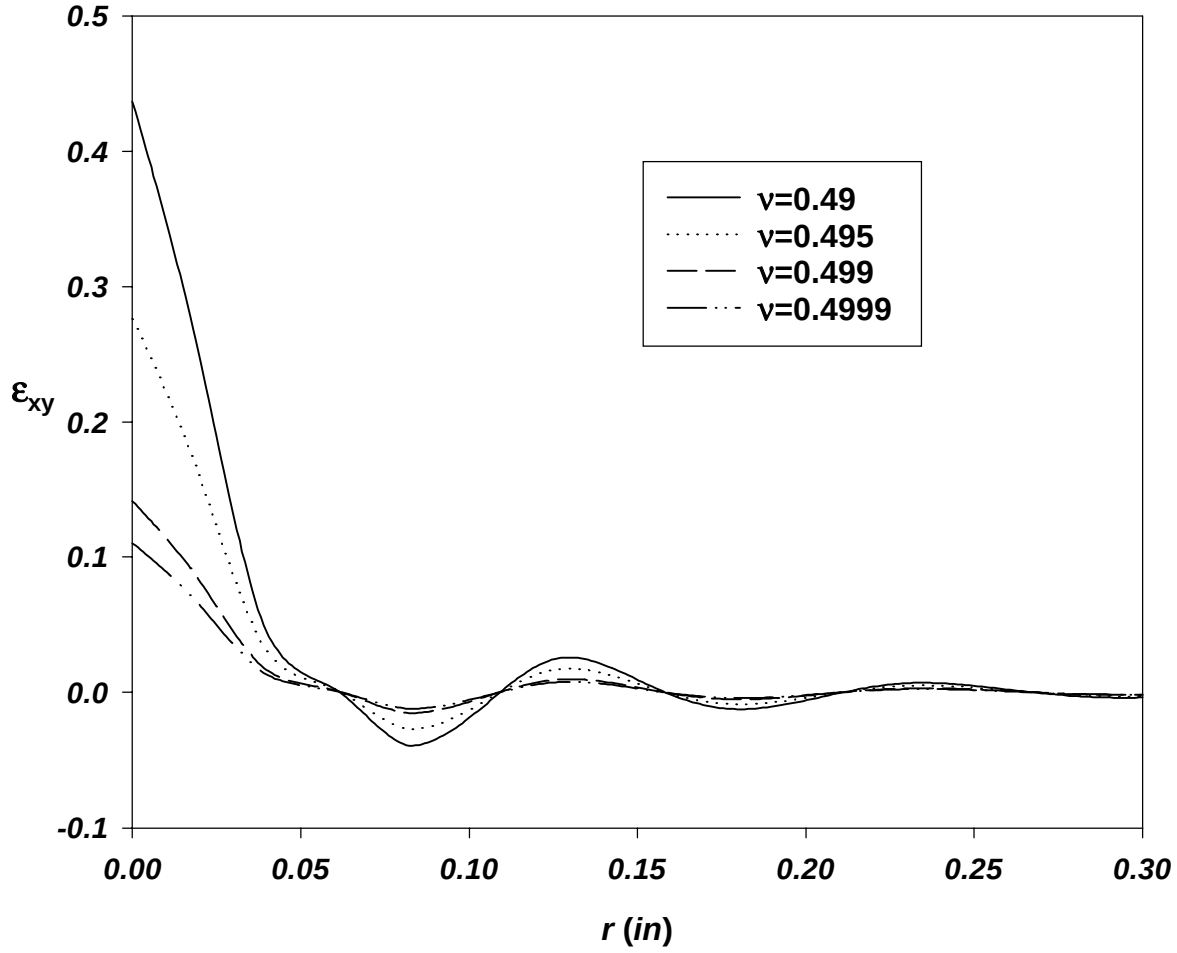

Fig. A.6b For Poisson's ratio equal to 0.49, 0.495, 0.499 and 0.4999, variation with the distance from the crack tip of the infinitesimal shear strain ε_{xy}

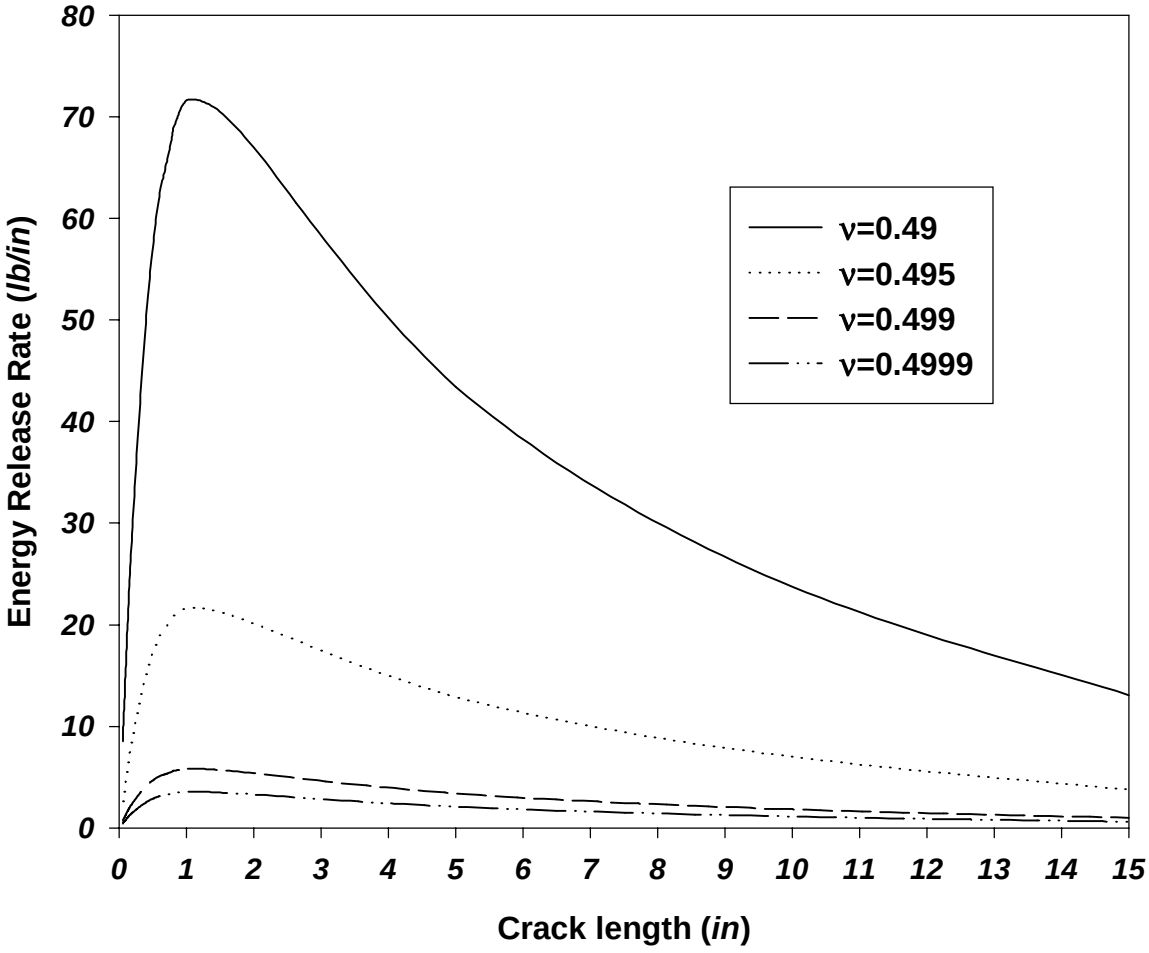

Fig. A.6c For a pressure of 1000 psi, variation of the energy release rate with the length of the starter crack for four values of Poisson's ratio

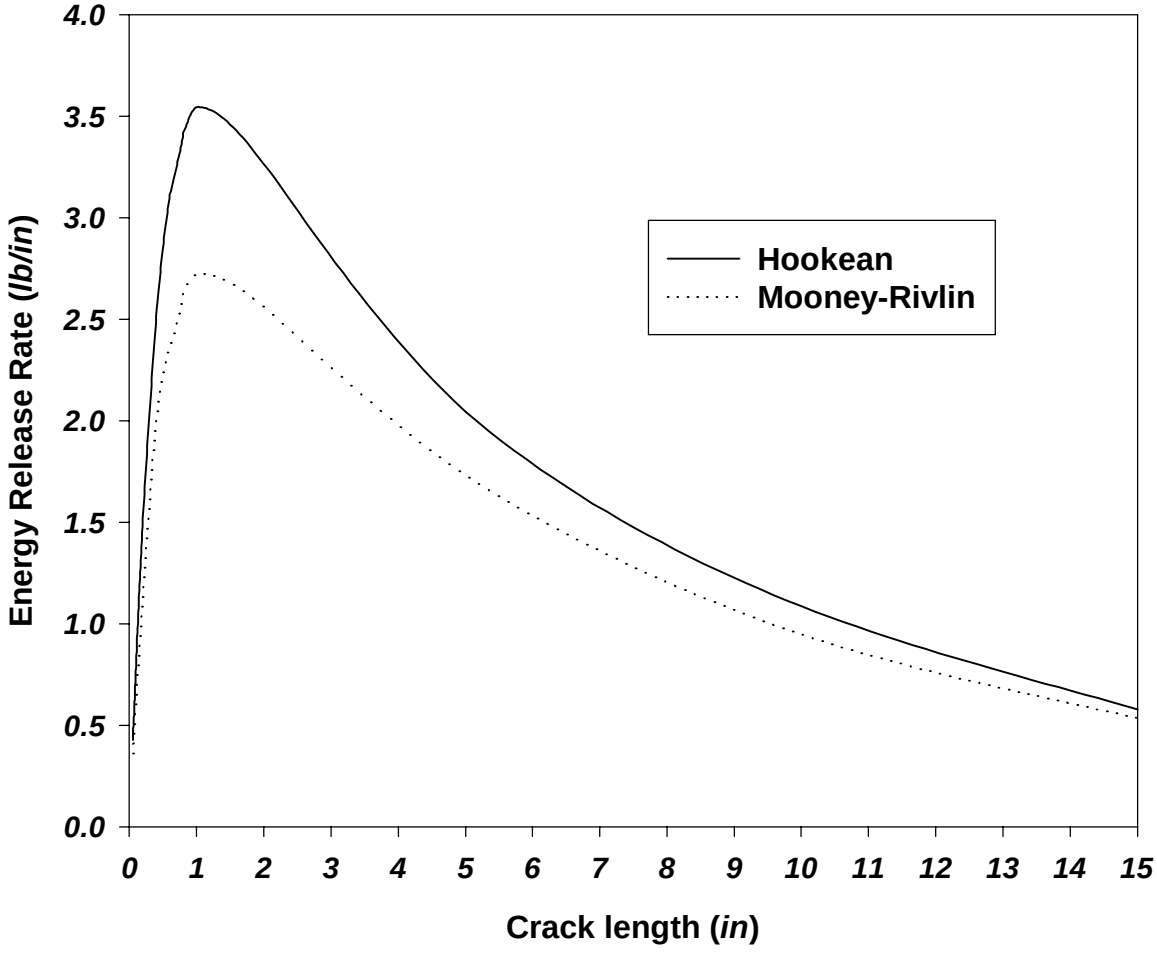

Fig. A.7 Variation of the energy release rate with the crack length when the disk material is modeled either as a Hookean material or as a Mooney-Rivlin material

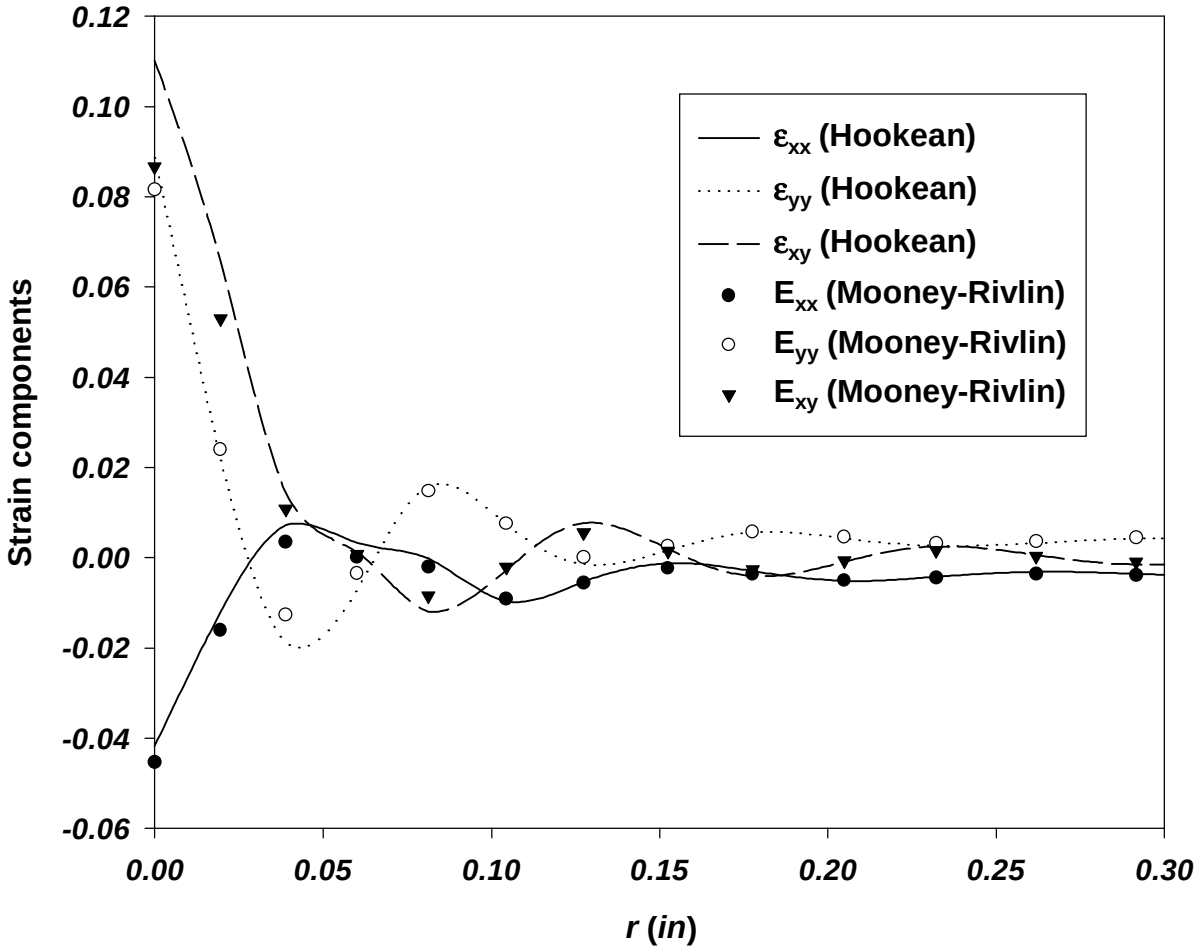

Fig. A.8 For the linear and nonlinear analyses, variation with the distance from the crack tip of strain components at points directly ahead of the starter crack of length 1 in.

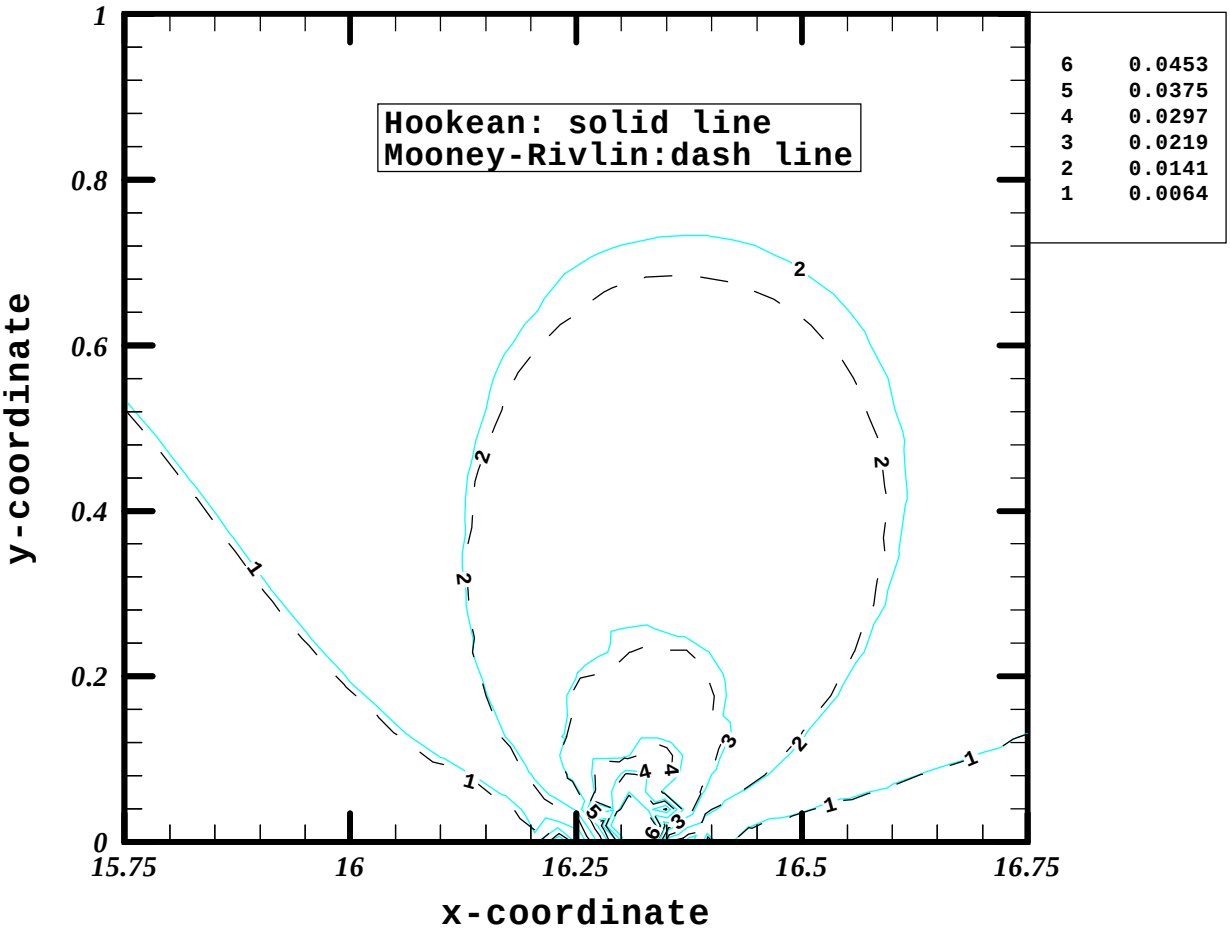

Fig. A.9a Contours of the in−plane maximum principal strain in a one square inch region around the crack tip of 1 in. long crack and applied pressure of 1000 psi

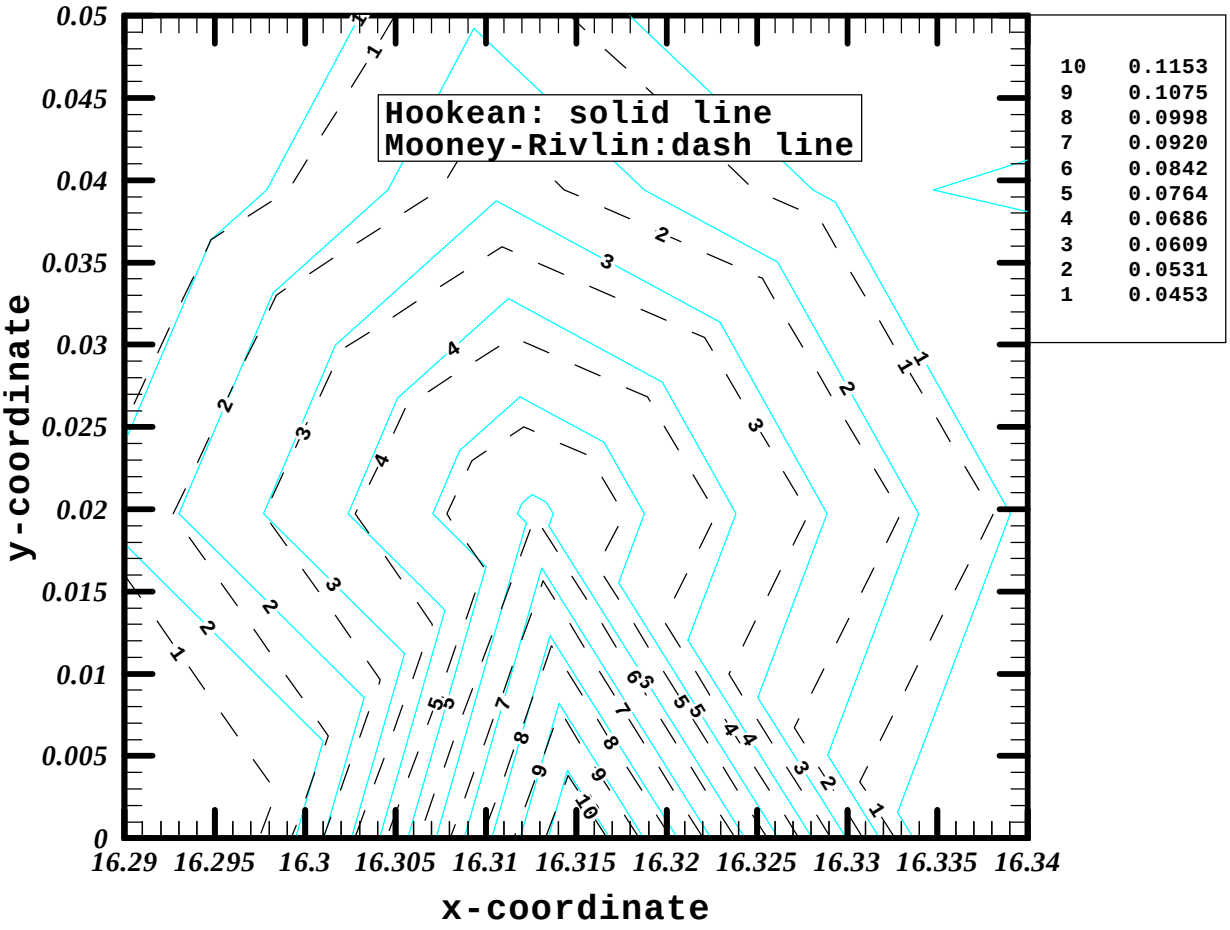

Fig. A.9b Contours of the in−plane maximum principal strain in a 0.05 square inch regioin around the crack tip of 1 in. long crack and applied pressure of 1000 psi

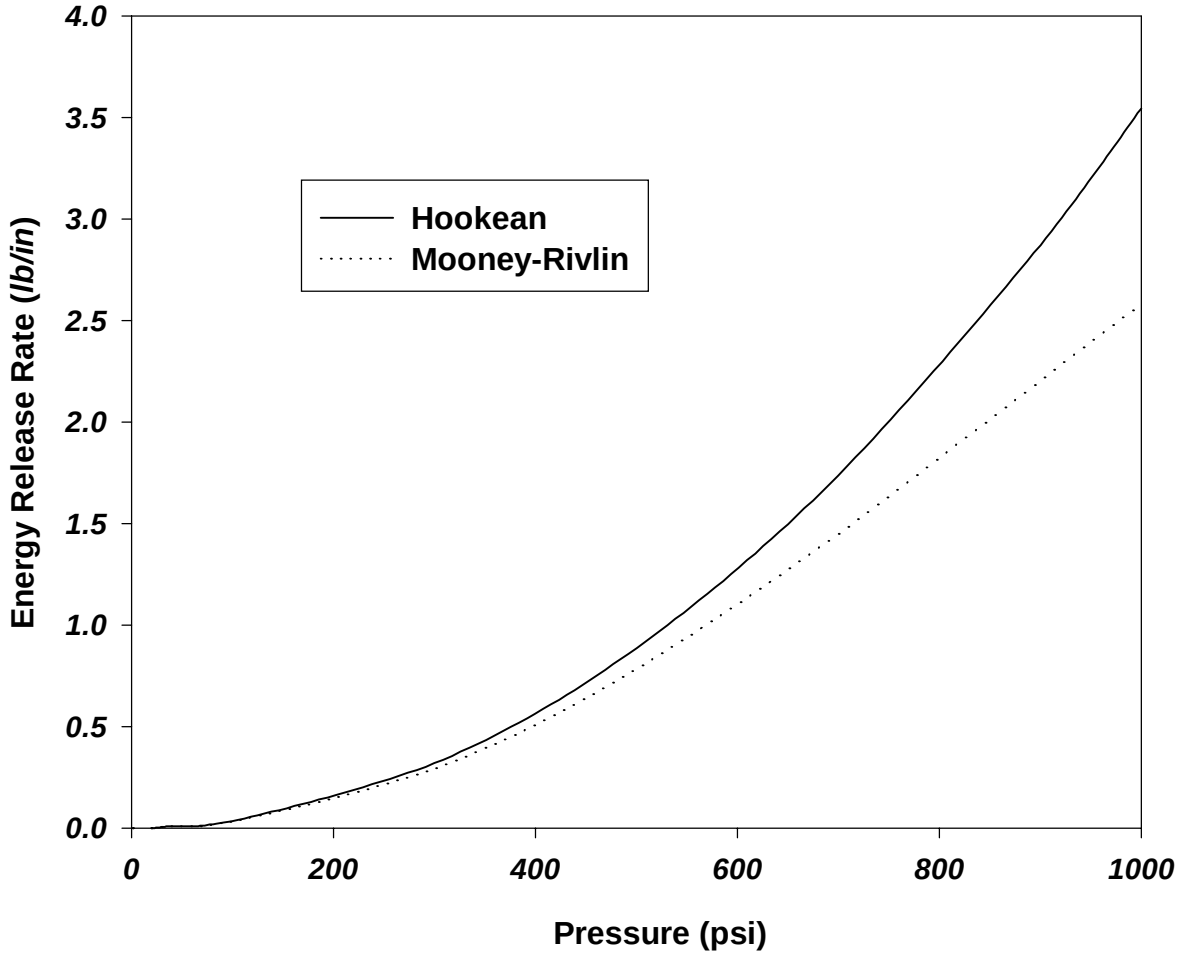

Fig. A.10 For a crack of length 1 in., variation of the value of the energy release rate with the applied pressure q for the linear and nonlinear analyses

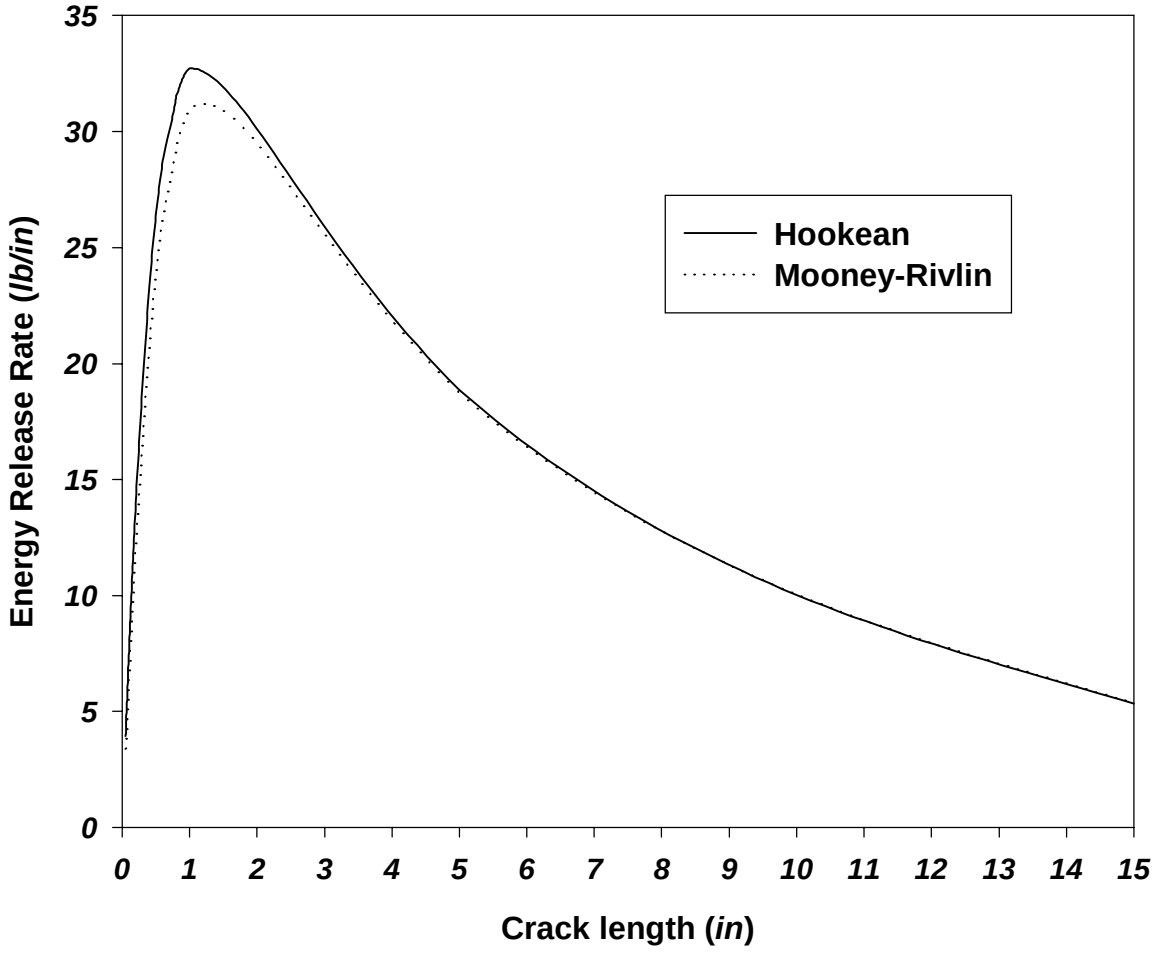

Fig. A.11 Variation of the energy release rate with the crack length for the thermal loading

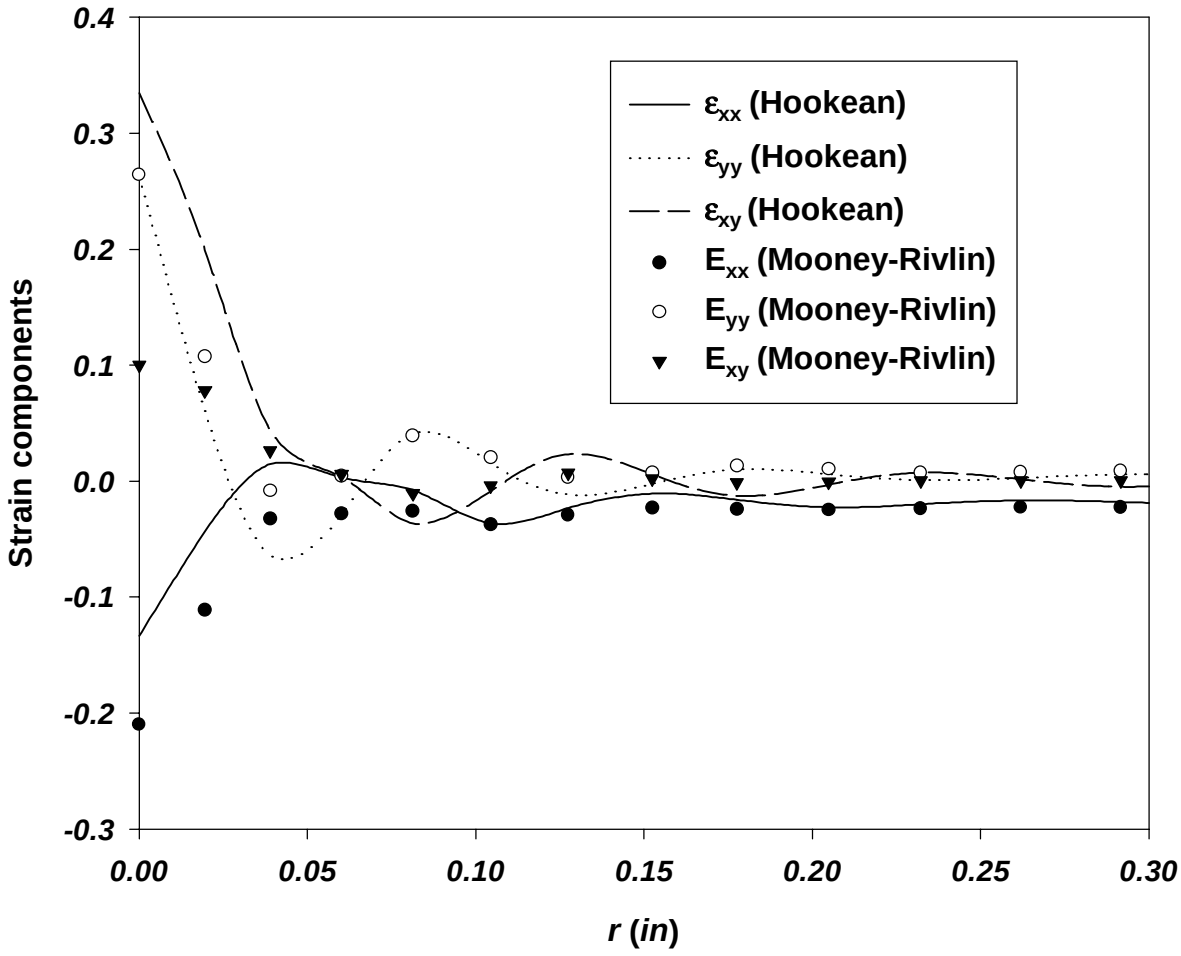

Fig. A.12 For the linear and nonlinear analyses, variation with the distance from the crack tip of strain components at points on the surface of the starter crack of length 1 in. and for a uniform temperature rise of 85°F

Vita

Hsu-Kuang Ching was born in Taoyuan, Taiwan, Republic of China. In June 1990, he graduated from National Chiao-Tung University with a B.S. degree in Civil Engineering. Upon graduation, He entered National Central University to begin graduate studies majoring in Mechanical Engineering and got his M.S. degree in 1992. He joined the doctoral program in the Department of Engineering Science and Mechanics at Virginia Polytechnic Institute and State University in the fall of 1996. He completed his Ph.D. degree in July 2002.